DOCTOR OF PHILOSOPHY

Combined effects of hydrodynamics and cohesive clay on bedform morphology and migration on sandy tidal flats

Lichtman, Ian

Award date:
2017

Awarding institution:
Bangor University

Combined effects of hydrodynamics and cohesive clay on bedform morphology and migration on sandy tidal flats

Ian Dougal Lichtman

A thesis submitted to the School of Ocean Sciences,

College of Natural Sciences,

for the degree of Doctor of Philosophy

University of Wales, Bangor

April 2017

Declaration and Consent

Details of the Work

I hereby agree to deposit the following item in the digital repository maintained by Bangor University and/or in any other repository authorized for use by Bangor University.

Author Name: Ian Dougal Lichtman

Title: Combined effects of hydrodynamics and cohesive clay on bedform morphology and migration on sandy tidal flats.

Supervisor/Department: J. H. Baas, School of Ocean Sciences

Funding body (if any): NERC

Qualification/Degree obtained: PhD.

This item is a product of my own research endeavours and is covered by the agreement below in which the item is referred to as "the Work". It is identical in content to that deposited in the Library, subject to point 4 below.

Non-exclusive Rights

Rights granted to the digital repository through this agreement are entirely non-exclusive. I am free to publish the Work in its present version or future versions elsewhere.

I agree that Bangor University may electronically store, copy or translate the Work to any approved medium or format for the purpose of future preservation and accessibility. Bangor University is not under any obligation to reproduce or display the Work in the same formats or resolutions in which it was originally deposited.

Bangor University Digital Repository

I understand that work deposited in the digital repository will be accessible to a wide variety of people and institutions, including automated agents and search engines via the World Wide Web.

I understand that once the Work is deposited, the item and its metadata may be incorporated into public access catalogues or services, national databases of electronic theses and dissertations such as the British Library's EThOS or any service provided by the National Library of Wales.

I understand that the Work may be made available via the National Library of Wales Online Electronic Theses Service under the declared terms and conditions of use (http://www.llgc.org.uk/index.php?id=4676). I agree that as part of this service the National Library of Wales may electronically store, copy or convert the Work to any approved medium or format for the purpose of future preservation and accessibility. The National Library of Wales is not under any obligation to reproduce or display the Work in the same formats or resolutions in which it was originally deposited.

Statement 1:

This work has not previously been accepted in substance for any degree and is not being concurrently submitted in candidature for any degree unless as agreed by the University for approved dual awards.

Signed …….. (candidate)

Date ……..

Statement 2:

This thesis is the result of my own investigations, except where otherwise stated. Where correction services have been used, the extent and nature of the correction is clearly marked in a footnote(s).

All other sources are acknowledged by footnotes and/or a bibliography.

Signed …….. (candidate)

Date ……..

Statement 3:

I hereby give consent for my thesis, if accepted, to be available for photocopying, for inter-library loan and for electronic repositories, and for the title and summary to be made available to outside organisations.

Signed …….. (candidate)

Date ……..

<u>Statement 4</u>:

I agree to deposit an electronic copy of my thesis (the Work) in the Bangor University (BU) Institutional Digital Repository, the British Library ETHOS system, and/or in any other repository authorized for use by Bangor University and where necessary have gained the required permissions for the use of third party material.

In addition to the above, I also agree to the following:

1. That I am the author or have the authority of the author(s) to make this agreement and do hereby give Bangor University the right to make available the Work in the way described above.

2. That the electronic copy of the Work deposited in the digital repository and covered by this agreement, is identical in content to the paper copy of the Work deposited in the Bangor University Library, subject to point 4 below.

3. That I have exercised reasonable care to ensure that the Work is original and, to the best of my knowledge, does not breach any laws – including those relating to defamation, libel and copyright.

4. That I have, in instances where the intellectual property of other authors or copyright holders is included in the Work, and where appropriate, gained explicit permission for the inclusion of that material in the Work, and in the electronic form of the Work as accessed through the open access digital repository, *or* that I have identified and removed that material for which adequate and appropriate permission has not been obtained and which will be inaccessible via the digital repository.

5. That Bangor University does not hold any obligation to take legal action on behalf of the Depositor, or other rights holders, in the event of a breach of intellectual property rights, or any other right, in the material deposited.

6. That I will indemnify and keep indemnified Bangor University and the National Library of Wales from and against any loss, liability, claim or damage, including without limitation any related legal fees and court costs (on a full indemnity bases), related to any breach by myself of any term of this agreement.

Signature: …… Date : ……..

Abstract

Natural sediments can be made up of a varied mixture of mineral and organic material, reworked and stabilised by physical and biological processes. Knowledge of sedimentary processes is required for sediment transport models, which are essential for managing morphological change in coastal and estuarine environments. Many of these environments are dominated by mixtures of sand and mud. While good sediment bedform predictors are available for clean sands, there is limited knowledge of the behaviour of mixed sediments composed of cohesive mud and non-cohesive sand and this could limit the applicability of predictors based on clean sand.

Recent laboratory experiments on cohesive and non-cohesive sediments, influenced by biogenic stabilisation, have shown that bedform dimensions decrease with increasing bed cohesive content. However, as bedforms developed and migrated along the bed, mud and biogenic polymers were winnowed from the bed into suspension. This thesis extends these laboratory results to assess the effect of cohesive material on sediment dynamics in a natural mixed sediment environment. To this end, fieldwork was carried out on tidal flats in the Dee estuary, UK, collecting measurements of the hydrodynamics, bed morphology and seabed properties, over a two week period covering a spring-neap cycle.

It was found that the cohesive content of the bed varies with hydrodynamic forcing, and increasing bed cohesive clay content reduces bedform dimensions, effects the development of bedform plan morphology and reduces the rate of bedform migration and bed material transport. The amount of biological cohesive material (Extracellular Polymeric Substances, EPS) in the bed sediment was found to vary linearly with the cohesive clay content. Increasing bed cohesive clay reduced bedform dimensions and it would not be expected for bedforms to develop above 4 vol% cohesive clay content, in these field conditions. Bed material transport rate is reduced by increasing bed cohesive clay below about 3 vol%, and above this limit the bedforms appeared to stop migrating. Overall, sediment cohesion has the effect of making bedforms lower in height and shorter in length, and slows the bedform migration and material transport. Some current bedforms were seen to scale with water depth and were larger than expected for current ripples; these are described as transitional bedforms between ripples and dunes. As mixed cohesive sediment is found in many coastal areas worldwide, there is the potential for aspects of these results to have global relevance, if applied to regional models for sediment transport and coastal morphology.

Keywords: mixed sediment dynamics, physical and biological cohesion, bedform morphology and migration, tidal flats, estuaries

Contents

List of figures

List of tables

Acknowledgements

Thanks to:

Peter Thorne, Jaco Baas and Laurent Amoudry for supervising this work. Also to Jonathon Malarkey for his additional comments and support.

National Oceanography Centre, Liverpool (NOCL) for hosting me during this project. This work used the NOC LIVLJOBS high performance computers, and relied on the support of NOCL IT and finance services.

Richard Cooke for organising the fieldwork and running the instrumentation. In addition, I am grateful to the NOCL Ocean Technology and Engineering group for instrument set up and deployment during the fieldwork, and to the Liverpool Bay Coastal Observatory for the weather data.

The algorithms for the 3D-ARP processing and the PUV method were written by Paul Bell and Judith Wolf, respectively. Paul Bell also kindly provided the Radon transform method for correcting the bedform orientation and the solution to the problem with swath offset of the ripple profiler.

The COHBED project team, Louise O'Boyle and Saulo Meirelles Nunes for discussions and comments.

The library services of Bangor University, National Oceanographic Library and University of Liverpool.

Thanks to the anonymous reviewers who commented on the material in the bedform migration and transport chapter.

Thanks to the examiners Robert Lafite and Martin Austin for their comments.

To my parents and Lucy.

This work was funded by NERC and carried out as part of the NERC funded project 'Realistic Sedimentary Bedform Prediction: Incorporating Physical and Biological Cohesion (COHBED)' (Grant reference: NE/I027223/1). All data are available upon request and are banked at the British Oceanographic Data Centre (http://www.bodc.ac.uk/).

1 Introduction

Sediments forming a mobile substrate can transport pollutants and nutrients in the marine environment. The processes that affect the transport of these sediments effect coastal morphology. Sediments provide a habitat for algae, invertebrates, fish and birds, and host dormant phytoplankton cysts and fish eggs. Natural sediments are usually complex and can be made up of a varied mixture of mineral and organic material, reworked and stabilised by physical and biological processes. The fate of sediment is important in the operation and maintenance dredging of channels and harbours, for the navigation of shipping in coastal and estuarine areas. These sedimentary environments are important for the ecology and economy of the UK, protecting the coastline from the forces of the sea and act as a filter where pollutants collect and are eventually degraded (Natural England, 1998; Halcrow, 2010a; Polton *et al*., 2011; Baas, 2013). Accurately modelling the sources, pathways and sinks of sediment can help improve environmental management and reduce dredging costs (Souza and Lane, 2013). In 2009, a UK wide workshop on sediment dynamics research strategy identified the need to prioritise research on the effects of cohesive and mixed sediments, sediment-biological interactions and near-shore sediment processes (Souza *et al*., 2010). Such research should aim to improve regional sediment transport models for developing better coastal protection and to understand the effects of renewable energy devices on coastal and estuarine sediment transport (Souza *et al*., 2010).

Sediment transport models are essential tools for managing coastal morphological change, maintaining navigation channels and understanding the impacts of climate-induced habitat change in coastal and estuarine environments (Cowell *et al*., 1995; Davies and Thorne, 2008; Amoudry and Souza, 2011; Jones *et al*., 2013; Souza and Lane, 2013). Many of these environments are dominated by mixtures of sand and mud (Flemming, 2002; Waeles *et al*., 2008). While reasonably accurate sediment transport predictors are available for pure sands, there is a gap in knowledge on the behaviour of mixed sediments composed of natural cohesive mud (clay and silt) and non-cohesive sand (Souza *et al*., 2010; Amoudry and Souza, 2011; Manning *et al*, 2011; Spearman *et al*., 2011; Aldridge *et al*., 2015). Existing predictors mostly use a median sediment grain diameter, assuming a narrow, unimodal, particle size distribution. Under natural conditions, deposited beds may be comprised of mixed sediments affected by both physical and biological cohesion. Physical cohesion is caused by electrostatic bonds between clay minerals. Biological cohesion results from the production of extracellular polymeric substances (EPS) by microphytobenthos and larger benthic organisms (Paterson and Black, 1999; van de Koppel *et al*., 2001; Black *et al*., 2002; Winterwerp and van Kesteren, 2004; Wotton, 2004; Tolhurst *et al*., 2009).

This natural complexity of mixed cohesive sandy sediment could limit the applicability of standard predictors based on clean sand. Recent laboratory experiments mixing cohesive and non-cohesive sediments, and adding bacterial polymers (xanthan gum) as a proxy for natural biogenic stabilisation, have shown that bedform dimensions decrease with increasing bed cohesive content (Baas *et al*., 2013; Malarkey *et al*., 2015; Schindler *et al*., 2015; Parsons *et al*., 2016). However, it has also been shown that as bedforms are formed and migrate along the bed, mud and biogenic polymers are selectively entrained from the bed into suspension, in a process known as winnowing (Baas *et al*., 2013; Malarkey *et al*., 2015; Parsons *et al*., 2016).

The overall goal of this work is to assess the effect of cohesive material on sediment dynamics, in a natural environment of mixed sediment tidal flats. To this end, fieldwork was carried out on tidal flats in the Dee estuary, UK. Collocated measurements of the hydrodynamics, bed morphology and seabed properties were taken, over a two week period covering a spring-neap cycle. Although limited to sediment with small amounts of cohesive clay content, 0.4 to 5.4 vol%, this research helps fill the gap between existing knowledge of pure sand sediment and mud dominated sediment. The dynamics of bedforms of mixed cohesive sand have not previously been studied in field conditions and the results of this thesis should help improve the modelling of bedform dynamics for mixed sediments. As mixed cohesive sediment is found in many coastal areas worldwide, there is the potential for aspects of these results to have global relevance, if applied to regional models for hydrodynamics, coastal morphology and sediment transport.

1.1 Motivation

The motivation for this project is to improve the formulation of the dynamical processes of mixed sediments, of mud and sand influenced by physical and biological cohesion, for the improvement of regional scale models used in coastal management. Accurate sediment transport models are essential for the management of sea defence, maintenance of navigation channels and understanding the impacts of climate-induced habitat change. By improving the ability of these regional models to reproduce mixed sediment processes (*e.g.* cohesive effects on bed roughness and bed material transport), the quality of information available for coastal management is improved, helping to make management interventions more cost effective.

1.2 Aims

The objective of this thesis is to improve the description of the dynamical processes of mixed sediments of sand and mud affected by physical and biological cohesion. This includes: the limit of sediment motion; the development and migration of bedforms; and the change in sediment composition due to hydrodynamics and sediment dynamics.

The last of these, the change in sediment composition, presents the greatest challenge as not all the processes involved in the removal and addition of cohesive material to and from the bed sediment can be easily measured or accounted for by proxy measurements. In order to explore ideas relating to these processes, and identify gaps in knowledge, a conceptual model has been developed of the transfer of cohesive material between water column and seabed. A diagram of the initial model is shown in Figure 1-1.

Specifically, the aims of this thesis are to:

- Determine if bedform dimensions and planform are affected by cohesive material in the bed, as well as the hydrodynamic and wave forcing, compared to pure sand bedforms.
- Assess the performance of a selection of existing bedform predictors and phase diagrams for bedforms influenced by cohesion.
- Determine the effect of cohesion on bedform migration and bed material transport rate.
- Explore ideas of how the bed changes from non-cohesive to cohesive dominated states, over a spring-neap cycle.

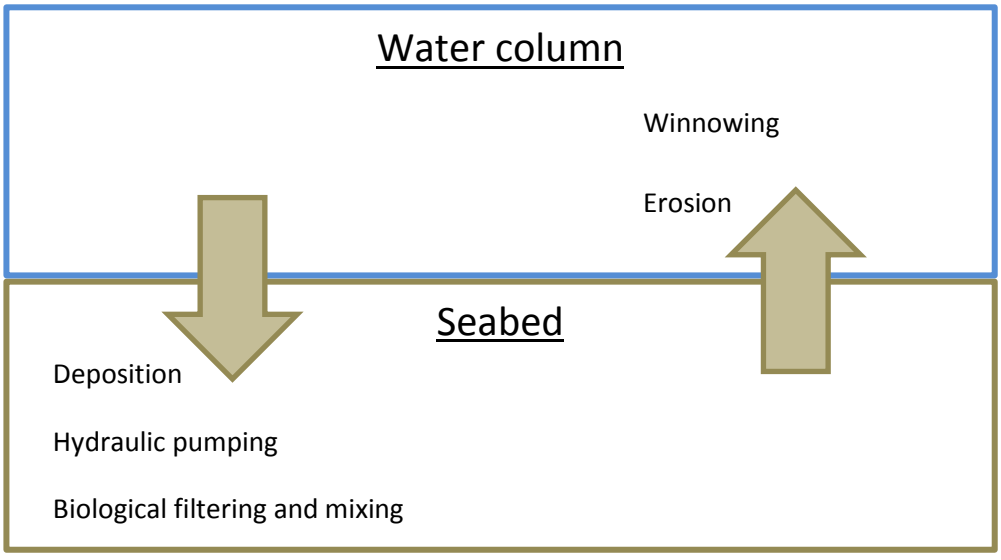

Figure 1-1: A simple conceptual model of the transfer of cohesive material between water column and seabed.

1.3 Approach to data collection and methods

In this thesis, data from field measurements have been used to validate results from laboratory flume experiments of bedforms in cohesive sand (clay and EPS) and to better understand the behaviour of natural cohesive sand sediment. The fieldwork focused on measurements from acoustic instrumentation, supported by auxiliary sensors and sediment sampling, and was carried out on tidal flats in the Dee Estuary. By studying the processes of small-scale bedforms, it was hoped to extend laboratory results of bedform development and migration in cohesive sand to the natural conditions found on the tidal flats. The fieldwork was carried out as part of the NERC funded COHBED project (Realistic Sedimentary Bedform Prediction: Incorporating Physical and Biological Cohesion), to improve understanding of how bedforms in mixed cohesive sand-mud sediments behave in the natural environment.

1.4 Chapter descriptions

Chapter 2: A review of properties, dynamics and processes of mixed cohesive sediments

A review of sediment dynamical processes with a focus on estuarine environments and intertidal flats. This covers sediment properties, hydrodynamic and wave processes, sediment dynamics, biological processes that effect sediment, an overview is given of methods of data collection, and how small-scale sediment dynamics relate to coastal morphology and regional sediment transport using numerical modelling.

Chapter 3: Field data collection and processing methodology

A description of the fieldwork carried out on the Hilbre tidal flats, on Wirral Peninsula in the UK, as part of the COHBED project. Data were collected using instruments mounted on a bed frame (SEDbed), deployed at low tide. Supplementary bed sediment samples were collected regularly at low water between inundation periods.

The methods of data processing and analysis common to the following chapters are described. This includes the processing of the water velocity and bed elevation data, sediment sample analysis, the processing of the data for water properties, and an overview of the mathematical and statistical methods used.

Chapter 4: Bedforms in mixed cohesive sediment forced by combined wave-current flow

The types of bedforms that were observed are described and classified. A comparison of the bedforms with commonly used bedform phase diagrams and bedform dimension predictors is made, with

respect to bed cohesion. Multiple linear regression is used to analyse the bedform planform dimensionality and dimensions to obtain a better understanding of the processes that affect them.

Chapter 5: Bedform migration and bed material transport in a mixed sand-mud intertidal environment

The effect of physical and biological cohesion on bedform migration and bed material transport is examined. Bed material transport rate is determined using the bedform migration rate and bedform dimensions. Multiple linear regression is used to relate the bed shear stress and bed cohesive clay content to the bed material transport rate.

Chapter 6: Discussion

A discussion of the results of the previous chapters. The limitations of the fieldwork and data analysis are examined. A conceptual model of the sediment dynamical processes of sandy sediment influenced by physical and biological cohesive materials is described and used to explore the processes involved in the change of bed cohesive composition and highlight gaps in current understanding. In addition, recommendations for future research are made.

Chapter 7: Conclusions

Conclusions of this thesis.

2 A review of properties, dynamics and processes of mixed cohesive sediments

2.1 Summary

A review of the current understanding of the processes that affect mixed sand, silt and clay sediments in estuaries is presented. The effects of the sedimentological and biological processes are also introduced, as these add extra complexity to the sediment transport processes. As the data used in this study were collected on tidal flats, the key properties of this particular environment are considered.

The properties of sediment particles are related to their mineralogy and the processes of formation. Sediment dynamics within estuaries are forced by a balance of tide, waves and river flow. In estuarine environments sediments from different sources mix, changing their overall behaviour, and can be stabilised or suspended by the action of biological organisms.

Improving predictors for the processes of mixed non-cohesive and cohesive sediment dynamics, including bedform development and the influence of biology, will contribute to regional sediment models. This would lead to better prediction of the transport of pollutants, management of dredging operations, planning of coastal protection and engineering works, and aid ecological management.

2.2 Introduction

This review forms the background to a study of mixed sediment processes of sand, silt and clay in estuaries. As the data collected for this study come from tidal flats in the Dee Estuary, the key properties of this particular environment are considered, as sediment transport processes on tidal flats differ from the wider estuarine environment. An overview will be presented of the current knowledge of the process dynamics of mixed sediment in estuaries and on tidal flats, the effect of biology on these processes, methods available to collect data to describe these processes and how this information feeds into regional models for environmental management.

Sedimentary processes within estuaries are important in understanding anthropological impacts on the environment. Estuaries are partially enclosed bodies of seawater that are measurably diluted by freshwater. They are associated with rivers or bays and can be influenced by the tide and waves. Towns and cities tend to be associated with estuaries as they can provide shelter from the sea and access further inland via rivers. Tidal flats are gently sloping sandy to muddy areas that are exposed during low tide. Found on coasts or within estuaries, they provide a home to biologically diverse

ecosystems and provide protection for the coast from extreme waves. As they are fully exposed during part of the tidal cycle, tidal flats have different characteristics to sub tidal areas or beaches.

The properties of sediment particles, size, shape and cohesiveness, are related to their mineralogy and the processes of formation (*e.g.* weathering, transport etc.). Sediments from a similar source will have a similar grain size range and/or similar shape. These sediments can behave with a degree of predictability depending on their mean grain size relative to the water velocity. In estuarine environments sediments from different sources mix, changing their overall behaviour, and can be stabilised or suspended by the action of biological organisms. In response to hydrodynamic forcing sediments can mix, form horizontal gradients or be layered vertically in the bed and thus retain a history of depositional events (Le Hir *et al.,* 2011).

The time scale of processes affecting sediments can range from geological to less than a second. This review will be restricted to time scale of less than a month, covering the forcing by waves and the tide. Measuring the characteristics and dynamic processes of mixed sediment requires a range of methods, using direct sampling techniques and instrumentation (*e.g.* sediment traps, acoustic backscatter sensors, *in situ* laser scattering, and acoustic bed profilers), and an overview of these will be given. To understand and predict the regional effects of sediment dynamical processes, numerical models are used to simulate sediment transport patterns in the coastal environment, a basic description of these models is given in relation to mixed cohesive sediment.

2.3 Estuaries

'An estuary is a semi-enclosed coastal body of water that has free connection to the open sea, extending upstream into the river as far as the limit of tidal influence, and within which seawater is measurably diluted with fresh water derived from land drainage' (Dyer, 1997 modified from Cameron and Pritchard, 1963). This definition was arrived at by Dyer (1997) from a number of other definitions, some of which considered: the sources of the sediments; specific tidal, wave and fluvial processes; and the ability to sustain euryhaline biological species. Yet the most important factor is the graduation between marine and freshwater conditions.

Estuaries can be classified according to their: geomorphology, fresh water balance, salinity structure, hydrodynamics, sediment type, ecosystem parameters and quantified classifications based on an algorithm of more than one factor from this list, with different types representing stages on a continuous sequence (Dyer, 1997; USACE, 2002c; Valle-Levinson, 2010). Estuarine geomorphology is related to how an estuary was formed by geological processes, and determines the relative influence

of tide, waves and river flow, and water circulation (Dyer, 1997; USACE, 2002c; Valle-Levinson, 2010). The balance of freshwater input relative to evaporation determines if an estuary: is positive, with a surface outflow of freshwater; low inflow, with the balance between freshwater and seawater flow creating a salt plug mid-estuary; or negative (inverse), with a surface inflow (Valle-Levinson, 2010). Salinity structure affects the circulation, stratification, mixing and sedimentation. The hydrodynamic state of an estuary is due to the balance of circulation relative to the stratification (Hansen and Rattray, 1966; Valle-Levinson, 2010). The geological sources of the sediment, either riverine, marine or from within the estuary, determine the composition of the bedload and the suspended sediment. Different biological species spend all or part of their life cycle within estuaries forming ecosystems that are distinct from riverine and full marine conditions.

2.3.1 Tidal flats

Tidal flats can be defined as sediment flats emerging during low tide and submerging during high tide. However, this definition can be ambiguous as the positions of low and high tides are time-variable (Amos, 1995). The frequency of tidal flat inundation and waves play a strong role in the resuspension of sediments, and the varying influence of waves is often apparent in the tidal flat zonation and associated sediment texture (Amos, 1995). Tidal flats are common in sediment-rich environments, with a low bed slope, where the tidal range is large relative to typical wave height (Short, 1991; Masselink & Short, 1993; Friedrichs, 2011). The absence of marsh or mangrove also defines tidal flats. Gradual transitions at the limits of low and high tide occur due to the varying tidal level, waves, storm surges and river floods, and it should be noted that the low slope criterion and transition to marsh or mangrove are not exact (Friedrichs, 2011). Due to these factors, the boundaries of a particular area of tidal flats will always be indistinct. Masselink and Short (1993) created a Relative Tidal Range parameter based on the tidal range and wave breaking height, which determines the presence of tidal flats in relation to beach morphology, where a value greater than 15 indicates the transition to tidal flats:

$$R = \frac{h_{hw} - h_{lw}}{H_b} \qquad \textbf{2-1}$$

where h_{hw} is the high tide level, h_{lw}, the low tide level and H_b is the wave height at point of breaking.

High velocities occur in the shallow water as the tidal front moves onto the flats with the flood, or off with the ebb, and can cause erosion (Friedrichs, 2011; Whitehouse *et al.,* 2000). As tidal flats are

exposed at low tide, there is a period of sediment consolidation as part of each tidal cycle. Bed shear strength increases with exposure due to evaporation, drainage and compaction, and atmospheric conditions have been found to have a greater effect than oceanographic or biological conditions during the summer (Amos *et al.,* 1988). The formation of ice in winter can reduce the strength of the bed and ice that contains sediment can be floated off the bed by the rising tide (Whitehouse *et al.,* 2000).

Deposition can return the bed to its pre-existing strength, resulting in a sequence of alternating hard and soft layers depending on the conditions (Amos *et al.,* 1988). This regular uncovering also exposes the tidal flats to rain that significantly reduces the erosion threshold of cohesive intertidal sediments, by disruption of the inter particle bonding due to the addition of freshwater and dissolution of adhesive carbohydrates, whereas sandy sediments are less effected by rainfall (Tolhurst *et al.*2006).

Tidal and wave energy gradients respectively favour landward and seaward net sediment transport on tidal flats, with coarse sediment being more sensitive to local asymmetries in maximum tidal velocity and fines more sensitive to duration of slack water (Friedrichs, 2011). Concentration gradients across tidal flats, and between the flats and adjacent channels, also result in net sediment transport (Friedrichs, 2011). In the following sections, hydrodynamic forcing and sediment dynamic processes will be looked at more closely.

2.4 Sediment properties

Knowing the properties of sediments is important in environmental management and coastal engineering for predicting their behaviour under hydrodynamic forcing, fate and organisation in morphological forms. This means characterising the size of the individual grains making up the sediment, mineralogical composition and the bulk properties. Grain size is of particular importance as it is related to how the sediment moves and suspends in the water column, its chemical composition and behaviour, and the morphological features it forms.

Marine sediments are created *in situ* from dissolved compounds, by precipitation and biological processes, or are carried into the ocean in solid phase from land, earth's interior or outer space (Libes, 1992). Sediments can be primarily classified according to grain size, shape, density, mineralogy (chemical composition) and cohesiveness (electrical charge). By defining these characteristics in natural sediments, as part of fieldwork and selecting for them in controlled experiments, these properties can be related to sediment motions and bedforms. These properties form narrow

distribution ranges at best and the hydrodynamic, chemical and biological forcing are often stochastic or chaotic in nature, therefore the interpretation of the results involves statistical distributions.

Good sources of information on sediment properties can be found in: *Dynamics of marine sands* (Soulsby, 1997) and *Dynamics of estuarine muds* (Whitehouse *et al.,* 2000), *An introduction to marine biogeochemistry* (Libes, 1992) and in part 3 of the *Coastal engineering manual* (USACE, 2002b). An overview of the key points is given below.

2.4.1 Physical properties of sediment grains

2.4.1.1 Grain size

Sediments can be roughly categorised as gravels, sands or muds based on size. There is a strong correlation between size, mineralogy and bulk properties as minerals weather in a particular way and small particles tend to be more flat and have a greater surface area for chemical reaction, with larger particles more inert and primarily affected by gravity (USACE, 2002b). Fine sediments or muds (silts, clays and colloids) can exhibit cohesive properties depending on their mineralogy.

The grain size is classified on a scale from boulder to colloid based on the longest diameter measurement, initially standardised by C. K. Wentworth based on the work of a number of authors including J. A. Udden (Wentworth, 1922) and updated for logarithmic units by Krumbein (1936). Grain size can be determined by measuring a representative number of grains under a microscope, sieve analysis, settling column, X-ray sedigraph, laser diffraction or digital imaging to get a size distribution of a sample (Blott & Pye, 2001; Liu, 2001; Pentney and Dickson, 2012). Grain size is not an exact measurement, due to the irregularity of the grain shape and as different techniques make different physical assumptions. Care must be taken when comparing measurements from different methods.

The grain size is a key parameter used to determine fundamental values of the bed surface roughness, settling velocity, porosity and mode of transport for a sediment. The median grain diameter, D_{50}, is often used to represent a unimodal sediment population for calculations. However, for mixed sediments this can be misleading and the size distribution needs to be considered, as it may be multi-modal. The grain diameter can also be represented as the dimensionless grain diameter, D_*,:

$$D_* = D\left[\frac{g(\rho_s/\rho - 1)}{\upsilon^2}\right]^{1/3}$$

2-2

where D is the grain diameter, ρ_s is the grain density, ρ is the water density, g is the acceleration due to gravity and v is the kinematic viscosity.

2.4.1.2 Mineralogy and cohesion

Coastal sediments are mainly comprised of quartz and feldspar grains from weathered rocks, and also silicates and carbonates formed by marine life, but the composition of individual sites can vary widely (Libes, 1992; USACE, 2002b). Quartz is inert and tends to accumulate, while feldspars are more subject to chemical weathering that converts them to clays and solutions (USACE, 2002b).

Clay minerals have a net negative surface charge that attracts free positive ions and organic matter in seawater (Libes, 1992; Whitehouse *et al.,* 2000). The charge distribution across the grain surface allows grains to bind together (*i.e.* cohesion), and form flocs in suspension (Whitehouse *et al.,* 2000). Cohesive attraction is strong at a short distance, but reduces inversely with the square or cube power of distance for plate-like grains (*i.e.* for clays) and inversely with the cube to seventh power for spheres or particle clusters (Whitehouse *et al.,* 2000; Winterwerp and van Kesteren, 2004). This means particles need to be brought close together before they can bind into flocs (Whitehouse *et al.,* 2000; Winterwerp and van Kesteren, 2004). The salinity and pH of seawater affects the cohesive properties due to the variation of electrostatic charge. Salinity is a measure of the concentration of free ions in seawater and pH is a measure of the activity of hydronium (H^+) ions in a solution, and these charged ions will bind to the surface of particles affecting how particles form flocs. An increase in salinity leads to an increase in attraction and increasing pH leads to greater repulsion between sediment grains (Winterwerp and van Kesteren, 2004).

From the view of sediment dynamics the mineralogy affects the density, size, shape, chemical and electrical properties, and rheology (flow of complex fluids) of the sediment. Biogenic sediments have a lower density than lithogenous or hydrogenous sediments, as they are complex products of organisms that have holes within the structure (USACE, 2002b).

2.4.1.3 Grain shape

The shape of a sediment grain is a function of the mineralogy, grain size, original shape and abrasion that has occurred during its history (USACE, 2002b; van Rijn, 1993). Grain shape is defined by: sphericity, overall shape of the particle; roundness, the amount of abrasion of the corners; and microtexture, the very fine scale roughness (USACE, 2002b). Rounding for quartz grains is a very lengthy weathering process and sediments found in the coastal environment can generally be

considered the stable end results (USACE, 2002b). The grain shape affects many properties of sediments including the initiation of motion, angle of repose, porosity, permeability and fall velocity. The angle of repose (or angle of internal friction) is a function of grain shape; the more irregular the grains the steeper they can be stacked before they start to roll or avalanche (Soulsby, 1997; USACE, 2002b). Observations of lee slopes of natural dunes show values in the range 30° to 40°, though in experiments angles range up to 50° (van Rijn, 1993).

2.4.1.4 Bulk properties

Porosity, bulk density and permeability are all properties related to how the sediment grains are packed together and how much space is left between grains. Loose packing is seen when sediments settle in still water, while close packing results from hydrodynamic forcing allowing grains re-orientate to fit better or from compression from sediment settling on top.

Ideal spheres have porosities in the range 26-48%, and natural sands 25-50%, while mixed sediments have relatively small porosities as the voids can be filled with fine particles (USACE, 2002b; van Rijn, 1993). Though deposits consisting of clay, silt, sand and organic material can have large porosities of up to 80% (van Rijn, 1993).

Bulk density refers to the density of an aggregation of grains, which will always be less than the density of the individual grains as it considers the volume of the pore spaces (USACE, 2002b). Permeability is the ability of water to flow through a sediment bed and is largely a function of size and shape of the pore spaces (USACE, 2002b). Bed permeability affects how wave energy is dissipated in shallow water, the transfer of pollutants into and out of the bed, and is a factor in determining foreshore steepness (Soulsby, 1997; Huettel *et al*., 1996; USACE, 2002b; Precht and Huettel, 2003). Fluid mud is a suspension of cohesive sediment that has become a gel and can dissipate wave energy in proportion to the density, which defines the viscosity of the mud, attenuating waves much faster than a smooth rigid bed (Jiang and Zhao, 1989; Winterwerp and van Kesteren, 2004).

2.4.1.5 Settling velocity

As a particle falls through a fluid it will accelerate until it reaches terminal velocity where the downward gravitational force equals the drag force on the particle. When working with sediment grains this terminal velocity is known as the settling velocity and is of great importance in determining how sediment is transported and deposited in the marine environment. The settling velocity is a function of many factors including grain size, shape & density and fluid density & viscosity. Because

the drag on a particle depends on its shape and texture, there is difficulty in theoretically defining the drag coefficient for natural sediment.

Stokes (1851) derived an equation for settling velocity in laminar flows, a variation of Newton's Impact Law, where form drag can be determined physically without resorting to experimentation. However, in non-laminar conditions form drag increases and the determination of settling velocity becomes semi-empirical and depends on experimental data. Over 150 years later researchers are still collecting data for different conditions and re-analysing old data (*e.g.* Hallermeier, 1981; Dietrich, 1982; Soulsby, 1997; Jiménez and Madsen, 2003; Maggi, 2013), and exploring the physics of how particles behave as they settle (Yam *et al.,* 2013).

The interaction between grains, both cohesive and non-cohesive, affects the settling velocity. Settling as population of sediment and as flocs will be looked at as part of the sediment dynamics section (Section 2.7.4).

2.5 Mixtures of sediments

2.5.1 Particle size distribution

Grain size distribution is changed by the processes of erosion, transport and deposition (Tucker, 1991). Rivers can release coarser sediment directly into the marine environment during flood events and generally grain size decreases with distance from the source, inferring the direction of sediment dispersal (Tucker, 1991). Sediments from a particular source tend to have a narrow size distribution as they are well sorted by marine processes.

Eisma and Kalf (1987) found two distinct populations of suspended sediment in the North Sea from offshore and coastal sources, with four overlapping intermediate types, based on the shape of the particle size distribution. Estuarine suspended sediment showed skewness towards a finer particle size with increased salinity (Eisma *et al.,* 1991). Fugate & Friedrichs (2002) found three distinct suspended sediment populations during a study in Chesapeake Bay that exhibited different settling rates over the tidal cycle. By using the statistical moments of the particle size distributions different populations can be determined and related to the hydrodynamics of the environment (Folk and Ward, 1957; Friedman, 1961).

2.5.2 Properties of sediment mixtures

Mixtures of cohesive and non-cohesive sediments of different grain size will have different properties depending on the relative proportions of the components. The dominant fraction of the sediment will form a skeleton, with the stiffness of sand skeletons orders of magnitude higher than a clay skeleton (Winterwerp and van Kesteren, 2004). Non-cohesive material in a sediment increases the distance between cohesive particles, reducing the overall cohesion and making it stiffer and less fluid. The porosity or grain packing efficiency is a controlling factor, as is the water content. The conceptual model of Panagiotopoulos *et al.* (1997) is shown in Figure 2-1, where the filling of the spaces between large grains increases the angle of friction and therefore the force required to initiate motion, until the sand grains are completely separated and pivoting stops being the main mechanism for initiating motion. Van Rijn (2007) found that the critical stress for initiation of motion strongly depends on the degree of exposure of a grain with respect to the surrounding grains.

Van Ledden *et al.* (2004) developed a conceptual framework of sand-mud mixtures based on the proportions, cohesion and network structure, which agreed well with laboratory data. Figure 2-2 shows their scheme, with the transition from non-cohesive to cohesive sediment, the different bed classifications and effect of the volume fraction of water (porosity) on the boundaries between classifications. Clays (IV) dominate the triangle due to their cohesive strength and for the non-cohesive mixed class (III) none of the three components is large enough to form the network structure by themselves (van Ledden *et al.,* 2004).

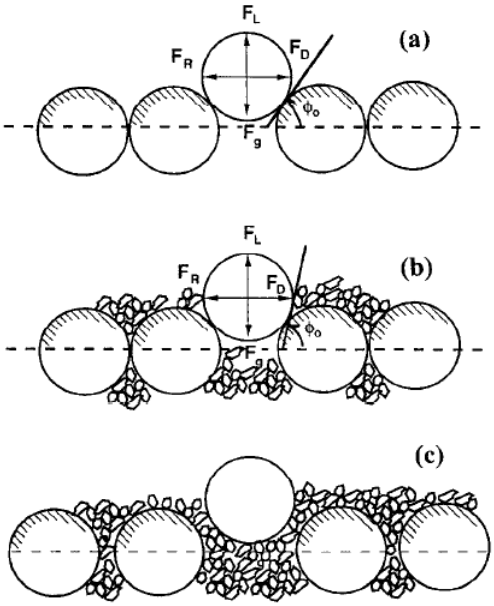

Figure 2-1: A conceptual model showing the mechanism for the initiation of sediment motion for (a) pure sand; (b) sand and mud mixtures with mud content M<30%; and (c) sand and mud mixtures with mud content M>30%, sand grains are separated and there is no angle of repose or internal friction. ϕ_0 - angle of internal friction, F_g - weight of the particle, F_L - lift force, F_D – drag and F_R – resistance force (Panagiotopoulos *et al.*, 1997 after Wiberg and Smith, 1987).

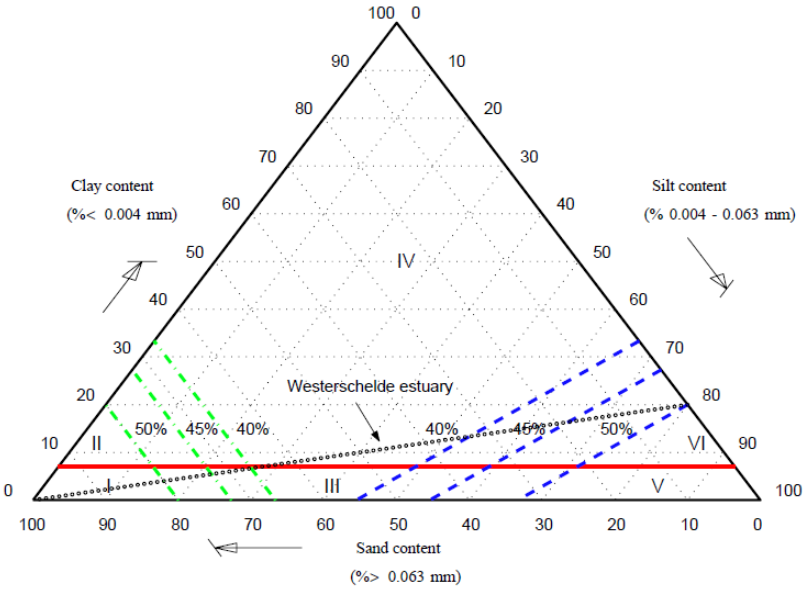

Figure 2-2: Ternary diagram of relative proportions of sand, silt and clay by dry weight. Red line – transition between non-cohesive and cohesive, green dashed line – boundary of sand-dominated structure for volume fractions of water and blue dashed line – boundary of silt-dominated structure for volume fractions of water. Bed structure types: I – non-cohesive sand dominated, II – cohesive sand-dominated, III – non-cohesive mixed, IV – cohesive clay-dominated, V – non-cohesive silt-dominated and VI – cohesive silt dominated. (van Ledden *et al.*, 2004).

Mixtures of sediment have been shown to have effects on the physical processes of sediment transport. The critical shear stress for erosion is increased for mixtures of mud and sand compared to uniform sand or mud (Mitchener and Torfs, 1996; Panagiotopoulos *et al.,* 1997). Suspended load transport above graded beds is 2-3 times greater than above an almost uniform bed (van Rijn, 2007). The different properties of mixed sediments in relation to physical processes will be explored further in the sediment dynamics section below (section 2.7).

2.6 Hydrodynamics

Hydrodynamics within estuaries are a balance of tide, waves and river flow. The tide is the main control of the depth of water and provides a constantly changing current. In their simplest form, currents can be considered either unidirectional or bi-directional. However, currents can be modified by environmental factors, including morphology, wind and tidal rotation. The hydrodynamic forcing on sediment motion can be complex, especially considering the varying properties of seawater in coastal and estuarine environments.

In a unidirectional current of a constant mean velocity, over a flat bed, there will be a logarithmic velocity profile as the bed shear stress resisting the flow is transmitted up through the water column (von Kármán, T., 1930; Nikuradse, 1933; Grant and Madsen 1986; Soulsby, 1997; Liu, 2001; USACE, 2002b). The shear stress between the current and the bed is important in the initiation of sediment motion, the formation of bedforms, and bed and suspended load transport. Further up in the water column the shear stress between water layers is related to the turbulent kinetic energy and helps keep material in suspension.

The top of the boundary layer is defined by the free stream velocity, where the bed shear stress no longer has a measureable effect on the flow, although in shallow waters the boundary layer can cover the full depth (von Kármán, T., 1930; Grant and Madsen 1986; Soulsby, 1997; Liu, 2001; USACE, 2002b). Under waves, the ideal logarithmic profile breaks down and there is an oscillating stress, which may be asymmetric resulting in a residual transport in one direction (Soulsby, 1997; Liu, 2001; USACE, 2002b). Over short time periods, tidal flow can be treated as unidirectional. Waves and unidirectional flow together is known as combined flow.

As the flow velocity increases from zero over the seabed, turbulence starts to occur as chaotic fluctuations in the flow. Turbulent eddies cascade from large to small, dissipating energy, until at the smallest scale molecular viscosity dissipates energy as heat (Tennekes and Lumley, 1972). The turbulent fluctuations in a flow form a continuous spectrum of eddy wave numbers or frequencies

(Tennekes and Lumley, 1972). This turbulence provides energy to move and suspend sediment, and keep it in suspension. Turbulence can also be introduced into the water column by breaking waves (Nielsen, 1984).

The reducing water depth in coastal and estuarine waters affects the height of the incident waves as they travel onshore. At a critical depth in relation to the wave height or critical wave steepness the waves will break, dissipating energy.

2.6.1 Water properties

Knowing the basic properties of the seawater is essential to understanding sediment properties and their dynamics. The properties of water as a fluid medium affect the way sediment particles respond to forcing and their chemical behaviour. Water molecules have a weak uneven charge distribution, which can form weak bonds and results in various properties (Libes, 1992). Water is a very good solvent, has a high viscosity and low compressibility (Libes, 1992).

Ionic compounds, salts, are split up into positive and negative ions when dissolved in water and increase the density and viscosity of the water (Libes, 1992). The most abundant ions in seawater are present in constant proportions, and their concentration is measured as salinity, though estuaries and coastal waters may deviate from this ideal due to land and river runoff (Libes, 1992).

The presence of salt in water has a very important impact on the physical behaviour of seawater (Libes, 1992). The density of seawater depends on the temperature and salinity, which will affect the buoyancy of the sediment grains due to the difference in density between the grains and water. The water viscosity is dependent on the temperature and affects the settling velocity of grains and the percolation of water through the sediment. Increasing the buoyancy of grains reduces the gravitational force making them easier to move, while increased seawater viscosity increases the resistance to motion of grains and flow through the seabed. The ions in seawater and the water molecules will adsorb to cohesive sediment affecting the properties of the sediment (see section 2.4.1.2 above).

2.6.2 Tides and unidirectional currents

The constantly changing water level due to the tide causes a varying water velocity and pressure that is one of the main forcing factors of sediment transport processes in estuaries. The tidal curve determines the variability of water velocity and length of slack water that influence the movement

and settlement of sediment. Asymmetry of the tide can result in net transport with the flood or ebb leading to increases deposition or erosion over a tidal cycle (Figure 2-3).

The logarithmic velocity profile of unidirectional currents has been well studied, so is a good place to start when considering sediment movement. Although the tidal current is not strictly unidirectional, it is assumed to be so for short time scales when studying small scale processes. The structure of unidirectional flow near the seabed, or bottom boundary layer, is shown in Figure 2-4. The bottom boundary layer is where the bed friction affects the water flow. In the turbulent logarithmic layer the shear stress is assumed to be constant with height and equal to the bed shear stress, and is known as the constant stress layer (Grant and Madsen 1986; Liu, 2001). In natural flows, the laminar viscous sub-layer is very thin, with turbulence dominating, and the time scale for the development of the logarithmic layer is much less than a tidal cycle.

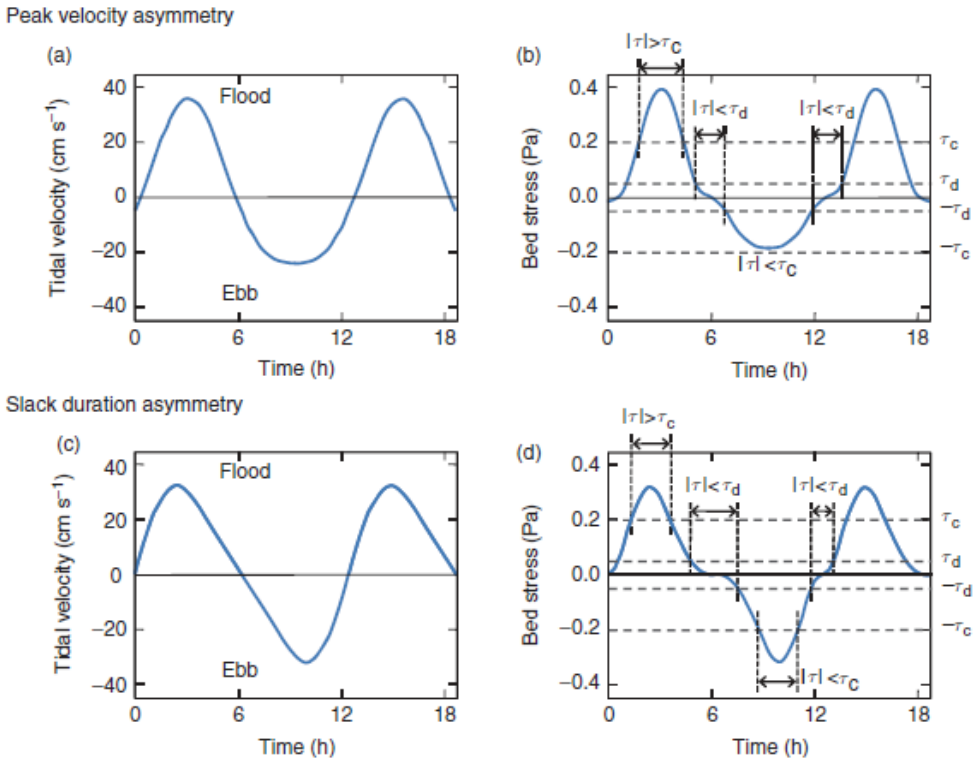

Figure 2-3: Idealized examples of peak flow asymmetry showing (a) flood-dominant current with no residual (b) resulting in asymmetry in peak stress favouring landward sediment transport (the ebb-dominant case would flip the curves along the horizontal axis.) and slack duration asymmetry showing (c) longer slack after flood with no residual (d) resulting in periods of low stress magnitude (longer duration after slack would flip curves along the vertical axis). Where τ is the shear stress, τ_c is the critical stress for erosion and τ_d is the critical stress for deposition (Friedrichs, 2011).

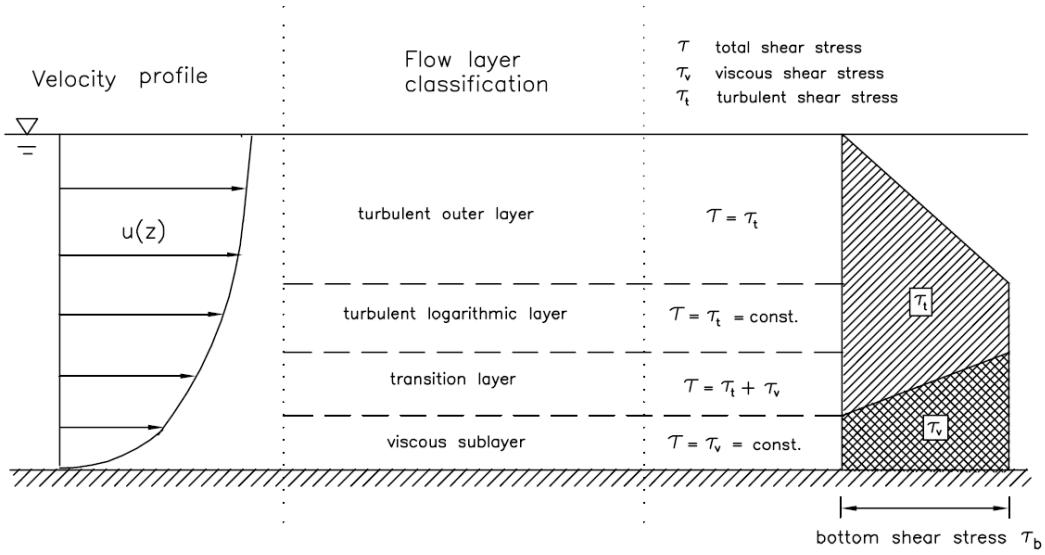

Figure 2-4: Classification of near bed unidirectional flow. The boundary layer thickness is not to scale. The turbulent outer layer accounts for 80-90% of the layer (Liu, 2001).

The logarithmic velocity profile is described by the Karman-Prandtl equation (law of the wall):

$$u(z) = \frac{u_*}{\kappa} \ln \frac{z}{z_0}$$

2-3

where *u(z)* is the velocity at the height of measurement in m/s, u_* is the shear velocity, κ is von Karman's constant and z_0 is the roughness length (the height where $u = 0$). (Grant and Madsen 1986; Soulsby, 1997; Liu, 2001). The roughness length, z_0, is a function of the bed roughness, or bedform height, for rough flows and is the height at which the velocity is zero (Grant and Madsen 1986; Soulsby, 1997; Liu, 2001; USACE, 2002b). The shear velocity, u_*, represents the bed shear stress, τ_0, in terms of velocity:

$$\tau_0 = \rho u_*^2$$

2-4

where ρ is the water density (Grant and Madsen 1986; Soulsby, 1997; Liu, 2001). The von Karman constant, κ, is an empirical constant, taken to be 0.4 for clear water, with the sediment-induced effects treated separately or κ varied for suspended sediment concentration (Vanoni and Brooks, 1957; Grant and Madsen 1986; Soulsby, 1997; Liu, 2001; USACE, 2002b; Castro-Orgaz *et al.*, 2012).

The flow of the incoming and outgoing tide deviates from the ideal logarithmic velocity profile due to: unsteady flow (acceleration of the tidal currents); non-uniformity of flow due to bed topography;

suspended sediment changing the water density or dampening turbulence; stratification within the water column due to salinity and temperature; changes in ripple geometry over the tidal cycle; bed-load transport that can change the flow near the sea-bed; rotary tidal currents; wind effects; wave action and topographically-induced secondary flows (Wilkinson, 1986; Collins *et al.,* 1998). Collins *et al.* (1998) found less than 40% of their 192 records over three sites were logarithmic, suggesting complex flow profiles are to be expected in field measurements. This needs to be considered when applying methods that make assumptions based on the logarithmic profile such as the law of the wall or the inertial dissipation method for turbulent shear stress.

Another method for determining the bed shear stress in unidirectional flow is the quadratic stress equation. The bed shear stress can be determined from the depth-averaged current velocity, water density and a drag coefficient:

$$\tau_0 = \rho C_D \overline{U}^2$$

2-5

where ρ is water density, $\bar{U}$ is depth mean current velocity and C_D is the drag coefficient (Soulsby, 1997). The drag coefficient is found empirically using a relationship with the roughness length and water depth. As this method relies on empirical results, one must be confident that the constant chosen is suitable for the conditions of the study.

2.6.3 Waves

Sea surface waves are generated by wind. These waves can be local or generated by distant storms, with waves crossing large distances with their maximum period limited by the fetch. Natural waves comprise a spectrum of heights, periods and directions, and are usually defined by the significant wave height (the mean of the highest third of the waves) and mean period (Soulsby, 1997). Swell waves that have travelled across the sea tend to have a narrow range of longer periods, as due to wave dispersion waves with longer wavelengths travel faster than waves with shorter wavelengths (USACE, 2002a). Also short waves tend to lose their energy more readily from internal dissipation within the fluid, interaction with the air and breaking (USACE, 2002a). The size and motion of wind waves are affected by the direction of the tidal current, which can reduce or increase the surface friction felt by the wind, and by the varying depth of water. The water depth due to the tide has a limiting effect on the waves; waves over tidal flats tend to be highest around high water (Friedrichs, 2011).

Waves provide an oscillating velocity, and stress, to the bed. This stress may be asymmetric resulting in a residual transport in one direction. Wave action will also cause pressure changes, pumping water in and out of the bed, increasing and decreasing the effective weight of the sediment grains over the wave cycle (Soulsby, 1997).

The bottom boundary layer due to waves is thought to be only a few centimetres in height (van Rijn, 1993) and is the same as the constant stress layer for wave only flow (Winterwerp and van Kesteren, 2004). Winterwerp and van Kesteren (2004) determined an approximation for the wave boundary layer thickness, δ_w, in terms of the eddy viscosity and angular frequency of the waves, with an empirical constant:

$$\delta_w \approx 15L_s \ \ where \ \ L_s = \sqrt{\frac{2\nu_e}{\omega}}$$

2-6

Where L_s is the Stokes length, ν_e is the eddy viscosity and ω is the angular frequency (Winterwerp and van Kesteren, 2004). Davies and Villaret (1999) determined a similar relationship for wave boundary layer thickness, δ_w, including the effect of bed roughness:

$$\delta_w = 5\sqrt{\frac{K_0}{\omega}} \ \ where \ \frac{K_0}{2} = 0.00253U_s k_s \sqrt{\frac{d_s}{2k_s}}$$

2-7

where K_0 is the cycle-mean eddy viscosity, U_s is the significant orbital velocity, d_s is the orbital diameter and k_s is the bed roughness (Davies and Villaret, 1999). Depending on the available measurements, another method may be to determine the boundary layer from the asymmetry of the wave orbital motions using a logarithmic function, where symmetric wave orbital motion is equivalent to the free stream velocity of unidirectional flow.

The bed shear stress due to waves, τ_w, can be defined by a variation of the drag equation:

$$\tau_w = \frac{1}{2}\rho f_w U_w^2$$

2-8

where ρ is water density, f_w is the wave friction factor and the wave orbital velocity is:

$$U_w = \frac{\pi H}{T sinh(kh)}$$

2-9

Where *H* is the wave height, *T* the wave period, *k* the wavenumber and *h* the water depth (Soulsby, 1997). The wave friction factor is found empirically using a relationship with horizontal wave amplitude at the bed and the roughness length, z_0 (Soulsby, 1997).

2.6.4 Combined flows

Waves and unidirectional currents occurring together are known as combined flow. In conditions where waves encounter an opposing current, wavelength decreases and wave height increases and the reverse happens with current and waves travelling in the same direction (Soulsby, 1997). Currents perpendicular to the direction of the waves have no effect on the waves (Soulsby, 1997). When waves and currents interact, they do so in a non-linear way causing a bed shear stress that is greater than the sum of the components (Soulsby and Clarke, 2005). There are many different relationships for combined flow, but Soulsby (1997) created a simple method that gives good results when compared to theoretical models and better than the existing data-based models, with the mean bed shear stress due to combined flow, τ_m**,**:

$$\tau_m = \tau_c \left[1 + 1.2 \left(\frac{\tau_w}{\tau_c + \tau_w}\right)^{3.2}\right]$$

2-10

where τ_c is the bed shear stress due to the unidirectional current and τ_w is the bed shear stress due to the waves, and τ_{max} is the maximum bed shear stress due to combined flow (Soulsby, 1997)**:**

$$\boldsymbol{\tau_{max} = [(\tau_m + \tau_w \cos \phi)^2 + (\tau_w \sin \phi)^2]^{1/2}}$$

2-11

Equation 2-11 has been improved on, to better represent the eddy viscosity and non-linear interaction of combined flow (Soulsby and Clarke, 2005; Malarkey and Davies, 2012), as further detailed in section3.8.1.2. For the wave boundary layer thickness, δ_{cw}, where waves and currents contribute to the turbulence and layer thickness, Grant and Madsen (1986) gave a theoretical relationship based on the law of the wall, shear velocity due to waves and currents, u_{*cw}, and the wave angular frequency, ω:

$$\delta_{cw} = \kappa u_{*cw} / \omega$$

2-12

where κ is von Karman's constant. This relationship has also been used for wave only conditions, giving a thickness in the order of centimetres that agreed with instrument measurements (Thompson *et al.,* 2012).

2.7 Sediment dynamics

Water motion imparts a force on the sediment. If the force of the flow is enough to counteract the resisting forces (gravity, cohesion and adhesion) then sediment transport will start. Initially this will be traction, as grains roll over the bed. With increasing water velocity saltation (jumping) starts to occur until the sediment becomes full suspended in the water. Fine sediments can go straight into suspension, bypassing the bedload and saltation phases. The differing behaviour of sediment in relation to water velocity according to grain properties has the effect of sorting the grains. Bedforms will develop with increasing flow velocity, further sorting the grains, modifying the flow and influencing the sediment suspension. The suspended sediment changes the overall density of the water and can decrease the rate of suspension. These three factors, the suspended sediment, water flow and bed morphology, dynamically interact with each other and are collectively known as the sediment process triad, Figure 2-5 (Thorne and Hanes, 2002).

Just as the bed erodes under increasing flow velocity, as the velocity decreases settlement starts to redeposit the sediment. Larger particles will come to rest before smaller ones. The variation in size distribution effects how the sediment is packed. A gradually changing flow can cause sediment to pack more efficiently, as grains readjust their position, requiring a greater force to erode the bed. However high suspended sediment concentration can hinder the rate of settling through particle interactions.

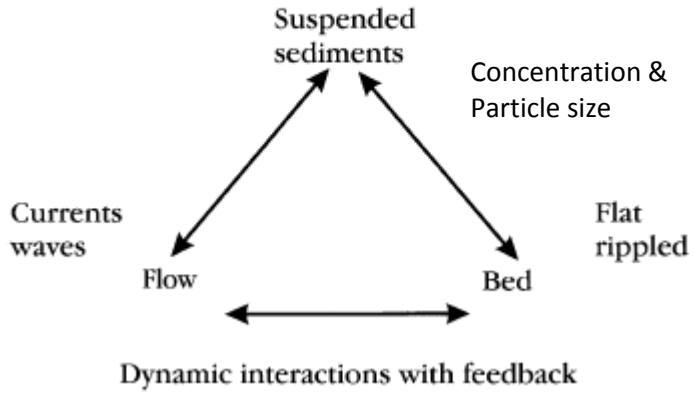

Figure 2-5: Illustration of the sediment processes triad and their interactions (Thorne & Hanes, 2002)

Table 2-1 gives an overview of the processes that affect non-cohesive and cohesive sediments. These processes can act successively or simultaneously, or in some cases not at all, depending on the hydrodynamic conditions and properties of the sediment (Winterwerp and van Kesteren, 2004). The complexity of the processes that affect sediment movement and settling has meant that work in this area is a combination of physical theory, empirical measurements and statistics. These processes are looked on as stochastic, rather than purely deterministic. This is due to the turbulent nature of marine currents and waves, and random effects on the distribution of sediment particle properties.

Table 2-1: Physical processes affecting sediment in an aquatic environment (after Winterwerp and van Kesteren, 2004)

Process	**Description**
Flocculation	Cohesive sediments will form flocs affecting the settling velocity and bed structure.
Settling and mixing	Particles fall through the water column due to gravity, opposed by turbulence.
Deposition	Particles become part of the bed.
Gelling	Deposited mud particles when left still for sufficient time will form a structure, causing an increase in bed strength that can resist resuspension. Clay suspensions can also form gels.
Consolidation	As the weight of the deposited sediment increases the pore size decreases, squeezing water out of the bed and the bed strength increases further.
Liquefaction	When subject to cyclical loading bonds between particles can be gradually broken, reversing the gelling and consolidation processes and weakening the bed.
Winnowing	Fine material is selectively suspended into the water column from the bed, according to difference in particle size between the fractions in the bed.
Erosion	Currents and waves can erode the bed even if it has achieved a considerable strength.
Bedload transport and bedform creation	Traction and saltation move the sediment to different locations and bedforms can develop depending on the flow velocity and period of forcing
Suspension	During accelerating flow, particles can be suspended into the water column by the turbulent flow.
Entrainment	Turbulent flow over or underneath a less turbulent fluid layer exchanges water and matter with this less turbulent layer.
Suspended load transport	Suspended sediment is advected to different locations

2.7.1 The onset of motion and erosion

When the bed shear stress due to the hydrodynamic force of the current exceeds a certain threshold sediment motion starts to occur. This threshold is determined by the grain properties of the sediment and how well it is packed. The mass, cohesiveness and pivot angle of the grains are factors in the resistive force. In mixed sediments, the larger grains can shield smaller ones from the flow and the smaller grains alter the pivot angle of the larger grains (Panagiotopoulos *et al.,* 1997). For a uniform grain size pivot angle depends on grain shape and packing. For mixed sediment, the ratio of protruding grain size to base grain size is also a factor (Komar and Li, 1986). These differences in size and shape allow the selective removal of finer fractions of the sediment into suspension, depending on the hydrodynamic conditions, known as winnowing (Komar and Li, 1986; Lisle and Hilton, 1992; Harris *et al*., 1993).

Parchure and Mehta (1985) found that the shear strength of cohesive sediment increased with depth of sediment and was influenced by the type of sediment, bed consolidation period and salinity. Such beds exhibit type I erosion, where the sediment erodes in bursts as the current velocity increases past the shear strength limit of each layer, then decreases asymptotically with time (Amos *et al.,* 1992; Sanford and Maa, 2001). This behaviour is expected from cohesive sediments. Type I erosion can be sub divided into two classes, type Ia and type Ib. Type Ia is characteristic of floc or pellet resuspension from the seabed at low stress, with a strong erosion peak then decay (Amos *et al.,* 1992). Type Ib is characterised by bed failure occurring as aggregates that are constrained by greater than normal consolidation and shows intermittent erosion events after the initial maximum (Amos *et al.,* 1992). Type II erosion is constant and occurs with uniform beds where the shear strength of the sediment does not vary with depth and is characteristic of silt rich layers (Amos *et al.,* 1992; Sanford and Maa, 2001). Both type I and II erosion can occur for the same sediment under different flow conditions (Amos *et al.,* 1992; Sanford and Maa, 2001). Sanford and Maa (2001) found that bed erosion was a function of the rate of change of forcing as well as the change of bed strength with depth, and derived an equation that models both type I and II erosion and the transition between them.

The bulk density is negatively correlated to erodibility, with dense beds having lower erosion rates and higher erosion thresholds, principally due to the cohesiveness (Grabowski *et al.,* 2011). Erosion increases with increasing temperature and two hypotheses have been proposed for this: weakening of inter-particle bonds and decreasing viscosity of pore water leading to higher permeability (Grabowski *et al.,* 2011). Although the time scale for changes in pore water temperature, salinity and pH is in the order of weeks, erodibility will not change much over a spring-neap cycle, but may change with the season (Winterwerp and van Kesteren, 2004).

As stated earlier, mixtures of mud and sand have increased resistance to erosion, and a reduced rate of erosion, but care should be taken when making comparisons with laboratory data as natural sediments were found to have lower critical shear stresses than artificial mixtures (Mitchener and Torfs, 1996). Thompson and Amos (2004) found that for cohesive beds where the bed shear strength exceeds the flow-induced stress, mobile sand grains provide the stress required to induce erosion. The erosion rate and stress increased with increasing sand grain weight and decreasing grain size, and were at a maximum when sand was in saltation (Thompson and Amos, 2004).

When the critical shear stress for the bed is reached, bedload transport will start to occur, first as rolling grains (traction), then saltation (short hops) and finally suspension occurs (Soulsby, 1997; Liu, 2001). However, as saltation involves grains being supported by the water, it can be seen as part of the sediment suspension in the water column and not a separate class of motion (Liu, 2001; Parsons *et al*., 2015). Mud can form a well defined fluid layer at the bed that is considered part of the bed load. The onset of motion is difficult to determine; how many grains must be moving to be considered bedload transport and should they be in constant motion? Video has been used to detect this motion, as well as instruments to measure the increase in suspended sediment concentration, in relation to hydrodynamic forcing. The point of initiation of motion can be extrapolated back from these measurements.

2.7.1.1 The Shields parameter for sediment motion

In 1936, Shields published his entrainment function, the Shields parameter, θ, the ratio of the bed shear stress to the submerged weight and diameter of the sediment grains in a dimensionless form:

$$\theta = \frac{\tau_0}{(\rho_s - \rho)gD}$$

2-13

where τ_0 is the bed shear stress, ρ_s is the grain density, ρ is the water density, g is the acceleration due to gravity and D is the grain diameter (Shields, 1936; Soulsby, 1997; Paphitis, 2001). Originally, Shields plotted data against the grain Reynolds number, Re_*, to show the relationship with flow type (Shields, 1936):

$$Re_* = \frac{u_* D}{\upsilon}$$

2-14

where u_* is the shear velocity, *D* is the grain diameter and *v* is the kinematic viscosity. Alternatively, to show how the threshold motion varies with the sediment size, dimensionless grain diameter, D_*, can be used instead of the grain Reynolds number (Figure 2-6). The plot shows a threshold curve (or envelope) of the limits of sediment motion for entrainment and deposition of sediment (Figure 2-6; Shields, 1936; Soulsby, 1997; Paphitis 2001). These threshold curves have been extended and improved upon over the years to improve understanding of the limits of sediment motion, transport and deposition for different sediments and hydrodynamic conditions (Shields, 1936; Soulsby, 1997; Paphitis 2001). However, they are based on sediments of a single grain size and the effects of mixtures of non-cohesive and cohesive sediments have not been considered. In addition, they are not suitable in conditions where breaking waves contribute turbulent energy to the bed shear stress (Paphitis, 2001). The Shields parameter is widely used to represent the bed shear stress in dimensionless form when relating forcing to sediment dynamical processes.

In shallow marine environments, submerged bed surface sediment moves predominantly by the combined forces of currents and waves. Equation 2-13 can be applied to waves (θ_w and τ_w), currents (θ_c and τ_c) and combined flows (θ_{max} and τ_{max}). The Shields parameter can incorporate the contributions of skin (sediment grain,) friction and form drag in the bed shear stress (Soulsby, 1997). The skin friction component of the shear stress determines the movement of sediment particles on the bed, and is therefore important for the development and migration of bedforms and the bed material transport rate. The form drag component of the shear stress, caused by bedforms acting as roughness elements, is more important for the transport of suspended sediment higher up in the flow (Soulsby, 1997). The notation θ' is used for mobility parameters that are based only on the skin friction contribution in the bed shear stress.

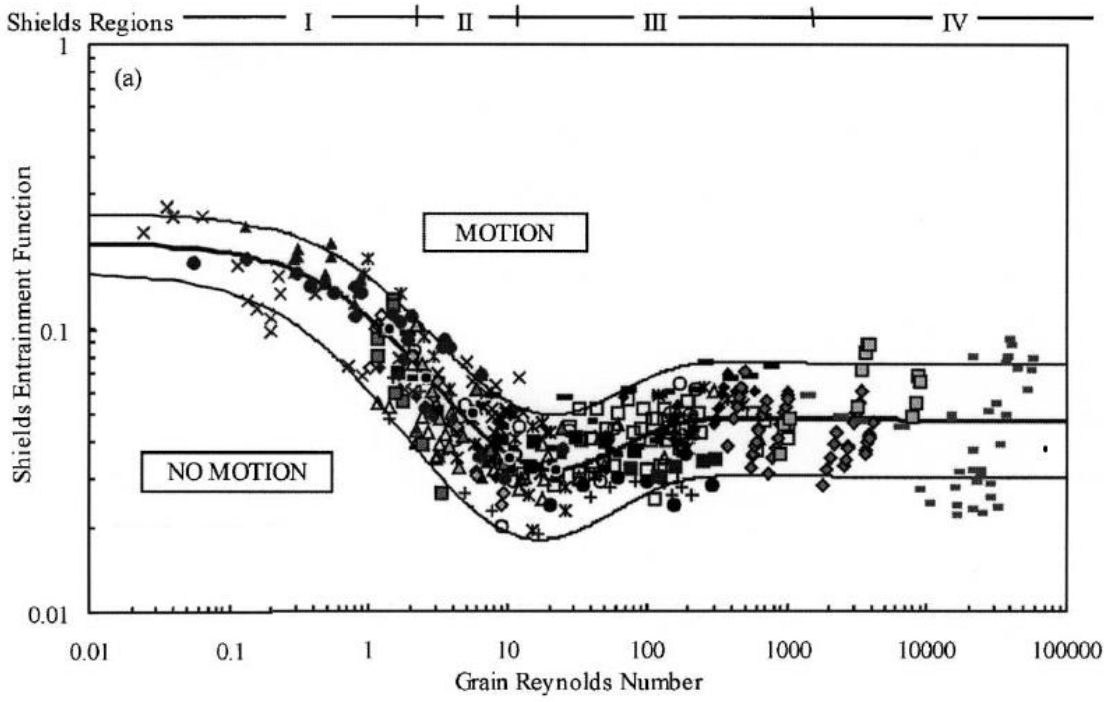

Figure 2-6: Shields threshold curve. Shields parameter plotted against grain Reynolds number. A collection of 29 datasets is plotted. The Shields regions are: I – hydrodynamic smooth flow, II – transitional 1 (sediment within viscous sub-layer), III – transitional 2 (viscous sub-layer ≈ grain size), IV – hydrodynamic rough flow. (Paphitis, 2001).

2.7.2 Entrainment and suspension

When the force from the water flow exceeds the settling force, sediment will cease to be part of the bed or bed load and become suspended in the water column. Entrainment of sediment into the water column depends on many factors, including water velocity, turbulence, relative density of the grains, grain size, grain shape and the suspended sediment concentration. For mixed sediment, each grain size fraction will suspend under different flow conditions and can be treated as separate classes (Soulsby, 1997). Suspended load can be transported at much larger amounts than bedload, as it involves a greater part of the water column and this is the main mode of transport for muds (Soulsby, 1997; Whitehouse *et al.,* 2000).

In a suspension, the upward dispersion of sediment due to turbulence is balanced by the settling of the sediment and under constant conditions gives an equilibrium concentration profile in the water column (Whitehouse *et al.,* 2000). If the law of the wall is used to define the turbulent stress distribution in a steady uniform current, the shape of the sediment concentration profile depends on the ratio of the settling velocity to the shear velocity times the von Karman constant,

$$b = \frac{w_s}{\kappa u_*}$$

2-15

where b is the Rouse number or suspension parameter, w_s is the settling velocity, κ is von Karman's constant and u_* is the shear velocity (Rouse *et al*. 1937; Soulsby, 1997). The Rouse number is used in the Rouse profile for sediment concentration:

$$C_z = C_a \left(\frac{z}{z_a} . \frac{h - z_a}{h - z}\right)^{-b}$$

2-16

where C_z is the concentration at height z, C_a is the reference sediment concentration at height z_a and h is the water depth (Rouse *et al*. 1937; Soulsby, 1997).

In oscillating flow under waves, there is limited time to allow for the development of turbulence and the boundary layer (van Rijn, 1993; Winterwerp and van Kesteren, 2004). The wave boundary layer is thought to be no more than a few tens of centimetres thick, because the flow reverses before the layer can grow in the vertical direction (van Rijn, 1993; Winterwerp and van Kesteren, 2004).

For cohesive sediments, the settling velocity is a function of concentration and varies with height (Whitehouse *et al.,* 2000). As the settling velocity for fine material is less than large coarse grains, the concentration becomes uniform with depth and the suspension reacts more slowly to changes in flow velocity (Whitehouse *et al.,* 2000). The concentration profile is sensitive to small variations in the settling velocity, shear velocity and eddy diffusivity (van Rijn, 1984b). In addition, the high suspended sediment concentration will dampen turbulence (van Rijn, 1984b; Whitehouse *et al.,* 2000).

The power relationship for sediment concentration uses a single reference concentration, an empirically determined profile and a single representative settling velocity, so they are not appropriate for mixed sediment. The interaction between different size classes, with different settling rates, is not accounted for by these relationships. Modern measurement methods that can obtain profiles of the suspended sediment concentration and turbulence offer solutions to better understand suspensions of mixed sediments.

2.7.3 Bedforms and bed roughness

Bedforms are features of bed morphology developed below a fluid flow due to unstable interaction between the flow and the bed material (Allen, 1968). Bedforms can induce the separation of the

bottom boundary layer and generate vortex structures that suspend sediment from the bed, increasing sediment transport and energy dissipation, and affect currents and wave propagation. Therefore, prediction of their presence and characteristics is important for hydrodynamic and morphodynamic models (Blondeaux, 2012). Bedforms occur as assemblages of structures similar in shape and scale, and in orientation relative to the flow that created them, with uniformity under any one set of conditions (Blondeaux, 2012). Allen's book on current ripples (1968) describes bedforms at all scales and provides a good background. This work is focused on small-scale bedforms, of lengths in the order of centimetres to tens of centimetres, which are dominated by the vertical flow structure. At much larger scales, bedform morphology is dominated by horizontal flow patterns, forming banks, bars, ridges, creeks and channels (Dronkers, 2005).

When bed features become large relative to the boundary-layer scales, they no longer act as roughness elements, but rather as topographic steering mechanisms for the flow (Grant and Madsen, 1986). At high velocities, the bed will return to flat for small grain sizes or for larger grains dunes will develop, Figure 2-7 (USACE, 2002c). Factors that affect bed morphology include: water velocity, particle size, shape and density, bed consolidation, cohesion, suspended sediment concentration and water depth.

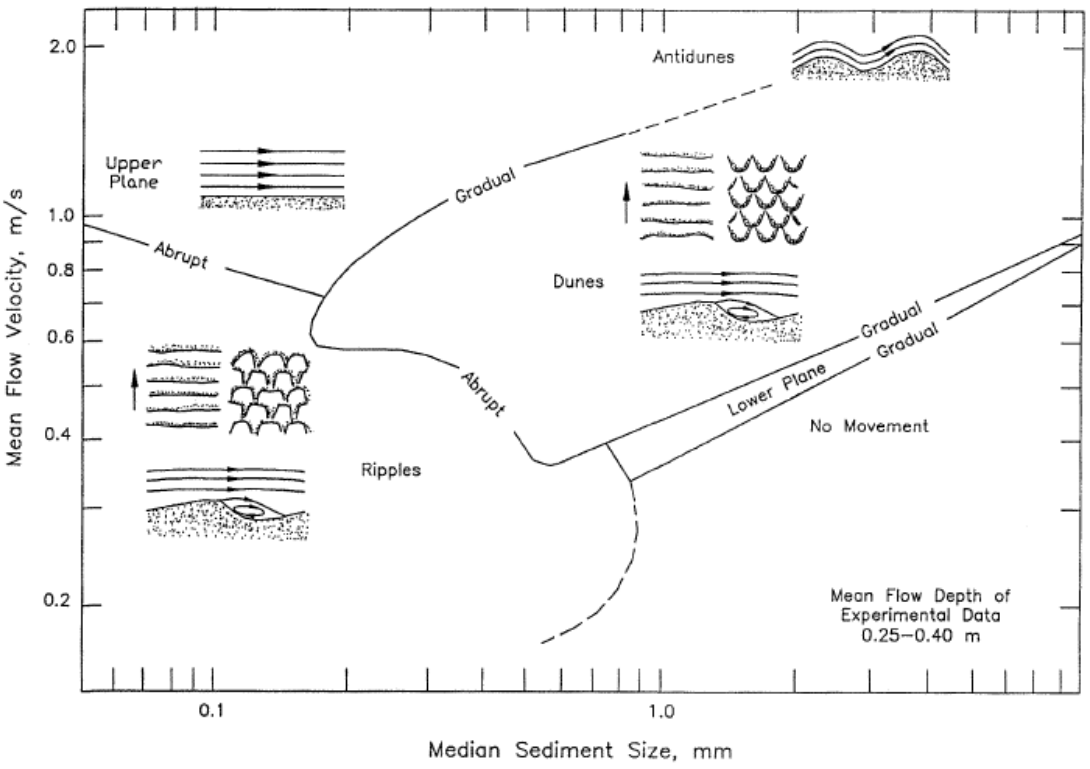

Figure 2-7: Bedform stability diagram. Plot of mean flow velocity against mean grain size, based on laboratory studies, showing the stability phases of subaqueous bedforms for steady unidirectional flow (USACE, 2002c; after Ashley 1990, and Southard and Boguchwal, 1990).

Unidirectional flows form strongly asymmetrical structures, while waves tend to form symmetrical and near symmetrical bedforms with sharp crests. The profile of a bedform can be described by its height from trough-point to crest-point, chord or length, the stoss slope length (upstream of the crest) and the lee slope length (downstream side) (Figure 2-8). The stoss slope experiences erosion and the lee slope deposition, and a platform may be formed at the crest of the ripple.

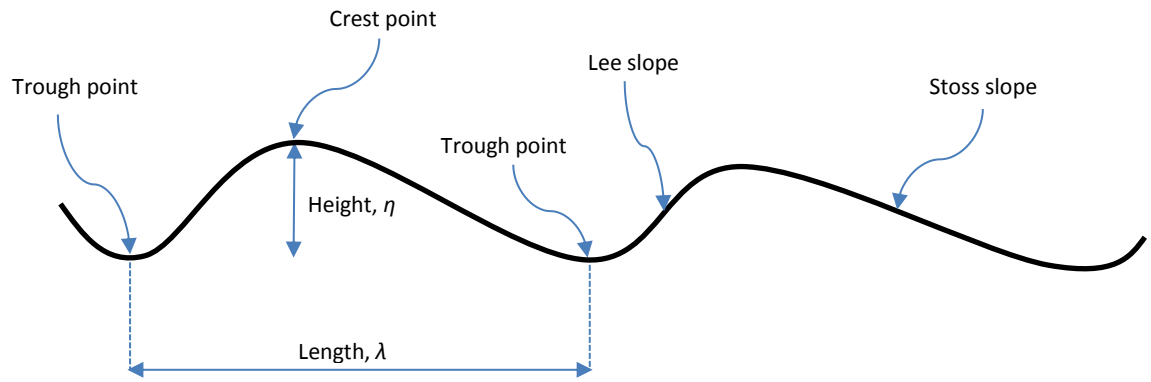

Figure 2-8: Bedforms in profile with terminology (after Allen, 1968)

Groups of ripples of a similar shape, scale and orientation are known as ripple-trains. Figure 2-9 shows ten ripple-train classes of the five basic patterns of ripple plan: straight, sinuous, catenary, linguoid and lunate. If the height along the crest line is uniform, the ripples are known as two-dimensional and if the height varies the ripples are known as three-dimensional. (Allen, 1968)

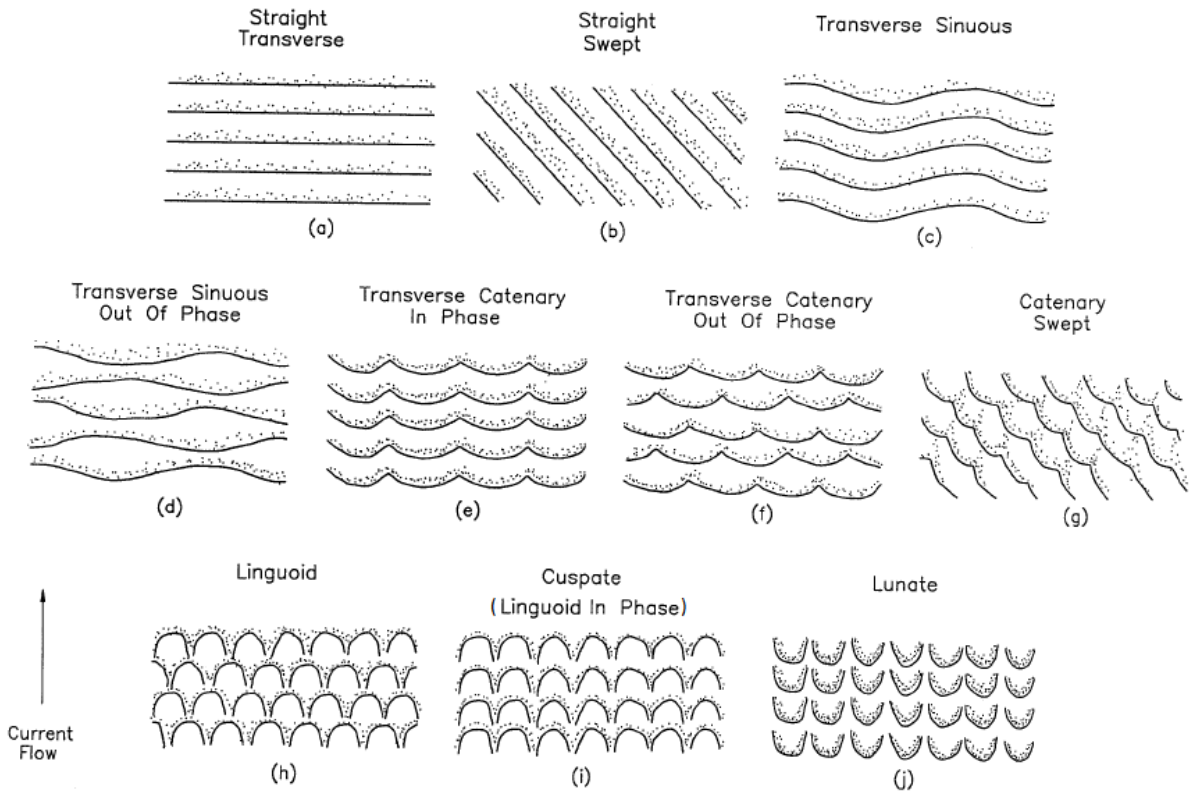

Figure 2-9: Idealised sediment ripple-trains. Lee sides and spurs are stippled. Water flow is from bottom to top (Morang and Parson, 2002 ; after Allen, 1968)

For combined flows, the ripple profile asymmetry alone cannot be used to determine if ripples are current or wave dominated. Wave-current ripples are more regular with rounded crests and current dominated ripples are more irregular, curved with sharp crests (Li and Amos, 1999). When waves and currents are at large angles to each other the ripples will co-exist to form cross-pattern ripples and at small angles, wave-current ripples occur (Li and Amos, 1999).

Ripples take time to reach equilibrium. In a steady flow, ripples in a flat bed of sand will develop in four stages: incipient ripples; straight and sinuous ripples; non-equilibrium linguoid ripples; and

equilibrium linguoid ripples (Baas, 1994; Baas, 1999). The time needed to reach equilibrium is related to the inverse power of flow velocity and equilibrium ripples have a linguoid form, which is independent of flow velocity (Baas, 1994; Baas, 1999). Due to constantly changing conditions, ripple parameters, such as wavelength and ripple height, are often not in equilibrium with hydrodynamic forcing and there is a lag between forcing and changes in the bedforms (Hay & Wilson, 1994; Masselink & Hughes, 2003; Austin, 2007; Traykovski, 2007; Soulsby *et al*., 2012). In varying tide, ripples may never reach an equilibrium form and will be constantly changing if the flow velocity is strong enough to move the sediment.

When ripples are present, the bed shear stress will increase from the trough to crest (Li and Amos, 1999). If the grain size distribution has a wide range, sorting is such that the coarse sediment accumulates at the crests and the fine sediment in the troughs of the bedforms, for cohesionless sediment (Blondeaux, 2012). In mixed beds of sand and clay, crests tend to become sandy over time (Baas *et al.,* 2013).

2.7.3.1 Bed roughness

For flat beds, the friction or shear stress is determined by the skin friction due to the sediment grains. Where bedforms are present, the form drag also affects the bed shear stress. The form drag may be many times larger than the skin friction (Soulsby, 1997). The skin friction is responsible for the bedload and entrainment of sediment from the bed (Soulsby, 1997). The form drag is associated with intense turbulence that mixes the suspended sediment further up into the water column (Soulsby, 1997).

In section 2.6.2, the roughness length, z_0, was defined as part of the function that described logarithmic flow profiles. For turbulent rough flow, z_0 is defined by the bed roughness or Nikuradse roughness, k_s (Soulsby, 1997; Liu, 2001):

$$z_0 = \frac{k_s}{30}$$

2-17

A multiple of the median grain size (empirically determined) defines the value of k_s for flat beds (Soulsby, 1997):

$$k_s = 2.5D_{50}$$

2-18

For a rippled bed, the values of k_s and z_0 can be determined from the logarithmic velocity profile or from the bedform dimensions. The form drag component of bed roughness, z_{0f}, has been related to the ripple height, η_r, and wavelength, λ_r, with an empirical constant, a_r (Grant and Madsen, 1982; Soulsby, 1997; Amoudry, 2008):

$$z_{0f} = a_r \frac{\eta_r^2}{\lambda_r}$$

2-19

The values of a_r and the roughness predictors used to determine η_r and λ_r from sediment properties are based on empirical data and may not be appropriate for all conditions (Amoudry, 2008).

Accelerating tidal flow can result in misleading values of u_* and z_0 if not accounted for (Soulsby and Dyer, 1980). The biggest variability in bed roughness length occurs for mixtures of sediments, as changes in the proportions of the mixture lead to large differences in the smoothness of the surface, as the interstices between the larger grains are filled (Wilkinson, 1986). Van Rijn (2007) suggested using the D_{90} value of the grain distribution (90%) for k_s in the case of well mixed non-cohesive beds. For bimodal beds van Rijn (2007) recommended using the grain sizes of the individual fractions separately.

2.7.3.2 Entrainment and ripples

In oscillatory flow above a steeply rippled bed, the boundary layer between the free flow and the bed can separate in the lee of the ripple forming a vortex, which at flow reversal is ejected higher into the water column and has a large effect on the entrainment of near bed suspended sediment (Thorne *et al*. 2003; O' Hara Murray *et al.,* 2011). Above ripple crests, the variation in near-bed suspended sediment within a wave cycle is dominated by half wave cycles where the orbital diameter is greater than 1.2 times the ripple wavelength and was found to be the main process of sediment entrainment higher into the water column (O' Hara Murray *et al.,* 2011). For asymmetric waves, this effect would result in substantial net sediment transport (O' Hara Murray *et al.,* 2011). With each successive wave cycle in a group, sediment is entrained to increasingly higher elevations, known as wave pumping, entraining sediment into the free stream (O' Hara Murray *et al.,* 2012). The substantially increased suspension time due to wave pumping could lead to increased cross-shore or long-shore transport, especially in the presence of currents (Nielsen, 2009; O' Hara Murray *et al.,* 2012).

2.7.3.3 Bedform size variation with bed composition

Sediment composition affects the dimensions bedforms attain. Ripples which are created by waves over a well sorted sandy bed are shorter than those observed of a poorly sorted sediment bed (Blondeaux, 2012). Laboratory flume experiments have found that ripple and dune size decreases with increasing bed mud content (Baas *et al.,* 2013; Schindler *et al.,* 2015). Preliminary results from the COHBED fieldwork agree well with this as ripple length was found to decrease with increasing mud content and no ripples were found above about 13% mud (Baas and Baker, 2013). Fully developed natural 3D ripples were found to contain about 5% mud (Baas and Baker, 2013). Winnowing of clay from mixed sand-mud eventually causes ripples to resemble clean sand, but bed cohesion and armouring may prevent mixed sediment ripples from reaching the size of pure sand ripples (Baas *et al.,* 2013).

1.4.1.1 Scour

Scour is an important process caused by objects embedded in sediment or close to the bed. Although not usually considered a bedform, scour is a change in the bed morphology due to the hydrodynamic effect of objects in the flow. In the context of this work it is an effect caused by the frame that the instruments used to measure the sediment processes were mounted on and may impact on the data interpretation. Clay in clay-sand mixtures has been found to reduce the scour depth and horizontal extent of the scour hole, as well as changing the pattern of scour from the front of the object to the sides (Debnath and Chaudhuri, 2010). For non-cohesive sediments erosion occurs as grains. Scouring of clay-sand mixtures occurred as chunks of aggregates and aggregate by aggregate as well as grain by grain (Debnath and Chaudhuri, 2010). The maximum scour depth increases with increasing water content of the clay-sand mixture, as does the length of the scour hole (Debnath and Chaudhuri, 2010).

2.7.3.4 Analysis of bedform train profiles

In nature, bedforms occur in irregular groups depending on the hydrodynamic conditions and sediment composition. Using modern instrumentation two and three-dimensional profiles of bedforms can be obtained at regular time intervals allowing the characterisation of bedform trains and their variation over time. Three techniques that have been used to analyse groups of bedforms of varying dimensions are zero crossing, Fourier (spectral) analysis and wavelet transforms (Davis *et al.,* 2004; Lindenbergh *et al.,* 2006; Traykovski, 2007; van Der Mark, Blom & Hulscher, 2008; Cataño-Lopera *et al.,* 2009; Englert, 2010; Lefebvre *et al.,* 2011).

The zero-crossing method detects where the bed profile crosses the mean level, troughs and crests can be located between these points (van Der Mark *et al*., 2008). The ripple lengths, heights, stoss slopes, lee slopes and bedform asymmetry can then be calculated (van Der Mark *et al*., 2008). This method will miss small bedforms that do not cross the zero level (van Der Mark *et al*., 2008).

Fourier analysis is useful for analysing superimposed harmonic bedforms, breaking up a signal into a series of constituent waves of different amplitudes and frequencies that correspond to bedform heights and wavelengths (Lindenbergh et al., 2006). For two dimensional ripples 1D Fourier analysis can be used to determine the significant height and wavelength of ripple trains and the bed roughness, 2D Fourier analysis provides information on the three-dimensionality and orientation of the ripples (Traykovski, 2007; Englert, 2010; Lefebvre *et al.,* 2011). Using spectral analysis changes in the ripple height, length, and/or shape can be considered as an energy transfer process (Davis *et al.,* 2004). Fourier analysis works best on stationary data, or where there is little change in the harmonic constituents over a record, as it produces an averaged amplitude for the whole record (Emery and Thomson, 1997).

For rapidly changing or non-stationary records, the wavelet transform produces local estimates of the spectral components, tracking the variation of signal characteristics through a dataset (Emery and Thomson, 1997). Wavelet analysis involves the convolution of a data series with a set of functions of different scales that are derived from a wavelet function, which are moved through the record (Emery and Thomson, 1997). The properties of the wavelet transform allow the local description of bedform dimensions and therefore characterisation of the change in bed morphology across the record (Cataño-Lopera *et al.,* 2009). The wavelet transform complements other statistical techniques, such as the Fourier transform, to obtain higher local-frequency and location resolution when analysing bed morphological patterns (Cataño-Lopera *et al.,* 2009).

2.7.4 Settling, flocculation, and deposition

2.7.4.1 Settling of suspensions

In section 2.4.1.5 an overview of the settling velocity of individual grains was given. For high concentrations of suspended sediment, the grains will interact with each other as they settle. Suspended sediments in natural flows have four components to their motion: Brownian motion, gravitational settling, the motion of the ambient fluid and rebounds from inter-particle collision (Mehta, 1989). Brownian motion is chaotic motion due to the molecules of the fluid, the gravitational

settling depends on the grain properties, the motion of the fluid depends on the hydrodynamic forcing and the inter-particle collisions depend on the concentration of the suspended sediment.

At high concentrations, hindered settling is caused by adjacent grains interacting to cause greater drag and return flow, particle collisions, increase of effective viscosity, the increase of buoyancy, and settling convection of sediment clouds (Mehta, 1989; Winterwerp and van Kesteren, 2004). For fine and medium sands, the settling velocity reduces to less than 20% of the clear water settling velocity for suspended sediment concentrations greater than about 30% (Baldock *et al*. 2004).

The settling velocities of cohesive particles are properties of a suspension, not unique properties of the individual sediment grains (Mehta *et al.,* 1987 in Mehta, 1989). Very fine sediment will not settle alone under gravity and can form a permanent wash load in the water column. As suspended sediment can be made up of a range of particle sizes, of different settling velocities, the deposition rate is not simply the product of the median settling velocity and suspended sediment concentration, but should be treated as different fractions (Winterwerp and van Kesteren, 2004).

2.7.4.2 Flocculation

Flocculation is the process where particles in suspension stick together to form groups that then settle as a single particle (Whitehouse *et al.,* 2000). This can be due to the cohesive forces between sediment grains or to adhesion from organic matter. Flocs of varying size can consist of varying compositions of clay, silt, fine sand and water (Winterwerp *et al.,* 2006). The adhesive effect of biological substances allows non-cohesive particles to be bound into flocs and sand particles engaging flocculation appear to be principally affected by turbulent shear stress (Spearman *et al.,* 2011). The size and settling velocity of flocs can be much larger than individual particles and because of this rapid deposition may occur (Whitehouse *et al.,* 2000).

As the suspended sediment concentration increases, free settling changes to flocculation settling because of increased inter-particle collision (Mehta, 1989). Collisions occur due to Brownian motion, internal shear of the water, turbulence, and differential settling velocities of particles or flocs (Whitehouse, 2000). Flocs are delicate and too much shear can break them apart. Rainwater can also cause deflocculation by reducing the salinity of the seawater (Whitehouse *et al.,* 2000).

Experiments with suspensions of mud-sand mixtures showed that as mud content decreased cohesion reduced, limiting the growth of potential of macroflocs (sizes>160 μm) (Manning *et al.,* 2013). By adding sand to a mud-sand suspension the settling velocity of the macroflocs fraction reduces and the

settling velocity of the microflocs (sizes<160 µm) increases (Manning *et al.,* 2013). These results suggest that the finer sand grains tend to bond better with smaller flocs, accounting for the quicker microfloc settling velocities (Manning *et al.,* 2013).

2.7.4.3 Deposition and consolidation

Layers in the bed occur due to different grain sizes settling at different rates. For mixtures of mud and sand, the stratigraphy of the bed is dependent on the initial conditions of the suspension and the chemical and biological properties of the mud (Torfs *et al.,* 1996). Before the gel point of the cohesive fraction is reached, heavier particles can sink through to form a bottom layer (Torfs *et al.,* 1996). Once the clay minerals have gelled into a matrix, further settling material is supported without falling through (Torfs *et al.,* 1996). The passage of sand down through the bed increases the consolidation rate (Torfs *et al.,* 1996).

Consolidation occurs when poorly packed sediments orientate into a denser matrix. This can occur because of vertical loading from other sediments, by draining of fluids from the sediment pore space or by desiccation, and by vibration (USACE, 2002c).

Hydrostatic pressure differences across ripples, due to currents and waves, cause water to flow through permeable sediment and traps fine particles in the bed (Huettel *et al*., 1996; Precht and Huettel *et al*., 2003). The topographic advective filtering, due to pressure differences across ripples, has a much greater effect than hydrostatic pumping by waves on a flat bed (Huettel *et al*., 1996; Precht and Huettel *et al*., 2003).

2.7.5 Sediment transport

Transport of sediment occurs as bedload, suspended load and wash load. The processes listed in Table 2-1 can occur in succession or at the same time, due to the mixture of sediment types present, as the sediment suspension, wash load and bed load interact. The distinction between the three modes of transport is not always clear (Dyer, 1995). The physics of how water moves sediment is not well understood, as it involves turbulence, and a large number of formulae have been created to predict transport rates, usually functions of water velocity or bed shear stress and sediment properties (Soulsby, 1997; USACE, 2002b).

In the 1920's Exner created an equation that related the change in bed level to the sediment flux based on the conservation of mass:

$$\frac{\partial \eta_b}{\partial t} + \frac{1}{(1-P)} \frac{\partial q_s}{\partial x} = 0$$

2-20

where η_b is the bed height, t is time, P is the sediment porosity (ratio) and q_s the sediment transport per unit width per second ($m^3\ m^{-1}\ s^{-1}$) in the downstream, x (m), direction (Vanoni, 1975; Paola & Voller, 2005). This related the rate of bed erosion or deposition to the change in concentration of sediment transport with distance in the stream-wise direction (Vanoni, 1975; Paola & Voller, 2005). Richardson, Simons and Posakony (1961, cited in Hubbell, 1964, p. 43; Simons *et al*., 1965) used the assumption of constant triangular bedform shape to create an equation for bedload transport of 2D bedforms:

$$q_b = 0.5\ (1 - P)\ u_b\ \eta$$

2-21

where q_b is the bedload volume transport per unit width per second ($m^3\ m^{-1}\ s^{-1}$), u_b is the mean velocity of the bedform crests ($m\ s^{-1}$), η is the mean bedform height (m). Equation 2-21 can be derived from the Exner equation (2-20) by rearranging and integrating. The coefficient of integration is made to zero by the boundary conditions (Hubbell, 1964). To better represent bedform shape, the ½ term in equation 2-21 can be replaced by a bedform shape factor, f:

$$f = \frac{2V}{HL}$$

2-22

where V is the bedform volume per unit width ($m^3\ m^{-1}$) and L is the bedform length (m) (van Rijn, 1986). It is assumed that there is no change in mean bedform height between measurements of bedform position and no loss or gain of sediment, from the sample area, by saltation or suspension (van den Berg, 1987). Hubbell (1964) proposed a factor to account for suspension loss or deposition gain, K, which he took to be close to unity. The three-dimension nature of ripples is not accounted for by these methods, an approximately two-dimensional form is assumed.

To calculate the bedload mass transport rate, Q_b ($kg\ m^{-1}\ s^{-1}$), the bedload volume transport rate is multiplied by the sediment density, with f and K the result is:

$$Q_b = K\rho_s(1 - P)f u_b \eta$$

2-23

Transport of a sediment lags behind changes in flow and can produce a residual flux even without an asymmetrical current, due to the time taken for sediment to settle out of the water column (Dyer, 1995). Lags can be produced by a variety of causes, such as the threshold of motion, bed strength, the threshold of deposition and settling velocity; with different processes being important for mud and sand (Dyer, 1995). Because suspended sediment concentration lags behind instantaneous bottom stress, tidal currents moving away from areas of higher energy will carry more sediment than tidal currents moving away from areas of lower energy, which results in a net flux of sediment advected by the tide toward areas of lower energy (Friedrichs, 2011).

For a graded bed of sand, calculating the transport as multiple fractions instead of using a single size produced values that were closer to experimental results, as finer sands contributed more to the total suspended transport rate (van Rijn, 2007). The fraction sizes used in the calculation should be based on the particle size distribution over the silt and sand range (van Rijn, 2007).

2.8 Biological action on sediment

Marine life living in the sediment modify the physical and chemical processes that affect sediment dynamics (Andersen and Pejrup, 2011; Passarelli *et al*., 2014). Sediment is reworked to form burrows to live in and find food in the processes of bioturbation. Algae and microbes grow on sediment, binding grains together with adhesive material, stabilising the bed. Suspended sediment and bed sediment is ingested to remove the organic material as food and excreted bound in adhesive material. Different organisms have different effects on the sediment: stabilising and destabilising, changing the bed roughness and hydrodynamics, and depositing and re-suspending material (Fries *et al.,* 1999, Widdows & Brinsley, 2002; Anderson, 2002; Anderson and Pejrup, 2011; Passarelli *et al*., 2014).

The net effect of these competing biological processes depends on many factors including the ecosystem composition, season, latitude and climate change (Anderson and Pejrup, 2011; Jones *et al*., 2013; Passarelli *et al*., 2014). Although a particular ecosystem may be unique in species composition, the functions carried out within the ecosystem will be duplicated by other species for different sites, meaning that the sediment dynamical processes are similar (Anderson and Pejrup, 2011; Passarelli *et al*., 2014).

2.8.1 Microorganisms

Many microorganisms in aquatic habitats secrete extracellular polymeric substances (EPS), which range from gels to a fully dissolved state, for attachment and locomotion and in sufficient quantities, the EPS can form biofilms stabilising the bed and reducing bottom roughness (Underwood and Paterson, 1995; Sutherland *et al.*1998; Decho, 2000). These biofilms reduce the physical stresses of the environment on the microorganism, improving their habitat by reducing UV irradiation and desiccation, and changing the salinity and temperature (Decho, 2000; Passarelli *et al*., 2014). Diatoms, single celled algae that have a silica cell wall, are a key group in biofilm production.

Trapped oxygen bubbles in the biofilm from photosynthesizing diatoms can cause positively buoyant bulk density values, however, these bubbles are rapidly depleted during dark periods due to aerobic respiration (Sutherland *et al*., 1998). Although the biofilm adhesion would resist this buoyant force, the daily cycle may affect the erodibility of the sediment (Sutherland *et al*., 1998). Trends in erosion threshold and rate were found to be strongly biofilm dependent, as adhesive and cohesive properties tend to dominate sediments with low densities (Sutherland *et al*., 1998). Tolhurst *et al*. (2003) described the sediment armouring effect literally, with diatoms acting as plates held together by elastic EPS. However, there is a time lag in the bed stability as the diatoms migrate to the sediment surface when the bed is covered by the incoming tide (Tolhurst *et al*., 2003). Ripple crests have a higher resistance to erosion than troughs due to diatoms stabilizing the crests more than the troughs (Lanuru *et al.,* 2007).

Bacterial production of EPS is constant, but diatoms are more efficient in sediment stabilisation even though this production is light dependent (Lundkvist *et al.,* 2007). Diatoms produce EPS and store energy when light is available for photosynthesis, but increase EPS production in darkness, using up the stored energy (Smith and Underwood, 1998). Newly produced EPS seems to have higher bonding efficiency and the EPS production rate is a better proxy for predicting the erosion threshold than total EPS content, though the biological system needs 2-3 days of adjustment to the environment before the erosion threshold increases (Lundkvist *et al.,* 2007). The adhesive properties of EPS will also influence sediment that is suspended from the bed (Decho, 2000) and are extremely important in the mixed sediment flocculation process, bonding both non-cohesive and cohesive particles within microflocs (Manning *et al.*, 2013).

Biological cohesion has much stronger effect on bedform dynamics that the physical cohesion due to clay (Malarkey *et al.,* 2015; Parsons *et al.,* 2016). As for physical cohesion, laboratory experiments have shown that bedform dimensions are reduced with increasing EPS content (Malarkey *et al.,* 2015; Parsons *et al.,* 2016). However, EPS is also subject to the winnowing process and bedforms will grow

as EPS is removed from the bed (Malarkey *et al.,* 2015; Parsons *et al.,* 2016). In the natural environment, there will be a balance between EPS production and winnowing.

2.8.2 Macro-organisms

Benthic invertebrates have been shown to vertically sort sediments, produce adhesive substances that increase sediment strength and alter the bed roughness (Fries *et al.,* 1999; Passarelli *et al*., 2014). They create mounds on the seabed from waste material, which may enhance local shear stress causing bed scour, and they can eject matter into the water column to be transported as bedload (Fries *et al.,* 1999; Passarelli *et al*., 2014). Ripple formation can be affected by the alteration in flow due to the presence of biogenic mounds (Fries *et al.,* 1999).

Bioturbation mixes the bed sediment, destabilising the bed, and redistributing nutrients making them available for consumption by other organisms (Grant and Daborn, 1994; van de Koppel *et al*., 2001; Passarelli *et al*., 2014). Filter feeders capture suspended material from the water column, by either using appendages or siphoning the flow, and mix it into the bed (Jørgensen *et al*., 1984; Shimeta and Jumars, 1991; Passarelli *et al*., 2014).

Different life stages of the same species may have different effects on the sediment. While the adult Mud shrimp (*Corophuim Volutator*) was found to have little effect on silt-clay sediments from bioturbation or binding of sediment for burrow creation, younger mud shrimp stabilised the sediment (Grant and Daborn, 1994). Seasonally the shrimp reduced the sediment erosion threshold by grazing on microflora, which would otherwise inhibit the initiation of grain motion (Grant and Daborn, 1994).

Macro-algae, such as seagrass, have stabilising effect on the sediment and bed shear stress, promoting sediment settling and deposition to the bed (Widdows & Brinsley, 2002; Anderson and Pejrup, 2011; Passarelli *et al*., 2014). The growth of plant beds can lead to the formation of saltmarsh and channel networks, changing the morphology of tidal flats (Fagherazzi *et al*. 2012; Kirwan and Guntenspergen, 2012).

2.9 Methods of sediment characterisation

Natural sediments can be sampled *in situ* and returned to the laboratory for analysis or their properties can be inferred from electronic instrumentation measuring the *in situ* response of the sediment to light or sound. Although the methods in this section have been split up based on the type of measurement, electronic instruments often measure multiple parameters. For instance, all acoustic

instruments measure backscattered sound, however, some are designed to primarily measure water velocity using a single frequency and others the concentration of scatterers, suspended in the water, at multiple frequencies. Many instruments also have built in pressure and temperature sensors to aid the data interpretation.

2.9.1 Sediment sampling and analysis

Direct sampling of the seabed can be done using a grab, corer or scoop. Samples from the water column can be taken using sampling bottles that are triggered at depth, systems that pump water samples or settling traps. For bulk samples, graded sieves can be used to determine the particle size distribution. In addition, bulk density, organic content and settling velocity can be determined by simple methods such as weighing, wet and dry volume determination, loss on ignition (using a furnace) and settling rate measurement. For smaller samples and sub-samples laboratory instruments are available that can determine particle size distribution through settling velocity and laser diffraction methods.

A settling column can be used to determine particle size by measuring the time it takes particles to fall a set distance. This method produces slightly different size distributions than from sieving, as the shape of the particle effects the settling velocity, but the particle size distributions from settling columns are at a much higher resolution.

In situ sediment strength can be measured using a shear strength vane, which applies a force until the sediment fails. Other methods involve the use of a mini-flume or water jets to erode the sediment and measure the temporal increase in suspended sediment concentration (Grabowski *et al.,* 2010). Recently a method has been developed to measure sediment adhesion by adding fluorescent magnetic particles to the sediment surface and applying an increasing magnetic field, called MagPI, which is particularly useful for biofilm measurement (Larson *et al.,* 2009). MagPI has a higher sensitivity and accuracy than other methods (Larson *et al.,* 2009).

2.9.2 Optical methods

Inorganic particulate matter scatters light intensely, particularly in the red-infrared section of the spectrum (Kirk, 1996). The scattering properties of sediment can be used to gain information about the concentration and size distribution of suspended sediment.

2.9.2.1 Optical Backscatter Sensor (OBS) and transmissometer

Optical backscatter sensors emit light in the red-infrared region and measure the light scattered from suspended particles in the water. A transmissometer measures the reduction of intensity of a beam of light transmitted over a set path length, in the same optical region. Over a certain range, the response is linear with suspended sediment concentration and with calibration samples the response from these instruments can be converted to concentration values.

Both transmissometer and OBS suffer from the same problems; the measurements are affected by particle size, shape composition and flocculation, dissolved organic matter, bubbles and biofouling of the sensor (Downing, 2006). Change in the particle size distribution causes a change in sensor response, even if there is not an actual change in concentration, due to the relationship between size and scattering efficiency (Downing, 2006). However, these instruments produce relatively stable measurements and there is a long record of their use (Bunt *et al*. 1999; Downing, 2006).

2.9.2.2 Laser diffraction

Laser diffraction is an improvement on the transmissometer and OBS methods, and can be used to obtain the particle size distribution (PSD) and volume concentration of the particles suspended in water (Agrawal and Pottsmith, 2000; Malvern Instruments Ltd, 2007; Sequoia Scientific Inc., 2009). This method is used by laboratory and *in situ* instruments, since the 1990's. Because of the variation of particle properties in estuaries, and the presence of flocs, the resulting size distributions and concentrations from in situ laser diffraction instruments are approximate (Fugate & Friedrichs, 2002). These *in situ* laser scattering instruments also measure the optical transmission through the water allowing for a comparison with historical transmissometer data, which have been in use since the late 1970's (Bunt *et al*. 1999).

2.9.3 Acoustic methods

Acoustic methods have the potential to measure the water currents, suspended sediment and bed morphology simultaneously and without intrusion, with the required temporal and spatial resolution to observe these properties and their variation (Thorne and Hanes, 2002). One of the main advantages of acoustic method is the ability to give a profile of the water column relative to the bed. Acoustics also have an advantage over optical methods in that sound is less easily attenuated than light in turbid water. However, acoustic signals are affected by bubbles, plankton and very high suspended sediment concentrations (Stanton *et al*., 1996; Thorne and Hanes, 2002; Mori *et al*., 2007).

The acoustic backscatter signal can be analysed to produce scattering intensity, suspended particle velocity and range to a boundary. Factors that affect these measurements include: sediment size, sediment density, attenuation due to water & sediment, sediment concentration and the speed of sound in water.

2.9.3.1 Bed morphology measurements: the Acoustic Ripple Profiler

Just as an echo sounder on a boat can build up a picture of the seabed topography from acoustic reflections, on a small-scale this can be done to resolve seabed morphology using an acoustic pulse backscattered from the bed to create an image of the bed morphology (Thorne and Hanes, 2002). In addition, by measuring the distance to the seabed, the rate of change of the bed level can be used to extract erosion and deposition events from a time series (Anderson *et al.,* 2007).

For measurements in two dimensions, errors occur if a 2D profiler is not orientated in the direction of the ripple migration (Thorne and Hanes, 2002). 3D Ripple Profilers rotate a transducer in two axes, which images a circular area of the seabed (Marine Electronics, 2009).

By collecting regular images of the seabed, the evolution of ripple morphology can be seen in relation to the changing hydrodynamic conditions (Thorne and Hanes, 2002). However, bed detection can be difficult in high concentrations of suspended sediment, which also degrades the images, and shadow zones at low grazing angles can limit results (Thorne and Hanes, 2002).

2.9.3.2 Concentration measurements: Acoustic Backscatter Sensor (ABS)

An acoustic transducer can transmit a short pulse down through the water column that is backscattered by any suspended material and the return echo used to estimate the concentration profile (Thorne *et al.,* 1993). However, considering suspended sediment particles as elastic spheres when modelling their acoustic response does not fit the available data, as resonance does not occur in natural particles (Sheng and Hay, 1988). Sheng and Hay (1988) found that better agreement was found with rigid movable particles. From acoustic measurements at known concentrations, and with an understanding of particle response, a relationship can be found for a particular sediment type between acoustic backscatter amplitude and suspended concentration, which can then be inverted to produce estimates of concentration values (Thorne *et al.,* 1991).

As the acoustic scattering of a particle depends on its size, certain frequencies of sound will be scattered more strongly by particular size fractions. Instruments that use multiple frequencies can

measure a wider range of particle sizes and get an indication of size distribution. For example, by transmitting on four frequencies, 1 MHz, 1.5 MHz, 2.5 MHz and 3.0 MHz, size inversion is feasible for particles 20 µm to 500 µm to give a profile of suspended sediment in the range 0.1 to 20 g/l (Aquatec, 2013).

2.9.3.3 Bedform & Acoustic Sediment Scattering Imager (BASSI)

By using a linear array of downward looking transducers, measurements of suspended sediment and bedforms can be made at the same time in a two-dimensional section (Moate *et al.,* 2011, 2016), a combination of a 2D ripple profiler and an ABS. The Bedform & Acoustic Suspended Sediment Imager consists of one or more transducer arrays mounted horizontally, looking down at the sea-bed, and simultaneously capturing a line of profiles of acoustic backscatter intensity with 15 transducers over the length of a single array (Marine Electronics, 2010). The operating frequencies are 0.75, 1.25 and 2.50 MHz, interleaved along the length of the array so that there are five channels of each frequency per array (Marine Electronics, 2010).

With multiple transducer arrays connected together in 'T' or '+' arrangements (Figure 2-10), sections of the seabed and the suspended sediment above it can be imaged perpendicular to the main axis of flow as well as parallel to the flow, the three dimensional nature of the bedforms and their effects on the suspended sediment can be measured.

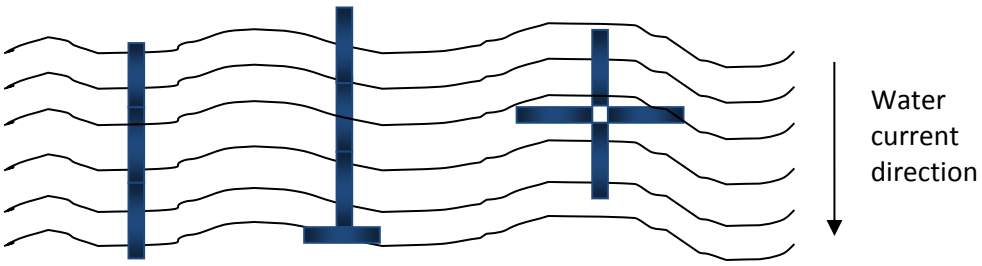

Figure 2-10: Different array configurations for the BASSI: 2D linear, 3D 'T' and 3D '+'.

2.9.4 Velocity measurements

2.9.4.1 Acoustic Doppler Velocimeter and velocity profiler

Acoustic Doppler instruments measure the water velocity in three axes at a single point, or in a profile, by transmitting acoustic pulses that are scattered back to multiple receivers by particles in the water. The velocity is then calculated from the Doppler shift in the frequency of the backscattered pulses.

These instruments offer unobstructed three axis flow measurements at high sampling rates and can be used in the field without some of the problems of other velocimetery methods, for example, flow blockage of impeller current meters (Voulgaris and Trowbridge, 1998). The method assumes that the water velocity is equal to the particle velocity and larger scatterers may not represent the water velocity accurately, but this can be corrected for using particle size information (Thorne and Hanes, 2002). To improve the spatial and temporal resolution, a technique called pulse coherent processing is used, where the phase shift between two pulses of a known time lag are compared (SonTek, 2001).

2.9.5 Supporting measurements

It is useful to know other properties of the seawater to support the measurement of the sediment processes and properties. The CTD is a standard oceanographic instrument that measures Conductivity, Temperature and pressure (Depth). Values for salinity, density and the speed of sound in water are derived from these data, which can then be used to check and correct the data from acoustic instruments that often use pre-set values of temperature and salinity when calculating parameters. This is important in estuarine waters, as a change in temperature of 5° C or salinity of 12 ppt results in a 1% change in speed of sound (SonTek, 2001).

Although many electronic oceanographic instruments measure pressure as a secondary reading, which can be used to determine the tide, air pressure can affect this signal and this can be corrected for with meteorological data. Also having data on the weather is useful when looking at the waves and the effects of atmospheric exposure on the bed strength when the tide is out. Often data on river flow are also available that can be related to the hydrodynamics and influence of freshwater.

2.10 Coastal morphology and regional numerical modelling of sediment processes

By taking the knowledge of small-scale sediment dynamical processes and applying them in computer models, a greater understanding of how they affect the coastal morphology of regional areas can be made (Cowell *et al*., 1995; Davies and Thorne, 2008; Amoudry and Souza, 2011). Large-scale features, such as beaches, tidal flats, bars, banks and spits, will change and move with the hydrodynamic conditions in a particular area. Modelling coastal morphological change and sediment transport is important for the management of coastal flood defence, navigation channels, natural habitats and marine renewable energy developments (Amoudry *et al*., 2009; Brown *et al*., 2010, 2016). This may be in the form of: hind-casting, understanding events in the past; now-casting, explaining what is going

on in the current environment; and forecasting, predicting what will happen in the future. These approaches are used to understand a particular area or system and make decisions based on the information generated for environmental management and marine operations. The quality of this information depends on the understanding of the hydrodynamic forces and sediment dynamic processes. A flowchart of the general structure of a sediment transport model is shown in Figure 2-11, which includes hydrodynamic forcing, bed and suspended load, bed morphology and structure, and the boundary layer (Amoudry and Souza, 2011).

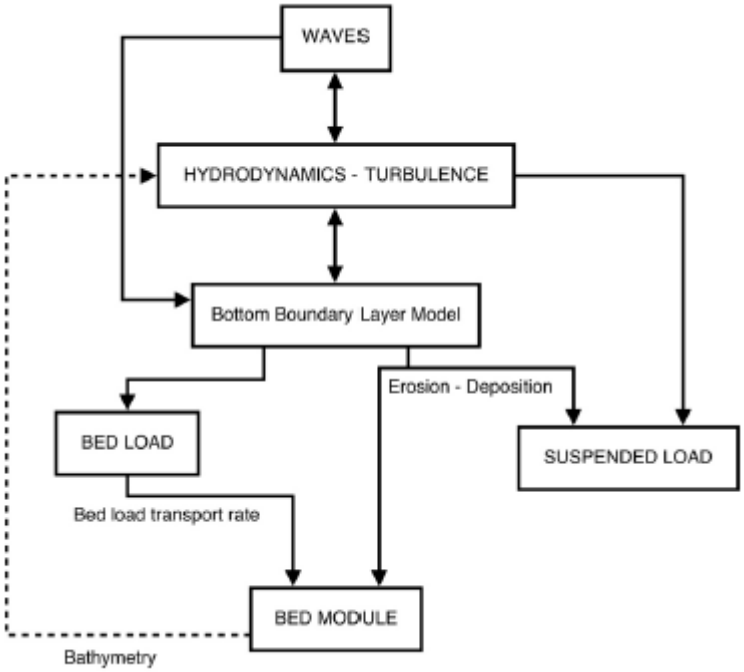

Figure 2-11: General structure of sediment transport models in coastal ocean models (Amoudry and Souza, 2011)

Many issues arise from the multi-scale nature of modelling, as the scale of models is much larger than the processes that affect the transport, which are implemented on a sub-grid scale (Amoudry, 2008). The gap between sediment process experiments and coastal area modelling highlights the need for modelling of small-scale process validated using measurements to represent the appropriate physical processes (Amoudry and Souza, 2011).

Many models of mixed sediment transport still separate the modelling of sand and mud fractions assuming that these different fractions do not interact, except at the bed, ignoring the effect of sediment flocculation (Amoudry *et al.*, 2009; Manning *et al.,* 2011). Models including biological effects

on sediment stability tend to assume a steady effect or do not account for long-term morphodynamic coupling processes, and the fact that the horizontal resolution of any morphological model is larger than the patchiness of the biota causes difficulty in scaling up biological processes (le Hir *et al.,* 2007). Sanford (2008) developed a one dimensional model of mixed non-cohesive and cohesive sediments with biota. Three-dimensional models of mixed sediments have been developed that include non-cohesive-cohesive behaviour but do not yet include the effects of biology (van Ledden, 2002; Waeles *et al.,* 2008; Le Hir *et al.,* 2011). Predictive models of sand ripples are important for determining the bed roughness for sediment transport models and have been shown to compare well to Acoustic Ripple Profiler data (Balaños *et al.,* 2012; Soulsby *et al.,* 2012). The parameterisations of mixed non-cohesive and cohesive sediment, ripple morphology and biological processes are still ongoing, and have yet to be integrated into any regional model (Amoudry *et al.* 2009).

The variation of sediment properties over a large area can be difficult to measure as the instrumentation used is expensive and works only over short distances. Using a processed-based sand and mud model, dimensionless parameters can be derived that can increase understanding of the horizontal and vertical bed composition variations (van Ledden, 2002). Modelling, field measurements and laboratory experimentation have to be used in conjunction to gain an understanding of a sediment transport system at all scales.

2.11 Discussion

Although an attempt has been made here to separate the different properties, forces and processes that contribute to the dynamics of sediments formed of mixtures of sand, silt, clay and biology, studies need to account for the complexity of the overall coastal and estuarine system. A comprehensive set of measurements should be collected in experiments and fieldwork in an attempt to describe these complex relationships.

Ideally, to relate *in situ* sediment properties to instrument measurements regular co-located physical samples should be taken over a spring-neap cycle for calibration, but this is not always possible. Samples from the tidal flats at low tide may not be representative of the material in the water column or in the bed during inundation, if there has been winnowing, advective transport and deposition, and flocculation cannot be accounted for.

The bed shear stress needs to be defined for studying the initiation of sediment motion, erosion and sediment transport. Methods for determining the bed shear stress that are based on different physical assumptions, created for different hydrodynamic conditions, give different results. Usually a selection

of methods are used and compared (Balaños *et al.,* 2012; Lichtman, 2012; Thompson, 2012) though this can make comparisons of different studies difficult, if the same methods are not used or different empirical constants are applied.

Due to constantly changing conditions, bedform parameters, such as wavelength and ripple height, are often not in equilibrium with hydrodynamic forcing, with a lag between forcing and response (Traykovski, 2007). How quickly a sediment responds to the hydrodynamic forcing will depend on its size distribution, composition and cohesion.

The effect of EPS production by diatoms, drying and compaction, stabilizing the crests more than the troughs (Lanuru *et al.,* 2007) could affect how ripples develop, by increasing the ripple steepness as the troughs erode faster than the crests. This stabilising effect would also increase the time lag between hydrodynamic forcing and the response of the bed morphology.

Sediment stabilisation by diatoms is light dependent as the diatoms rely on photosynthesis to provide energy, but they can be damaged by exposure so only migrate to the sediment surface when the tide is covering the bed (Lundkvist *et al.,* 2007). The result is a varying response of surface sediment strength to the cycles of the tide and daylight when diatoms are present in abundance and producing adhesive Extracellular Polymeric Substances (EPS).

Worm mounds stabilised by EPS may cause scour patterns similar to solid fixed objects on the seabed. This would create irregular bed morphology and mobile bedforms would be affected by the mounds and scour. From predictions of bedform development and dimensions, based on the hydrodynamics, and data from a 3D ripple profiler, the patchy distribution of these features could be assessed as they would be relatively stationary compared to ripples in clean sediment.

There is still much work to be done on integrating the behaviour of mixed non-cohesive and cohesive sediment and biological effects into models. The patchy nature of these processes interacting at small scales poses a problem for scaling up to regional models. Defining these processes, using experimental and field data, relative to factors that can be easily measured or modelled, such as water level, light exposure, wind, wave height or water velocity, could improve regional models.

Modelling the biology is very difficult, as the composition of an ecosystem may be unique to a particular area, even if the species it is composed of are common. The overall biological effect on the sediment dynamics are site and time specific and will require surveys to characterise the ecosystems of a region.

2.12 Conclusions

This review has given a general overview of the current understanding of the processes that affect mixed sand, silt and clay sediments in estuaries and on tidal flats. The effect of the biology of tidal flats has also been introduced, as this adds extra complexity to the sediment dynamics.

One of the first tasks leading on from this work, using the data from the Dee, is to show in field conditions, that bedform dimensions are significantly different for mixed cohesive sediment beds compared to beds with pure sand. This would confirm laboratory results that showed reduced bedform dimensions due to cohesive mud content

The improvement of predictors for the processes of mixed non-cohesive and cohesive sediments, the bedforms they develop, and the influence of biology on these processes will contribute to improved regional sediment models. These can then be used to predict the transport of pollutants, manage dredging of navigation channels, plan coastal protection and engineering works, and aid ecological management.

3 Field data collection and processing methodology

3.1 Introduction

This chapter describes the fieldwork carried out as part of the COHBED project, the methods used to process and analyse the data, and the sediment composition data that support the subsequent chapters on bedform morphology and bed-material transport. The fieldwork campaign produced a collocated data set of the hydrodynamics, including tide and waves, and sediment dynamics on tidal flats in the Dee Estuary. From these data, a selection was made to focus on the processes associated with bedform morphology and migration rate. The sediment samples provided data on particle size distribution and cohesive content of the bed surface.

Initially, descriptions of the COHBED project and the Dee Estuary will be given as background. This will be followed by descriptions of the instruments used and samples collected during the fieldwork. The methods of data processing and sediment sample analysis are detailed. The results of the sediment analysis are presented in this chapter, as these form the background to the following chapters. Finally, the main mathematical methods used for the data analysis in this thesis, and how their data were assessed, are briefly described.

3.2 The COHBED project

The COHBED project (Realistic Sedimentary Bedform Prediction: Incorporating Physical and Biological Cohesion) was set up to improve understanding of how bedforms in mixed cohesive sand-mud sediments behave in the natural environment (Baas, 2013). As part of the COHBED project, a series of laboratory flume experiments (Baas *et al*., 2013d; Malarkey *et al*., 2015; Schindler *et al*., 2015; Parsons *et al*., 2016) and a fieldwork campaign in the Dee Estuary were carried out, collecting data on changing bed properties and hydrodynamics. Physical cohesion is mainly caused by clay minerals in mud and biological cohesion is mainly the result of extra-cellular polymeric substances (EPS), produced by organisms living in the sediment. The sediment dynamical processes of initiation of motion, bedform development and migration, sediment suspension, clay winnowing, flocculation and biological binding were studied with a view to improving regional scale sediment transport models, the understanding of benthic biological habitats and better environmental management of the coastal system (Baas, 2013).

The laboratory flume experiments were carried out with mixed sediment of sand and clay, mixed sand and an EPS proxy, called xanthan gum, and sand, clay and xanthan gum together (Baas *et al*. 2013d;

Malarkey *et al*., 2015; Schindler *et al*., 2015; Parsons *et al*., 2016). The results of these experiments demonstrated the effect of physical and biological cohesion on sedimentary bedforms in controlled conditions. For the fieldwork campaign, measurements were taken from the area near Hilbre Island on the eastern side of the Dee Estuary (UK) to extend the results of the laboratory work into the natural environment. This thesis is based on the results of the COHBED fieldwork.

3.3 The Dee Estuary

The Dee Estuary is a hypertidal, funnel-shaped estuary in the eastern Irish Sea between England and Wales, bifurcated into two main channels at the mouth (Moore *et al.*, 2009; Bolaños *et al*., 2013). The estuary is tidally dominated, with a mean spring tidal range at Hilbre Island of approximately 10 m (Moore *et al.*, 2009; Bolaños *et al*., 2013). Hilbre Island separates Hilbre Channel from intertidal flats on the Wirral coast (Figure 3-1). These tidal flats significantly distort the tide and increase the tidal asymmetry, causing flood dominated advection that has resulted in the accretion of fine-grained sediment (Moore et al., 2009; Amoudry *et al.*, 2014). Compared to high water spring tide, over 90% of the Dee Estuary is exposed at low water spring tide and this area is dominated by tidal flats (Natural England and the Countryside Commission for Wales, 2010). These tidal flats make up the fifth largest area of this type within the UK estuaries, covering an area of over 10,000 ha (Natural England and the Countryside Commission for Wales, 2010).

Waves affecting the Hilbre tidal flats are mainly generated locally within Liverpool Bay, with north-westerly waves having the largest influence on the sedimentary processes in the Dee Estuary (Brown and Wolf, 2009; Villaret et al., 2011). Swell from the North Atlantic is unable to reach the Dee Estuary. On average, the freshwater discharge at the head of the estuary is approximately 35 m^3 s^{-1} and the salinity varies from about 26 ppt near the head of the estuary, to about 33 ppt near the mouth (Bolaños *et al*., 2013; Halcrow, 2013).

Sediment in the Dee Estuary mainly comes from the Irish Sea and coastal areas in the west (Figure 3-2), with a small additional contribution from local cliff erosion (Turner, 1994; Halcrow, 2010b; Halcrow, 2013). Sediment in the lower intertidal areas near the mouth is mainly sandy, becoming muddier towards the head of the estuary (Halcrow, 2013; Rahman and Plater, 2014). In the long term, the particle size distribution of seabed sediment, on intertidal areas of the Dee Estuary, is controlled by the spring-neap cycle and change in the mean sea level, relative to the seabed elevation (Rahman and Plater, 2014).The distribution of suspended sediment in the Dee Estuary has been shown to be the result of the of the spatial variation in bed sediment composition and the spatial variation in bed

shear stress (Amoudry *et al.*, 2014). This implies that the distribution of fine bed sediment across the intertidal areas is mainly the result of a small influx from sea and riverine sources, reworked by tidal processes over a long period.

The sediment in the Dee Estuary is mainly populated by polychaete worms, amphipod crustaceans and molluscs, providing a source of food for fish and birds (Natural England and the Countryside Commission for Wales, 2010). European Union and UK legislation protect the Dee Estuary for features including intertidal sand and mud flats, saltmarshes and its international importance for the wintering of waterfowl (Natural England, 1998). The shore of the English side is mainly residential properties and recreational facilities, while the Welsh side is more industrialised, and the wider estuary has been subjected to several engineering modifications affecting the sediment dynamics (Bolaños and Souza, 2010). In the Liverpool Bay area, sediment dynamics are a key issue, as beaches, dunes and tidal flats provide natural defence against flooding and coastal erosion, and are also a major tourist attraction, providing income to the region (Halcrow, 2010a; Polton *et al.*, 2011). The Dee Estuary and Liverpool Bay are managed through the North-West England and North Wales Shoreline Management Plan (SMP2) and fall under the responsibility of North-West & North Wales Coastal Group, made up of local councils and national government bodies (Halcrow, 2010a).

Figure 3-1: Aerial photo of Hilbre Island, looking south-east towards West Kirby, on the Wirral Peninsula (UK), showing the morphology of the tidal flats (Mills Media Ltd.). See Figure 3-3 for location map.

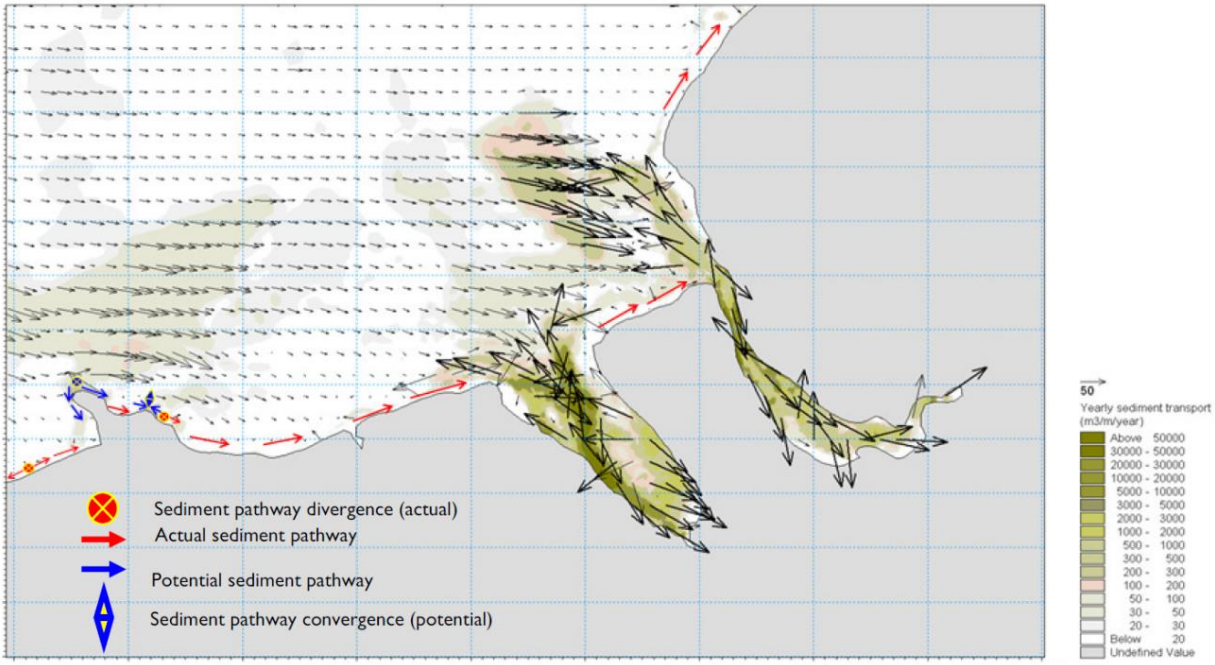

Figure 3-2: Modelled sand transport in Liverpool Bay (shore management region cell 11a). Black arrows: yearly subtidal transport. Red arrows: actual littoral transport pathways. Blue arrows: potential littoral transport pathway if sediment was present. (Halcrow, 2010b)

3.4 An overview of the COHBED fieldwork

For the fieldwork component of the COHBED project, a team of researchers from National Oceanography Centre, Liverpool (NOCL) and the universities of Bangor, Hull, Plymouth and St Andrews spent two weeks, from 21 May to 4 June 2013, surveying an area of tidal flats next to Hilbre Island in the Dee Estuary (Figure 3-3 and Figure 3-4). This period covered a spring-neap cycle. Data were collected on the intertidal flats and in the subtidal Hilbre channel. A wide range of techniques were used, from terrestrial laser scanning and cryopreservation of biological samples, to optical and acoustic instrumentation. The instrument deployment strategy for the project was to collect data from separate sites of contrasting bed properties, with a continuous progression of hydrodynamic forcing over a spring-neap cycle. NOCL deployed their instrument frame (SEDbed) at three sites and Plymouth University deployed their instrument frame at two sites, corresponding to NOCL Sites 1 and 3. The deployment sites were located on relatively flat areas, away from large-scale dunes, rock outcrops and islands (Figure 3-4). All the sites were in the same area and exposed to similar hydrodynamic forcing over the tidal cycles during the study period. The author had no influence on the location of the instrument deployment sites or when the change of site occurred.

This thesis focuses on the data collected as part of the deployment of NOCL's SEDbed (Sediment Experiments on Dynamics and bedforms) suite of acoustic and optical instruments on the tidal flats, to measure the near-bed hydrodynamics, bed morphology, and suspended material in the water. Bed samples were collected and analysed for cohesive clay and EPS content, to support the interpretation of the data provided by the SEDbed instrument suite.

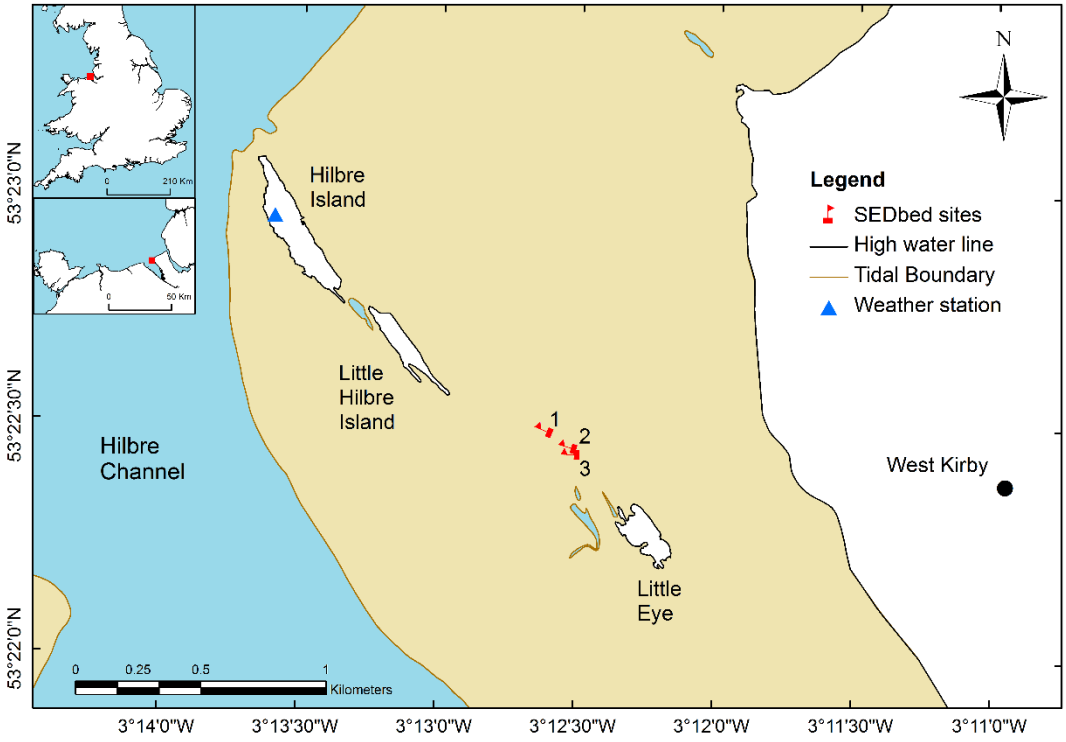

Figure 3-3: Map of the Dee Estuary, United Kingdom, showing the three deployment sites of the SEDbed frame (The direction of the flags on the red markers indicate the orientation of the SEDbed frame) on the intertidal flat (light brown) between West Kirby and the subtidal Hilbre Channel (light blue) (map contains Ordnance Survey data © Crown copyright and database 2013).

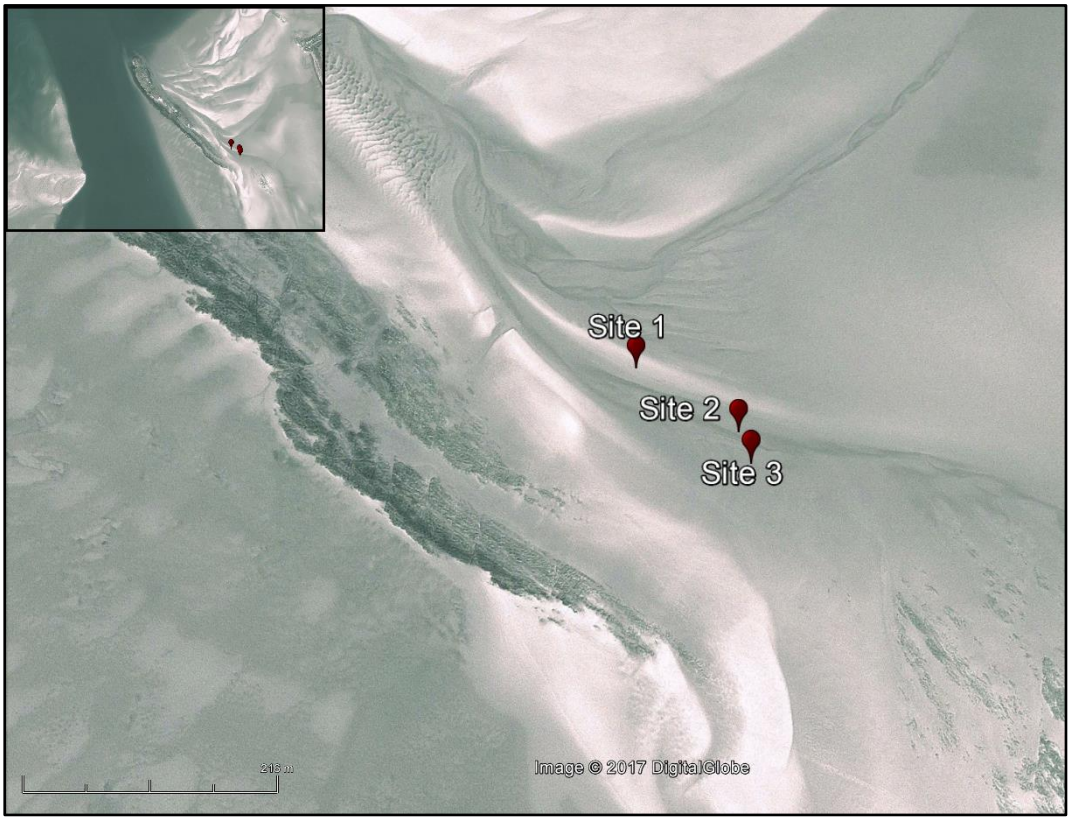

Figure 3-4: Digital Globe satellite image of Hilbre tidal flats at low tide (19/03/2009) with the NOCL SEDbed deployment sites shown. The inset shows the Hilbre Channel and wider morphology of the area. (© Digital Globe/Google Earth 2017).

3.4.1 Assumptions for SEDbed deployments

The following assumptions were made during the fieldwork planning and data processing (Table 3-1). These assumptions will be returned to in the discussion chapter for re-examination.

Table 3-1: Assumptions made during the fieldwork planning and data processing.

1) The bed sediment composition at the three deployment sites are contrasting, composed of clean sand, weakly cohesive sand and strongly cohesive sand.
2) Tidal current direction is mainly linear, back and forth with the flood and ebb through the SEDbed frame, rather than rotational.
3) There is no spatial variation in hydrodynamic and wave forcing between the three sites.
4) There is no spatial variation in the effect of biological cohesion between the sites.
5) The sampling area of the bed and volume under frame have uniform flow conditions, so that all measurements can be considered co-located.
6) The frame does not move or settle during the deployments.

3.4.2 SEDbed sites

The SEDbed frame was deployed at three sites consecutively, chosen to cover areas of clean sand, and weakly and strongly cohesive, biologically active, mixed sand-mud. The three deployment sites were within 140 m of each other, and differed in bed elevation by only 0.2 m (Figure 3-3). The SEDbed frame positions and orientations are given in Table 3-2. In this thesis, the sites are considered temporally, as part of a continuous deployment record. The tide, wind and wave forcing varied over the study period, covering the spring-neap cycle from neap to spring to neap tide.

3.4.2.1 Site 1, sand, 21-24 May

The first site was selected in an area of clean sand as the control to which the other sites could be compared (Figure 3-5). During the deployment at Site 1, high waves were present as neap tide progressed towards spring tide. The sediment was sandy in the top few centimetres, with consolidated mud beneath this. Scour was seen to develop at the corners of the frame and the mud layer could be seen in the scour holes and in the troughs of ripples. By the end of this deployment water pooled underneath the frame as the result of minor erosion.

Figure 3-5: Site 1, sandy site.

3.4.2.2 Site 2, mixed sediment in a creek, 24-29 May

Site 2 was in a creek with the bed always under at least a few centimetres of water (Figure 3-6). The deployment was dominated by currents as the tide progressed to and across the peak of spring tide. The sediment was composed of mixed sand and mud with worm casts. During high spring ebb, water drained into the creek from its edges, causing runnels to form in the rippled bed. This type of drainage

suggests that there was significant flow lateral to the course of the creek. Over time, scour was seen to develop around the frame.

Figure 3-6: Site 2, mixed sediment in a creek.

3.4.2.3 Site 3, mixed sediment on the edge of the creek, 29 May–4 June

Site 3 was muddier than Site 2, and dried out completely at low tide (Figure 3-7). During the deployment, the current strength reduced towards neap tide. Scour around the frame was least for Site 3, compared to the other two sites, and the depth of the scour holes at the corners of the frame reduced with time.

Figure 3-7: SEDbed at Site 3, mixed sediment on the edge of the creek.

3.5 The SEDbed frame and instrumentation

The focus of this thesis is the bedform morphology and migration, in relation to the changing current and wave conditions. A 3D Acoustic Ripple Profiler (3D-ARP) was used to provide data on the bed morphology. An Acoustic Doppler Velocimeter (ADV) provided data on currents and waves, and a Conductivity, Temperature and Depth system (CTD) provided data on water properties. Instruments on the SEDbed frame that were not used are briefly described below.

3.5.1 SEDbed

The SEDbed system was developed in order to collect collocated near-bed measurements of hydrodynamics, sediment dynamics and changing seabed morphology (Moate *et al.*, 2016). For ease of transport to and from the deployment area, the SEDbed frame has been designed to be modular, splitting into two main parts to fit on a trailer. Once a site is selected the frame can be assembled quickly, and the instruments and battery packs attached. Each instrument mounted on the SEDbed frame has a clear, uninterrupted, area of flow to collect data from, and the battery packs are offset to the side to minimise their effects on the flow (Figure 3-8) (Moate *et al.*, 2016). For the COHBED fieldwork, the SEDbed frame faced the main direction of flow at each site (Figure 3-4), perpendicular to the crest lines of bedforms when the flats were exposed. The corners of the frame were sunk into the seabed and weighed down with lead weights (Figure 3-4). The SEDbed frame deployments were carried out by the National Oceanography Centre's Ocean Technology and Engineering Group, with the aid of the author.

A Trimble 5800 Real Time Kinematic Differential Global Positioning System (RTK-DGPS) was used to record the positions of the SEDbed frame corners at each site with a specified accuracy in ideal conditions of ± 10 mm. The individual readings were used to calculate the orientation of the frame to geographic North and compared to the compass readings taken (corrected for magnetic declination). Averages of the four corners were used to plot the SEDbed positions (Figure 3-3; Table 3-2). Figure 3-9 and Figure 3-10 show the SEDbed frame, and the positions instruments on the frame, in plan and profile views, respectively. Instrument specifications and settings are shown in Table 3-3 and described in the following sections.

Table 3-2: SEDbed frame locations and orientations for each deployment site.

Site	Latitude decimal degrees	Longitude decimal degrees	Altitude metres	Direction Degrees, N
1	53.3751	-3.2117	1.76	293
2	53.3745	-3.2102	1.57	287
3	53.3742	-3.2101	1.71	273
average	53.3746	-3.2107	1.68	
GPS altitude is measure from global mean sea level (WGS-84)				

1 3D Acoustic Ripple Profiler (3D-ARP)
2 Bedform And Suspended Sediment Imager (BASSI)
3 Acoustic Doppler Velocity Profiler (ADVP)
4 Acoustic Backscatter Profiler (ABS)
5 Acoustic Doppler Velocimeter (ADV)
6 Optical Backscatter Sensor (OBS)
7 Salinity, temperature & depth (CTD)
8 Multi-tier sediment trap
9 Laser in situ Scattering and Transmissometry (LISST)

Figure 3-8: Instrument frame SEDbed at Site 2. The numbering corresponds to Table 3-3, Figure 3-9, and Figure 3-10.

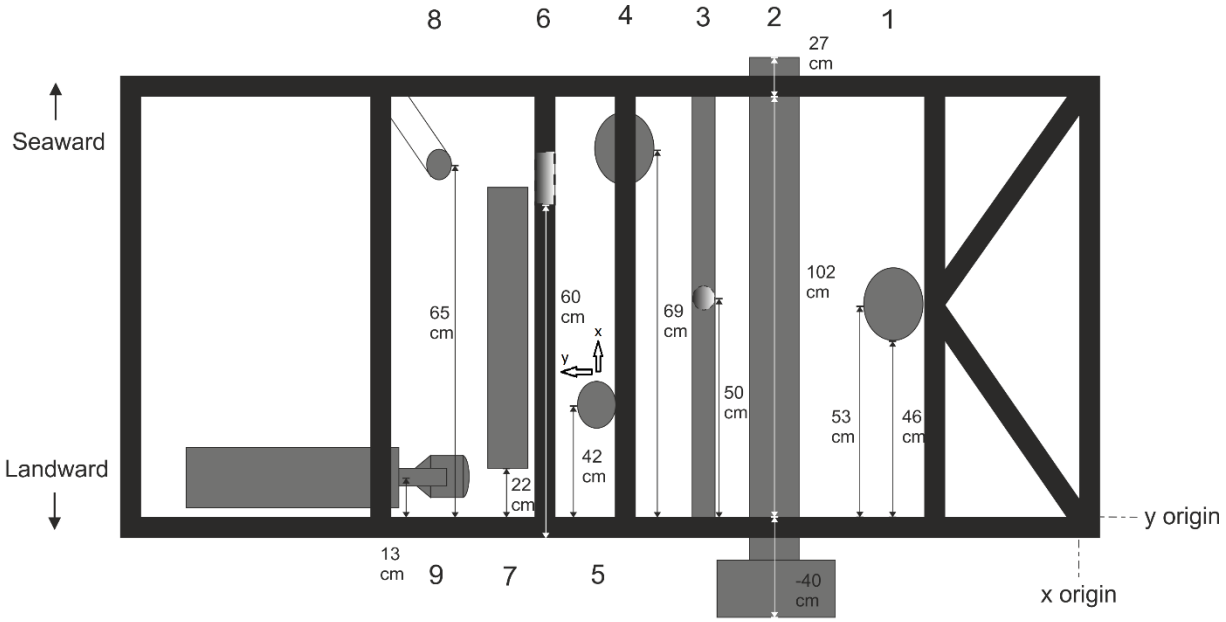

Figure 3-9: Plan view of the SEDbed frame, showing instrument positions. Measurements are from the bottom right corner. The numbering corresponds to Table 3-3, Figure 3-8, and Figure 3-10.

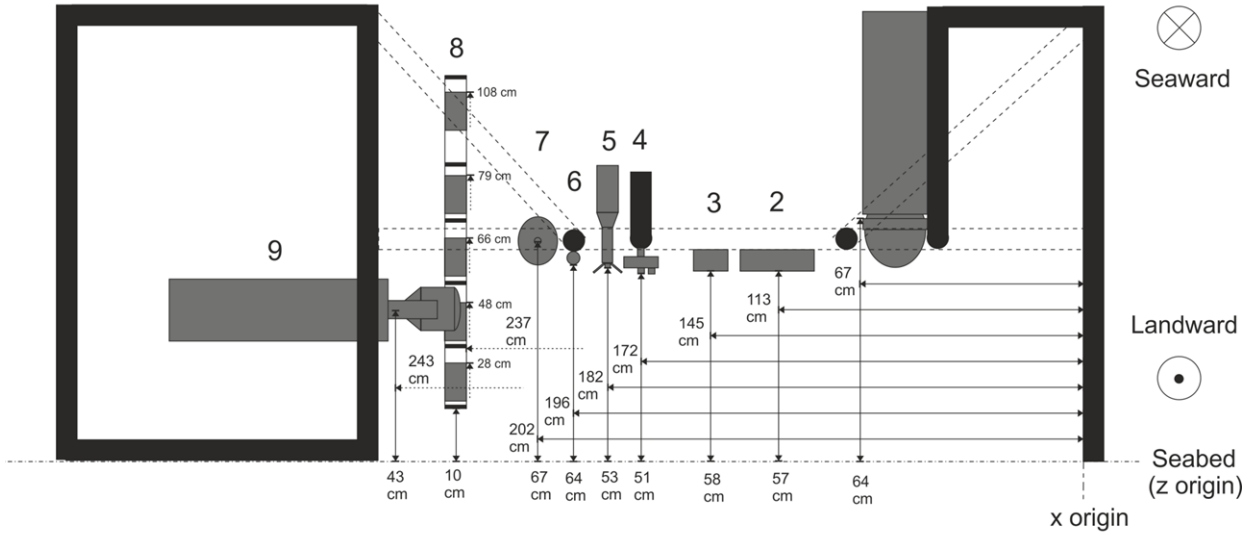

Figure 3-10: Profile view of the SEDbed frame, showing instrument positions. Initial heights above the sediment bed are shown, with horizontal distance relative to the right edge of the frame. The instrument height measurements were made at 02/05/2013. The numbering corresponds to Table 3-3, Figure 3-8, and Figure 3-9.

Table 3-3: Specifications and settings of instruments deployed in the COHBED field study.

No. [a]	Instrument	Specifications and settings	
1	**Marine Electronics 3D Sand Ripple Profiling Logging Sonar (3D-Acoustic Ripple Profiler)**	**Swath angle:** **Vertical resolution:** **Angle resolution:** **Range:** **Sample interval:**	**±75° to vertical** **0.003 m** **0.9°** **2.5 m** **30 minutes**
2	Marine Electronics Suspended Sediment Imaging Sonar(BASSI), with 0-20 dbar pressure sensor	Profile rate : Recording rate: Bin size: Range: Burst Length: Sample interval:	500 Hz 12.5 Hz 5 mm 1 m range 10 minutes 30 minutes
3	NOCL Acoustic Doppler Velocity Profiler (ADVP)	Recording rate : Bin size: Range:	8 Hz 10 mm 0.6 m
4	Aquatec Aquascat 1000 Acoustic Backscatter System (ABS)	Transmit frequencies: Pulse rate: Recording rate : Bin size: Range: Burst Length: Sample interval:	1, 1.5, 2.5 & 3.0 MHz 64 Hz 4 Hz 5 mm 1 m 55 minutes 60 minutes
5	**SonTek Hydra-ADV**	**Velocity resolution:** **Velocity accuracy:** **Range to bed resolution:** **Pressure resolution:** **Recording rate:** **Burst Length:** **Sample interval:**	**0.001 m s^{-1}** **± 1%** **0.0001 m** **0.008 bar** **8 Hz** **55 minutes** **60 minutes**
6	Seapoint turbidity or optical backscatter sensor	Range: Sample interval:	0-500 FTU 1 minute
7	**SeaBird SBE16+ CTD, v. 1.8c**	**Pressure resolution:** **Pressure accuracy:** **Temperature precision:** **Temperature accuracy:** **Conductivity precision:** **Conductivity accuracy:** **Sample interval:**	**0.005 dbar** **0.08 dbar** **0.0001 °C** **0.005 °C** **0.00005 S m^{-1}** **0.0005 S m^{-1}** **1 minute**
8	Multi-tiered Sediment Trap	Traps at five heights	
9	Sequoia Scientific LISST 100X (50% Path Reduction Module (PRM) installed)	Sample interval:	10 seconds

[a] Numbering corresponds to Figure 3-8, Figure 3-9, and Figure 3-10. Instruments in bold were used for this thesis.

3.5.2 3D Acoustic Ripple Profiler (3D-ARP)

The 3D Ripple Profiler is a dual axis pencil-beam scanning sonar, with an internally rotated transducer operating at 1.1 MHz, which scans a circular area of the seabed (Marine Electronics, 2009). From the acoustic pulses backscattered from the bed, the signal level is used to identify the bed location and thereby measure the local bed morphology (Thorne and Hanes, 2002). By collecting regular scans of the seabed, the evolution in bed morphology can be seen in relation to the changing hydrodynamic conditions (Thorne and Hanes, 2002). The 3D-ARP also has a built-in conductivity cell, for salinity measurement, and a pressure sensor with a 0-150 dbar range.

For the fieldwork in the Dee Estuary, one bed scan was made every 30 minutes, with each scan taking about 12-15 minutes to complete. From 21 May 2013, 18:00 to 3 June 2013, 10:30 594 scans were recorded; 15 scans failed to record during this period.

3.5.3 Acoustic Doppler Velocimeter (ADV)

A SonTek Ocean-Hydra ADV was used to measure water velocity in three-axes, horizontal and vertical (u, v and w), at a single point in the water column (SonTek, 2001). It also measured the distance to the bed, water temperature, hydrostatic pressure and instrument orientation (SonTek, 2001). The ADV samples a cylindrical volume, 12 mm in diameter and 18 mm in height, 0.18 m from the probe (SonTek, 2001). The velocities were measured approximately 0.35 m above the bed during the Dee Estuary deployment (Figure 3-10). This height varied with changing bed morphology. The ADV transmits 150-250 pings per second, depending on the velocity range setting, that are averaged in order to reduce noise in the data (SonTek, 2001). The sampling rate was set to 8 Hz for a 55-minute burst (recording period) each hour. The velocity range was set to the highest setting of ± 5 m s^{-1} in the horizontal and ± 1.2 m s^{-1} in the vertical. The ADV has a velocity resolution of 0.001 m s^{-1} and the distance to the bed is recorded for each burst at a resolution of 0.1 mm (SonTek, 2001). The temperature sensor on the ADV has a resolution of 0.01 °C and an accuracy of ±0.1 °C. Temperature readings are used to calculate the speed of sound for each burst. The resolution of the pressure sensor is 0.0008 dbar. The heading and tilt sensor has a resolution of 0.1°, with an accuracy of ±2° for heading and ±1° for tilt. A single file containing 334 bursts was recorded from 21 May 2013, 18:00 to 4 June 2013, 16:00.

The x-axis of the ADV was aligned parallel to the main tidal flow at the field sites, as recommended in the instrument manual (SonTek, 2001). For comparison with the 3D-ARP data, the data were rotated so that the axes of the ADV coordinate system matched that of the SEDbed frame and 3D-ARP.

The ADV's orientation data of pitch and roll variation measured a tilt of about one degree. This confirms that the SEDbed frame did not move significantly during the measurement period (assumption 6, section 3.4.1).

3.5.4 Conductivity, Temperature and Depth system (CTD)

The Seabird Electronics 16+ CTD is a standard oceanographic instrument that measures conductivity, temperature and hydrostatic pressure. Time-series of salinity, depth, density and the speed of sound in water may be calculated from these data, which can then be used to check and correct the data from acoustic instruments that often use set values of temperature and salinity. This is important in estuarine waters as a change in temperature of 5° C or a change in salinity of 12 PSU results in a 1% change in the speed of sound (SonTek, 2001).

The CTD pressure sensor has a 400 dbar range with an accuracy of 0.08 dbar and resolution of about 0.005 dbar (Sea-Bird Electronics, 2007). The temperature range is -5 to 35 °C, with an accuracy of 0.005 °C and a precision of 0.0001 °C. The conductivity range is 0-9 S/m, with an accuracy of 0.0005 S/m and a precision of 0.00005 S/m (Sea-Bird Electronics, 2007). The conductivity and temperature sensors are situated 6.5 cm above the pressure sensor. Samples were recorded every minute, with four measurements averaged for each sample, from 21 May 2013, 18:00 to 5 June 2013, 00:00.

3.5.5 Other instruments

The instruments summarised in this section were not used in the main part of this thesis, but are included as the suspended sediment is discussed as part of a conceptual model of the sediment system in the discussion chapter (6.4.3).

3.5.5.1 Acoustic Backscatter Sensor or System (ABS)

The Acoustic Backscatter Sensor (ABS) transmits a short pulse down through the water column that is backscattered by any suspended material and the return echo is used to estimate the concentration profile (Thorne *et al.*, 1993). The instrument used here is an Aquatec Aquascat that transmits at four frequencies, 1 MHz, 1.5 MHz, 2.5 MHz and 3.0 MHz, with size inversion feasible for particles 20 µm to 500 µm, to give a profile of suspended sediment in the range 0.1 to 20 g/l (kg m^{-3}) (Aquatec, 2013). The distance to the bed is recorded, so a bed-level time series is collected.

The vertical cell resolution is 5 mm, for a speed of sound in water of 1500 m/s. The pulse rate is 64 Hz with profiles recorded at 4 Hz. The burst length was 55 minutes and the Sample interval to 60 minutes.

335 files were recorded from 21 May 2013, 18:00 to 4 June 2013, 17:30. As the transducers are offset on the frame, and each acoustic frequency will have different distance for the peak reflection, the heights measured will be different.

3.5.5.2 Laser in situ scattering and transmissometry (LISST)

The Sequoia Scientific LISST-100X uses laser diffraction to obtain the particle size distribution (PSD) of particles suspended in water at a single point, as well as measuring the optical transmission, volume concentration of particles, pressure and temperature (Sequoia, 2009). The PSD is measured in 32 logarithmic size bins, in the range 2.5-500 µm (Type C), in units of µl l^{-1} and the inversion was carried out separately using both the spherical and random shape particle models (Sequoia, 2009). For comparison with other laser diffraction instruments, such as a laboratory based analyser, the spherical model data should be used; otherwise the random shape model is closer to real marine particles (Sequoia, 2009).

In addition to particle size distribution, optical transmission, volume concentration, volume scattering function, pressure and temperature were also measured by the LISST. The range of the pressure sensor is 0 to 300 m (of water), with a resolution of 0.08 m. The temperature sensor measures in the range -10 to 45 °C, with a resolution of 0.01 °C. To increase the maximum sediment concentration that can be measured by the LISST, a 50% Path Reduction Module (PRM) was fitted (Sequoia, 2012). The LISST was mounted about 0.43 m above the bed, with the opening to the optical sensing area orientated into the main direction of tidal flow. The sampling interval was set to 1 Hz averaging every 10 seconds. A single file was recorded from 21 May 2013, 18:00 to 4 June 2013, 16:30.

3.6 Manual samples and measurements

During the field deployments, manual samples and measurements were taken daily by the author as time allowed. These measurements were used to inform the data processing and analysis, and gain a wider understanding of the processes occurring. All tasks were recorded in a logbook (reproduced in the appendices, section 8.3).

3.6.1 Bed sediment samples

Surface sediment samples were collected regularly during the field deployment period. Sediment was taken from the top 1-2 cm below the crests and troughs of the bedforms within one meter of the

SEDbed frame, encompassing the active layer of the mobile bedforms, and each sample was then homogenized prior to subsequent analysis. Fourteen bed samples were collected (details can be found in appendix 0) and analysed for particle size distribution (see Section 3.9.2). Additional bed surface samples were collected near the three sites for the analysis of biological cohesion by the University of St. Andrews (see Section 3.9.4).

3.6.2 Bedform dimension and instrument height measurements

Using a tape measure or ruler, the length and height of selected bedforms were measured seaward of the frame, below the instruments, and landward of the frame (appendix 8.7). The heights of the instruments above the sediment bed were recorded regularly (appendix 8.8). The bottom of the multi-tier trap was close to the bed, and scour below the trap was monitored. The depth of scouring below the SEDbed frame was also recorded (appendix 8.9).

3.6.3 Photographs

Each day, photographs were taken of bedforms seaward and landward of the frame, as well as underneath it, using a tape measure or ruler for scale. These photographs also recorded the effects of macro-biology on the sediment surface. The frame and the instruments were also photographed regularly to trace back the source of any erroneous data due to, for example, damage or malfunction.

3.7 Auxiliary data

3.7.1 Hilbre Island weather station

As part of the Liverpool Bay Coastal Observatory, NOCL installed an automatic weather station on Hilbre Island (Figure 3-3), which recorded air pressure, wind speed, wind gust speed, wind direction, humidity, air temperature, Photosynthetically Active Radiation (PAR), and rainfall. The station was operational during the COHBED fieldwork. Although the weather station has now been decommissioned, the historic data are still available for use through the Coastal Observatory web site (http://cobs.noc.ac.uk/cobs/met/hilbre/) or the British Oceanographic Data Centre (https://www.bodc.ac.uk/). These data are useful for understanding the conditions affecting the sedimentary processes at the study sites and for correcting the water pressure data of the SEDbed instruments.

The Hilbre Island weather station was mounted on an old radar tower at approximately 10 m above ground level, with the tower base standing approximately 16.49 m above the UK Hydrographic Office ordinance datum at Newlyn. The atmospheric pressure data were corrected to sea level.

The wind records shown in Figure 3-11a,b show that northerly winds dominated the deployment periods. However, other directions were also present. The wind strength ranged from light breezes to gale force (Beaufort scale 4-8; 5.8 - 17.6 m s^{-1}; Figure 3-11b). Rain was rare during the deployments, with periods of heavy rainfall only on 23 and 29 May (Figure 3-11c). The air pressure anomaly data were used to correct the water pressure values of the instruments on the SEDbed frame before the depth was calculated (Figure 3-11d).

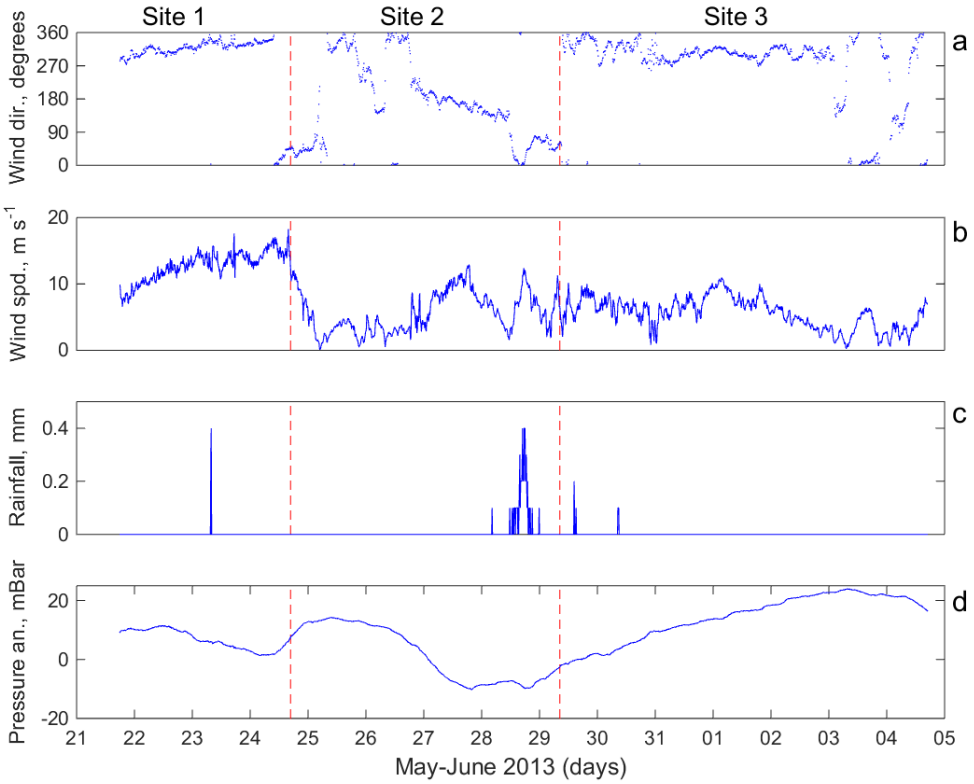

Figure 3-11: Hilbre Island weather station, wind direction & speed, rainfall in mm per 10 minutes and air pressure anomaly. The vertical red dashed lines mark the times when the SEDbed frame was moved between sites.

3.7.2 Tidal predictions

The high and low water tidal height predictions for Hilbre Island over the fieldwork period are shown in Figure 3-12. The tidal range increased to 26-27 May when it peaked at spring tide, then decreased until 4 June. From the peak of spring tide towards neap tide, the diurnal inequality becomes more pronounced, with alternating peaks of high water.

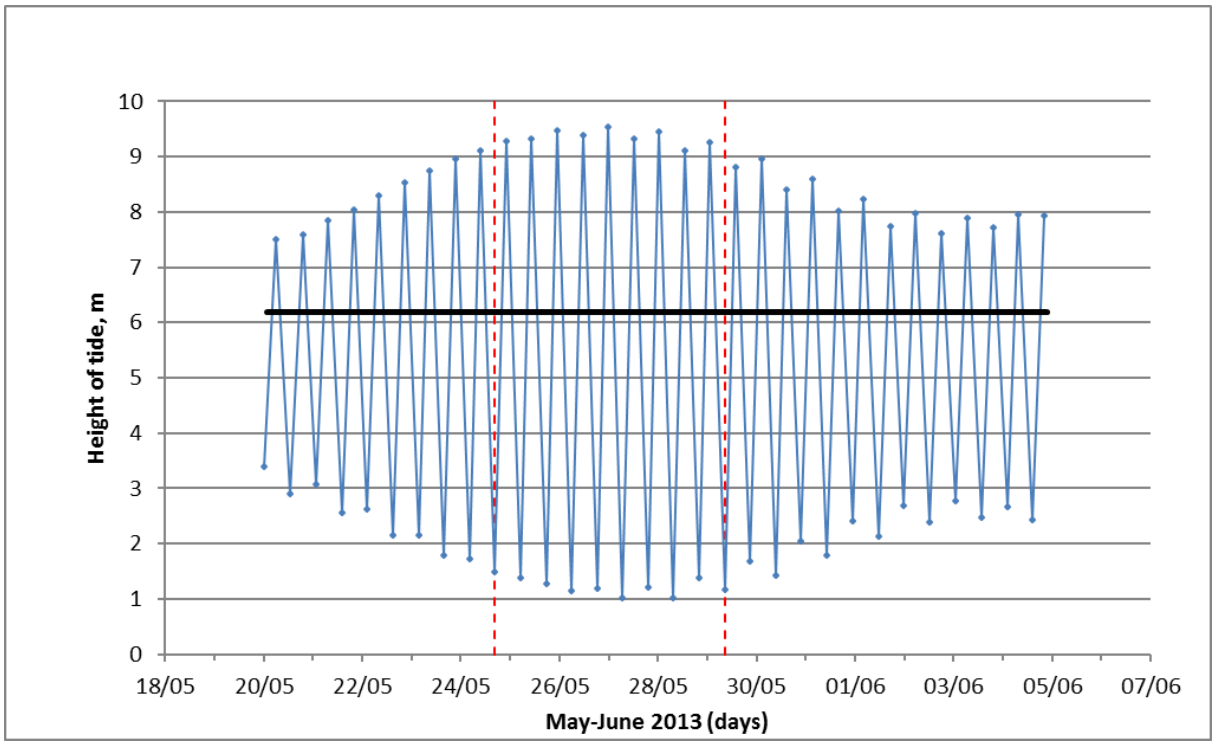

Figure 3-12: Tidal height predictions of low and high water, above chart datum, for Hilbre Island from 20 May to 5 June 2013 (computed by POLTIPS software, National Oceanography Centre. Chart datum is 4.93 m below Ordnance Datum, Newlyn). Black line: level of deployment sites on tidal flats. Red dashed lines: times when the SEDbed frame was moved between sites.

3.8 Processing the instrument data

3.8.1 Acoustic Doppler Velocimeter (ADV)

As well as measuring 3-axis velocity, the SonTek Hydra ADV also measures the distance to the seabed and water pressure. Current, wave and water level parameters were determined from these raw data. The steps involved in processing the ADV data are described in the following sections. An overview of this procedure is given in Table 3-4 below.

Table 3-4: Summary of procedure for processing the ADV data for tide and waves.

1. Remove data below 70% correlation limit
2. Remove tide and wave trend from record
3. De-spike record, with interpolation, and check (subtract de-spiked from raw)
4. Replace tide and wave trend
5. Filter for wave and current frequency ranges (interpolate current data over gaps)
6. Calculate wave parameters (interpolate wave data over gaps)
7. Calculate bed shear stress and Shields stress parameters

3.8.1.1 De-spiking of the ADV data

Initially, the ADV beam correlation values were used to check the data quality, with values below 70% removed (SonTek, 2001). The pulse coherent method used by the ADV improves the measurement resolution, however, if the water velocity is outside the expected range setting, aliasing of the Doppler signal causes spikes, as the phase shift between pulses lies out of the -180° to +180° range of the current acoustic wave (SonTek, 2001; Goring & Nikora, 2002). Spikes can also be caused by reflections from a boundary (Goring & Nikora, 2002; SonTek, 2001), although for this deployment, the ADV was far enough from the seabed to keep this effect to a minimum. Removal of spikes has to be done carefully, as flow fluctuations due to turbulent burst and sweep events may be removed. The replacement of spikes should be done sparingly, because it introduces artificial values into the data. Single point spikes can be easily detected using a threshold compared to the local values, but multi-point spikes are harder to deal with.

To de-spike the velocity data, Mori *et al.*'s (2007) MATLAB function for the 3D phase-space method was used (Goring and Nikora, 2002; Wahl, 2003; Mori *et al.*, 2007; Thompson *et al.*, 2013). The mean and low frequency periodicities were removed before de-spiking, to be added back in after de-spiking. Once identified, spikes were replaced with interpolated values (Figure 3-13). The Mori *et al.* (2007)

MATLAB function was applied to each burst of the ADV data separately to avoid problems with the gaps between bursts. It was assumed that the replaced spikes represented instrument errors, with the remaining peaks due to turbulence.

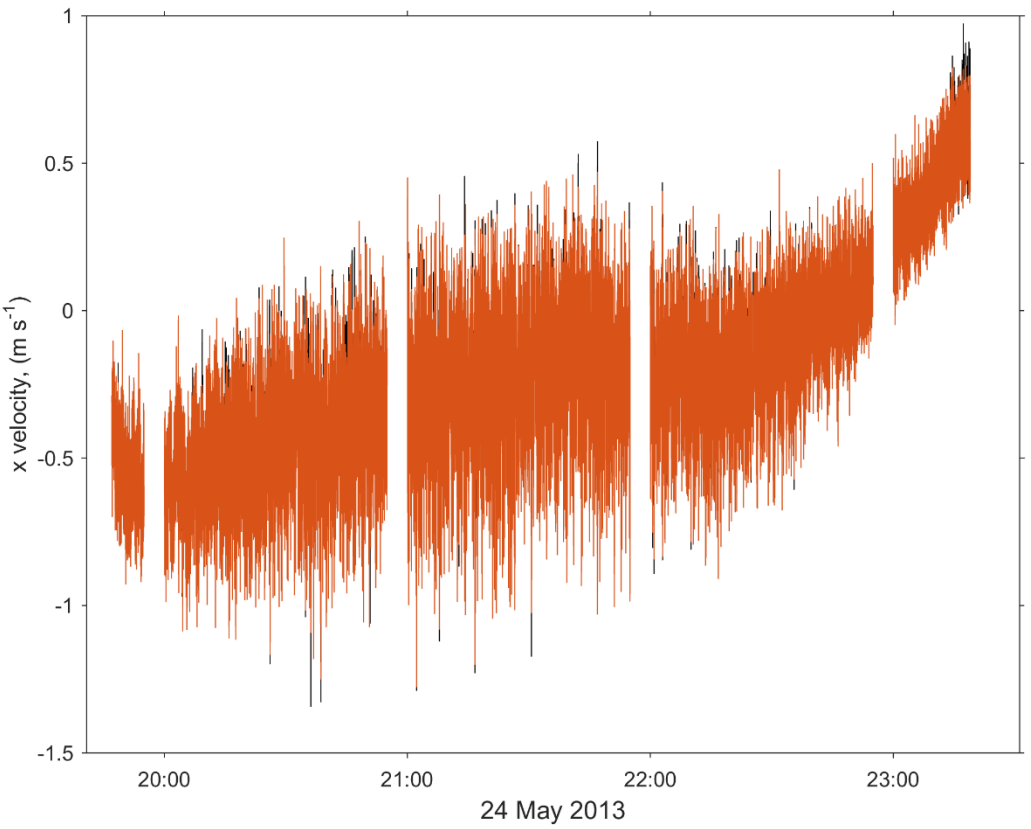

Figure 3-13: An example of ADV velocity data for the fifth tidal period of the record, for raw (black) and de-spiked data (orange). Tidal period five shows tidal current in between neaps and springs, with wind driven flow and strong wave forcing.

3.8.1.2 Water depth, current and wave parameters

The pressure data from the ADV were corrected using air pressure data from the Hilbre weather station, and then converted to water depths and adjusted for the ADV acoustic range to the seabed, so that the calculated depth values were for the depth of water to the seabed. The ADV was set to use a salinity of 34.5 PSU for the speed of sound correction. However, the actual salinity varied, with an average of 31 PSU from the CTD data. A correction for the variation in salinity was not applied, as this represented an error of less than 1% in the speed of sound calculation (Sontek, 2001). The speed of sound correction for the velocity data was checked using the data in the ADV header file and showed a mean difference of about 1% in the horizontal velocity and 0.5% in the vertical velocity.

The Dee Estuary is dominated by short period waves, which are generated by local winds (Brown and Wolf, 2009; Villaret *et al*., 2011). Short waves generally have periods in the range of 2 to 25 seconds (USACE, 2002a). Tidal currents and wind driven flow were extracted from the ADV data by applying a 5-minute running mean, at an interval of one minute, to remove the high-frequency signals caused by waves and turbulence (Figure 3-14a). Vector trigonometry was used to find the angle of the current and waves to the x-axis (Emery and Thomson, 1997). The tidal velocity was then subtracted from the full velocity record to obtain the wave signal (Figure 3-14b).

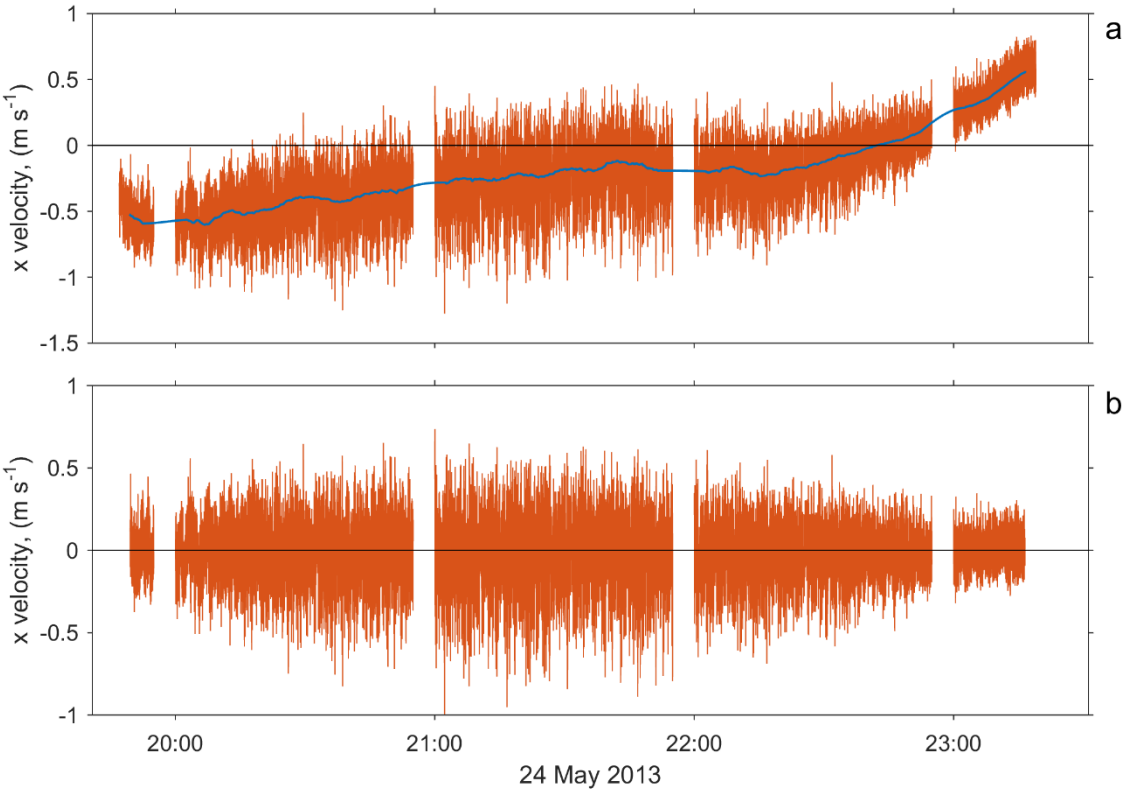

Figure 3-14: An example of ADV velocity data for the fifth tidal period of the record. a) De-spiked data (orange) and the five-minute running mean data for the current (blue). b) Wave velocity. Tidal period five shows tidal current in between neaps and springs, with wind driven flow and strong wave forcing.

The depth-averaged velocity was calculated using the two-layer logarithmic model of Malarkey and Davies (2012), in which roughness length accounted for both skin friction and bedform drag. Roughness length, z_0, was determined from the bedform dimensions obtained with the 3D-ARP, the form drag, and the mean D_{50} (median grain diameter) of the bed sediment samples for each site: $z_0 = \eta^2/\lambda + D_{50}/12$, where η and λ are the bedform height and length, respectively (Soulsby, 1997)).

Sea-surface wave parameters were obtained from the pressure and velocity spectra using the PUV method (Gordon and Lohrmann, 2001). This corrects for the instrument height above the bed using linear wave theory, and accounts for the current-induced Doppler shift. As the field dataset lacked direct measurements of wavelength, the wave number was determined by applying the Newton-Raphson iteration method to the dispersion equation (Fenton and McKee, 1990; Soulsby, 1997, 2006; Wiberg and Sherwood, 2008). The PUV method accounts for the effect of currents, including the angle between the wave and current direction, φ (Fenton and McKee 1990; Soulsby, 1997). Pressure, horizontal velocity, and depth-averaged velocity were used to calculate the wave number, the wave attenuation factor, and the wave pressure spectrum, which were then used to calculate the surface elevation spectrum, $C_{\eta p}$ (Fenton and McKee, 1990; Wolf, 1997; Gordon and Lohrmann, 2001; Bolaños *et al.*, 2012):

$$C_{\eta p} = \left[\frac{\cosh(kh)}{\cosh(kz_h)}\right]^2 \frac{C_p}{\rho^2 g^2}$$

3-1

where C_p is the wave pressure spectrum, ρ is the water density, g is acceleration due to gravity, k is the wave number, h is the water depth, and z_h is the height of the instrument above the bed. Wave height and wave period were determined from the statistical moments of the surface elevation spectrum, $C_{\eta p}$:

$$m_n = \int f^n C_{\eta p}\, df$$

3-2

where f is the frequency, and m_n is the nth moment, *e.g.* $H_s = 4\sqrt{m_0}$ for significant wave height (Wolf, 1997; Gordon and Lohrmann, 2001; Bolaños *et al.*, 2012). The average wave direction, ϕ_{wm}, was estimated from the pressure-velocity cross-spectra for u and v:

$$\boldsymbol{\phi_{wm} = tan^{-1}\left(\frac{C_{pu}}{C_{pv}}\right)}$$

3-3

Prior knowledge of the wave parameters is required to calculate the depth-averaged current velocity in combined flow. Therefore, an iterative procedure was used to determine the depth-averaged current velocity, $\langle u \rangle$, and the wave parameters, H_s, T_p and u_w (Figure 3-15). An initial estimate of the depth-averaged current velocity was made, assuming a logarithmic profile and using the ADV mean current velocity, before iterating between the two-stage logarithmic model (Malarkey and Davies,

2012) and the PUV method (Gordon and Lohrmann, 2001) until the difference in depth-averaged velocity was less than 0.0001 m s^{-1} between iterations.

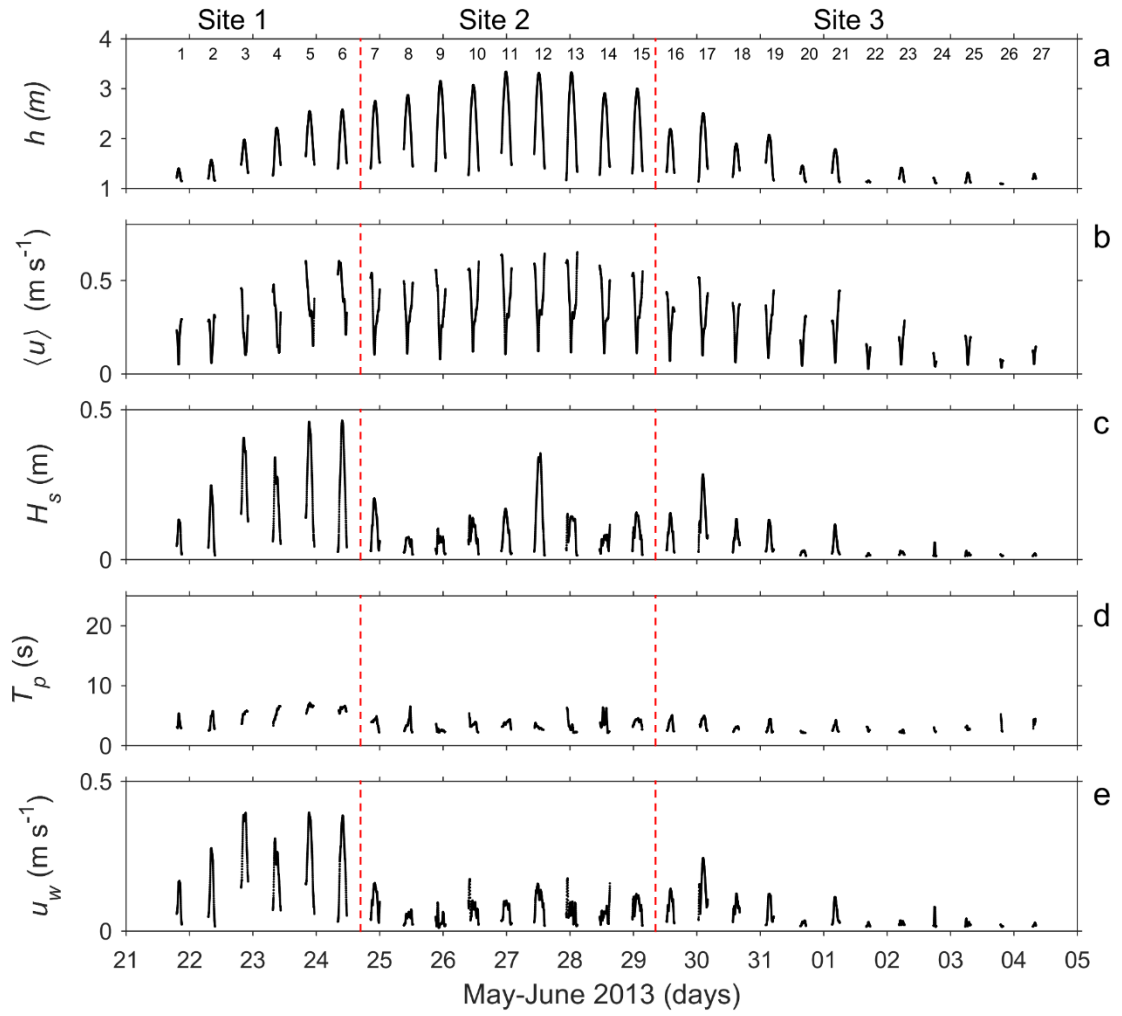

Figure 3-15: Times series of (a) water depth, *h*; (b) depth-averaged flow velocity, ⟨*u*⟩; (c) significant wave height, H_s; (d) peak wave period, T_p; and (e) wave bottom orbital amplitude velocity, u_w. The vertical red dashed lines mark the times when the instruments were moved between sites. The data shown are for the times when the tidal flats were inundated with water above the height of the sensors, processed for a 15-minute window. The wave period data have been filtered to show only the wind-generated waves of periods less than 25 seconds (USACE, 2002a). The data have been smoothed to show the overall trends clearly. The numbers in (a) denote the tidal periods for reference.

As the ADV measures for 55 minutes and then five minutes are used for burst setup, statistical calculations and sleep to increase battery endurance, a 5-minute gap in the data occurs every hour. To fill the 5-minute gaps in the ADV data, the 5-minute smoothed ADV data were interpolated using a

piecewise cubic hermite interpolating polynomial (PCHIP) function for the current velocities. The window for calculating the wave parameters was defined by the time range instead of the number of samples, which effectively ignored the time gap. A cubic spline interpolation was used to smooth the gaps in the water level data, as this produced the best results for the sinusoidal data from the interpolation methods available. The current and wave parameters were processed using a window size appropriate to the analysis undertaken, 15 minutes for the bedform dimensions analysis and 30 minutes for the bedform migration component of the project.

The time-series of the peak wave period was de-spiked separately for each tidal inundation period, removing points greater than four standard deviations from a mode filter value and replacing these with the mean. The significant wave height, H_s, the peak wave period, T_p, and water depth, h, were then used to calculate the bottom orbital velocity amplitude velocity, u_w, for subsequent bed shear stress calculations (Equation 2-9, Soulsby, 1997, 2006). As the bottom orbital amplitude velocity is determined by the wave height divided by the wave period (Equation 2-9), therefore for a given wave height, when the period is large, u_w is small and therefore has less effect on the bed shear stress. The tide and wave directions were corrected for the ADV and frame orientation at each site, to obtain values that were relative to true North.

The maximum bed shear stress in combined wave-current flow is not a straightforward sum of the unidirectional and oscillatory components, as the interactions between the waves and the current in the near-bed wave boundary layer are non-linear. Various models that account for these non-linear interactions have been introduced to calculate bed shear stresses in combined wave and current flows (e.g., Grant and Madsen, 1979; Soulsby *et al*., 1993; Madsen, 1994; Soulsby and Clarke, 2005; Malarkey and Davies, 2012). These models are typically based on the assumption of a simple two-layer eddy viscosity profile (Grant and Madsen, 1979). The models differ in the degree of non-linearity within the wave boundary layer. The theoretically derived Grant and Madsen (1979) and Madsen (1994) iterative models are the strongest non-linear models, because the eddy viscosity is scaled on the peak stress in the wave cycle. The Soulsby and Clarke (2005) non-iterative model is the weakest non-linear model, because the eddy viscosity is scaled on an effective velocity. The Soulsby and Clarke (2005) model output is closest to available experimental data. The non-iterative Malarkey and Davies (2012) model (a modification of Soulsby and Clarke, 2005), which represents a compromise between the two extremes of the purely theoretical strong non-linearity and the weak non-linearity associated with experimental data, agrees well with numerical modelling results (Soulsby *et al*., 1997) and was chosen for this project.

The combined maximum wave and current bed shear stress, τ'_{max}, was calculated with the Malarkey and Davies' (2012) model, using their stronger non-linear interaction option. In this case, the roughness length, z_0, for the bed shear stress calculation was based on skin friction only, $D_{50}/12$ (Soulsby, 1997). The model produces combined maximum bed shear stress, τ'_{max}; a combined-mean stress; and a combined-wave stress. Values are also calculated for the corresponding linear stresses: current-only, τ'_c; wave-only, τ'_w; and the maximum linear stress, τ'_{maxl}, which would result if the process was a linear vector addition of the current and wave stresses without any wave-current interaction (Figure 3-16. See appendix 8.10 for more details). The skin friction Shields parameters for current, waves and combined flow, θ'_c, θ'_w & θ'_{max}, were calculated from τ'_c, τ'_w & τ'_{max}, using (Shields, 1936; Soulsby, 1997; Paphitis, 2001):

$$\theta = \frac{\tau_0}{(\rho_s - \rho) g D_{50}}$$

3-4

where ρ_s is the sediment density.

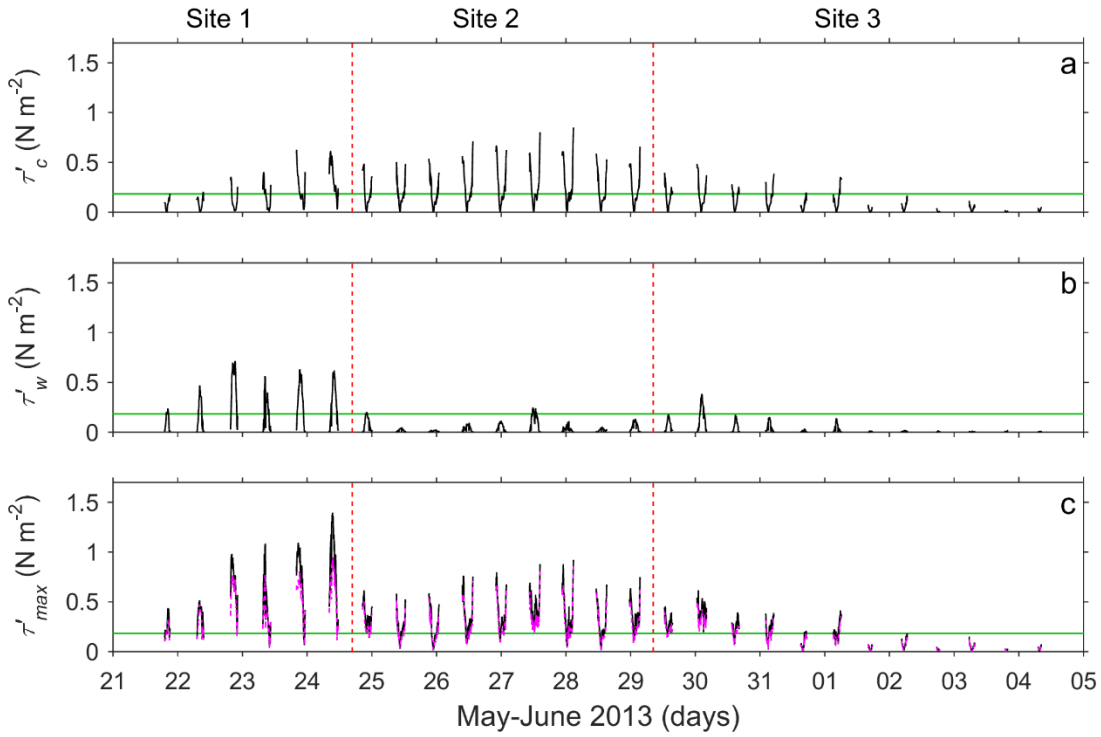

Figure 3-16: Times series of (a) current-only bed shear stress, τ'_c; (b) wave-only bed shear stress, τ'_w; (c) combined maximum bed shear stress, τ'_{max}, and linear maximum bed shear stress, τ'_{maxl} (magenta dashed line). The vertical red dashed lines mark the times when the instruments were moved between sites. The horizontal green lines denote the critical stress limit of sediment motion from Soulsby and Whitehouse's equation (Soulsby, 1997), for D_{50} = 227 µm, θ = 0.18 N m^{-2}. The data shown are for the times when the tidal flats were inundated with water above the height of the sensors.

3.8.2 3D Acoustic Ripple Profiler

To build an elevation map of the seabed, the 3D-ARP scans an acoustic beam over the bed in an arc that is rotated to measure a circular area of the bed. The backscattered signal is used to determine the range to the bed. The average speed of sound in water of 1480 m s^{-1}, derived from the CTD record, was used to calculate the 3D-ARP ranges. The vertical resolution of the 3D-ARP is 3 mm directly below the transducer. The radial data are resampled and smoothed to a Cartesian grid of 5 mm horizontal resolution. Bell and Thorne (1997b) found, based on laboratory tests of a similar 2D-ARP, that bedforms can be accurately measured over a length of up to 50 cm from the point directly below the transducer. For the present project, the 3D-ARP scans were sub-sampled to remove problems with frame interference and shadowing at the limits of the scan.

3.8.2.1 3D-ARP head offset artefact

Data quality assessment found a split in the data, with different ranges for the left and right hemispheres of the 3D-ARP scans. The bedforms on the scans crossed both hemispheres. Initially, this was thought to result from a problem with the processing algorithm of the raw data, an instrument fault, or fast moving bedforms, as moving bedforms tend to cause a dislocation between the two hemispheres due to the time taken to complete a full scan. However, there was a visible step in the images between the two hemispheres that suggested an instrument fault (Bell, 2013).

Marine Electronics Ltd., the instrument manufacturers, confirmed that the problem was an offset in the drive mechanism (Collier, 2014). Later, it was found that one of the internal (firmware) settings had an incorrect value, which had not been updated when the instrument was last calibrated (Cooke, 2015). An algorithm was included in the pre-processing routine, which solved the problem by adding a small but progressively increasing azimuth head offset to each successive swath, $1/200^{th}$ of the difference in angle between the first and last swath multiplied by the swath number (Bell, 2013; Collier, 2014).

Because the head offset angle is determined from the first and last swaths, any bed movement in the time period between these swaths causes an error. Assuming that the scatter was random, a simple mean of the offset values was taken for the whole data set, 3.36°, and used as the correction factor for reprocessing the 3D-ARP data.

3.8.2.2 Detection and correction of the bedform orientation

As bedform geometry is forced by the hydrodynamics, and the orientation of the frame is fixed, bedform dimensions will have decreased accuracy if the frame is not aligned to the flow (Williams, 2012). This could be a problem in the case of constantly changing flow direction during tidal rotation. In order to correct for this effect, each of 3D-ARP scans were rotated so that the orientation of the bedform crest lines were aligned perpendicular to the y-axis, before calculating the bedform dimensions.

A Radon transform was applied to 2D auto-correlations of the 3D-ARP scans to determine the crest line orientation angle of the bedforms relative to the measurement coordinate system, before rotating the 3D-ARP scans over this angle (Bell, 2016; Jafari-Khouzani and Soltanian-Zadeh, 2005). The 2D auto-correlation highlights the orientation of the bedforms in the 3D-ARP image. The peak in the Radon transformed data corresponds to the dominant crest line orientation angle of the bedforms within the auto-correlation data, and this angle was used to correct the 3D-ARP data by matrix rotation, with bi-

cubic resampling. These rotated data were then be used to determine the heights and lengths of the bedforms.

3.8.2.3 Zero-crossing method for bedform analysis

Of the different methods available for determining bedform dimensions from an elevation record (zero-crossing, spectral analysis, auto-correlation, standard deviation, and wavelet analysis), the zero-crossing method was found to be the most suitable for the 3D-ARP data (Williams *et al*. 2005; Masselink *et al.*, 2007; van der Mark *et al.*, 2008; Cataño-Lopera *et al.*, 2009; Cazenave *et al.*, 2013). A simple zero-crossing method for determining bedform dimensions was used, as there was only one scale of bedforms in the record, the method works well on short record lengths, and it can be easily automated for a large number of scans.

Before applying the zero-crossing method, the bed elevation data were de-trended making the mean level of the records zero and filtering out small fluctuations, 1 cm or less in length, around the zero line in order to reduce false positive zero crossings (Figure 3-17). The zero-crossing points, *i.e.* between the troughs and crests of bedforms, were determined by the crossing function of Brueckner (2007). The trough and crest points were then determined from the maximum and minimum *z*-values and the corresponding *x*-values. Subsequently, bedform height, length, stoss slope angle, lee slope angle and asymmetry were calculated for each bedform in each of the 101 profiles in a scan, and then averaged for each scan. The bedform asymmetry is the horizontal distance between the bedform crest and upstream trough divided by the horizontal distance between the crest and downstream trough. The mean bedform height was determined from the root mean square average of all stoss trough to crest heights and crest to lee trough heights in each scan. Before averaging the bedform parameters, extreme outliers greater than 4 standard deviations were removed. Calculated bedform lengths equal to or less than 15 mm, *i.e.* three times the grid resolution, were removed, as these lengths were below the horizontal resolution of the 3D-ARP. Bedform heights less than the vertical resolution of the 3D-ARP were also removed. The results of the zero-crossing method were checked with the manual measurements taken when the tidal flats were exposed (section 3.6.2). An exact match was not expected as the exposed bedforms were modified by the last part of the ebb tide, which was not recorded by the instruments. However, the two sets of bedform dimensions agreed well in magnitude with bedform heights in the range 1 to 5 cm and lengths in the range 10 to 21 cm for the manual measurements, compared to the 3D-ARP values in the range 1 to 3 cm for height and length in the range 13 to 25 cm. The main steps in the simple zero-crossing method are summarised in Table 3-5.

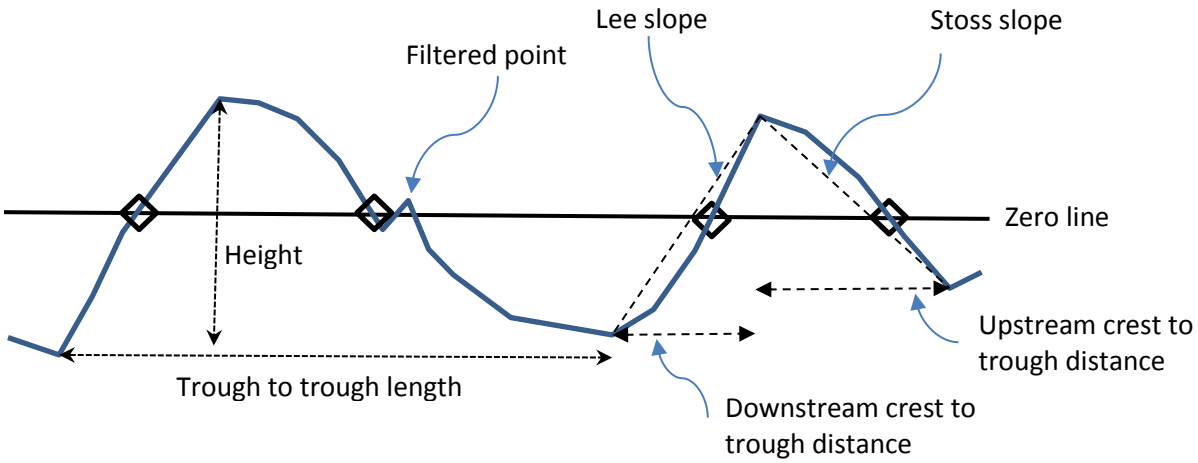

Figure 3-17: Zero-crossing analysis of a bed elevation profile for bedform height, length and slopes. Black diamonds are zero-crossing points.

Table 3-5: Processing steps for the simple zero-crossing bedform dimensions method.

1. De-trend the bed elevation profile (BEP), so the profile fluctuates about zero
2. Smooth small fluctuations around the zero line to reduce false positive zero crossings
3. Determine the zero up and down crossings
4. Determine the crests, troughs, lee slopes and stoss slopes in the original BEP
5. Determine the geometry of the bedforms in the de-trended BEP

3.8.3 CTD data

Pressure data from the CTD were corrected using the air pressure from the Hilbre Island weather station. Seawater density, water depth and speed of sound were calculated using the IOC-UNESCO Gibbs-SeaWater Oceanographic Toolbox (v3.03; http://www.teos-10.org (McDougall and Barker, 2011)).

3.9 Sediment sample analysis

3.9.1 Sediment particle size distribution

Bed sediment samples were collected, when the tidal flats were exposed during low slack water, from the top 1-2 cm below the crests and troughs of the bedforms, within one metre of the SEDbed frame (bed sample set 1). The particle size distribution (PSD) of these bed samples was measured using a Malvern Mastersizer 2000 at the School of Ocean Sciences, Bangor University.

The Mastersizer uses red and blue lasers to resolve a wide range of particle by means of Mie scattering and Fraunhofer diffraction theories (Malvern Instruments Ltd, 2013). Bangor University's Mastersizer 2000 has a Hydro 2000mu wet dispersion unit that keeps the sample in suspension during analysis and uses ultrasound to break up aggregations of particles. The results are reported as percentage volume concentrations in 100 size classes from 0.2 to 2000 µm. A full description of the Mastersizer 2000 instrument and software can be found in the user manual (Malvern Instruments Ltd, 2007).

Before the bed samples were analysed, they were dried and sieved with a 2 mm sieve to remove any large particles that would get wedged in the piping of the Mastersizer. Drying and sieving was not required for the multi-tier sediment trap samples, as these samples only contained fine-grained sediment. The procedure used for the analysis can be found in appendix 8.12.

The 14 bed samples from the Dee estuary were analysed for particle size distribution, and subsequently separated into clay, silt and sand volume fractions. 62.5 µm and 3.9 µm were taken as the upper size limits for silt and clay particles, respectively (Wentworth, 1922). By definition, 'mud' refers to both silt- and clay-sized particles. The sediment characteristics are given in Table 3-6. The median grain sizes, D_{50}, of the samples were in the range 217 to 238 µm. The last two samples at Site 3 show a reduction in D_{10} with increasing fine particles. The mud fractions were in the range 0.7% to 15.8% and the clay fractions were in the range 0.2% to 3.6%. The average particle size distributions of the three sites are shown in Figure 3-18 and the sand dominated multi-modal nature of the sediment can be seen. The lack of silt particles above 10 µm in diameter at Site 2 may be due to the location in a creek feature and this anomaly was not seen in any of the other sediment samples from the bed or settling column.

Table 3-6: Sediment characteristics of the field samples.

Sample	Time	Site	D_{10} µm	D_{50} µm	D_{90} µm	% clay	% cohesive clay (XRD corrected)	% silt	% mud	% sand
1	21/05/2013 15:21	1	134	222	340	1.20	1.80	3.71	4.91	95.09
2	22/05/2013 17:00	1	146	228	335	0.98	1.47	3.24	4.22	95.78
3	23/05/2013 16:20	1	147	230	338	1.09	1.64	3.32	4.41	95.59
4	26/05/2013 18:41	2	149	231	351	0.24	0.36	0.41	0.65	99.35
5	27/05/2013 08:25	2	143	220	333	0.59	0.89	0.95	1.54	98.46
6	27/05/2013 18:44	2	150	229	345	0.31	0.47	0.50	0.81	99.19
7	29/05/2013 07:43	2	145	224	342	0.27	0.41	0.44	0.72	99.29
8	29/05/2013 10:28	3	139	230	349	1.18	1.77	3.85	5.03	94.97
9	30/05/2013 10:54	3	150	238	351	1.14	1.71	3.94	5.08	94.92
10	31/05/2013 12:07	3	138	234	356	1.46	2.19	4.83	6.29	93.71
11	01/06/2013 11:56	3	127	233	355	1.98	2.97	6.21	8.19	91.81
12	02/06/2013 13:20	3	128	234	356	2.05	3.08	6.33	8.38	91.62
13	03/06/2013 12:13	3	101	234	353	2.19	3.29	6.87	9.06	90.94
14	04/06/2013 13:30	3	13	217	348	3.57	5.36	12.26	15.83	84.17

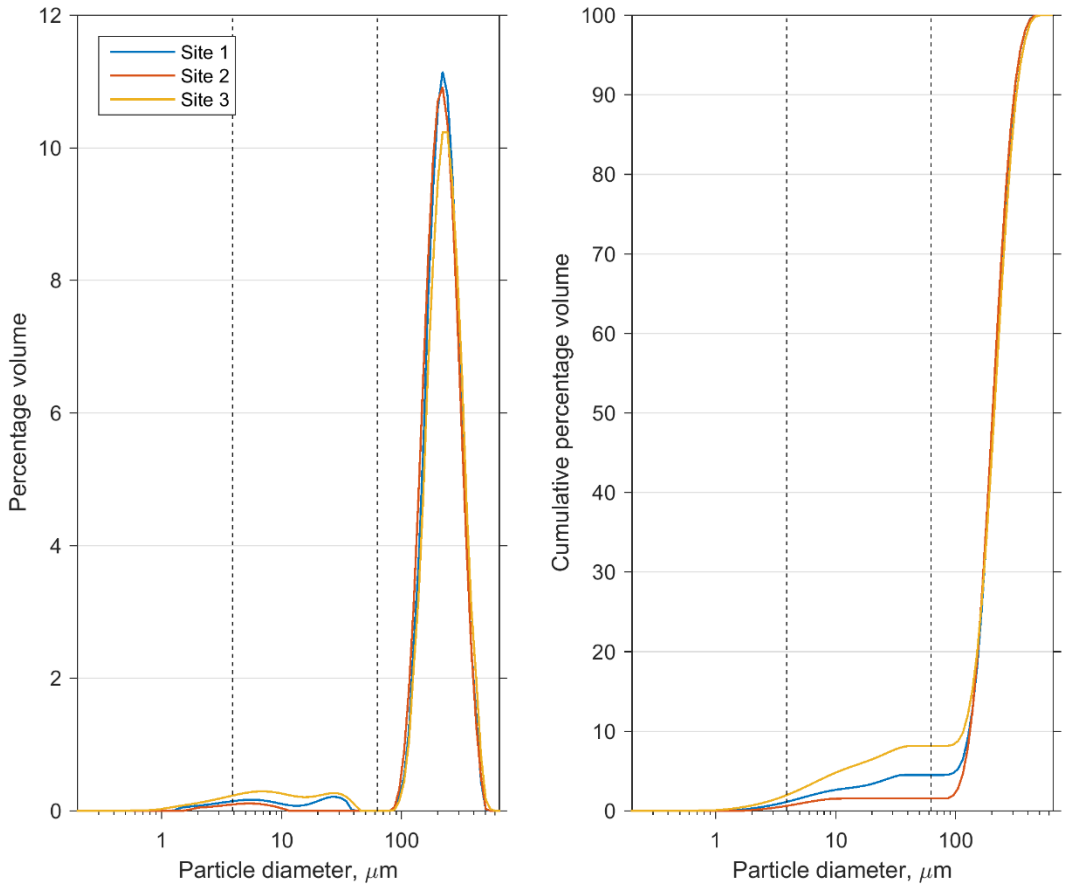

Figure 3-18: Particle size distribution of the bed samples averaged for each site. The vertical dashed lines denote the 3.9 and 62.5 µm limits separating clay, silt and sand.

3.9.2 Vertical lithology of the bed sediment

Of three cores collected on 26 May 2013, along a line on the bank at right angles to the creek at Site 2, one was analysed for particle size distribution at one-centimetre intervals using the Malvern Mastersizer (Baas and Baker, 2014). This core may be used to characterise the vertical lithology of the bed sediment in the study area. The core sample was taken on the bank, away from the influence of the creek (Baas and Baker, 2014). The vertical trend of clay, silt and mud content from the core can be seen in Figure 3-19. The high clay and silt concentration of the surface sub-sample (0 cm) may be due to settling and deposition at end the outgoing ebb tide (Baas and Baker, 2014; Baas, 2017). The clay and silt content are reduced 1 to 3 cm below the surface, compared to the other sub-samples in the profile, and this is probably due to winnowing of fine material from the sediment in the mobile layer of bedform migration (Baas and Baker, 2014; Baas, 2017). The processes in the actively migrating layer of bedforms, affecting the 1 to 3 cm from the sediment surface, strongly reduces the amount of silt in sediment compared to the clay content. This could be due to low cohesiveness of silt making it more easily winnowed from the mobile sediment layer than clay.

Although there was a large change in clay and silt content between the sub-samples at 3 and 4 cm, Figure 3-19, this was not seen as a colour change in the sediment (Baas and Baker, 2014). Between 5 and 6 cm, the sediment became darker in colour with only a small increase in clay and silt content, and sand filled burrows were seen at this level in the trench dug at the core site (Baas and Baker, 2014). The dark colouring of the sediment, without a large increase in mud, suggests that the sediment becomes anoxic at this level caused by the absence of sediment re-working by sediment transport and the lack of biological mixing, resulting in a reduction oxygen transfer, and this would be the lower limit of the active layer. The lower value of clay and silt at 5 cm below the surface could be due to an increase in sand, rather than a decrease in mud, caused by the biological action of burrow creation and maintenance. Below 6 cm there is little change in the clay and silt content, apart from an anomalously low sample at 11 cm (Baas and Baker, 2014).

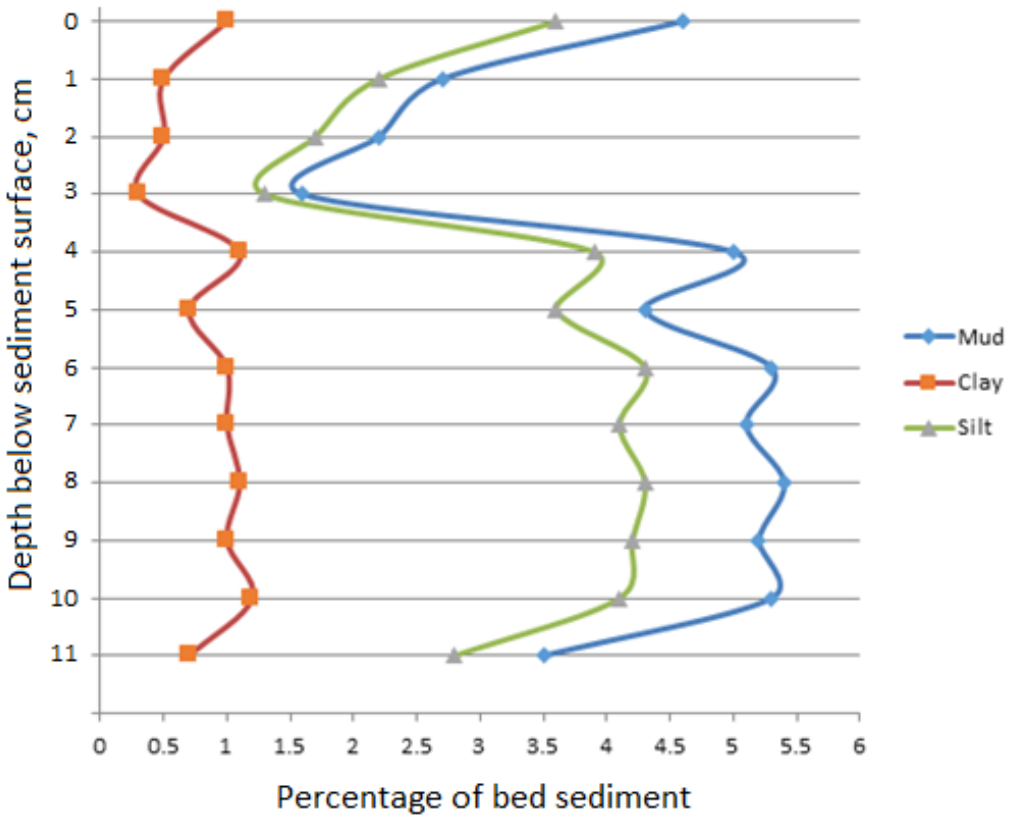

Figure 3-19: Sediment composition profile from a representative push core collected in study area. (Baas and Baker, 2014)

3.9.3 Bed cohesive clay composition

To characterise the mineral composition of the bed sediment in the survey area, a separate set of seven randomly selected bed samples were analysed by X-ray powder diffraction (XRD), using standard methodology for bulk sediment analysis (Moore and Reynolds, 1997). The mud fraction at the field sites contained 36 vol% ± 4 vol% clay minerals, where 4% denotes the standard deviation of the mean. In decreasing order of abundance, the clay mineral assemblage comprised illite, chlorite and kaolinite, where illite is the most cohesive clay mineral and chlorite is the least cohesive clay mineral (*e.g.* Mehta, 2014). Therefore, Illite made up the majority of the cohesive fraction. Quartz made up the majority of the non-cohesive fraction.

This 36 vol% clay fraction is inferred to represent the cohesive fraction within the mud more accurately than the particle size limit for the clay fraction derived from the Mastersizer 2000, as the remaining 64 vol% was dominated by non-cohesive quartz and feldspar. The bed clay content values from the Mastersizer analysis (bed sample set 1) were converted to cohesive clay content using the XRD-

derived fraction, which yielded cohesive clay fractions in the range of 0.4% to 5.4 vol%. These values will be referred to as cohesive clay fraction from here onwards. As the bed sediment was dominated by quartz, a density value of 2650 kg m^{-3} was used in the computations of the Shields stress parameters.

3.9.4 Bed EPS content

Additional bed surface samples were collected, by the University of St Andrew's Sediment Ecology Research Group, near the three sites for the determination of EPS content, as a measure of the biologically cohesive materials in the sediment (bed sample set 2). The EPS fraction is represented by the total carbohydrate content of the sediment by weight (Underwood *et al*., 1995) determined using the standard Dubois assay (Dubois *et al*., 1956). The EPS fractions of the bed samples ranged from 0.02 to 0.30 wt%. These bed samples were also analysed for clay content, using the Mastersizer 2000 and then corrected using the XRD data to obtain the cohesive clay content (see Sections 3.9.1 and 3.9.2). These samples were from the area of three sites, but did not form a matching time series to bed sample set 1, due to the different sampling strategy used (section 3.9.1). However, using results of bed sample set 2 for EPS and cohesive clay content, the EPS content of bed sample set 1 can be estimated.

The EPS fractions are plotted against the cohesive clay fractions in Figure 3-20. The thick grey lines represent the thresholds of bedform formation for a bed cohesive clay fraction of 2.5 vol%, based on Baas *et al*. (2013), and an EPS fraction of 0.063 wt%, based on Malarkey *et al*. (2015). Low EPS fractions correspond to low cohesive clay fractions (Sites 1 and 2) below the limits of Baas *et al*. (2013) and Malarkey *et al*. (2015) for bedform formation. High EPS fractions matched high cohesive clay fractions (Site 3), where bedform development in the laboratory flume experiments was found to be substantially reduced due to cohesion (Baas *et al*., 2013; Malarkey *et al*., 2015). The scatter in the data may be attributed to the patchiness of the EPS and cohesive clay across the sampled areas, inherent in biological processes. A robust linear regression describes the relationship between bed EPS content and bed clay content (R^2 = 0.64, p < 0.05 and RMS error = 0.048, for n = 16):

$$e = 0.0134c + 0.0152 \quad \textbf{3-5}$$

where e and c are the weight and volumetric percentages of EPS and cohesive clay, respectively (Figure 3-20). It is assumed that this simple linear relationship also applies to the bed sample set 1 (Sections 3.9.1 and 3.9.5), for which no EPS data are available. As the amount of EPS in the bed sediment is

related to the cohesive clay content, the cohesive clay content refers to both physical and biological cohesion in this thesis.

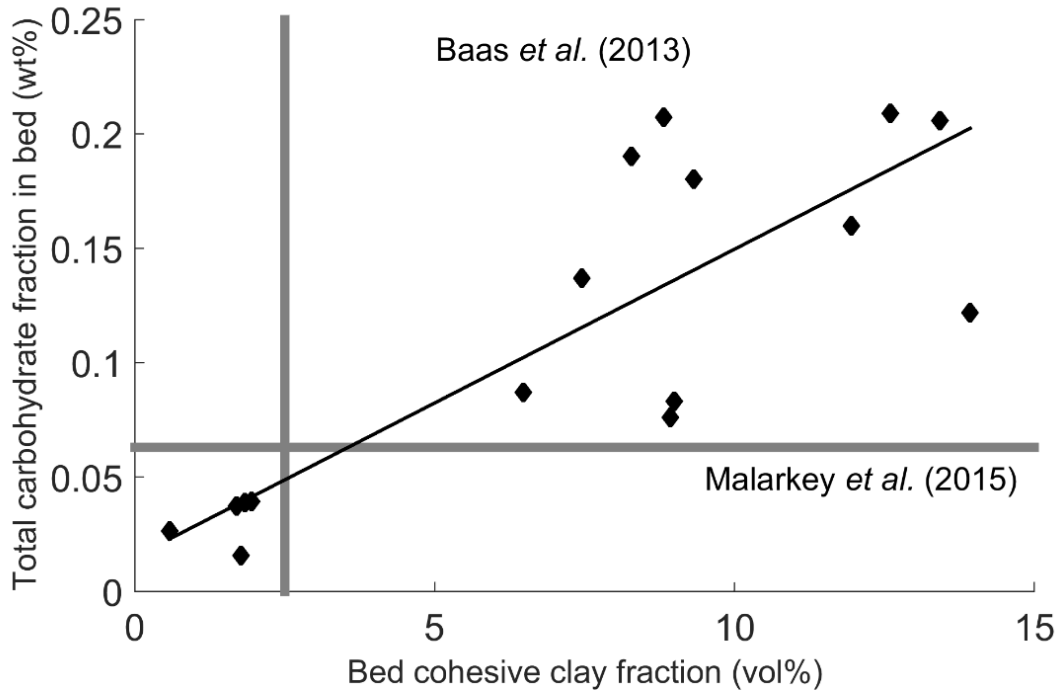

Figure 3-20: Total carbohydrate fraction (EPS) against bed cohesive clay fraction, derived from bed samples collected in the vicinity of Sites 1 to 3 (bed sample set 2, analysed for EPS and particle size). The thick grey lines represent the thresholds of bedform formation for a bed clay fraction of 2.5%, based on Baas *et al*. (2013), and a bed EPS fraction of 0.063%, based on Malarkey *et al*. (2015). The values from Site 3 fall to the right of the Baas *et al*. (2013) line and above the Malarkey *et al*. (2015) line. The black line represents a robust linear regression fit (R^2 = 0.64, p < 0.05 and RMS error = 0.048, for n = 16) between the clay and EPS values, with four outliers excluded for > 90% residual error from the fit (outliers not shown).

3.9.5 Variation in bed composition

The cohesive clay content of the bed varied over the deployment record (Bed sample set 1, Figure 3-21). A linear fit was used to describe the changes in bed clay fraction at Sites 1 and 2, whereas a second-order polynomial fit was used to describe the temporal trend in bed clay fraction at Site 3 (Figure 3-21). While the discontinuities in the fits between sites shows evidence of spatial variation, this difference is assumed to have a small effect on the results. Waves are known to enhance the winnowing process (Baas *et al*., 2014) and high wave stress was only present at Site 1 (Figure 3-16b). Site 2 was at the lowest bed elevation, placed in a creek that never completely drained, and includes the peak of spring tide. At Site 3, there is a trend of increasing bed clay content as the tide progressed

from springs to neaps at the end of the record (Figure 3-21). The tide dominates the bed composition with the lowest bed cohesive clay content seen at Site 2 during spring tide and the variation of cohesive clay content at Site 3 with the progression of the tide to neaps.

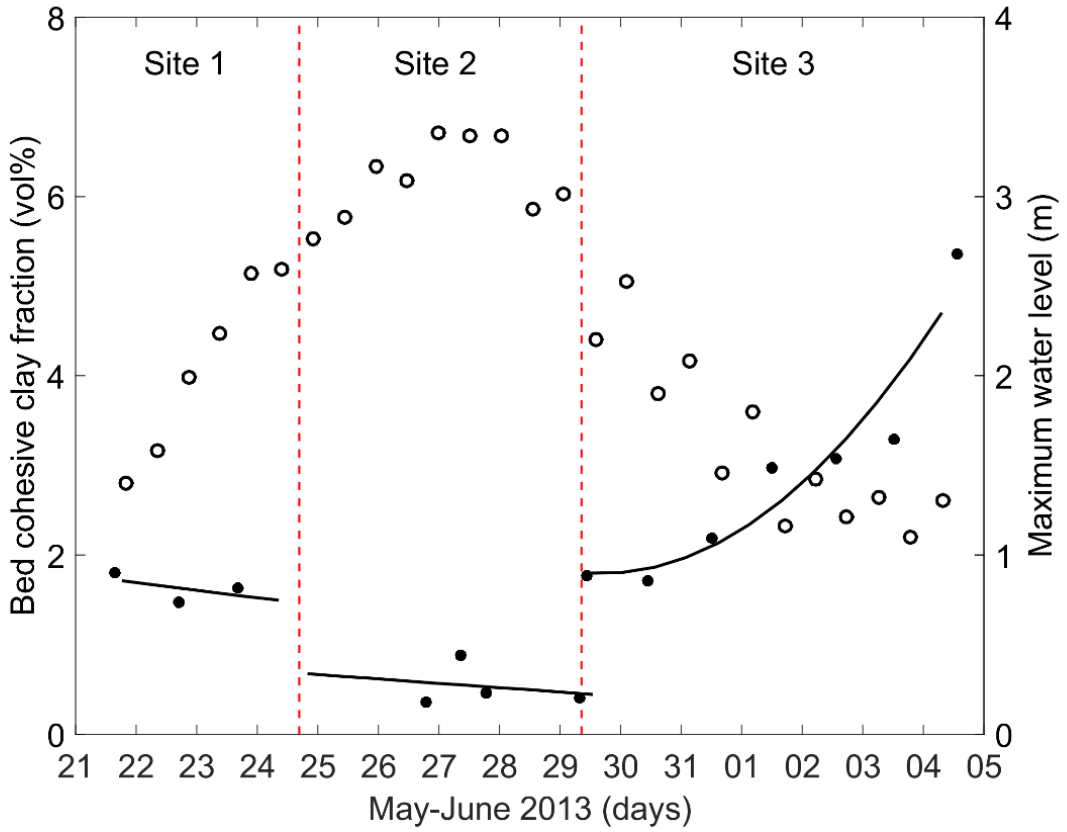

Figure 3-21: Time-series of bed cohesive clay fraction (●) and maximum water height (o) for each tidal period (bed sample set 1, only analysed for particle size). A linear fit was used to describe changes in bed clay fraction at Sites 1 and 2, whereas a second-order polynomial fit was used to describe the temporal trend in bed clay fraction at Site 3. The bed cohesive clay fraction represents the total percentage of cohesive clay minerals within the sediment. The vertical dashed red lines mark the times when the instruments were moved between sites.

The bed clay content results from the local availability of clay and the processes that add and remove clay to and from the bed. These processes are influenced by, amongst other factors, bed shear stress and duration of applied stress; bedform migration rate; median grain size of the sand; physical and biological cohesive strength of the bed; filtering, excretion and bed re-working by benthic organisms; and bed strengthening during tidal flat exposure (Winterwerp and van Kesteren, 2004). The duration of tidal inundation encompasses many of these factors, as it is controlled by the spring-neap tidal

cycle, and governs, for example, the maximum stress of the tide, the duration of stress and the duration of bed strengthening. The bed cohesive clay content, modelled from the regression fits in Figure 3-21, correlates well with the duration of the tidal inundation period for all 27 inundations over the studied spring-neap cycle (Figure 3-22; $R^2 = 0.82$, $p < 0.05$ and RMS error = 0.52, for $n = 27$).

While the duration of tidal inundation shows a strong correlation to the bed cohesive clay content, using duration of inundation in the analysis of sediment dynamical processes would limit the application of the results of this thesis to tidal flats. In order to make the results of the following chapters more widely applicable, the bed shear stress and water depth are the main parameters used. However, the duration of tidal inundation will be mentioned in the discussion chapter, where a conceptual model of the processes affecting bed cohesive content outlined.

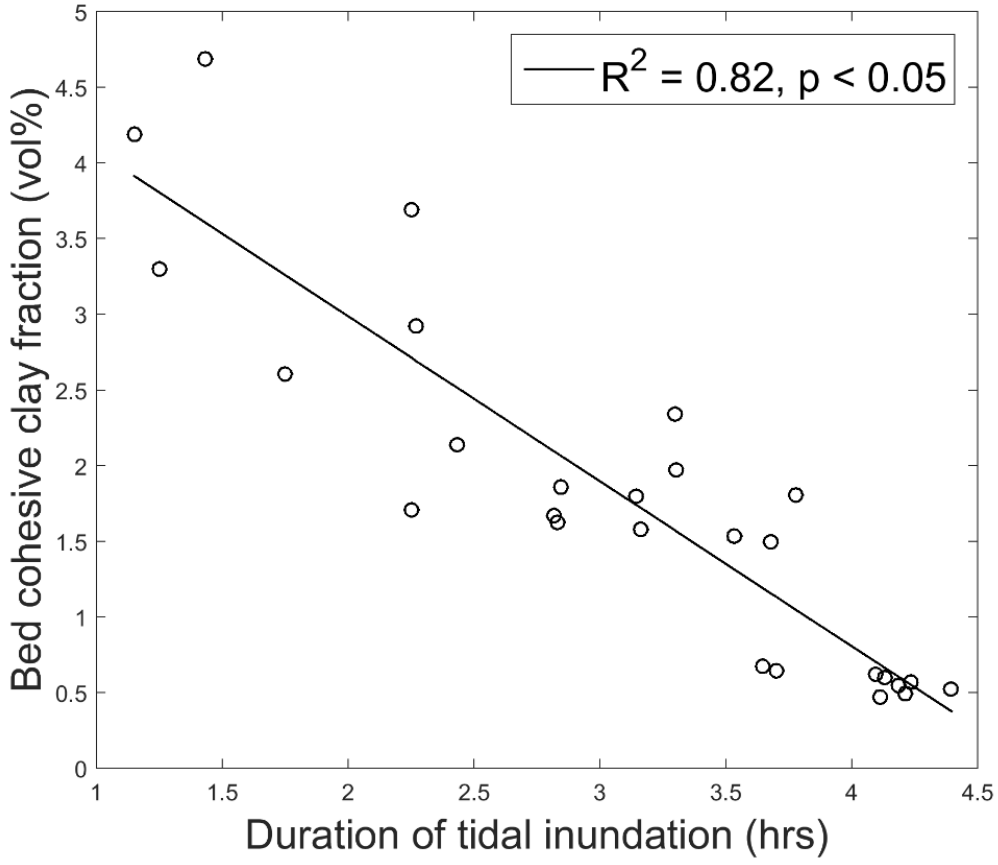

Figure 3-22: Relationship between duration of tidal inundation, in hours, and bed cohesive clay content for each tidal inundation period (*n* = 27).

3.10 Mathematical methods used in the data analysis

This section describes the key mathematical methods used for the interpretation of the data. As some of these methods are related to each other, they are described here together. All these methods are functions in Matlab (in the statistics and digital signal processing toolboxes).

3.10.1 Linear regression

To describe a relationship between two sets of variables, a linear function of the form $y = a + bx$ can be used, where x is the independent variable, y the dependent variable, b the slope of the line and a is the value at which the line crosses the y-axis (Kennedy and Neville, 1976; Chatterjee and Hadi, 2015). The ordinary least squares regression method creates a 'best fit' for the linear function by minimising the sum of squares of the deviations in the dependent variable from the fitted regression line (Kennedy and Neville, 1976; Chatterjee and Hadi, 2015). The ordinary least squares method assumes that the errors in the independent variable are negligible and extreme values do not affect the fit. In the case where the errors are known for both the independent and dependent variables, major axis or orthogonal regression can be used. Orthogonal regression minimises the sum of squares in both variables, perpendicular to the regression line (Chatterjee and Hadi, 2015).

To reduce the effect of extreme values and deviation from a normal distribution in a data set, robust regression can be used (Wilcox, 2012; Chatterjee and Hadi, 2015). As the overall regression model should not change greatly with the removal or addition of individual values, robust methods reweight the data reducing the weight of individual points that have an extreme influence, or high 'leverage', on the overall fit (Wilcox, 2012; Chatterjee and Hadi, 2015). This avoids the need of manually removing outlying values, which may be subjective (Chatterjee and Hadi, 2015).

Non-linear data can be analysed using linear methods by first transforming the data (Chatterjee and Hadi, 2015).This can be done using a range of functions, such as sine, logarithmic and square-root functions. For example, in this thesis, a logarithmic function was found to be most appropriate for the bedform migration and transport data.

The R^2-value of a regression fit is one of the statistics used to assess the quality of a regression. R^2 is the proportion of variability in the dependent variable that is explained by the independent variable, with a value of one being perfect agreement between the variables. For linear regression, R^2 is equal to the square of the correlation coefficient (Chatterjee and Hadi, 2015). A low value of R^2 may still be significant, if it is supported by a large data set, but with factors not explained by the independent variable (Kennedy and Neville, 1976).

The t-statistic is a measure of the difference between the estimate of a coefficient *(e.g.* the slope of the fit) and the expected value, and the associated p-value is the probability of a random variable having a t-statistic larger than the observed value (Chatterjee and Hadi, 2015). The confidence limit of the p-value should be set before the analysis is carried out. In this thesis, a limit of 0.05 or 95% confidence is used, unless otherwise stated. The values of t, p and R^2 are checked against standard statistical tables to show that the regression model is significant (Kennedy and Neville, 1976; Chatterjee and Hadi, 2015).

3.10.2 Cross-correlation and autocorrelation

The correlation between two series of variables is a measure of their similarity (*i.e.* the correlation coefficient of a linear regression indicates the similarity between the dependent and independent variables). Cross-correlation is used to determine the lag between two different data series containing similar patterns. More specifically, cross-correlation is often used to relate features shifted in time or space, or to investigate the delayed response of one variable to another (Emery and Thomson, 2001; Sutton *et al.*, 2009). In this thesis, cross-correlation is used to determine the migration distance of bedforms between the 3D-ARP scans (Giachetti, 2000; Smyth and Li, 2005; Masselink *et al.*, 2007; Sutton *et al.*, 2009). Autocorrelation is the cross-correlation of a data series with itself; this method highlights repeated patterns in the data (Emery and Thomson, 2001).

3.10.3 Multiple linear regression

Multiple linear regression is an extension of linear regression to more than one independent parameter (Chatterjee and Hadi, 2015). This enables modelling of a dependent variable with more than one influencing factor, allowing for more variance in a data set to be accounted for. However, problems can arise if independent parameters co-vary (e.g. current velocity and water height), are multicollinear, so care must be taken when adding parameters to the regression analysis (Chatterjee and Hadi, 2015). Interactions between parameters can be accounted for by creating secondary parameters of products of the primary parameters, *e.g.* $\theta'_c \times \theta'_w$ for wave-current stress enhancement (Chatterjee and Hadi, 2015).

An F test *versus* a constant model is used to determine if the regression model is significantly different from a constant value, *i.e.* the variability is better explained by the model than a constant for a given level of significance (Chatterjee and Hadi, 2015). As for the linear regression, the values of F, p and R^2 are checked against standard statistical tables to show that the regression model is significant overall

(Kennedy and Neville, 1976; Chatterjee and Hadi, 2015). The t statistic can be used to check the individual parameters for significance. Individual parameters may be not significant, even though the overall model is significant, and conclusions should not be drawn from these parameters separately from the model. The relative influence of the individual parameters on the predicted values can be determined by dividing the model coefficients by their standard errors (t-statistic) and comparing the magnitude of the values (Borradaile, 2003). By comparing the relative importance of the parameters in this way, the dominant processes can be determined and assessed.

3.10.3.1 Stepwise multiple linear regression

For data sets with many parameters, it may not be obvious which parameters are of significance to a process. Stepwise multiple linear regression is an automated procedure where parameters are tested for significance in a regression model, adding and rejecting parameters based on a set limit of significance (Chatterjee and Hadi, 2015). This keeps the model to a minimum number of parameters, with the greatest effect. However, care must be taken, as the resulting model may be under-parameterised, too simplistic, or over-parameterised, to complex and account for random error as well as the desired processes. By starting with a constant parameter (intercept) and adding parameters to the model, the number of parameters used to create an overall significant model is kept to a minimum. This method can highlight which parameters are important in a process, but also highlight any limitations of the data set if key parameters are excluded.

3.10.3.2 Logistic regression

Logistic regression is a multiple linear regression method that creates a regression fit of continuous data to discrete classes, relative to a reference class (Borradaile, 2003; Chatterjee and Hadi, 2015). From the resulting fitted relationship and statistics, the different effects of the parameters that make up the regression model can be assessed and predictions can be made of the probability that a particular combination of values belongs to a class. This method is useful in relating data from a manual classification to continuous recorded data, and assessing the processes that result in assignment to a particular class. An example would be classifying patients as having a probability of being high risk for a disease *versus* low risk, based on data of age, weight, gender, smoking, diet and family history (Chatterjee and Hadi, 2015).

3.11 Conclusions

The SEDbed suite of acoustic and optical instruments was deployed on the Hilbre tidal flats in the Dee Estuary, as part of the COHBED project, to collect data on the effect of physical and biological cohesion on near-bed sediment dynamics. This field campaign focussed on the acquisition of near-bed hydrodynamics, changing bed morphology and suspended material over a spring-neap cycle. In addition, bed sediment samples were collected for particle size analysis and biological analysis, to measure the amounts of cohesive material within the sediments.

The cohesive clay content of the bed was found to vary with the hydrodynamic forcing within the studied spring-neap cycle, and the amount of EPS in the bed sediment was found to correlate linearly with the cohesive clay content. As the amount of EPS in the bed sediment is related to the cohesive clay content, the cohesive clay represents both physical and biological cohesion. Over the study period, the sediment bed changed quite rapidly from less cohesive (below 2 vol% cohesive clay) to more cohesive (up to 5.4 vol%), as the tide progressed from springs towards neaps, in the absence of strong wave forcing.

All the data described in this chapter, and used in the following chapters together with the mathematical methods, are available from the British Oceanographic Data Centre (https://www.bodc.ac.uk/).

4 Bedforms in mixed cohesive sediment forced by combined wave-current flow

4.1 Summary

Few bedform predictors have considered the effect of bed cohesion on bedform dynamics or transitions between bedform types. Recent laboratory flume studies have shown that bedform height and length decrease, and the plan morphology of the bedforms changes from 3D to 2D, as the bed cohesive content is increased (Baas *et al*., 2013; Schindler *et al*., 2015; Parsons *et al*., 2016). In this thesis, these laboratory studies were extended to field conditions to study the changes in bedform dimensions, on tidal flats in the Dee estuary, as a function of a wide range of wave and tidal flow conditions, water depth, and bed cohesive content.

The field data were found to support the laboratory flume data of Baas *et al*. (2013), Schindler *et al*. (2015) and Parsons *et al*. (2016) in that the presence of bed cohesive clay reduced the bedform dimensions, and hindered the development of 3D plan morphology of these bedforms. Increasing cohesive clay content had a greater influence on bedform height than on bedform length. A significant number of the current-dominated bedforms present on the tidal flats did not conform well to standard current ripples, because these bedforms scaled with the water depth and were larger than predicted for current ripples. They were therefore interpreted as bedforms transitional between current ripples and dunes in this study (*cf.* Bennet and Best, 1996; Baas, 1999).

Empirical relationships between bedform height and length, wave and current forcing, water depth, and bed cohesive fraction were determined. In addition, the critical cohesive clay limit for bedform development was found to increase with increasing water depth, and this may be due to the relationship of tidal height with current stress. Although the direct application of these regression equations might be limited to the mixed sand-mud at the study site, they offer generic insights into the key processes that control the feedback mechanisms between mobile sandy cohesive sediment and hydrodynamic forcing in intertidal areas elsewhere. These new predictors may help improve the parameterisation of bedform dimensions in mixed cohesive sediment for shallow tidal and oscillatory flows, and therefore improve bed roughness parameterisations for use in sediment transport calculations, flooding management, and the design of coastal structures. The present results could also aid in the interpretation of the origin and evolution of bedforms in the sedimentary record.

4.2 Introduction

Sedimentary bedforms define the roughness of the seabed, cause flow modification and energy dissipation, and enhance sediment suspension and mixing (Allen, 1968; Soulsby and Whitehouse, 2005a,b; Soulsby *et al*., 2012). Since different types of bedform form under currents, waves, and combined flows, bedforms in the sedimentary record have been used as a proxy for reconstructing depositional environments and near-bed hydrodynamic processes (*e.g.* Allen 1968; Clifton and Dingler, 1984; van den Berg and van Gelder, 1993b; Parsons *et al*., 2016).

Improved predictions of bedform dimensions, and parameterisation of bed roughness, would enable the development of more accurate models for tidal and wave energy dissipation, sediment transport, flooding, and acoustic reflectivity of the seabed (Soulsby *et al*. 2012; Aldridge *et al*., 2015). Existing bedform predictors are mainly restricted to specific bedform types, such as wave ripples, current ripples, and dunes (van Rijn, 1984c; Soulsby, 1997; Soulsby & Whitehouse, 2005a,b; Camenen, 2009; Pedocchi & García, 2009a,b; and Nelson *et al*., 2013). The data used to create these predictors have come from both laboratory flumes and the field, and cover predominantly steady flow and a fixed water depth (Soulsby & Whitehouse, 2005a,b; Camenen, 2009; Goldstein *et al*., 2013; Nelson *et al*., 2013). Few bedform predictors have considered the transition between different types of bedform, the effect of bed cohesion, bedform development towards equilibrium dimensions, and changing water depth (Li & Amos, 1998; Soulsby *et al*., 2012; Baas *et al*., 2013; Bartholdy *et al*., 2015), all of which are common on tidal flats.

The effect of sediment cohesion on bedform dimensions and bedform development rate has only recently been the subject of laboratory flume studies (Baas *et al*., 2013; Malarkey *et al*., 2015; Schindler *et al*., 2015). Laboratory flume work as part of the COHBED project has shown that current ripple and dune height and length decrease with increasing bed fraction of cohesive clay and biological polymers, if the bedforms are given the same amount of time to develop (Baas *et al*., 2013; Malarkey *et al*., 2015; Schindler *et al*., 2015). In addition, bedforms change from 3D to 2D, as bed clay content is increased in steady flow conditions (Baas *et al*., 2013; Schindler *et al*., 2015; Parsons *et al*., 2016). Biological cohesion has a much greater effect than clay cohesion in mixed sediments (Malarkey *et al*., 2015).

Malarkey *et al.* (2015) showed that biological binding of the sediment by the EPS-proxy xanthan gum can greatly slow down the development of current ripples on a flat bed. However, the equilibrium dimensions of the current ripples were independent of bed EPS content; reaching this equilibrium took progressively longer, as bed EPS content was increased.

The present project extended the laboratory flume studies of the COHBED project into the natural environment by studying bedform dynamics on tidal flats in the Dee estuary. This fieldwork covered a wide range of wave and tidal flow conditions, varying water depths, and different mixed sand-mud-EPS beds. Below, these data are described, compared to a selection of existing bedform phase diagrams and bedform predictors, and then used to explore the relative contribution to bedform dimensions of wave-current flow, water depth and bed cohesive clay content.

4.3 Aims

- Determine how the dimensions and the plan morphology of intertidal bedforms are affected by physical and biological cohesion in the bed sediment under waves, currents, and combined flows, compared to pure-sand bedforms.
- Assess the performance of existing bedform phase diagrams and bedform predictors for bedforms formed in cohesive sand-mud-EPS on intertidal flats.
- Develop field-based empirical relationships between small-scale bedform dimensions, current and wave forcing, water depth, and cohesive forces within the substrate.

4.4 Background

4.4.1 Formation of bedforms and bedform classification

Bedforms result from the shear of waves, currents, or combined flow with a mobile sediment bed (Allen 1968; Soulsby *et al*, 1997). Waves generate bedforms with vertical profiles close to symmetrical, while asymmetrical bedforms are formed by currents and most combined flows. An ideal bedform profile with commonly used terminology is shown in Figure 2-8. Strong hydrodynamic forcing can flatten or wash out bedforms below the transition to an upper stage plane bed, and weak forcing below the Shields criterion can leave the bed 'frozen' and produce relict bedforms (Baas and De Koning, 1995; Baas, 1999; Soulsby *et al*, 1997; Soulsby *et al*, 2012). Bedforms tend to orientate relative to the direction of the hydrodynamic forcing, with a time lag as the hydrodynamic forcing changes (Soulsby *et al*, 1997; Soulsby *et al*, 2012).

Bedforms in sand reach a constant mean height, wavelength and planform, if given sufficient time to develop to equilibrium (Allen, 1968; Baas *et al*., 1993; Baas, 1994; Oost & Baas, 1994; Baas, 1999). The time taken for current ripples to reach equilibrium dimensions is related to the inverse of the flow velocity, and the median grain size (Baas, 1999). For current ripples developing on a flat bed, this time

lag may range from tens of minutes to hundreds of hours (Baas, 1994). It follows that bedforms in time-varying flow may not be in equilibrium with the flow at all times (Hay & Wilson, 1994; Masselink & Hughes, 2003; Austin, 2007; Traykovski, 2007; Soulsby *et al*., 2012).

Bedforms can be classified based on the planform, height, length, profile symmetry, grain size, water depth, wave velocity, current velocity, and flow regime. However, transitional forms stretching across class boundaries and superposition of bedform types can make classification difficult. In a small area of seabed, multiple bedform types may co-exist. Below, the main classes of bedform relevant to the field area in the Dee estuary are described.

Bedform orientation is considered relative to the dominant flow direction, with transverse bedforms perpendicular to the flow and swept bedforms deviating significantly from perpendicular (Allen, 1968; Figure 2-9). Although non-equilibrium bedforms can have straight 2D crests in currents (Figure 4-1), these forms are also associated with wave action. Wave ripples have bifurcations, connected junctions, whereas current ripples have open junctions, as shown in Figure 4-2 (Reineck & Singh, 1980). Sinuous bedforms can be non-equilibrium current-generated bedforms (Figure 4-1) or current-dominated bedforms modified by perpendicular wave forcing (Lee Young and Sleath, 1990; Andersen and Faraci, 2003). Under sediment-starved conditions, solitary, unconnected bedforms form, which are known as barchans.

As mentioned above, cohesion due to mud and biological polymers (Extracellular Polymeric Substances, EPS) may stabilise the sediment, decreasing bedform size and increasing the time taken by bedforms to respond to changes in flow forcing (Baas *et al*. 2013; Passarelli *et al.*, 2014; Malarkey *et al*., 2015; Schindler *et al*., 2015; Parsons *et al*., 2016). However, biological action by benthic organisms may also destabilise and rework the bed (Grant and Daborn, 1994; Fries *et al.*, 1999; Passarelli *et al.*, 2014).

Over an area of seabed, different types of bedforms may be present in groups at different stages of development. This may be caused by differences in preceding morphology, spatial variation of sediment properties, and non-uniform current and wave forcing (Allen, 1968).

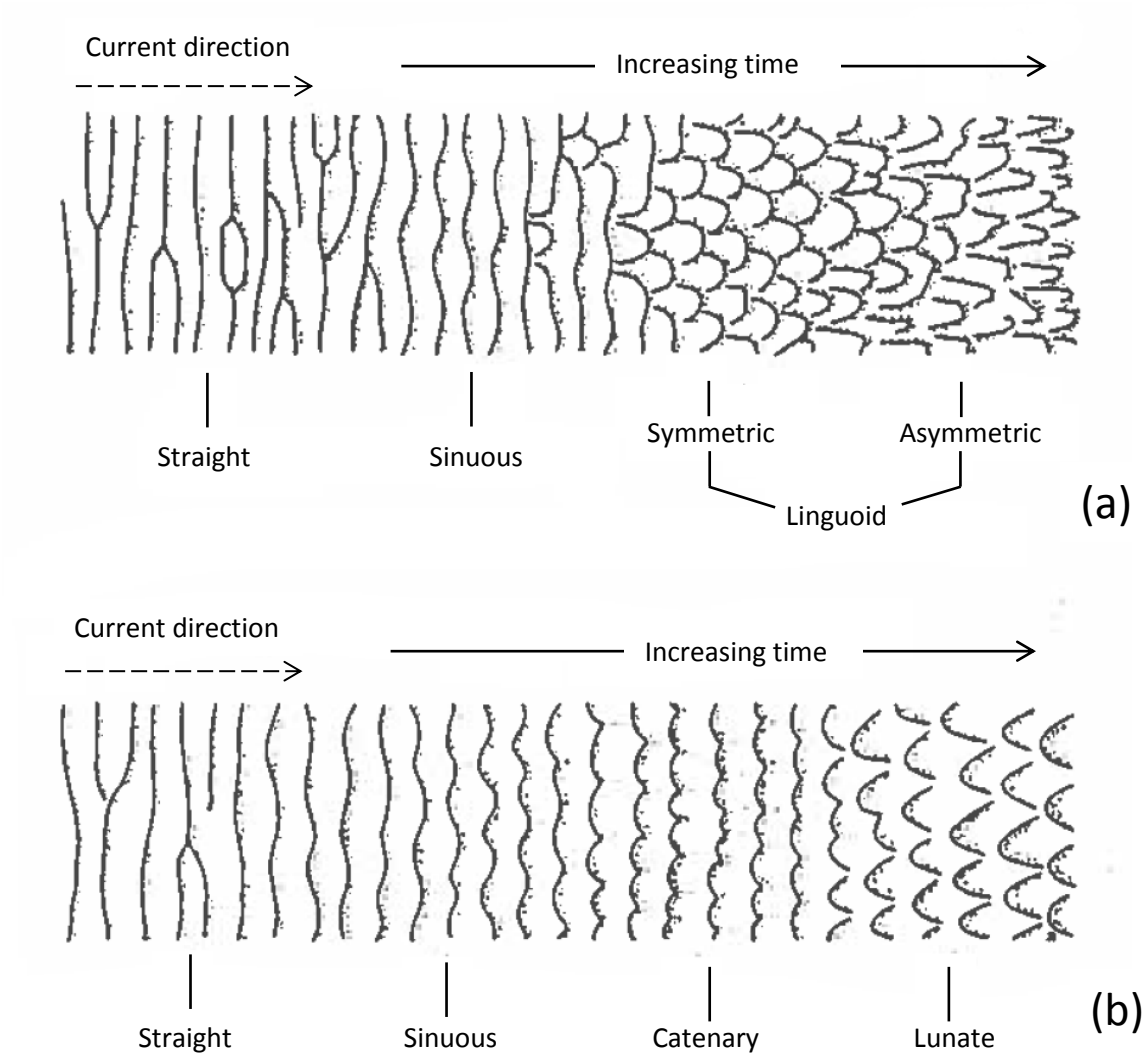

Figure 4-1: Bedform development sequence in unidirectional flow for: (a) Ripples and (b) dunes (After Allen, 1968; Baas *et al*., 1993, 1994; Baas, 1999; Venditti *et al*., 2005).

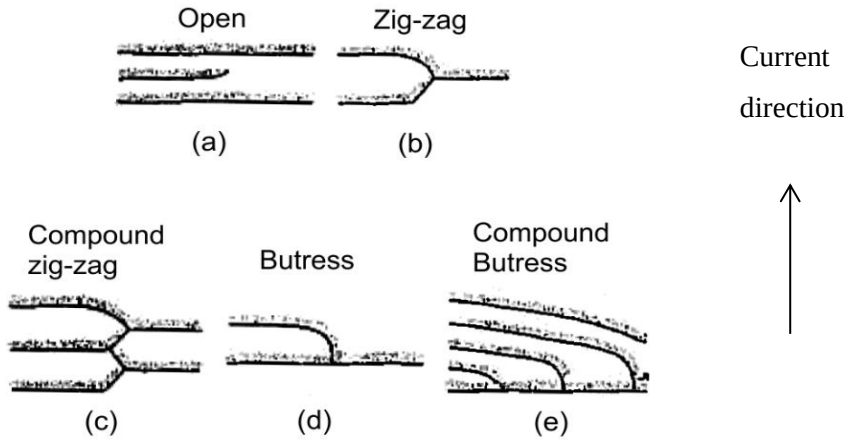

Figure 4-2: Types of ripple juncture (Allen, 1968).

4.4.1.1 Current ripples

Current ripples are small-scale bedforms formed in currents and found in groups, ripple trains, with crestlines orientated perpendicular to the main flow direction (Allen, 1968; Soulsby, 1997). In steady flow, individual current ripples reach equilibrium heights and lengths in the range of 0.01 to 0.06 m and 0.1 to 0.6 m, respectively (Baas *et al*., 1993; Baas, 1999; Soulsby et al., 2012; Perillo *et al*., 2014). However, in natural conditions, the mean height and length in a train of current ripples are usually less than 0.02 m and less than 0.2 m, respectively (Baas, 2003). Current ripples scale with the sediment size on the bed (Yalin, 1977; Baas, 1993; Raudkivi, 1997; Soulsby et al., 2012). As current ripples progress to equilibrium size from a flat bed, their planform changes from 2D to 3D linguoid (Figure 4-1a; Baas *et al*., 1993; Baas, 1999).

4.4.1.2 Dunes

Dunes are large-scale current-generated bedforms, with crestlines orientated perpendicular to the main flow direction. Dune height scales with water depth and bed shear stress, whereas dune length only scales with water depth (Allen 1968; Yalin, 1977; van Rijn, 1984c; Southard and Boguchwal, 1990; Soulsby, 1997). Like current ripples, dunes progress from 2D to 3D forms as they grow to equilibrium size (Figure 4-1b; Allen, 1968; Venditti *et al*., 2005). Dunes are larger than current ripples, by definition, with heights ranging from 0.06 m to over 5 m and lengths ranging from 0.6 m to over 100 m (Allen 1968; Ashley, 1990; Soulsby, 1997).

Some authors have considered current ripples and dunes as part of a continuum of bedform dimensions (*e.g.* Flemming, 1988; Bartholdy *et al.*, 2015). Flemming (1988) suggested that both current ripples and dunes scale with grain size, and that water depth and sediment supply modulate the bedform height. However, Ashley (1990) re-assessed Flemming's (1988) data, noting a gap in height and length data that separates bedforms into small-scale current ripples and large-scale dunes. Laboratory flume studies have shown that the hydrodynamic character of flow separation and flow re-attachment over bedforms changes across the transition from current ripples to dunes (Bennett and Best, 1996; Schindler and Robert, 2005; Fernandez *et al*., 2006). Here, current ripples and dunes are considered as separate classes, with current ripple dimensions scaling with grain size, and dune dimensions scaling with water depth, current velocity and grain size.

4.4.1.3 Wave ripples

Wave ripples are wave-generated bedforms, with the crestlines orientated perpendicular to the wave propagation direction (Figure 4-3a). Wave ripples scale with the maximum near-bed orbital velocity, and the sediment size (*e.g.* Clifton and Dingler, 1984). As waves are modulated by water depth, wave ripple dimensions will also change with water depth (Brown, 2010; Friedrichs, 2011). Ideal wave ripples have a symmetrical profile and straight continuous crestlines.

With increasing wave forcing, wave ripples may develop into hummocks, which are semi-spherical bedforms arranged irregularly on the seabed (Kleinhans, 2005). Hummocks have heights in the order of 0.1 – 0.5 m and lengths of 1 – 10 m (Swift *et al*., 1983; Kleinhans, 2005).

4.4.1.4 Combined flow bedforms

Depending on the relative influence of currents and waves, combined flow bedforms can take a variety of shapes and sizes (Allen, 1982; Amos *et al*., 1988b; Arnott and Southard, 1990; Lee Young and Sleath, 1990; Andersen and Faraci, 2003; Dumas *et al*., 2005; Perillo *et al*., 2014). The complex interaction of waves and currents leads to bedforms that may be difficult to interpret without additional information on the forcing conditions. Wave-dominated ripples may form regular tiled patterns with crestlines surrounding a central depression, if multiple wave trains meet from different directions (Allen, 1982). Combined flow ripples may have discontinuous crestlines, due to waves moving at an angle to the current, or form sinuous bedforms (Figure 4-3; Lee Young and Sleath, 1990; Andersen and Faraci, 2003). “Ladder-back patterns” are also produced by combined flows, with smaller ripples forming in the troughs of larger bedforms at an oblique angle to the primary bedform direction (*e.g.*, Reddering, 1987; Ramsay *et al*., 1989). The Bedform Symmetry Index (BSI), the ratio of lee slope length to stoss slope length, can be used to determine the relative influence of waves and currents on bedforms, as wave-dominated bedforms should be close to symmetrical and have a BSI < 1.3 (Dumas *et al*., 2005; Perillo *et al*., 2014).

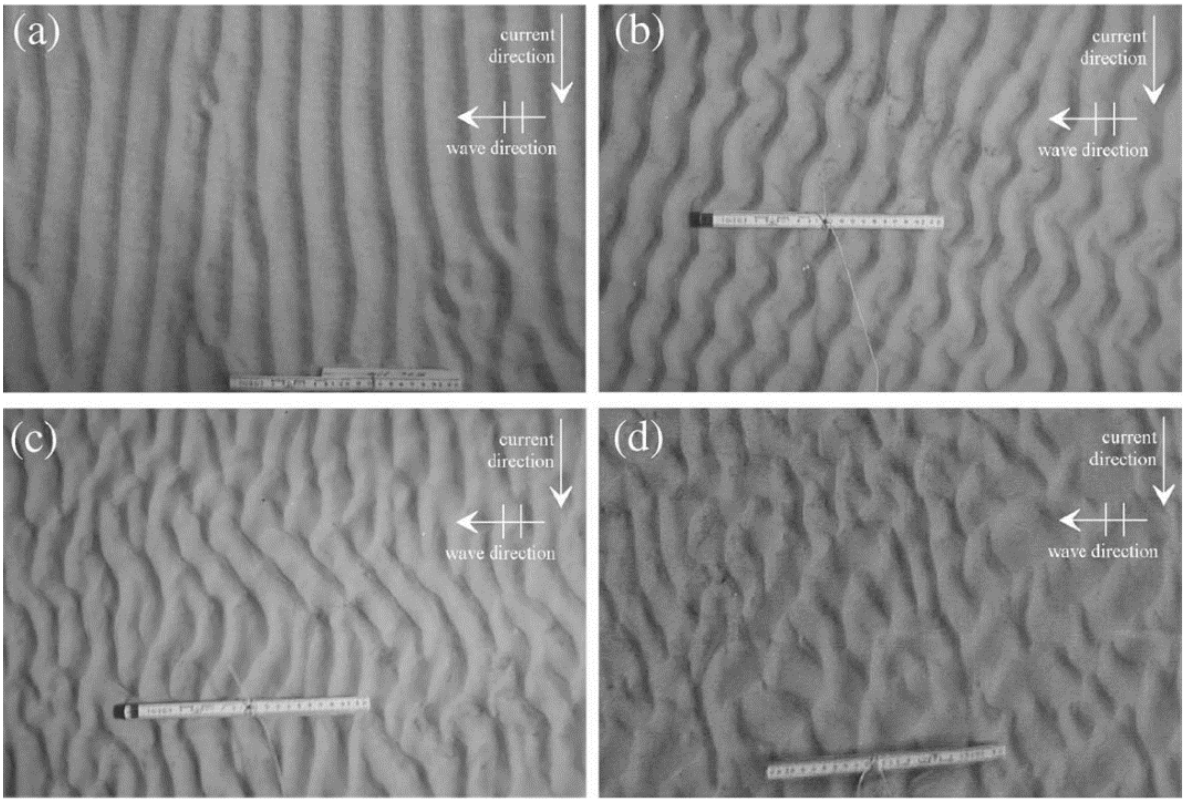

Figure 4-3: Combined wave-current ripple patterns. (a) 2D wave ripples (U_c/U_w = 0.13; for U_c/U_w < 0.2, currents have no influence); (b) sinuous ripples (U_c/U_w = 0.5); (c) segmented ripples (U_c/U_w = 0.9); (d) irregular bedforms (U_c/U_w = 1.5). The length of the ruler is 0.2 m (Andersen and Faraci, 2003).

4.4.1.5 Sand ribbons, washed-out bedforms and flat beds

Sand ribbons are long, narrow, low relief features oriented parallel to the flow (Figure 4-4), usually associated with high flow and sediment starved conditions (Allen, 1968; Kenyon, 1970; McLean, 1981). In shelf seas, sand ribbons form over gravel beds and can be as wide as 200 m and as long as 15 km, with a height of less than one metre (Kenyon, 1970; Amos and King, 1984). However, small-scale sand ribbons, a few centimetres in width and about 0.2 m apart, have been created in the laboratory (Günter, 1971; McLean, 1981; Figure 4-4).

An upper stage plane bed occurs when high bed shear stress removes all the bedforms and sheet flow conditions prevail, whereas a lower stage plane bed occurs when deposition smooths the bed and the bed shear stress is too weak to create bedforms (Southard and Boguchwal, 1990; van den Berg and van Gelder, 1993b). Washed-out ripples and dunes are stable in the transitional regime from current ripples and dunes to sheet flow. Wash out is reflected in a reduction in bedform height (Baas, 1994;

Oost and Baas, 1994; Baas and De Koning, 1995). The same authors also found that washed-out ripples have the same length as their lower-velocity counterpart.

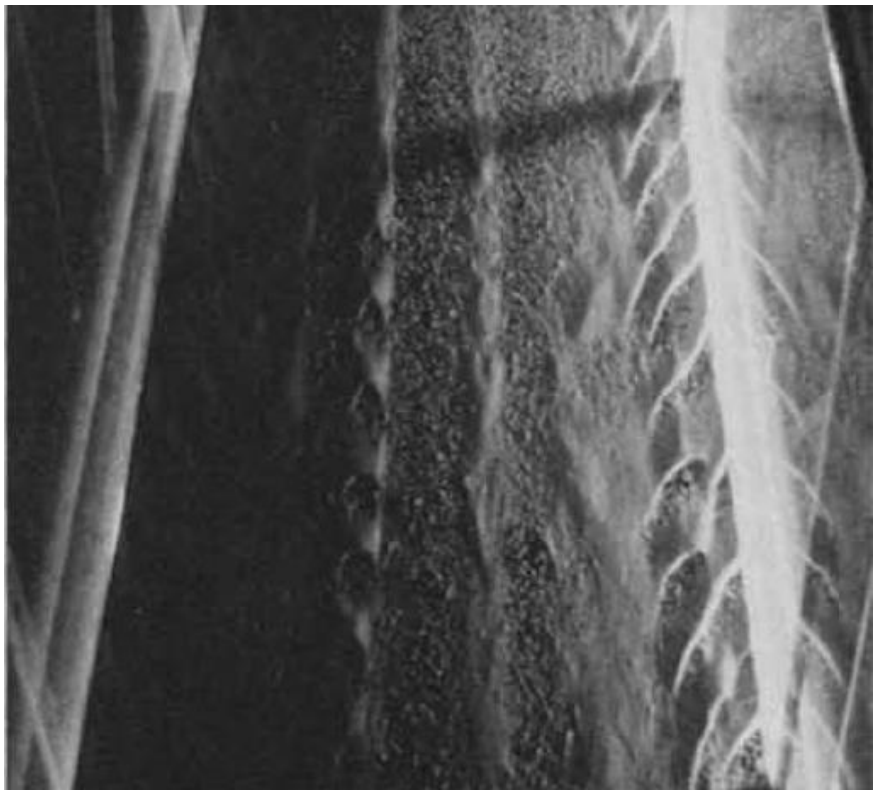

Figure 4-4: Sand ribbons in a 0.57-m wide laboratory flume. After McLean (1981).

4.4.1.6 Biogenic bedforms

Benthic organisms living on and in the sediment can modify the bed surface, for example by creating mounds and scour holes (Fries *et al.*, 1999; Passarelli *et al.*, 2014). Mounds created by benthic invertebrates can alter the flow, initiating ripple formation (Fries *et al.*, 1999). However, bioturbation can also flatten bedforms (Grant and Daborn, 1994; Amos *et al.*, 1988b; Soulsby *et al.*, 2012). These competing processes are specific to the site, the composition of the benthic ecosystem, and the sediment dynamical processes, and may change seasonally and interannually (Passarelli *et al.*, 2014).

4.4.2 Classification of the dimensionality of the plan morphology of bedforms

Bedforms may have 2D and 3D planforms, depending on the strength and duration of current forcing and wave forcing, and water depth (Allen, 1968; Baas *et al*., 1993; Baas, 1999; Venditti *et al*., 2005). As mentioned above, current ripples are linguoid at equilibrium, and current ripples with straight or sinuous crests are non-equilibrium bedforms (Baas *et al*., 1993). Waves predominantly produce

symmetrical straight-crested ripples, with sharp peaks, normal to the direction of wave propagation (Amos, 1988b). Figure 4-5 shows a dimensionality classification scheme of the plan morphology of bedforms, proposed by Perillo *et al.* (2014). Two-dimensional (2D) bedforms have straight and continuous crestlines, whereas 2.5D bedforms show either straight and discontinuous crestlines, or sinuous and continuous crestlines. Three-dimensional (3D) bedforms exhibit curved and discontinuous crestlines (Perillo *et al*, 2014). Because bedforms change in dimensionality with time (Figure 4-1), as they progress towards equilibrium dimensions, this visual classification is a useful first step in understanding bed development stage under field conditions.

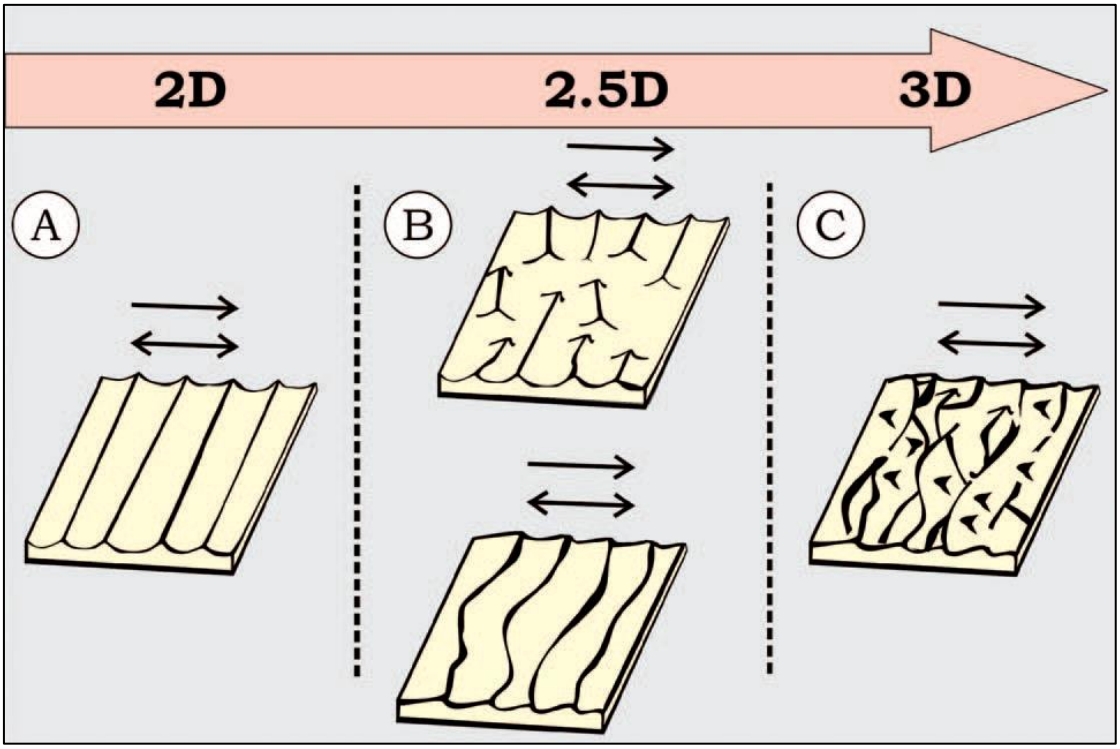

Figure 4-5: Dimensionality classification of bedform plan morphology according to Perillo *et al*. (2014).

4.4.3 Bedform phase diagrams

Bed phase is the term used to describe the stable morphological state of the bed within a certain range of hydrodynamic conditions and sediment types (Southard, 1991; Kleinhans, 2005). Bedform phase diagrams are useful in determining the bedforms likely to be present in known flow conditions, or to determine the possible flow conditions at which relict bedforms were created (Kleinhans, 2005). Using the skin-friction Shields parameter in bedform phase diagrams reduces the effect of the water depth,

as this is accounted for in the bed shear stress, compared to using the flow velocity (Southard, 1991; van den Berg & van Gelder, 1993).

4.4.3.1 Current-generated bedforms

Phase diagrams for current-generated bedforms use grain size and current flow (mostly current velocity or skin-friction bed shear stress) to delineate different types of bedform (Southard and Boguchwal, 1990; Southard, 1991; van den Berg and van Gelder, 1993b). With increasing water depth, the phase boundaries shift upwards to higher Shields stress values (Southard, 1991). Figure 4-6 shows the current-generated bedform phase diagram of van den Berg and van Gelder (1993).

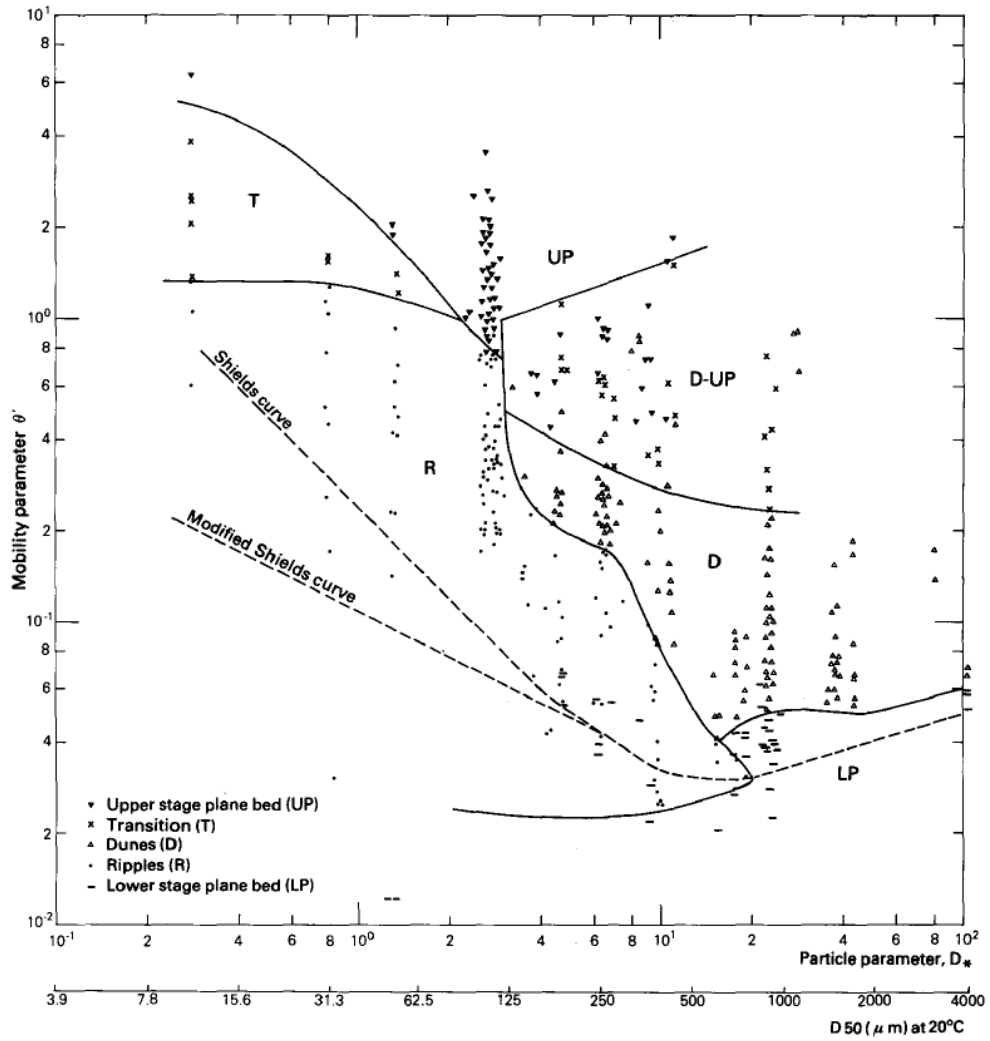

Figure 4-6: Current-generated bedform phases defined by skin-friction Shields mobility parameter, θ', and grain size (median grain size, D_{50} and dimensionless grain size, D_*). Shields curves for the threshold of sediment motion are also shown.

4.4.3.2 Wave ripples

As for current-generated bedforms, wave-generated ripples can be classified using phase diagrams. The following parameters have been used: near-bed amplitude orbital velocity, wave bed shear stress, wave orbital diameter, bedform length, bedform steepness and grain size (Allen, 1982; Clifton and Dingler, 1984; Southard, 1991; Wiberg and Harris, 1994; Traykovski, 1999; Kleinhans, 2005). Phase diagrams for wave-generated bedforms that use near-bed amplitude orbital velocity, or wave bed shear stress, and grain size compare best to phase diagrams for current-generated bedforms, and classify the bedforms into no motion, wave ripples and plane bed (Allen, 1982; Kleinhans, 2005). Wave orbital diameter, bedform length, and grain size can be used to classify wave ripples into three classes: orbital ripples that scale with the wave orbital excursion; anorbital ripples that scale with the grain size; suborbital ripples that scale with both the wave orbital diameter and sediment grain size (Clifton and Dingler, 1984).

4.4.3.3 Bedforms in combined waves and currents

Combined-flow bedforms can be defined according to the relative influence of wave and current forcing (Amos *et al*., 1988b; Li and Amos, 1998; Kleinhans, 2005; Dumas *et al*., 2005; Perillo *et al*. 2014). Kleinhans (2005) created a wave-current bedform phase diagram that summarises existing knowledge of bedform types between the critical threshold of sediment motion and sheet flow (Figure 4-7).

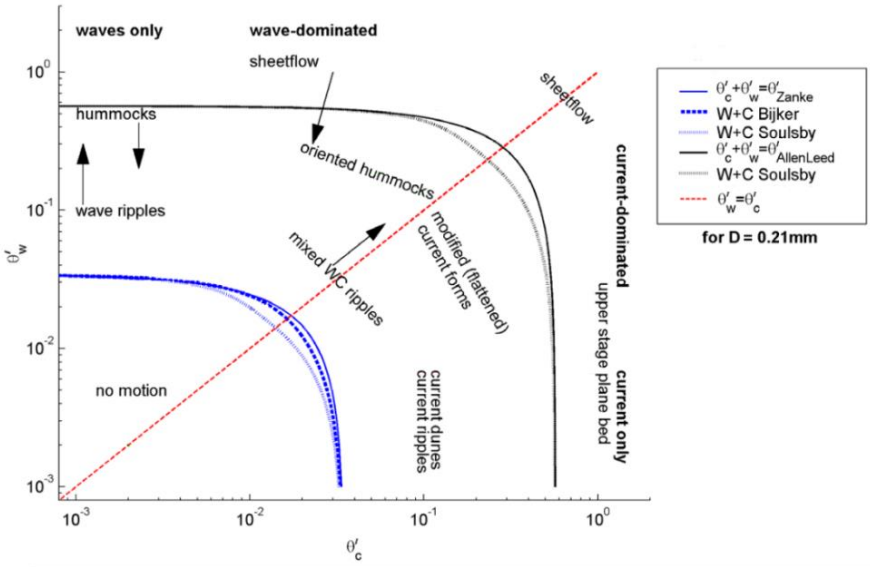

Figure 4-7: Wave-current bedform phase diagram using skin-friction Shields mobility parameter, θ', for currents and waves. The critical threshold for sediment motion of Zanke (2003), Bijker (in Soulsby, 1997) and Soulsby (1997) are shown in blue, and the limits for sheet flow of Allen and Leeder (1980) and Soulsby (1997) are shown in black. The red dashed line indicates the line of equal wave and current stress. (Modified from Kleinhans, 2005; after Amos *et al.*, 1988b)

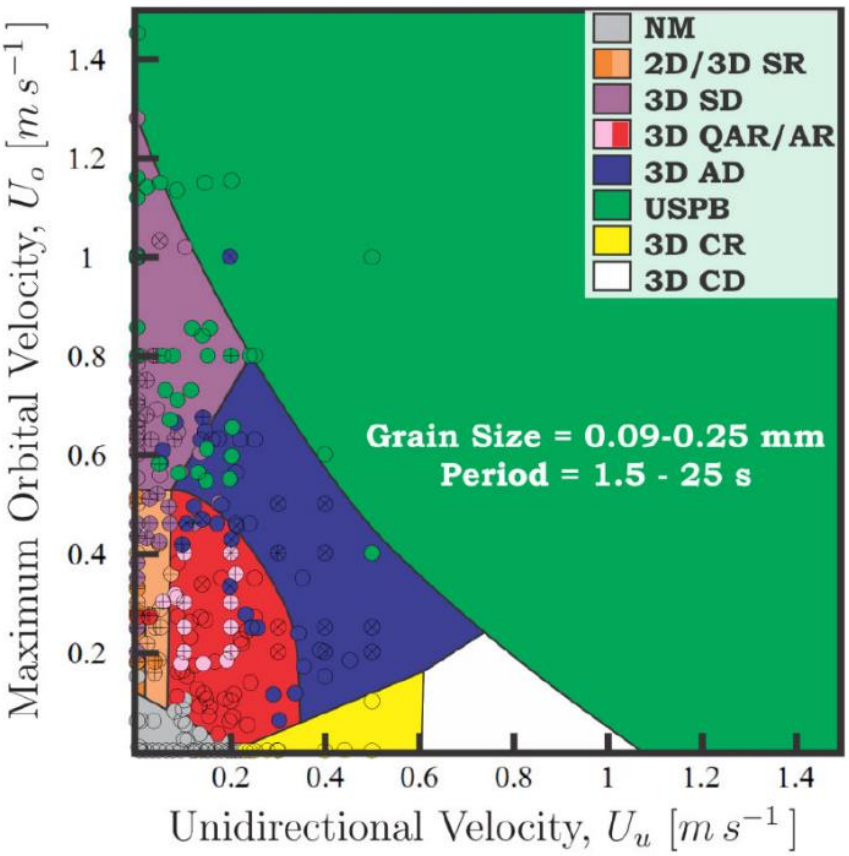

Figure 4-8: Bedform phase diagram for combined currents and waves (Perillo, 2013; Perillo *et al.* 2014). Data from flume experiments are shown for comparison (Arnott and Southard, 1990; Yokokawa, 1995; Amos *et al*. 1988b; Dumas *et al*., 2005; Sekiguchi and Yokokawa, 2008; Pedocchi, 2009; and Perillo *et al*., 2013). +, x and * signs represent symmetrical, rounded, and two-dimensional (2D) bedforms, respectively. Plain circles are asymmetric and three-dimensional (3D) bedforms. NM – no motion, SR – symmetrical ripples, SD – symmetrical dunes, QAR – quasi-asymmetrical ripples, AR – asymmetrical ripples, AD – asymmetrical dunes, USPB – upper stage plan bed (sheet flow), CR – current ripples, and CD – current dunes. (n = 264).

More recently, Perillo *et al*. (2014) created a wave-current bedform phase diagram from existing data and new measurements, based on free-stream current velocity and maximum near-bed orbital velocity (Figure 4-8). Perillo *et al*. (2014) differentiated ripples from dunes using a height of 0.05 m and a length of 0.5 m. The lee-stoss length symmetry ratio (Bedform Symmetry Index, BSI) was used to define the following classes: BSI < 1.3, symmetrical (S) bedform; *c.* 1.3 < BSI < 1.5, quasi-symmetrical bedform; and BSI > 1.5, asymmetrical bedform (Perillo *et al*., 2014). Current ripples were further defined by a maximum near-bed orbital velocity < 0.15 m s^{-1} and a unidirectional current velocity < 0.6 m s^{-1} (Perillo, 2013).

The above bedform phase diagrams are only valid for conditions where the waves and current are closely aligned. When the wave-current angle is high, more complicated morphologies, such as superimposed bedforms, develop (Amos *et al.*, 1988b). In the present study, visually classified bedforms in the 3D-ARP images collected in the mixed sand-mud are compared with the predicted bedforms in the wave-current bedform phase diagrams.

4.4.4 Bedform predictors

Bedform predictors are empirical equations that relate the size of bedforms to hydrodynamic forcing and sediment properties, based on laboratory and field data. So far, few predictors have considered transitional bedform types, such as across the transition from current ripples to dunes, ripples formed by combined wave-current flow, and washed-out bedforms (Baas and De Koning, 1995; Kleinhans, 2005; Soulsby and Whitehouse, 2005b; Soulsby *et al.*, 2012; Bartholdy *et al.*, 2015). Bedform predictors are only valid for bedforms that are in equilibrium with hydrodynamic conditions, and bedforms present on the seabed while flow strength is below the threshold of sediment motion must be relics of the previous forcing conditions that were able to move the bed sediment (Traykovski, 2007; Soulsby, 2012). In combined flows, threshold values for wave and current forcing have been used to determine if a wave or current ripple predictor should be applied (Li & Amos, 1998; Soulsby *et al*. 2012). In the present study, a selection of widely used bedform predictors was made for comparison with the field data from the Hilbre tidal flats (Soulsby 1997; Soulsby *et al*. 2012; Aldridge *et al*., 2015; Parsons *et al*., 2016).

4.4.4.1 Current ripples

Current ripples scale with the sediment size on the seabed (Soulsby, 1997). Current ripple height, η, and length, λ, can be predicted from the median grain diameter, D_{50}, and the dimensionless grain parameter, D_*, by means of the following empirical relationships (Soulsby *et al.*, 2012):

$$\eta = D_{50} 202 D_*^{-0.554}$$

$$\lambda = D_{50}(500 + 1881 D_*^{-1.5})$$

4-1

for $1.2 < D_* < 16$, where $D_* = D_{50}(g(s-1)/\nu^2)^{1/3}$, ν is the temperature-dependent kinematic viscosity of water ($\nu = 1\times10^{-6}$ m^2 s^{-1} at 20°C), $s = \rho_s/\rho$ is the relative density of the sediment, ρ_s is taken to be the density of quartz, 2650 kg m^{-3}, and ρ is the density of seawater, nominally 1023 kg m^{-3}. The equilibrium

ripple height of 0.017 m and length of 0.141 m for D_{50} = 238 µm, as measured by Baas (1999), were used in this study as an additional check.

4.4.4.2 Dunes

The dune predictors of Yalin (1964; in Soulsby, 1997) and van Rijn (1984c) were derived from laboratory flume and river studies. Dune length was found to scale with water depth, whereas dune height was found to scale with bed shear stress and water depth. According to van Rijn (1984c), dune height also scales with the median grain diameter.

Yalin's (1964 in Soulsby, 1997) predictor for dune height and length is:

$$\eta = \frac{h}{6}(1 - \frac{\tau_{cr}}{\tau})$$

$$\lambda = 2\pi h$$

$$for \quad \tau_{cr} < \tau < 17.6\tau_{cr}$$

4-2

where h is the water depth, τ is the skin-friction bed shear stress, and τ_{cr} is the critical skin-friction bed shear stress for sediment motion.

Van Rijn's (1984c) predictor for dune height and length is:

$$\eta = 0.11h(D_{50}/h)^{0.3}\ (1 - e^{-0.5T_s})(25 - T_s)$$

$$\lambda = 7.3h$$

$$for \quad \tau_{cr} < \tau < 26\tau_{cr}$$

4-3

4.4.4.3 Wave ripples

Wave ripples scale with the near-bed orbital diameter, d_0, and the median grain diameter, D_{50} (Wiberg & Harris 1994; Soulsby *et al*. 2012). Soulsby *et al*.'s (2012) predictor for wave ripple length, λ, and height, η, is:

$$\lambda = \frac{1}{2}d_0 \times \left[1 + 0.935 \times 10^{-3} \frac{d_0}{D_{50}} \left(1 - \exp\left\{-\left(\frac{d_0}{D_{50}} \times 10^{-4}\right)^{1.5}\right\}\right)\right]^{-1}$$

$$\eta = \lambda \times 0.15 \left[1 - \exp\left\{-\left(\frac{2500 D_{50}}{d_0}\right)^{3.5}\right\}\right]$$

4-4

Malarkey and Davies' (2003) non-iterative version of the Wiberg & Harris' (1994) predictor for the length and height of orbital, sub-orbital, and anorbital wave ripples is (from top to bottom):

$$\frac{d_o}{\lambda} = \begin{cases} \dfrac{1}{0.62} & \dfrac{d_o}{\eta_{ano}} < 20 \\ \dfrac{d_o}{535 D_{50}} e^{f(d_0/\eta_{ano})} & 20 \leq \dfrac{d_o}{\eta_{ano}} \leq 100 \\ \dfrac{d_o}{535 D_{50}} & \dfrac{d_o}{\eta_{ano}} > 100 \end{cases}$$

$$\frac{d_o}{\eta} = exp\left[B_2 - \sqrt{B_3 - B_1 ln\left(\frac{d_o}{\lambda}\right)}\right]$$

4-5

where $B_1 = 1/A_1$, $B_2 = 0.5(1+A_2)$, $B_3 = B_2^2 - A_3 B_1$, $A_1 = 0.095$, $A_2 = 0.442$, $A_3 = 2.28$, $f(d_0/\eta_{ano}) = \ln(0.62 d_0/535 D_{50}) \ln(0.01 d_0/\eta_{ano})/\ln 5$, and d_0/η_{ano} is given by d_0/η, with $d_0/\lambda = d_0/535 D_{50}$.

4.4.5 Multiple linear regression methods for bedform characteristics

Multiple linear regression creates a model with more than one independent parameter. Interactions between parameters can be accounted for by creating a separate new parameter of the product of the primary parameters involved, allowing the modelling of processes that require multiple factors (*e.g.* wave-current stress enhancement). For large data sets, it may not be obvious which parameters or interactions between parameters are of significance to a process. Stepwise multiple linear regression can be used to automatically test parameters for significance in a regression, then add parameters to or reject parameters from the model, based on a limit of significance. Therefore, a large

data set can be reduced to a few key parameters without prior knowledge. However, the results should be interpreted with physical processes and limitations of the data in mind. The relative influence of the independent parameters on the dependent parameter can be determined by dividing the coefficients by their standard errors (t-statistic), and comparing the magnitude of these values (Borradaile, 2003). In this study, stepwise multiple linear regression was used to analyse the factors and processes that influence the bedform dimensions.

Logistic regression is a multiple linear regression method that creates a regression fit of continuous data to discrete classes, relative to a reference class. The resulting relationship is for the probability that a particular combination of values results in the membership of a class. This method was used here to analyse the relationship between the continuous field data and the visual classification of bedform dimensionality.

4.5 Methods

4.5.1 Field measurements

The background to the field site and details of the instrumentation deployed were described in Chapter 3; a brief overview is given here. Three sites on the intertidal flats near West Kirby were selected in order to cover a range of mixtures of sand and mud. These sites were studied over a spring-neap cycle in May and June 2013. This chapter uses the hydrodynamic data collected using an Acoustic Doppler Velocimeter (ADV), the seabed topography data provided by a 3D Acoustic Ripple Profiler (3D-ARP), and the results of the bed samples analysed for cohesive clay and biological content (Chapter 3). A Conductivity, Temperature and Density (CTD) system provided data for the water properties, density and kinematic viscosity.

During the deployment at Site 1, 21-24 May 2013, waves dominated as neap tide progressed towards spring tide. The period at Site 2, 24-29 May 2013, was dominated by currents, as the tide progressed to and across the peak of spring tide. During the deployment at Site 3, 29 May to 4 June 2013, the maximum current strength reduced towards neap tide. The three sites were within 140 m of each other, differing in bed elevation by 0.2 m. Here, the sites are considered temporally, as part of a continuous deployment record, with tide, wind and wave forcing varying over the record covering a spring-neap cycle from neap tide to neap tide.

4.5.1.1 Manual measurements during the exposure of the tidal flats

Bed sediment samples were collected during exposure at low slack water from the top 1-2 cm below the crests and troughs of the bedforms within 1 m of the SEDbed frame. Fourteen samples in total were collected and analysed for clay, silt and sand volume fractions, using a Malvern 2000 Laser Particle Sizer. The average median grain size, D_{50}, for all the bed samples was 227 µm. The bed clay content values were then converted to percentage cohesive clay content using XRD data, resulting in cohesive clay content values in the range of 0.6 to 5.4 vol% (see section 3.9).

A separate set of bed samples was collected and analysed for both particle size and biological cohesive material, Extracellular Polymeric Substances (EPS), showing a linear relationship between cohesive clay content and EPS (see section 3.9.4). As the effects of physical and biological cohesion cannot be separated for this data set, the cohesive clay content is considered a measure of total cohesion.

Each day, the bedforms were photographed with a tape measure or ruler to provide scale. The photographs also documented the presence of biological organisms, mainly burrow holes and cast mounds.

4.5.1.2 Matching the hydrodynamics to changing bedforms

To assess the temporal changes in bedform dimensions, the wave and current data from the ADV were matched to the 3D-ARP scans. Each 3D-ARP scan took about 12 minutes to collect. The ADV data were processed for a fifteen-minute window, at a one-minute interval, for the current and wave parameters (see section 3.8.1). The ADV data were then matched to the mid-point of the 3D-ARP scan period.

It is assumed that the ADV data are representative of the hydrodynamic forcing during the scan period. Moreover, it is assumed that the lag between forcing and bedform response is small, and therefore the bedforms are close to equilibrium with the flow, unless there is clear evidence for the opposite, such as for relict bedforms associated with very low wave and current forcing. The time taken for bedforms to adjust to flow conditions is in the order of ten minutes to weeks, depending on the strength of the flow forcing (Baas, 1994; Baas, 1999; Traykovski *et al*., 1999; Kleinhans, 2005) and with addition of cohesive material this might further increase (Baas *et al*., 2013). Due to the temporal resolution of the 3D-ARP and the constantly changing conditions, the effect of hysteresis on the bedforms cannot be quantified. However, bedforms observed at bed shear stress below the threshold of sediment motion can be considered relics of previous flow conditions. Most of the data analysis below excludes relict bedforms.

4.5.2 Determining the bedform dimensions

Large-scale bed morphology was removed from the 3D-ARP scans using a linear fit. The 3D-ARP scans were corrected for the bedform orientation relative to the frame using a Radon transform and matrix rotation, before the zero-crossing method was used to calculate the bedform height, length and symmetry (Jafari-Khouzani and Soltanian-Zadeh, 2005; van der Mark *et al.*, 2008; Bell, 2016). The zero-crossing method was chosen to determine the bedform dimensions, as it works well on short record lengths and can be easily automated.

4.5.3 Bedform classification

Based on the work of Allen (1968, 1982), Reineck & Singh (1980), Reddering (1987), Amos *et al*. (1988b), and Andersen and Faraci (2003), a set of descriptors was used to classify the planform of the bedforms in the 3D-ARP scans (Table 4-1). These classes are based on visual observations in flumes, in shallow water, on exposed tidal flats, and in sub-tidal areas by means of autonomous cameras.

As the 3D-ARP has a comparatively low spatial resolution, 5x5 mm, small features cannot be discerned and bedform symmetry is difficult to determine visually. Superposition of, for example, current ripples and wave ripples, is also difficult to determine. High bed shear stress may cause bedforms to move quickly and change type rapidly within the time taken to collect a scan, and this can cause the 3D-ARP scans to look blurred. Rotating flow can cause features to spiral in the 3D-ARP images. Scans collected around high slack water, when the current stress is low, may show relict current-generated bedforms, and there can be ambiguity in the classification of linguoid and lunate bedforms upon switching of the direction of tide from flood to ebb (Figure 2-9).

Allen (1982) used the term ‘tiled’ to describe interference ripple patterns created by sets of waves with different propagation directions. These tiled ripples have crestlines that surround a central trough. Ladder-back ripples form in combined flows, with smaller ripples forming at an oblique angle to larger bedforms (Reddering, 1987; Ramsay *et al*., 1989). Andersen and Faraci (2003) used the term ‘segmented’ for ripples that have discontinuous crestlines, because the wave direction is at an angle with the current direction. Here, the definition of ‘segmented’ bedforms is extended and generalised to bedforms that are formed or modified by flows from different directions, non-parallel waves and currents, rotating tidal currents, and veering wave directions. The segmented bedform class includes ladder-back and tiled ripples (Allen, 1982; Reddering, 1987).

Table 4-1: Bedform classification scheme.

Type	Symmetry	Juncture	Dimensionality
straight	asymmetric	open	2D
sinuous	symmetric	zig-zag	2D/3D
catenary		buttress	3D
cuspate			
lunate			
linguoid			
Segmented			
Sand ribbons			
flat bed/washed-out			

For the bedform classification, the 3D-ARP data were reprocessed to create images of 1.4 by 1.08 m. This widened the area of analysis, but also introduced more artefacts in the data. The full area of the 3D-ARP scans included the frame, scour pits at the base of the frame, and shadowing at the extremes of the scan. The scans were also colour-scaled separately, for bed height, to make features easier to discern. Some images were contrast-enhanced manually, using photo editor software (Corel photo-paint X5), to aid with interpretation.

The dimensionality of the bedforms was categorised into thee classes: 2D (straight, continuous crestlines), 2.5D (sinuous and continuous crestlines or discontinuous and straight crestlines), and 3D (curved and discontinuous crestlines) (Section 4.4.2; Perillo *et al*. 2014).

4.5.4 Logistic regression of the bedform planform dimensionality

Binominal logistic regression was used to analyse the origin of 2D, 2.5D, and 3D bedforms in terms of the following key factors: current forcing, wave forcing, and bed cohesive clay content. Binominal logistic linear regression relates the continuous hydrodynamic and cohesive clay data to the discrete bedform dimensionality data. The resulting regression equation gives the probability of sets of measurements producing 3D bedforms versus 2D bedforms, from zero to one.

The effect of cohesive clay content is of primary interest in this study. As the bed sediment at all the sites was composed of mixed sand-clay, the 238 µm sand data of Baas *et al*. (2000) were added to the

present data set to provide a control for clean-sand 3D linguoid current ripples (number of data points, n = 7). In the analysis, only data with a combined skin-friction related Shields parameter (θ'_{max}) above the threshold of sediment motion (Soulsby, 1997) were included, in order to reduce the effect of relict bedforms. Bedforms classified as 2.5D were excluded from the regression model (leaving n = 114), because this approach simplifies the problem to a binominal analysis, instead of ordered multinomial regression analysis. Instead, the 2.5D bedforms were used as an independent comparison to the model results. The parameters used in the regression analysis were current skin-friction Shields parameter, θ'_c, wave skin-friction Shields parameter, θ'_w, water depth, h, wave-current angle, φ, and vol% cohesive clay content, c. These parameters were considered to be the main controls on the variation in bedform plan morphology (Section 4.4.1). Interactions between the current, wave and cohesive clay content parameters were not included in the regression analysis, in order to simplify the interpretations.

4.5.5 Stepwise regression of the bedform dimensions

Existing bedform predictors are based on empirical studies of sediment movement and hydrodynamics, and tend to be limited to single classes of bedform for a fixed water depth, *e.g.* current ripples, wave ripples or dunes (Soulsby and Whitehouse, 2005a,b). Using the stepwise multiple linear regression method, the key factors that affect the bedform dimensions in the field data can be determined based on the variance in the data, without reference to existing classification boundaries. In this way, the continuous transition of bedform dimensions with the variance of different forcing parameters can be studied.

The 238 μm sand data of Baas *et al*. (2000) were added to the data set to provide values for clean sand ripples (n = 7), as the field data contained clay in all the measurements. A sub-set of the field data was extracted for combined Shields stress above the threshold of motion (n = 121), in order to reduce the effects of relict bedforms that do not have a relationship to the magnitude of forcing at the time of measurement. In total, the combined data set contained 128 records.

Stepwise multiple linear regression was applied separately to the bedform height and length data. The parameters used in the stepwise regression were current skin-friction Shields parameter, θ'_c, wave skin-friction Shields parameter, θ'_w, water depth, h, wave-current angle, φ, near-bed orbital amplitude velocity, u_w, wave period, T, near-bed orbital excursion, d_o, median grain size, D_{50}, and dimensionless grain size, D_*. Interaction parameters were created by multiplying pairs of primary parameters, *e.g.* $\theta'_c \times \theta'_w$ for wave-current stress enhancement. Squares of the primary parameters

were also added. These interaction and squared parameters were included to determine the effects of secondary and non-linear processes on the bedform dimensions. The wave-current angle, φ, is in the range 0-90°, as the wave forcing is bidirectional. The parameters are based on the wave height and period without velocity asymmetry, and the effect assumed to be symmetrical for the two hemispheres of the 3D-ARP. In total, a set of 55 parameters was tested derived from the nine primary parameters.

The stepwise process starts with a constant model (*i.e.* a single constant parameter or intercept) and individually tests the parameters, one by one, adding and removing parameters to and from the model. After experimentation, a p-value < 0.05, or 95% significance, was set for the limit of inclusion in the model and p > 0.051 for rejection, for an F-test of the change in the sum of squared error by adding or removing the parameter. The overall model was tested to a limit of p-value < 0.05 or 95% significance.

4.6 Results

4.6.1 Flow forcing and bedform dimensions

The deployment period covered a tidal cycle from neap to spring to neap, and a range of different hydrodynamic and wave conditions (Figure 4-9). Twenty-seven separate periods of tidal inundation of the flats were measured from 21 May – 4 June 2013. North-westerly winds dominated 21-25 May, with wind conditions from moderate breezes up to gale force (Beaufort scale 4-8; 5.8 - 17.6 m s^{-1}). These high winds caused wave height and near-bed orbital amplitude to increase (Figure 4-9c,e), modulated by the depth of the tidal flows (Brown, 2010; Friedrichs, 2011).

The bed shear stress for current, waves, and combined waves and currents were calculated from the hydrodynamic data (Figure 4-10a-c). The mean bedform heights and lengths, for each 3D-ARP scan, are shown in Figure 4-10d,e, with current ripple height and length predictions of Baas (1999) and Soulsby *et al*. (2012) shown for comparison (section 4.4.4.1). The standard deviation of the bedform heights and lengths were in the range 0.002 to 0.014 m, and 0.042 to 0.114 m, respectively. Soulsby *et al.*'s (2012) predictors for equilibrium current ripple dimensions, for D_{50} = 227 µm, result in a height, η_{eq}, = 0.019 m, and length, λ_{eq}, = 0.153 m. Baas' (1999) equilibrium ripple heights and lengths for D_{50} = 238 µm were η_{eq}, = 0.017 m and λ_{eq}, = 0.141 m, respectively. The current ripple predictors highlight how the field data deviates from expected equilibrium ripple dimensions (Figure 4-10d,e). However, all the measured bedforms fall within the size limits for current ripples, and dunes would not be expected (*cf.* Section 4.4.1). In the sections below, the reasons why the bedform heights and lengths

deviate from the predicted dimensions, especially for Sites 1 and 2, are explored. These include: (1) the effect of wave forcing at Site 1, which may cause the bedforms to scale with wave bed shear stress, τ'_w, and water depth for the tidal periods 2 to 4 (Figure 4-10b,d); (2) potential wash-out of the bedforms at tidal periods 5 and 6; and (3) the dependence of the bedform dimensions on variations in water depth in the absence of strong wave forcing at Site 2, *e.g.* at tidal periods 8 to 10 (*cf.* Figure 4-9a and Figure 4-10d).

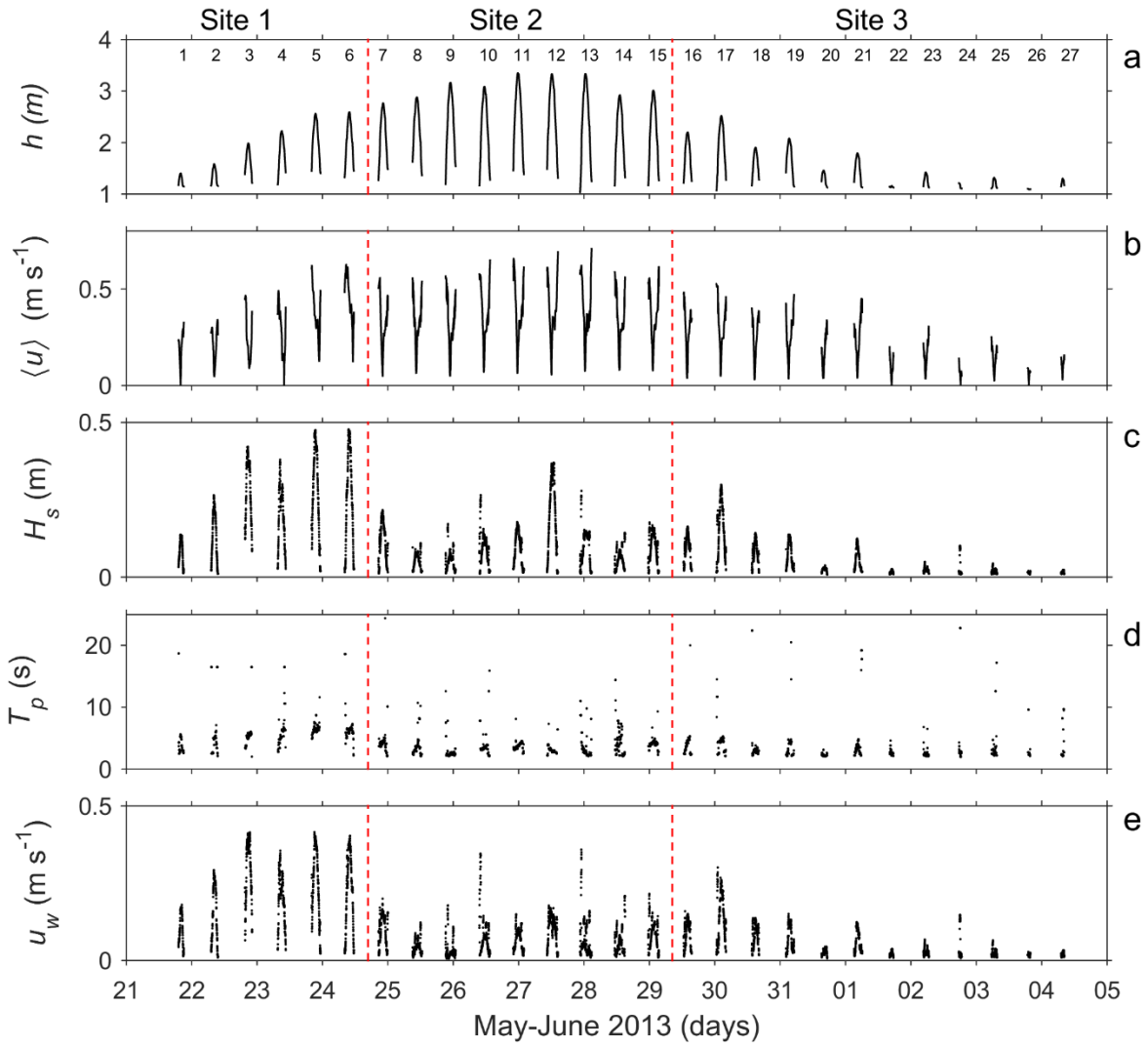

Figure 4-9: Times series of (a) water depth, h; (b) depth-averaged flow velocity (15 minute running mean), ⟨u⟩; (c) significant wave height, H_s; (d) peak wave period, T_p; and (e) near-bed orbital amplitude velocity, u_w. The vertical red dashed lines mark the times when the instruments were moved between sites. The data shown are for when the tidal flats were inundated with water above the height of the sensors, processed for a 15-minute window. The wave period data have been filtered to show only the wind-generated waves of periods less than 25 seconds (USACE, 2002a). The numbers in (a) denote the tidal periods for reference.

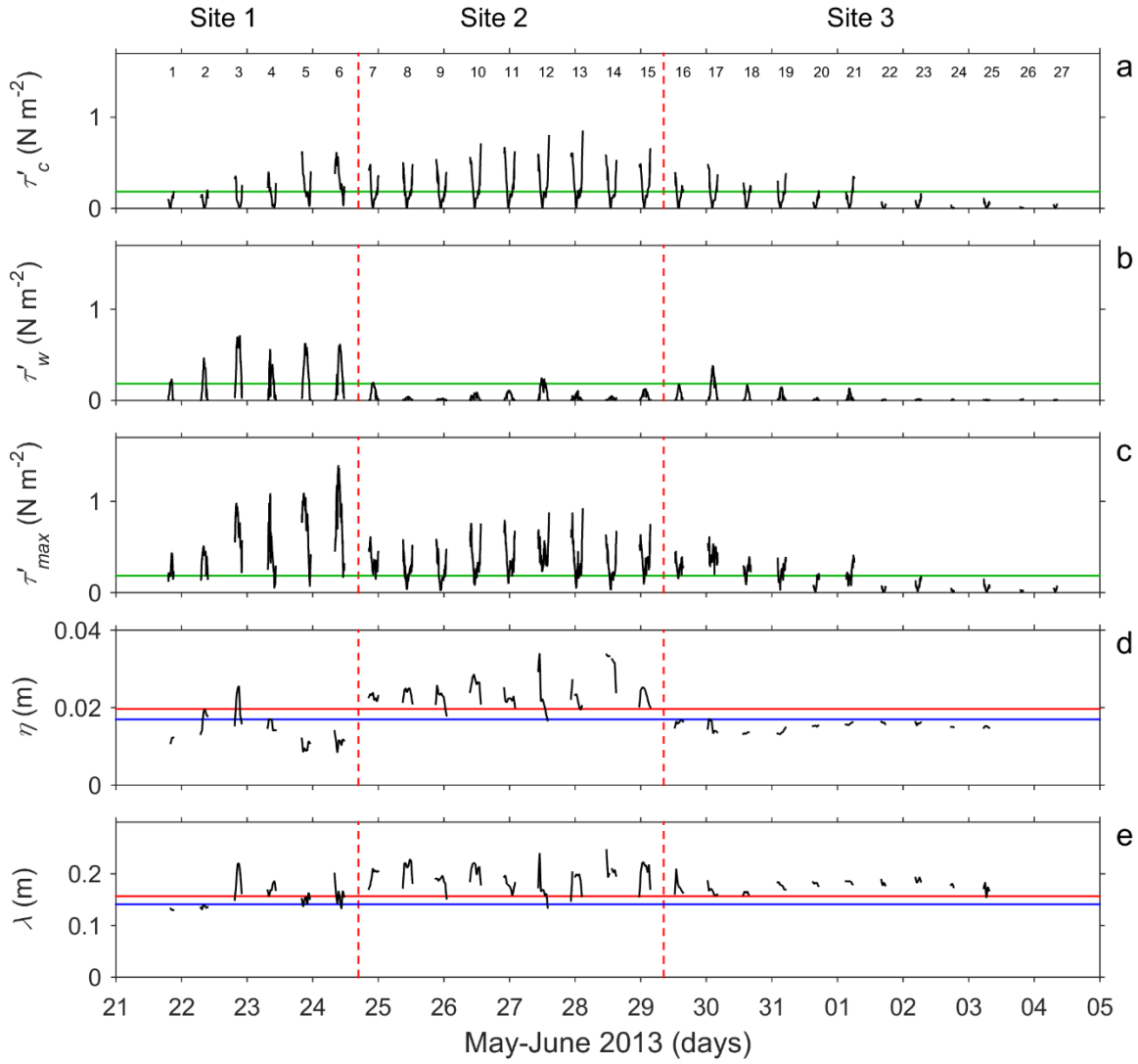

Figure 4-10: Times series of (a) current-only bed shear stress, τ'_c; (b) wave-only bed shear stress, τ'_w; (c) combined maximum bed shear stress, τ'_{max}; (d) bedform height, η; and (e) bedform length, λ. The vertical red dashed lines mark the times when the instruments were moved between sites. The horizontal green lines denote the critical stress threshold of sediment motion from Soulsby and Whitehouse's equation (Soulsby, 1997), for D_{50} = 227 µm, 0.18 N m^{-2}. The blue and red lines are the equilibrium ripple dimensions of Baas (1999) and Soulsby *et al.* (2012), respectively. The data shown are from when the tidal flats were inundated with water above the height of the sensors, processed for a 15-minute window. The numbers in (a) denote the tidal periods for reference.

A time-series of the direction of the current and waves, relative to North, is plotted in Figure 4-11. The current starts propagating easterly with the flood tide and then rotates to an ebb tide directed towards the west. The waves mainly head easterly, shifting towards the north slightly at Site 2, and then more to the south for Site 3, before weak forcing makes the direction more scattered. At Site 1, the current and wave angles were distinct, with waves constantly heading easterly while the current floods and ebbs. The orientation of the waves and currents at Sites 2 and 3 were similar to each other, with both current and wave angles varying over the tide. This shows that the assumption of linear, non-rotating, flow does not hold true (section 3.4.1). Although the 5-minute mean of the velocity in *x* and *y* were subtracted from the raw ADV velocities to remove the current signal and the Doppler effect of the current on wavelength was accounted for, there may be an effect of wave translation by the current. During the deployment at Site 1, strong winds dominate the wave direction and there is no correlation with the changing direction of tide (Figure 4-11 *cf*. Figure 3-11). However, during Site 2 and Site 3 the smaller waves, from lighter and more variable winds, could be affected by the stronger currents around spring tide. Towards the end of the record, when the wind is light and constantly veering in direction and the tide has progressed to neaps, there is little correlation between current and wave direction.

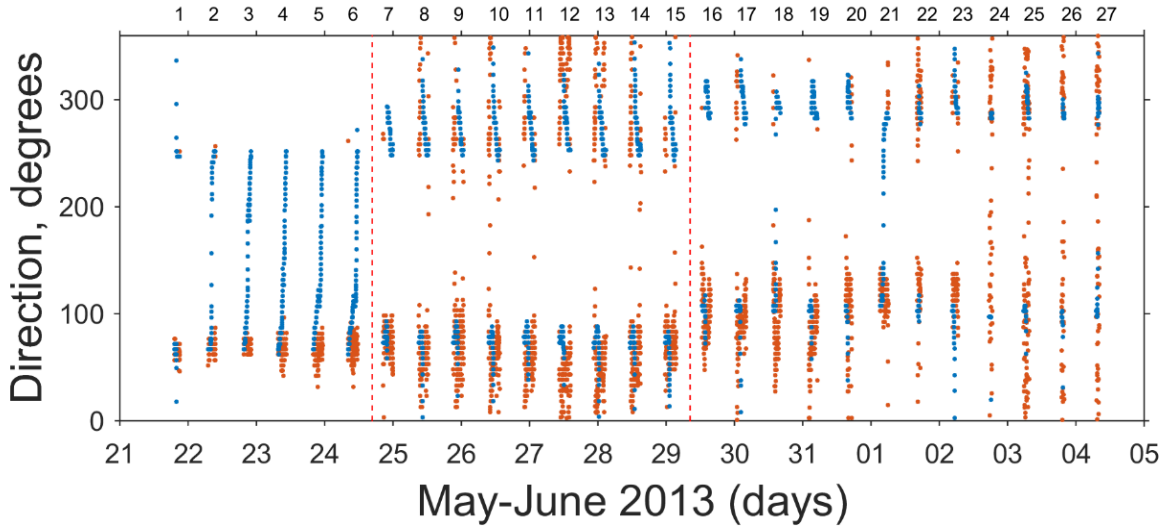

Figure 4-11: Current (blue) and wave (orange) direction in degrees (propagation towards the compass point).

4.6.1.1 Bedform symmetry

Waves usually produce symmetrical bedforms, whereas currents produce asymmetrical bedforms. The bedform symmetry index, the ratio of lee to stoss slope length (Figure 2-8), can be used to approximate the relative forcing of waves and currents. The field data shows mainly asymmetrical bedforms, suggesting that the effects of the wind-driven flow and tidal currents dominate (Figure

4-12). However, the change in dominance between currents and waves is shown by the trends in bedform symmetry within flood-ebb tidal periods, with the bedforms becoming more symmetrical towards high water, when the tidal current is weakest and wave forcing has a greater influence (Figure 4-12, *e.g.* tidal periods 9 and 10). Wind-driven flow can invert this trend by causing strong currents at high water (Figure 4-12, tidal periods 5 and 6). Overall, tidal current forcing was strongest at Sites 2 and 3, and wind-driven forces appeared strongest at the end of Site 1 (Figure 4-12).

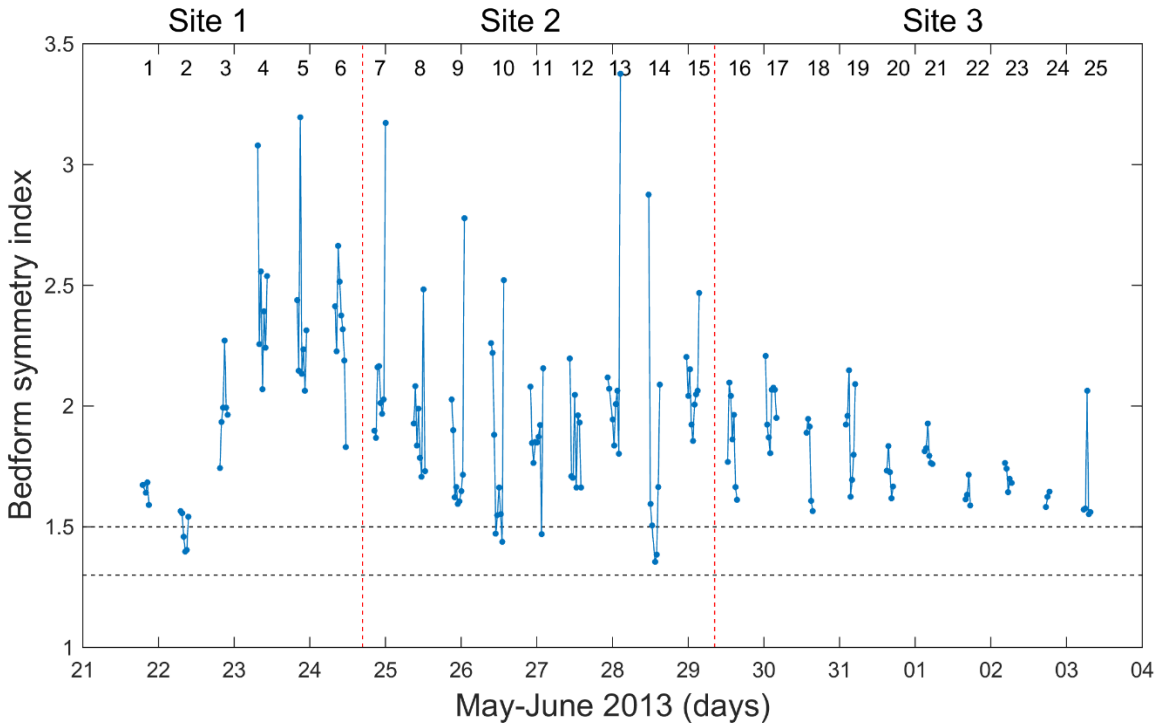

Figure 4-12: Bedform symmetry index against time. An asymmetry < 1.3 is considered symmetrical, 1.3-1.5 is quasi-asymmetric and > 1.5 asymmetric (Perillo *et al*., 2014). The vertical red dashed lines mark the times when the instruments were moved between sites. The numbers at the top denote the tidal periods for reference.

4.6.2 Bedform description and classification

In this section, the bedforms in the 3D-ARP scans are described and classified, using the scheme outlined in Section 4.5.3. The strength and direction of the current and wave bed shear stress, as well as the tidal range of the spring-neap cycle, were used to inform the classification. In addition, biological surface features are also highlighted. The bedform classes are then compared with the predicted bedform types in bedform phase diagrams in the Section 0.

4.6.2.1 Definition of bedform classes

Nine unique bedform types were identified in the 3D-ARP scans, but the bedforms were classified into 25 classes (Table 4-2), because multiple bedform types were present in several scans. The full classification of the scans is given in the appendices (section 8.4).

Table 4-2: Bedform classes determined based on the classification scheme outlined in Section 4.5.3, with the number of scans assigned to each class.

	Class	Count
1	sinuous/straight	10
2	sinuous	7
3	sinuous/straight/lunate	1
4	sinuous/lunate	2
5	sinuous/linguoid	1
6	linguoid/sinuous	1
7	sinuous/linguoid/lunate	7
8	sinuous/segmented/linguoid/lunate	2
9	sinuous/linguoid/lunate/segmented	5
10	sinuous/segmented	66
11	segmented/sinuous	4
12	segmented	7
13	segmented/linguoid/lunate	3
14	lunate	7
15	linguoid/lunate	2
16	linguoid/lunate/segmented	12
17	linguoid/lunate/segmented/sinuous	8
18	sinuous/sand ribbons	2
19	lunate/sand ribbons	1
20	lunate/washed-out	1
21	segmented/washed-out/sand ribbons	1
22	washed-out/sinuous	2
23	washed-out/sinuous/segmented	3
24	washed-out/sand ribbons	4
25	washed-out	2
	unclassified	8
	Total number of scans	169

For practical purposes, the number of bedform classes was reduced from 25 to 6, based on the dominant bedforms present in each scan and the numbers in each class (Table 4-3). This facilitated further analysis, in particular the comparison with bedform types in phase diagrams and subsequent statistical analysis. Table 4-3 shows that each merged class has at least 10 members, and all six classes are composed of the primary bedform types described in Section 4.5.3 (*cf.* Table 4-1).

Table 4-3: Merged classes from Table 4-2, with the number of scans assigned to each class.

	Class	Count	Example shown in Figure
1	sinuous/straight	18	Figure 4-13, Figure 4-14
2	sinuous/segmented	68	Figure 4-20
3	sinuous/linguoid/lunate	17	Figure 4-21
4	linguoid/lunate	32	Figure 4-15
5	segmented	15	Figure 4-16, Figure 4-23
6	washed-out	11	Figure 4-17, Figure 4-18
	unclassified	8	
	Total number of scans	169	

4.6.2.2 Site 1 description

The record at Site 1 starts on 21 May 2013, 19:00, at neap tide. Two-dimensional bedforms dominated tidal periods 1 and 2. In tidal period 1, these bedforms resemble wave ripples with long and weakly sinuous crestlines, crestline junctions, and relatively low symmetry index values (Figure 4-13; *cf*. Figure 4-12). Given that the wave and current forcing was weak during tidal periods 1, these bedforms are interpreted as relict. For tidal period 2, increasing tidal range progressing towards spring tide allows waves to grow and wave forcing has a greater influence, resulting in wave-dominated bedforms also with long and weakly sinuous crestlines, crestline junctions, and relatively low symmetry index values (Figure 4-14).

The wave stress reached a maximum value in tidal period 3, with a combination of high winds and a water depth allowing the waves to grow to nearly 0.5 m in height at high water and strongly affect the seabed (Figure 4-9a and Figure 4-10b). Initially during tidal period 3, currents dominate starting with more sinuous/straight bedforms, then progressing to lunate bedforms (Figure 4-15), that become reworked by wave stress at high water into more sinuous and segmented forms. The direction of oscillatory flow at this stage in tidal period 3 was parallel to the current direction, which should have

promoted the formation of the lunate shapes. As the tide turns and rotates at peak high water, when the current is at its weakest, the lunate bedforms are reworked by the strong wave stress, producing sinuous and segmented bedforms (Figure 4-16). The bedforms in tidal period 4 followed a similar pattern to tidal period 3, in that straight/sinuous current ripples developed into lunate forms and finally into segmented forms, with the influence of waves.

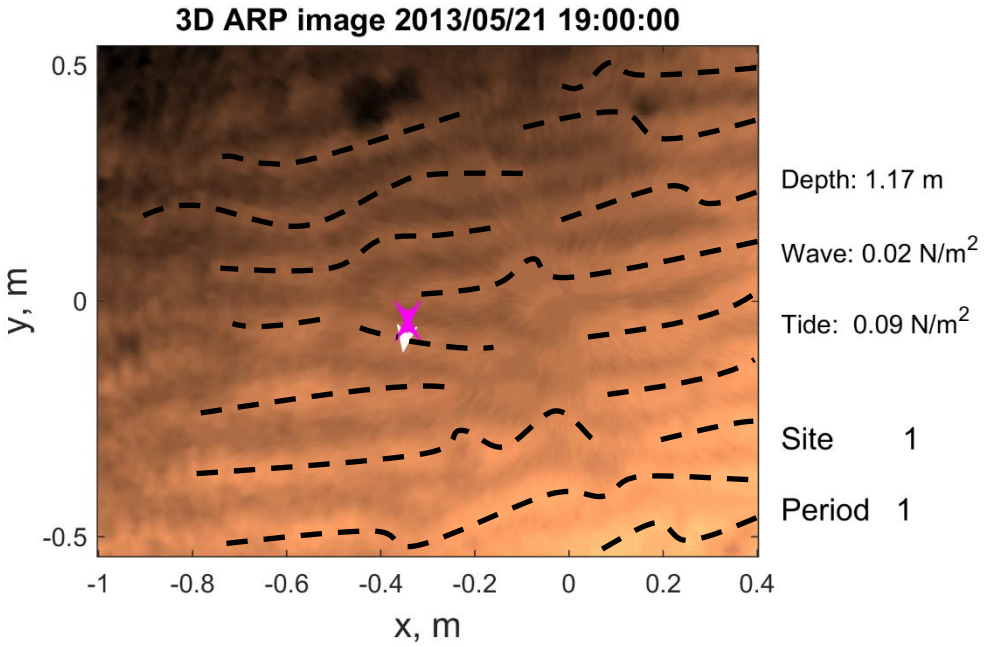

Figure 4-13: Sinuous/straight ripples with open juncture. Tidal period 1, Site 1. Black dashed lines highlight the bedform crestline. The wave and current bed shear stress magnitude and direction is shown by the arrows (magenta – wave stress, white – current stress).

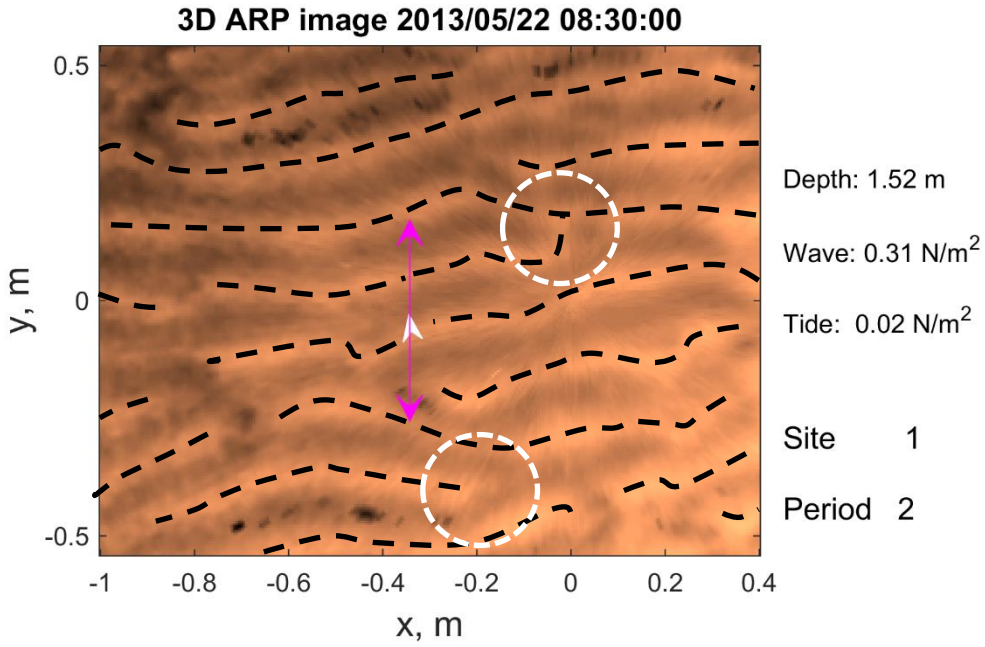

Figure 4-14: Sinuous/straight ripples with open and buttress juncture (examples highlighted by white dashed circles). Tidal period 2, Site 1. Black dashed lines highlight the bedform crestline. The wave and current bed shear stress magnitude and direction is shown by the arrows (magenta – wave stress, white – current stress).

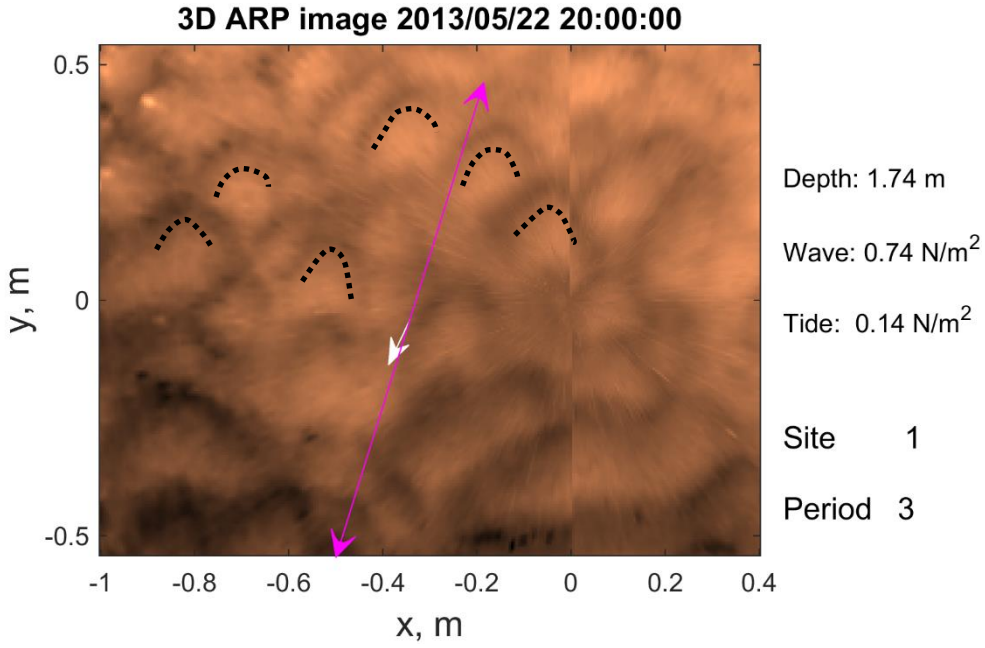

Figure 4-15: Lunate bedforms, out of phase. Tidal period 3, Site 1. Black dotted lines highlight example lunate planforms. The wave and current bed shear stress magnitude and direction is shown by the arrows (magenta – wave stress, white – current stress).

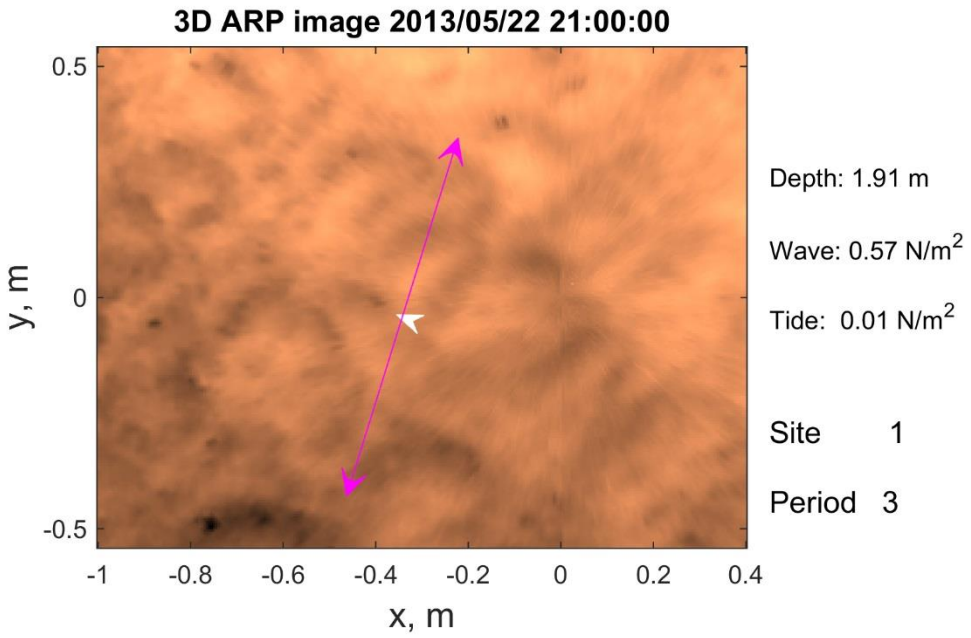

Figure 4-16: Segmented/ladder-back bedforms created by wave stress re-working current bedforms. Tidal period 3, Site 1. The wave and current bed shear stress magnitude and direction is shown by the arrows (magenta – wave stress, white – current stress).

Tidal period 5 at Site 1 was dominated by washed-out bedforms. These bedforms appear to be wave-dominated in Figure 4-17, which agrees with the strong wave forcing, even though the current stress continued to increase as well (Figure 4-10). Segmented bedforms formed around high tide and during the subsequent ebb, which was weaker than the flood because of the presence of wind-driven flow; the wave stress continued to be high (Figure 4-10). 2D straight/sinuous ripples were present at the start of tidal period 6. These wave ripples quickly change into washed-out lunate forms and then into an upper stage plane bed with elongate furrows that resemble small-scale sand ribbons (Günter, 1971; McLean, 1981; Figure 4-18). These sand ribbons were 0.20-0.60 m apart in the 3D-ARP scans. Sand ribbons have been associated with fast unidirectional flows over gravel bed, where the sand supply is starved. In this case, the strong waves and currents could have eroded part of the sand in elongate streaks down to a more cohesive or consolidated layer underneath. This can be seen on the bed shown in Figure 4-18, in that the crests of the ribbons are at the same height as the flat bed in the upper part of the picture, which suggests that the troughs of the ribbons were erosive features. Lunate bedforms appeared around high water in tidal period 6, when the wind driven current was strong, and then changed to sinuous bedforms during ebb flow, when the tidal current was weakened by the opposition of the wind driven flow and the wave stress was still high.

In summary, the bedforms at Site 1 were affected by both wave and current action, with periods of wave dominance. Occasionally, the combined wave and current stresses during flood tides were high enough to impose sheet flow conditions and erosive flows. The strong wind conditions present during most of the deployment of the SedBed frame at Site 1 constituted a major control on the bedform type by the creation of waves, wind driven flow and wave-current stress enhancement.

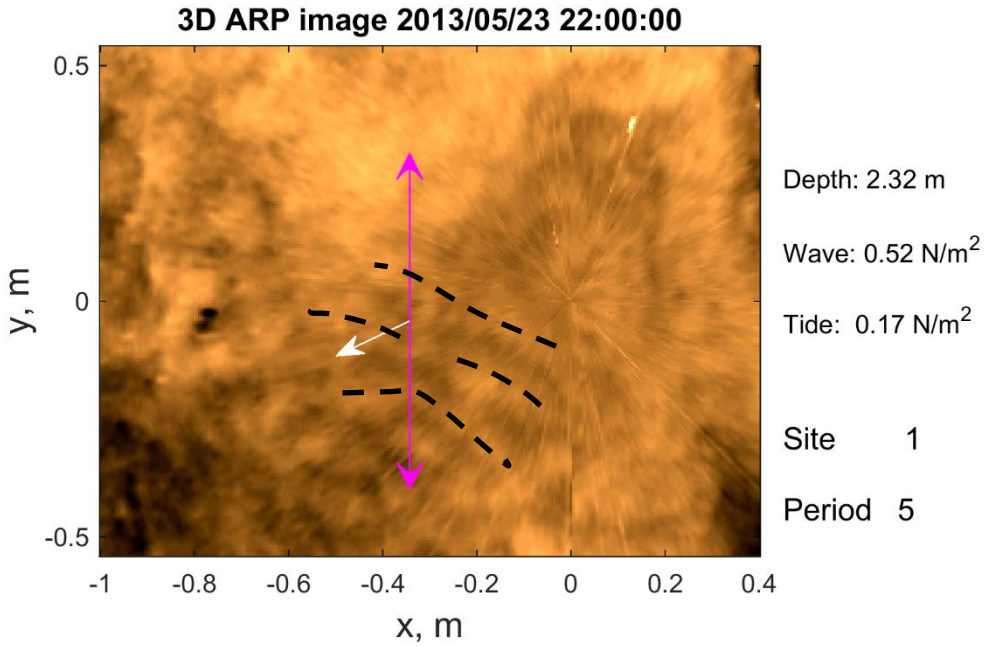

Figure 4-17: Washed-out bed, with some sinuous/segmented ripples starting to form. Tidal period 5, Site 1. Black dotted lines highlight crestlines. The wave and current bed shear stress magnitude and direction is shown by the arrows (magenta – wave stress, white – current stress).

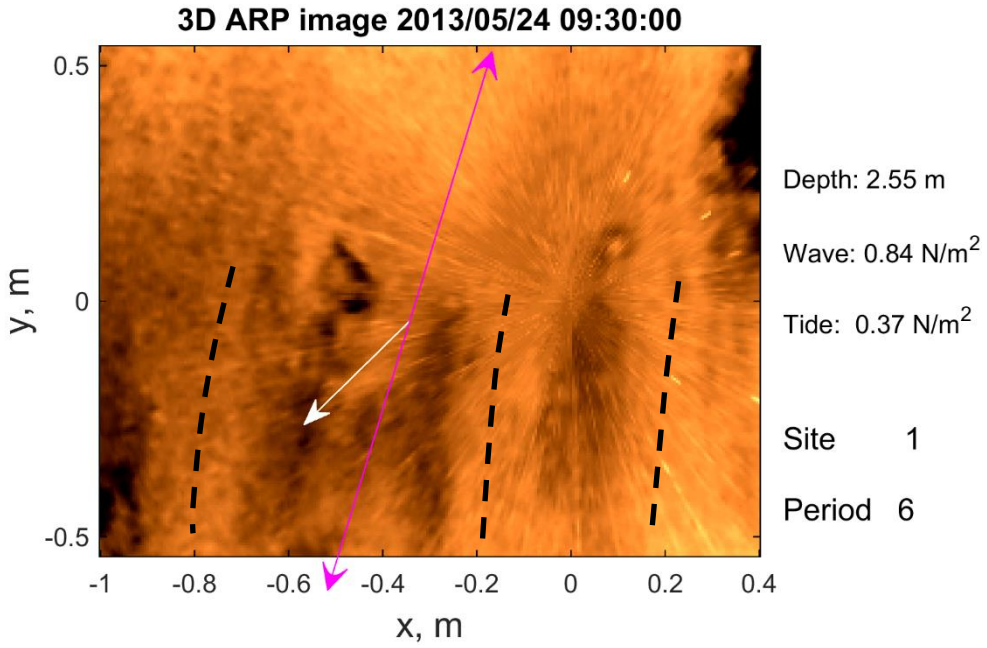

Figure 4-18: Sand ribbons and partially washed-out bed, with a developing scour pit in the top right of the scan. Tidal period 6, Site 1. The wave and current bed shear stress magnitude and direction is shown by the arrows (magenta – wave stress, white – current stress).

4.6.2.3 Site 2 description

In tidal period 7 at Site 2 (24 May, 20:30 - 25 May 2013, 00:00), the bedforms changed from straight/sinuous to lunate during the flood tide, and returned to straight/sinuous during the ebb tide (Figure 4-19). The 2D straight/sinuous ripples resemble wave ripples, but they were more sinuous than at Site 1 (Figure 4-19), which might indicate a larger influence of the currents. This interpretation is supported by the weakened wave conditions in tidal period 7. As wave stress was below the critical value for sediment movement after tidal period 7 at site 2, except for a short time in tidal period 12, the bedforms should have been current-dominated. This is supported by the symmetry indices centring on a value of 2, and the generally 3D planform of the bedforms in tidal periods 8 to 15, ranging from sinuous/segmented at tidal periods 8 to 10 via linguoid/lunate in tidal period 11 to a mixture of 3D forms in tidal periods 13 to 15. Figure 4-20 shows an example of 3D bedforms that can be described as segmented. Figure 4-21 shows an example of a 3D-ARP scan, where linguoid current ripples are dominant, and sinuous crestlines are subordinate. The variation in 3D shape of the bedforms might be associated with the rotation of the tidal flows, as shown in Figure 4-11, with the rather unusual segmented bedforms possibly having been particularly prone to tidal rotation.

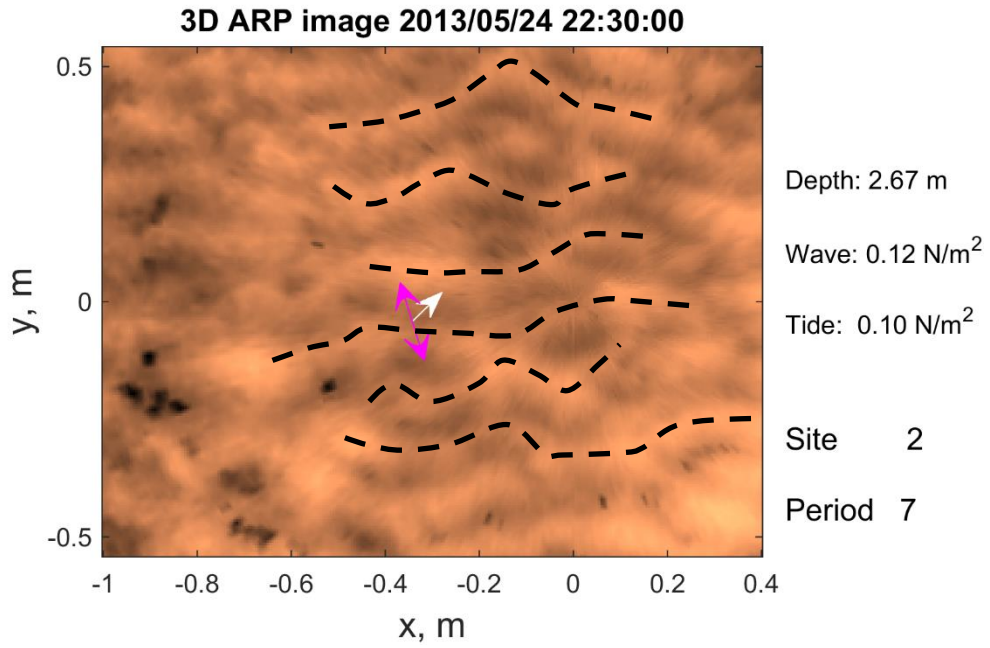

Figure 4-19: Straight/sinuous bedforms, with current and wave direction closely aligned. Tidal period 7. Black dashed lines highlight the bedform crestline. The wave and current bed shear stress magnitude and direction is shown by the arrows (magenta – wave stress, white – current stress).

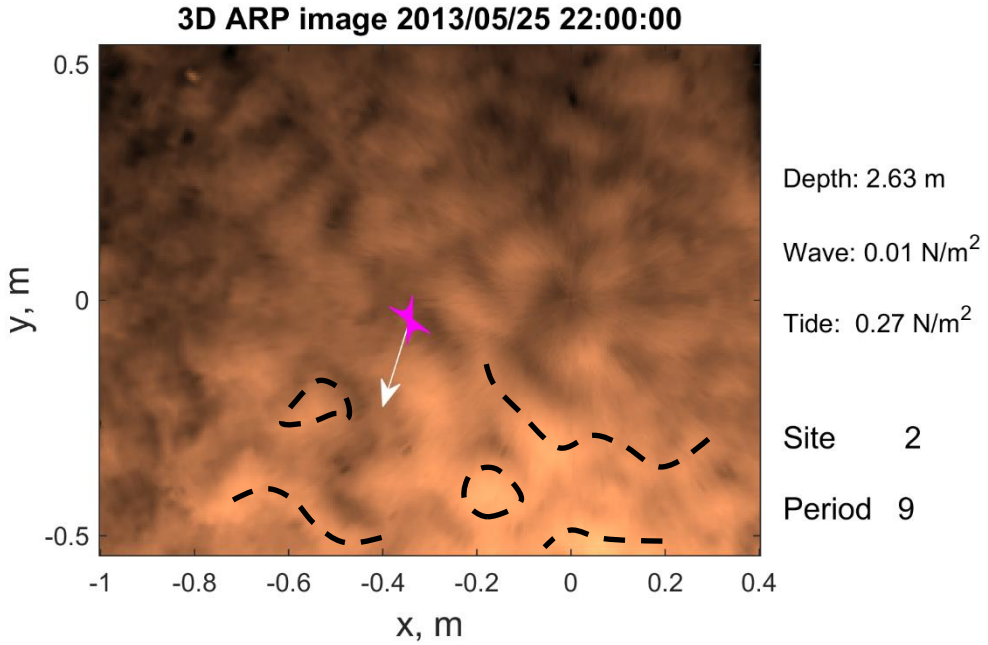

Figure 4-20: Predominantly segmented bedforms in tidal period 9 at Site 2. Black dashed lines highlight selected bedform crestlines. The wave and current bed shear stress magnitude and direction is shown by the arrows (magenta – wave stress, white – current stress).

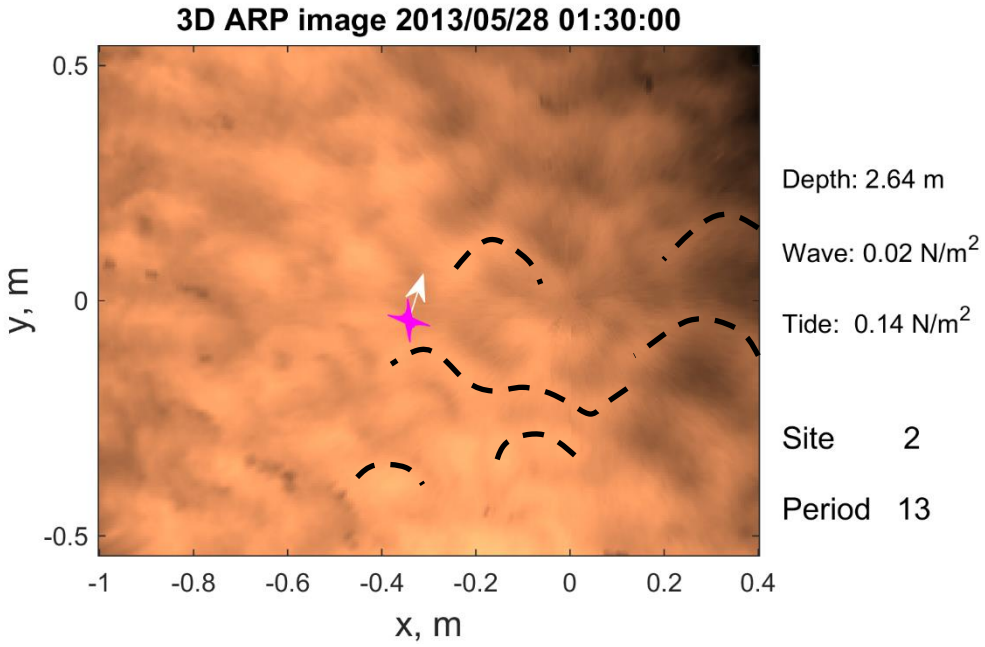

Figure 4-21: Predominantly linguoid bedforms, with sinuous bedforms also present, in tidal period 13 at Site 2. The wave and current bed shear stress magnitude and direction is shown by the arrows (magenta – wave stress, white – current stress).

4.6.2.4 Site 3 description

Tidal period 16 at Site 3 was dominated by irregular, somewhat rounded and segmented, linguoid/lunate bedforms (Figure 4-22). As at Site 2, the segmented character and the rounded crests may be associated with rotating tidal flow. Tidal period 17 also had linguoid/lunate bedforms, but only during the flood tide. These bedforms became segmented shapes at high water, which remained the stable bedform type during the ebb (Figure 4-23; *cf.* Figure 4-10b), and are interpreted as combined flow ripples, as this was a period of increased wave stress at a significant angle to the current stress.

From tidal section 18 onward, the current stress gradually decreased and dropped below the critical value for sediment motion on the neap tide and also the wave focing was not strong enough to move sediment on the bed (Figure 4-10a,b). Relict current-generated bedforms with sinuous, linguoid, lunate and segmented plan form prevailed during tidal periods 18-25 (Figure 4-24).

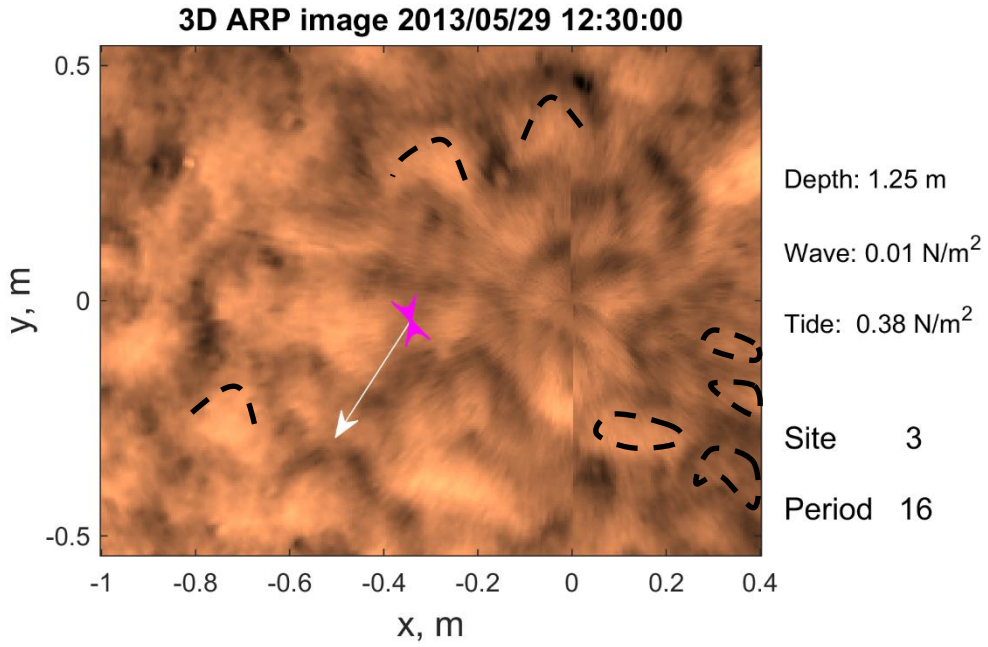

Figure 4-22: Linguoid/lunate bedforms. Tidal period 16, Site 3. Black dashed lines highlight the bedform crestlines or segmented feature. The wave and current bed shear stress magnitude and direction is shown by the arrows (magenta – wave stress, white – current stress).

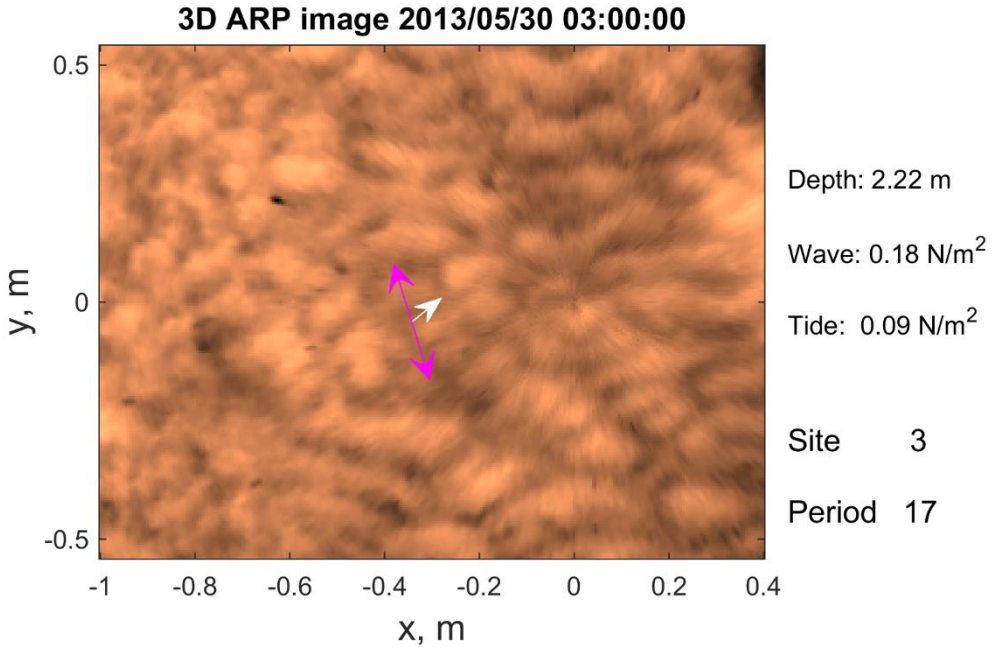

Figure 4-23: Segmented bedforms. Tidal period 17, Site 3. The wave and current bed shear stress magnitude and direction is shown by the arrows (magenta – wave stress, white – current stress).

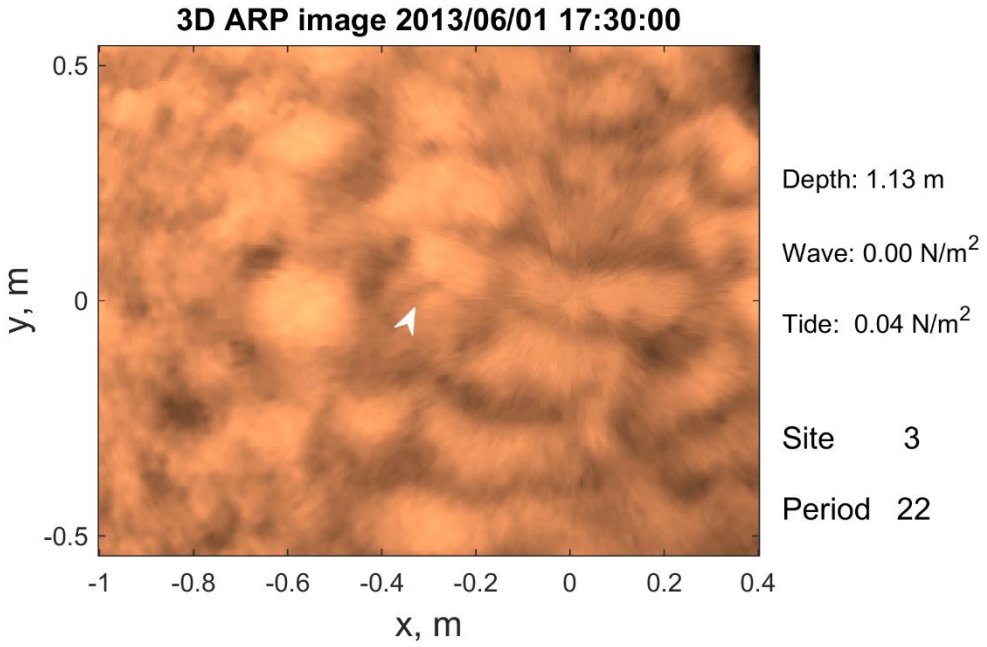

Figure 4-24: Relict sinuous bed during progression to neap tide. Tidal period 22, Site 3. The wave and current bed shear stress magnitude and direction is shown by the arrows (magenta – wave stress, white – current stress).

4.6.2.5 Description of bedform classification trend

A time series of the six merged bedform classes, listed in Table 4-3, is shown in Figure 4-25. Plotting against the water depth allows the bedform classes to be compared with tidal phase.

Sinuous/straight bedforms were present in tidal periods 1 and 2 at Site 1. During tidal periods 3 and 4, sinuous/straight bedforms changed to linguoid/lunate bedforms on the flood, and segmented bedforms dominated around high tide and during ebb. Tidal periods 5 and 6 were characterised by washed-out bedforms during flood and at high tide, due to high combined stress when wind driven flow and high wave forcing combined with increasing current stress progressing towards spring tide (Figure 4-10). At other stages in tidal periods 5 and 6, various types of 3D bedforms were present.

Site 2 was dominated by the tidal current, as the wind and waves had died down, and the tide progressed towards spring tide (Figure 4-9). During tidal period 7, the bedforms developed from sinuous/straight to linguoid/lunate on the flood and then became more sinuous and straight-crested again after high slack water. The bedforms in tidal periods 8, 9 and 10 were mainly sinuous/segmented, with some washed-out bedforms during fast flood and ebb flows. Tidal periods 11 and 12 show mainly linguoid/lunate bedforms, which became more sinuous and segmented on the ebb. The bedforms in tidal period 13 were mainly sinuous/linguoid/lunate. The bedforms generated

during tidal period 14 were indistinct and therefore not classified. Tidal period 15 had mainly sinuous and segmented bedforms.

The entire tidal period 16 and the flood tide in tidal period 17 at Site 3 exhibited linguoid/lunate bedforms, whereas the bedforms on the ebb phase of tidal period 17 were segmented. The entire tidal period 18 had sinuous/linguoid/lunate bedforms. These bedforms changed to sinuous/segmented in tidal period 19, and this bedform type was then stable until the end of the record.

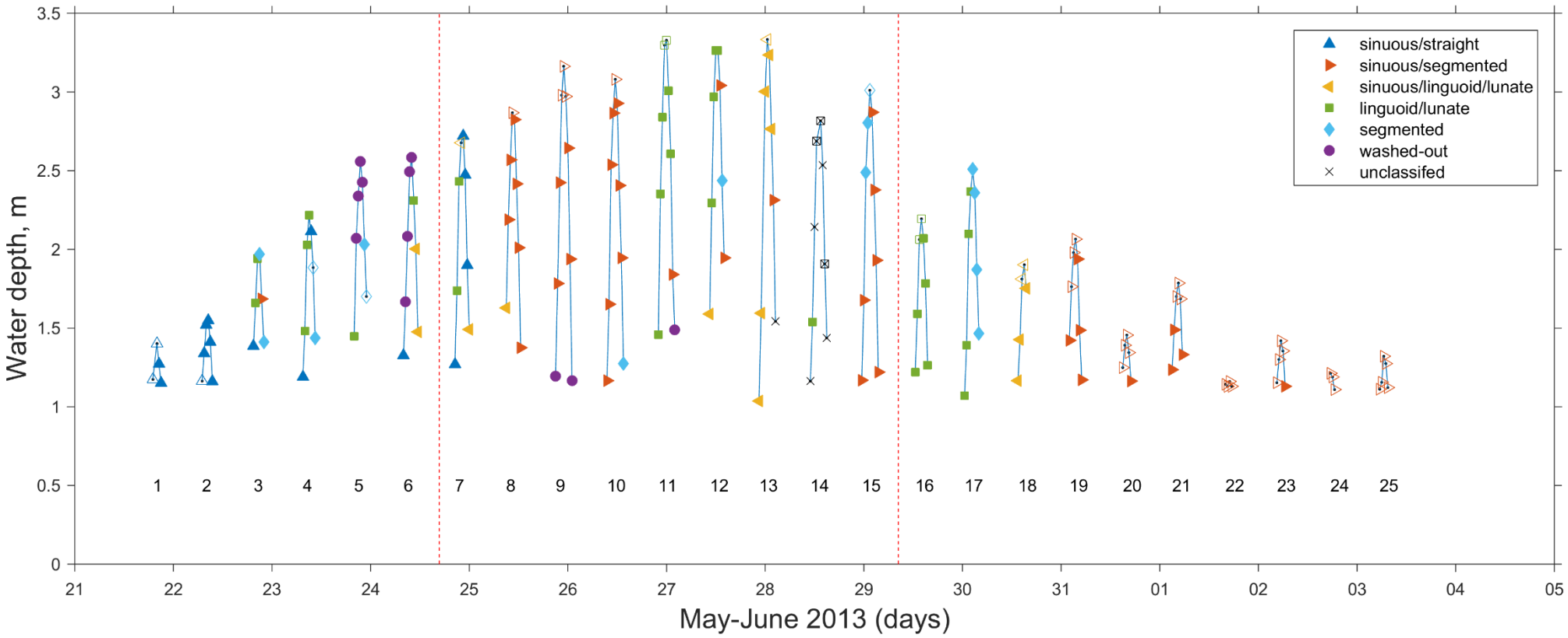

Figure 4-25: Time series of the merged classification plotted with water depth, to show the effect of the tide. The vertical red dashed lines mark the times when the instruments were moved between sites. The numbers in denote the tidal periods for reference. The open markers denote points that have combined maximum skin-friction Shields parameter below the critical stress threshold of sediment motion (from Soulsby and Whitehouse's equation (Soulsby, 1997), for D_{50} = 227 µm), and are relic bedforms. (n = 169)

4.6.2.6 Biogenic bedforms

Worm burrows may form 'U' shapes with an entrance and an exit at the sediment surface (Figure 4-26). The worm feeds at the entrance, creating a pit, and excretes waste at the exit, creating a mound (Fries *et al.*, 1999). The black circular area near the top of the 3D-ARP scan in Figure 4-13 (at x = -0.4 m, y = 0.4 m), may be the entrance of a worm burrow, as it persists in all four scans of tidal period 1. The effect of biological modification of the bed morphology has not been investigated in this study, as the resolution of the data collected was not sufficient to resolve the scale of these features and their effect on the hydrodynamics. However, it appears from Figure 4-26, which shows the area under the 3D-ARP, that these features can cover the entire surface of the sediment on scales from millimetres to centimetres, and therefore may have affected bedform development.

Figure 4-26: Photograph of the bed under the 3D-ARP showing worm burrow entrances and cast piles, with examples highlighted by dashed circles. A 30 cm ruler is shown for scale. The sediment surface shows pockmarks and scour trails from other biological activity, as well as shell fragments. This photograph was taken on 03/06/2013 at 14:01 at Site 3.

4.6.3 Bedform phase diagrams

In this section, the bedforms from the study area in the Dee estuary are compared to standard bedform types in various bedform phase diagrams (*cf.* Section 4.4.3). The principal aim is to verify if the hydrodynamic and morphological conditions found on the tidal flats are properly represented in phase diagrams for current-generated bedforms, wave-generated bedforms, and combined flow bedforms.

4.6.3.1 Current bedforms

A comparison of the field data with the predicted bedform types in the phase diagram of van den Berg and van Gelder (1993) is made in Figure 4-27. The points shown in Figure 4-27 are for the current-dominated conditions only, where the skin-friction Shields stress for waves was below the threshold of sediment motion. Most of these data reside within the stability field of current ripples and no motion. The orange dots in Figure 4-27 represent θ'_{max}, showing that some points are clearly within the stability field for dunes. With the exception of two points, these data are from Site 2, where the height and the length of the bedforms were considerable greater than the equilibrium ripple dimensions predicted by Baas (1999) and Soulsby (2012). Even though the waves were generally small at Site 2, the non-linear wave enhancement of the current stress might have enabled the development of dune-scale bedforms. Alternatively, these bedforms may be transitional between current ripples and dunes. As these relatively large bedforms did not reach the minimum height and length for dunes of 0.06 m and 0.6 m, respectively, they could be classified as non-equilibrium dunes or large current ripples. It is interesting to note that Baas (1999) described large current ripples around the phase boundary between current ripples and dunes, which had heights up to about 0.07 m and length about 0.3 m, and were interpreted as merged current ripples in the initial stage of transition to dunes (*cf*. Bennet and Best, 1996).

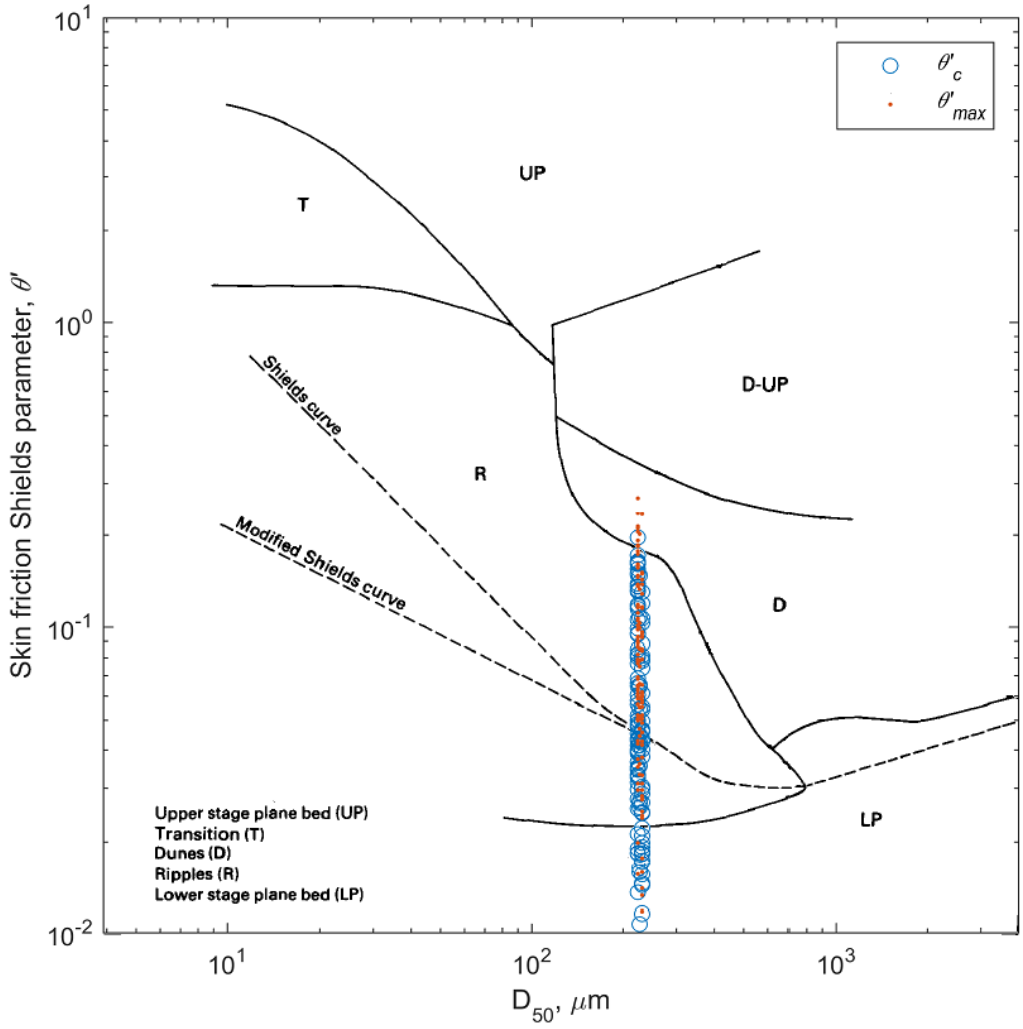

Figure 4-27: Bedform phase diagram for current-generated bedforms by van den Berg and van Gelder (1993b). The field data are plotted for current skin-friction Shields parameter, θ'_c (blue circles) and combined skin-friction Shields parameter, θ'_{max} (orange dots). In order to show current dominated points only, the values have been selected for wave skin-friction Shields parameter below the critical stress threshold of sediment motion of Soulsby and Whitehouse (Soulsby, 1997), for D_{50} = 227 µm (n = 145). Of the blue circles above the 'no motion limit', five are from Site 1, 37 are from Site 2 and 11 are from Site 3.

4.6.3.2 Wave ripples

As for the current-generated bedforms, the field data can be plotted on a bedform phase diagram for wave ripples (Figure 4-28; Allen, 1982; Kleinhans, 2005). The critical stress threshold of sediment motion of Soulsby and Whitehouse (Soulsby, 1997) and the sheet flow limit of Allen and Leeder (1980), for D_{50} = 227 µm, separate the data points into classes of no motion, wave ripples and sheet flow. The points shown in Figure 4-28 are for wave-dominated conditions only, where the skin-friction Shields

stress for current was below the threshold of sediment motion. For θ'_w, only ten data points were above the threshold of sediment motion, implying that many wave ripples were relict bedforms. However, for θ'_{max}, many more data points end up in the wave ripple regime, despite the weak current forcing. This shows that wave-current enhancement may produce more wave-dominated bedforms than would be expected if currents below the critical threshold for sediment movement were ignored altogether.

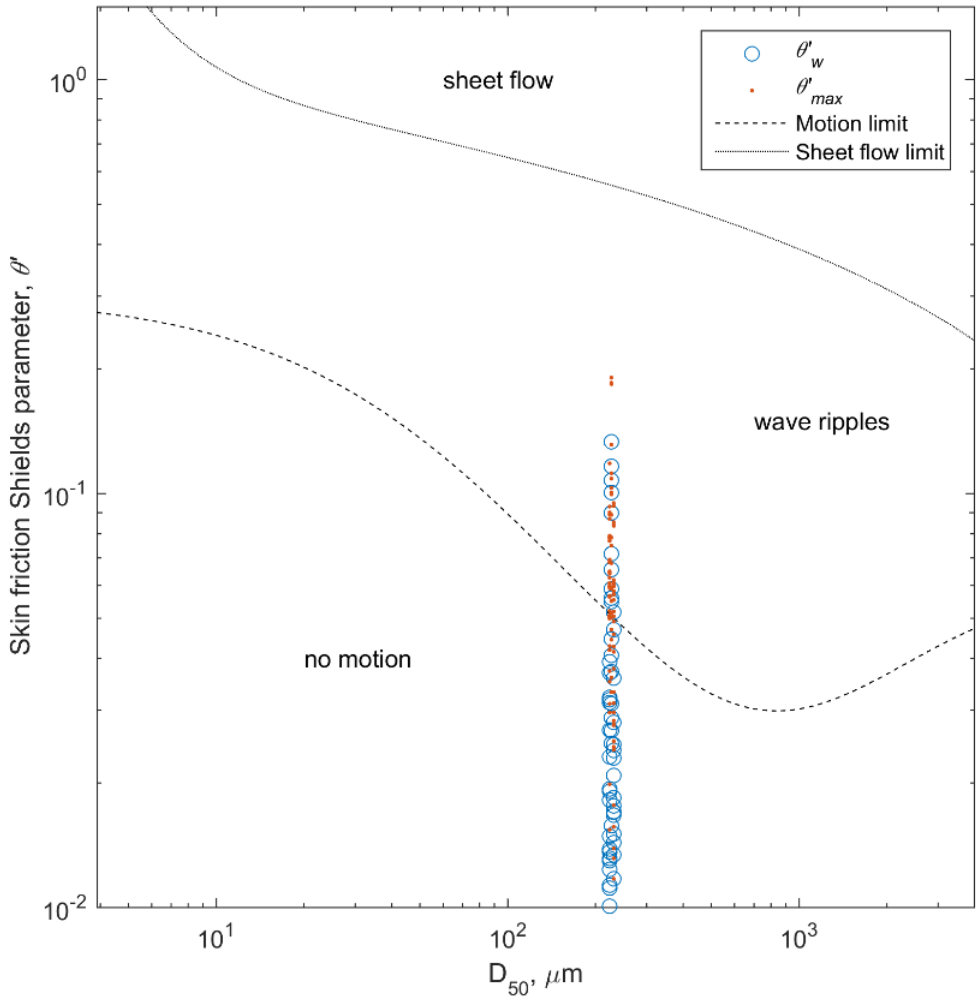

Figure 4-28: Bedform phase diagram for wave-generated bedforms (after Allen, 1982; Kleinhans, 2005). The field data are plotted for wave skin-friction Shields parameter, θ'_w (blue circles) and combined skin-friction Shields parameter, θ'_{max} (orange dots). In order to show wave-dominated data points only, the values have been selected for current skin-friction Shields parameter below the critical stress threshold of sediment motion of Soulsby and Whitehouse (Soulsby, 1997), for D_{50} = 227 µm (n = 103). Of the blue circles above the 'no motion limit', 10 are from Site 1, zero are from Site 2 and one is from Site 3.

4.6.3.3 Wave-current bedforms

In Figure 4-29, the merged classification bedform types of the field data are plotted on the combined wave-current bedform phase diagram of Kleinhans (2005). Despite a significant amount of scatter, several patterns emerge. The sinuous/straight bedforms mainly scatter around the threshold of sediment motion, both for wave- and current-dominated flow. This agrees with the fact that straight-crested and sinuous bedforms are expected to represent wave ripples, and current ripples in the early stage of development (Allen, 1968; Baas, 1994, 1999).

The vast majority of the sinuous/segmented bedforms appear below the line of equal wave and current stress in Figure 4-29, confirming the observations in Section 5.6.2 that these bedforms are current-dominated, and their segmented character may have been caused by tidal rotation. Many sinuous/segmented bedforms were relict, since both θ'_c and θ'_w were below the threshold of sediment movement.

The segmented bedforms cluster mainly in the wave-current ripple area of the bedform phase diagram, suggesting that combined wave-current flow generated these bedforms. Large angles between the current and waves may have promoted the segmentation. The current-generated segmented ripples may have been subjected to tidal rotation.

The washed-out bedforms correctly cluster closest to the sheet flow limit in Kleinhans' (2005) "oriented hummocks" and "flattened current forms" regimes, hence in areas of combined-flow domination and current domination, respectively.

The remaining bedform types, i.e. the linguoid/lunate and sinuous/linguoid/lunate forms, show a wide distribution in Kleinhans' (2005) phase diagram, but most of these bedforms fall below the line of equal wave and current influence, confirming the earlier interpretations that most of these bedforms were active and relict current ripples. Their 3D planform indicates that the active current ripples were at or close to equilibrium with the flow conditions. The linguoid bedforms in which the current domination was strongest tend to plot close to the stress limit of the transition from ripples to dunes; the relatively large size of these bedforms agrees with this position in the phase diagram. With reducing current dominance, towards to the wave-current line, the points spread out ranging between the threshold of motion line and the high stress limit. Despite the dominance of large current ripples at Site 2 and smaller current ripples at Site 3, the linguoid/lunate ripples may have been shaped by both current and waves, such as at in tidal period 3 at Site 1, tidal period 12 at Site 2 and tidal period 17 at Site 3.

In addition to the straightforward evidence for relict bedforms, for example at Site 3, more subtle hysteresis may be present, yet difficult to detect, in the field dataset. Hysteresis is a likely source of scatter in the bedform phase diagram, as some bedforms might not have been in equilibrium with the flow conditions during the acquisition of bed scans. Especially during rapid changes in bed stress, the effect of hysteresis could have been most pronounced. The cohesive properties of the sediment may also have slowed the adaptation of the bedforms to changing flow (Baas *et al.*, 2013; Malarkey *et al.*, 2015).

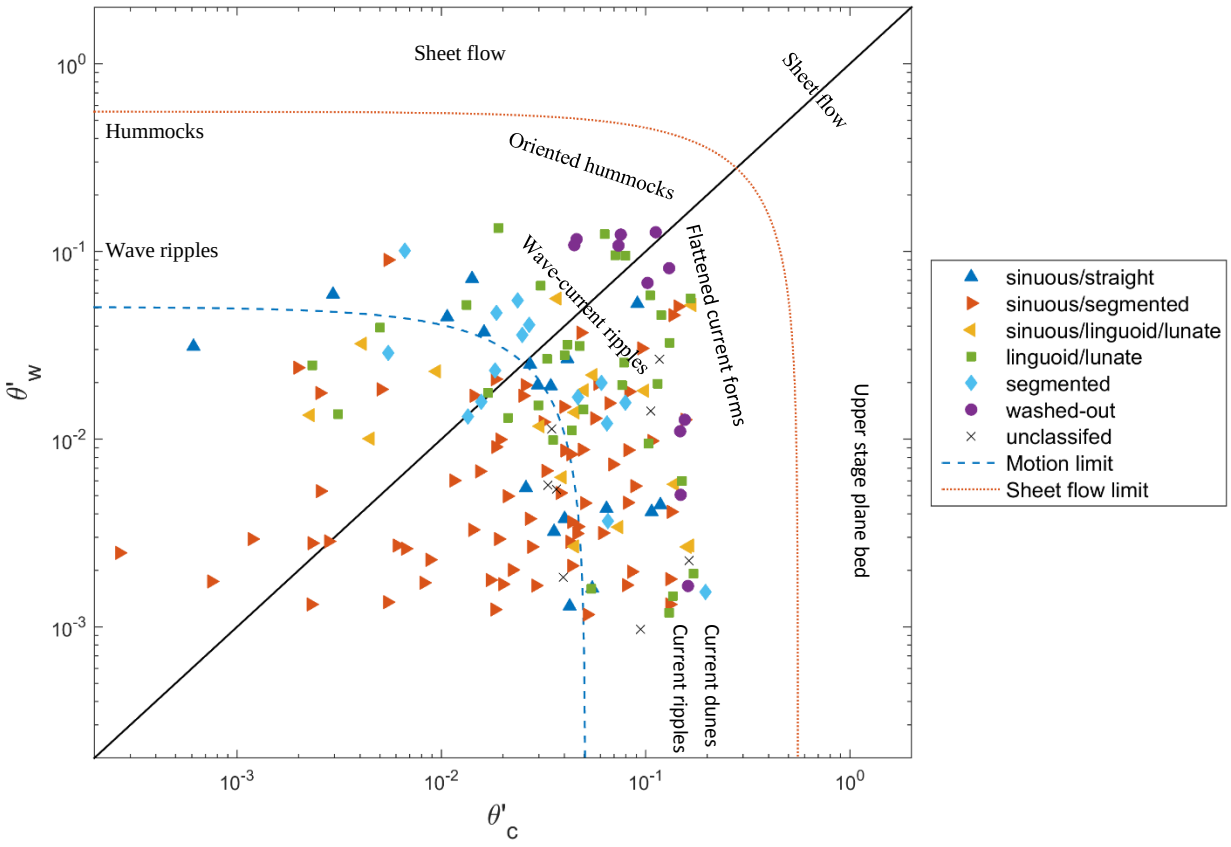

Figure 4-29: Combined wave-current bedform phase diagram for current and wave skin-friction Shields parameter (Amos *et al.*, 1988b; Kleinhans, 2005). The black line is for equal wave and current stress. The critical stress threshold of sediment motion is from Soulsby and Whitehouse's equation (Soulsby, 1997), for D_{50} = 227 µm, and the sheet flow limit from Allen and Leeder's equation (1980). The main classifications from Kleinhans (2005, Figure 4-7 above) are shown for comparison.

The classification scheme of Perillo *et al.* (2014) for combined-flow bedforms was applied to the field data from the Dee estuary and then added to the combined wave-current phase diagram of Perillo *et al.* (2014) (Figure 4-30). There is generally good agreement for the current ripple and no motion classes

(Figure 4-30). However, there is scatter of some 3D current ripples into the area of quasi-asymmetrical ripples and asymmetrical ripples, as these ripples had a higher symmetry index value than expected from the predicted flow conditions. Likewise, many quasi-asymmetrical ripples and asymmetrical ripples plot outside the predicted range of combined flow conditions for these bedform types. Perillo *et al.*'s (2014) boundary between asymmetric ripples and asymmetric dunes is not supported by the field data. The experiments of Perillo *et al.* (2014) were conducted at current velocities up to of 0.5 m s^{-1}, and at a constant depth, with currents and waves aligned, and washed-out forms not considered. Rotational tidal flow was also not considered by Perillo *et al.* (2014). The phase boundaries, as defined by Perillo *et al.* (2014), should therefore be regarded as approximate at best, and not fully applicable to the much wider range of hydrodynamic data from the Dee estuary.

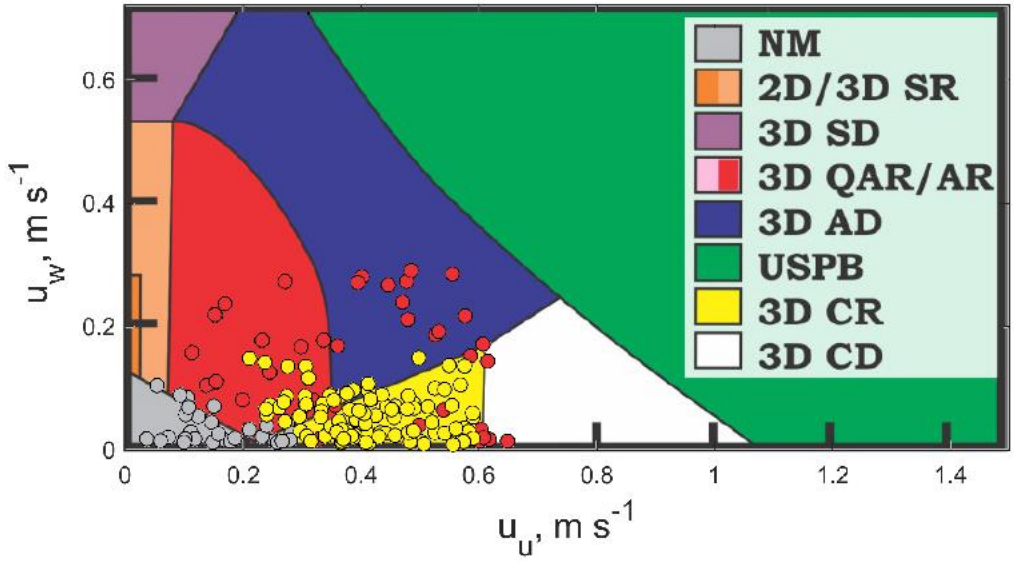

Figure 4-30: Combined wave-current phase diagram of Perillo *et al*. (2014), with field data classified using the scheme of Perillo *et al*. (2014). NM – no motion, SR – symmetrical ripples, SD – symmetrical dunes, QAR – quasi-asymmetrical ripples, AR – asymmetrical ripples, AD – asymmetrical dunes, USPB – upper stage plan bed (sheet flow), CR – current ripples and CD – current dunes. (Modified after Perillo *et al*., 2014).

4.6.3.4 A new phase diagram for the effect cohesive clay on the planform of bedforms

The effect of cohesive clay content and hydrodynamic forcing, using θ'_{max}, on bedform type is summarised in Figure 4-31. This plot indicates that the bedforms changed from washed-out, via linguoid/lunate, sinuous/straight and segmented planform, to current-dominated sinuous/linguoid/lunate planform and sinuous/segmented, as the cohesive clay content increased and θ'_{max} decreased. This relationship is hypothesised to have resulted from differences in clay winnowing.

High-velocity flows are probably most effective in removing cohesive clay from the bed, followed by the waves and combined flows – with wave-current enhancement of bed shear stress – that formed the sinuous/straight and segmented bedforms. The currents that formed the various types of current ripples were least effective in clay winnowing. When testing this hypothesis in the future, work should also include re-working of cohesive clay into the bed in between winnowing events.

The bedform types in the lower cluster in Figure 4-31, below about 1% bed cohesive clay content, which are all from Site 2, do not appear to be related to cohesive clay content. This suggests that bed cohesion has no effect on the bedform morphology at the low bed cohesive clay content of 0.5% at Site 2.

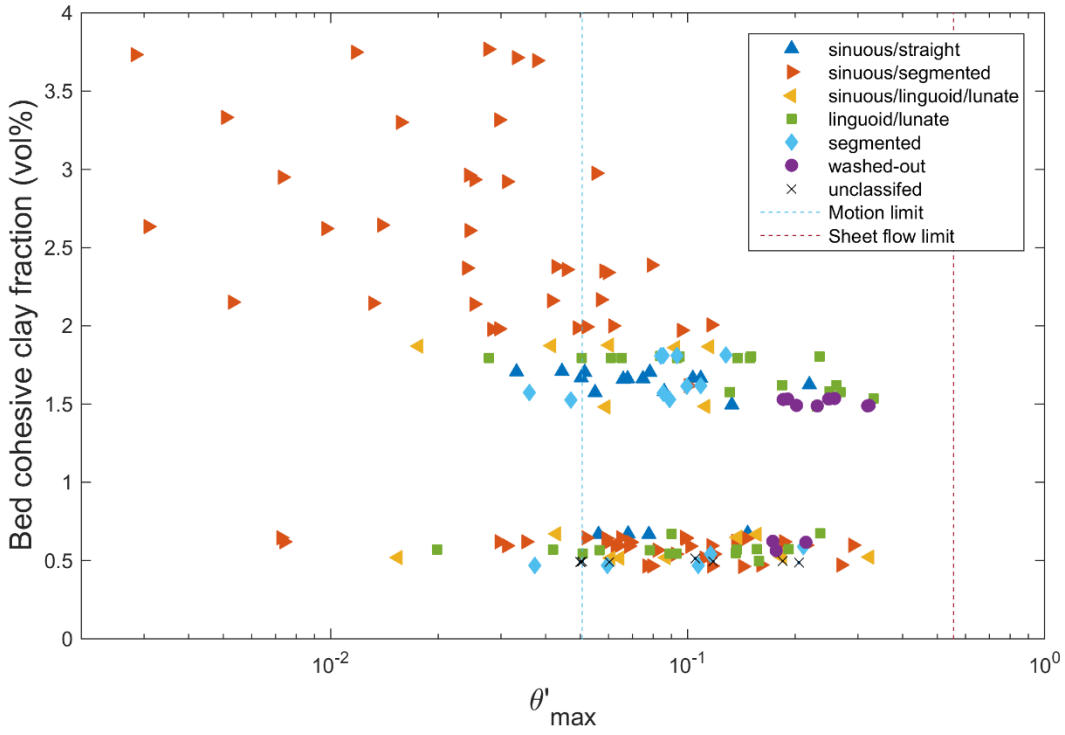

Figure 4-31: Phase diagram of combined skin-friction Shields parameter, θ'_{max}, and bed cohesive clay content. The critical stress threshold of sediment motion is from Soulsby and Whitehouse's equation (Soulsby, 1997), for D_{50} = 227 µm, and the sheet flow limit from Allen and Leeder's equation (1980).

4.6.4 Bedform predictors

4.6.4.1 Current ripples

Figure 4-32 depicts relationships between the current ripple dimensions, θ'_c, and water depth for the field data. Also shown are the predicted bedform height and length according to Soulsby *et al.* (2012). Only data for current-dominated flow above the mobility threshold, $\theta'_w < \theta'_{crit}$ and $\theta'_{crit} < \theta'_{max}$, are plotted in Figure 4-32.

Current ripples in equilibrium with the hydrodynamic forcing, and below the washout limit, are expected to have constant mean dimensions, independent of the current forcing (Baas, 1999; Soulsby *et al.*, 2012). If the field bedforms were current ripples, the dimensions should be constant with current skin-friction Shields parameter, θ'_c, and close to the predicted values. However, although the bedform height regression fit has an intercept close to the predicted values, it varies with current Shields parameter (Figure 4-32a). The bedform length, although constant, is offset from the predictor (Figure 4-32b). The bedform dimensions vary with changing water depth (Figure 4-32c,d) suggesting that the field bedforms are not current ripples. These results show that the field bedforms are not behaving like standard current ripples and are behaving like dunes, varying with current stress and depth, despite their small-scale dimensions.

Although the R^2 values for the regression fits in Figure 4-32 are small, they are significant at the p = 0.05 or 95% confidence level, except for bedform length and current Shields stress (Figure 4-32b). The low R^2 values show that the individual parameters do not model the variance of the field data well and better approach would be to consider multiple factors in a single analysis, which is investigated using multiple linear regression in section 4.6.6.

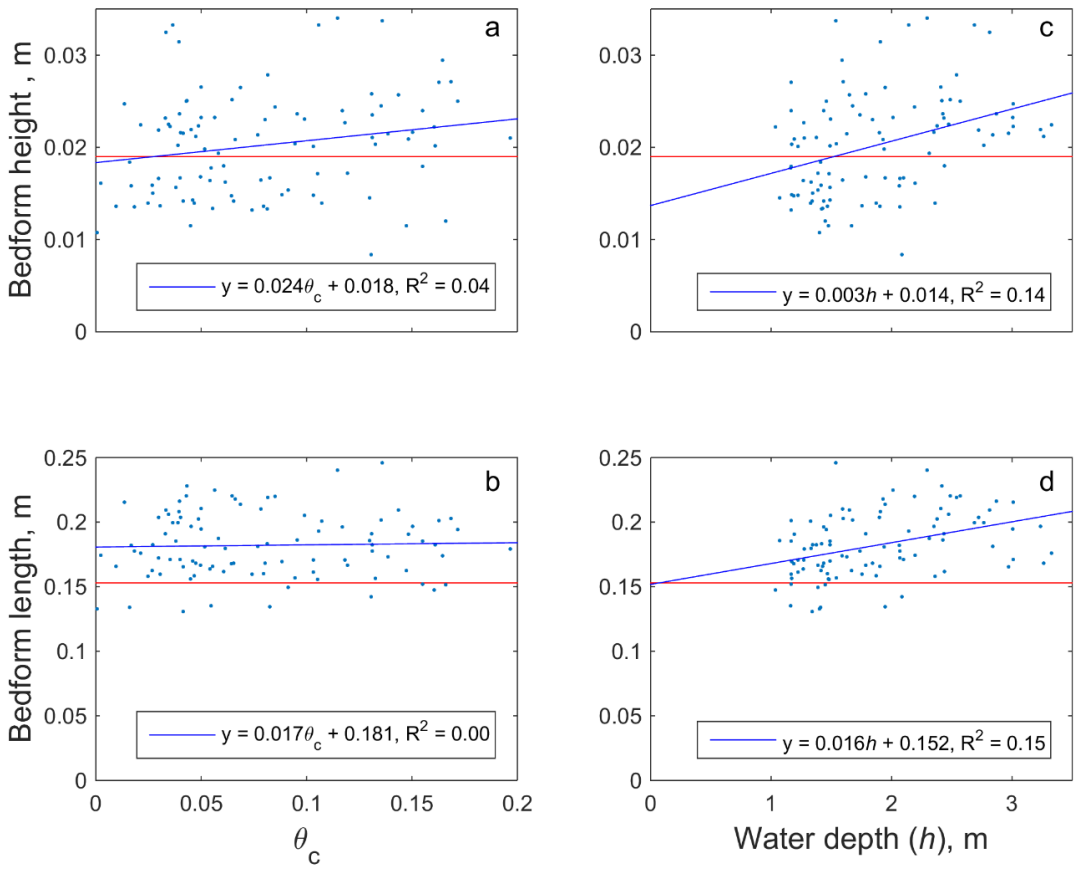

Figure 4-32: Comparison of current ripple dimensions prediction for grain size D_{50} = 227 µm (Soulsby *et al.*, 2012. Red line) with field data, for current skin-friction Shields parameter, θ'_c and water depth, *h*. In order to only show current dominated points in motion, the values have been selected for wave skin-friction Shields parameter below the critical threshold of sediment motion and for combined skin-friction Shields parameter above this threshold, from Soulsby and Whitehouse's equation (Soulsby, 1997), for D_{50} = 227 µm (n = 97).

4.6.4.2 Dunes

A comparison between dune predictors, for height and length (van Rijn, 1984c; Yalin, 1964; section 4.4.4.2), and the field data is shown in Figure 4-33. There is very poor agreement of the field data with these predictors, as the bedforms are much smaller than expected by the dune predictors. The most likely explanation is that the current-dominated bedforms at the study sites were not dunes, but equilibrium current ripples at Site 3, and equilibrium bedforms transitional between current ripples and dunes at Site 2 (Bennet and Best, 1996; Baas 1999). Since the dune predictors of Yalin (1977) and van Rijn (1984c) are based on data from rivers and laboratory flumes, where, in contrast to the field sites, the water depth was constant and the flows were steady and unidirectional, the field bedforms at Site 2 may have been non-equilibrium bedforms. Hence, these bedforms did not have enough time to reach equilibrium dune dimensions under the influence of the constantly changing flow forcing in the Dee estuary.

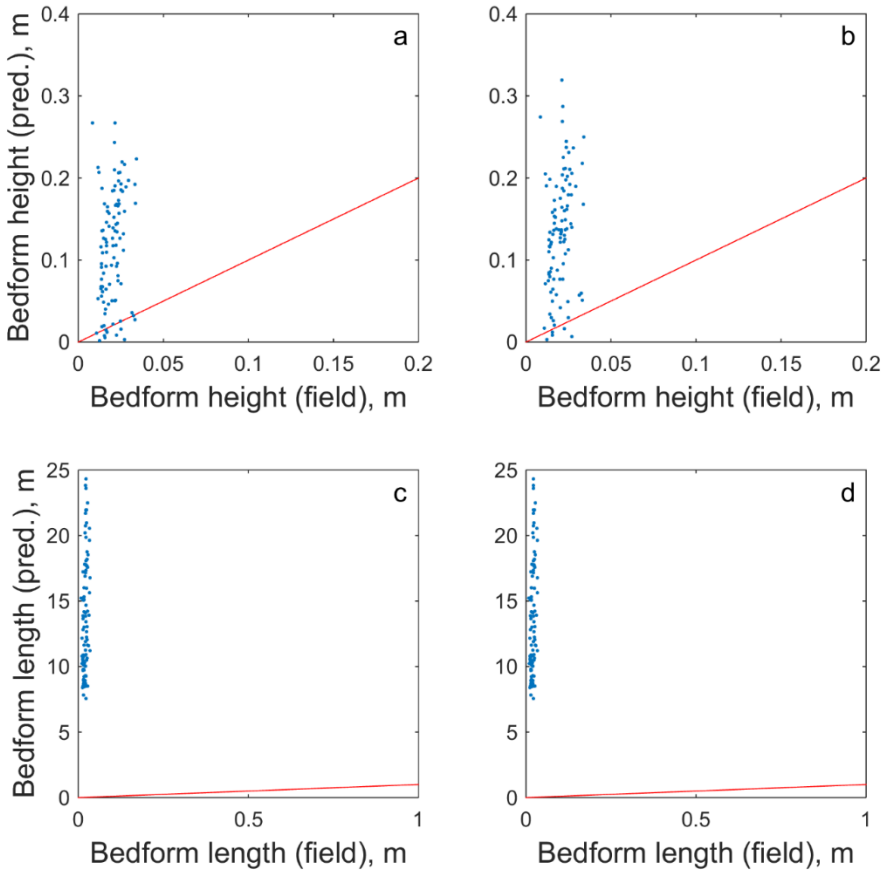

Figure 4-33: Bedform height and length, field data against predicted values, for: (a, c) dune predictor of van Rijn (1984c), and (b, d) dune predictor of Yalin (1964; in Soulsby, 1997). Red line – 1:1 relationship. In order to show current dominated points only, the values have been selected for wave skin-friction Shields parameter below the critical threshold of sediment motion from Soulsby and Whitehouse's equation (Soulsby, 1997), for D_{50} = 227 µm (n = 145).

4.6.4.3 Wave ripples

In order to compare the field measurement with the wave ripple predictors of Soulsby *et al*. (2012) and Wiberg & Harris (1994; modified by Malarkey and Davies, 2003), data were selected from tidal periods 2 to 4 only, because during these periods the waves dominated and the current stress was below the threshold of motion (Figure 4-34). Considering that the bedforms may have been affected by wave-current enhancement, the predicted bedform dimensions correspond reasonably well with the field data. The predictor of Soulsby *et al*. (2012) performed better than the Wiberg & Harris (1994) predictor.

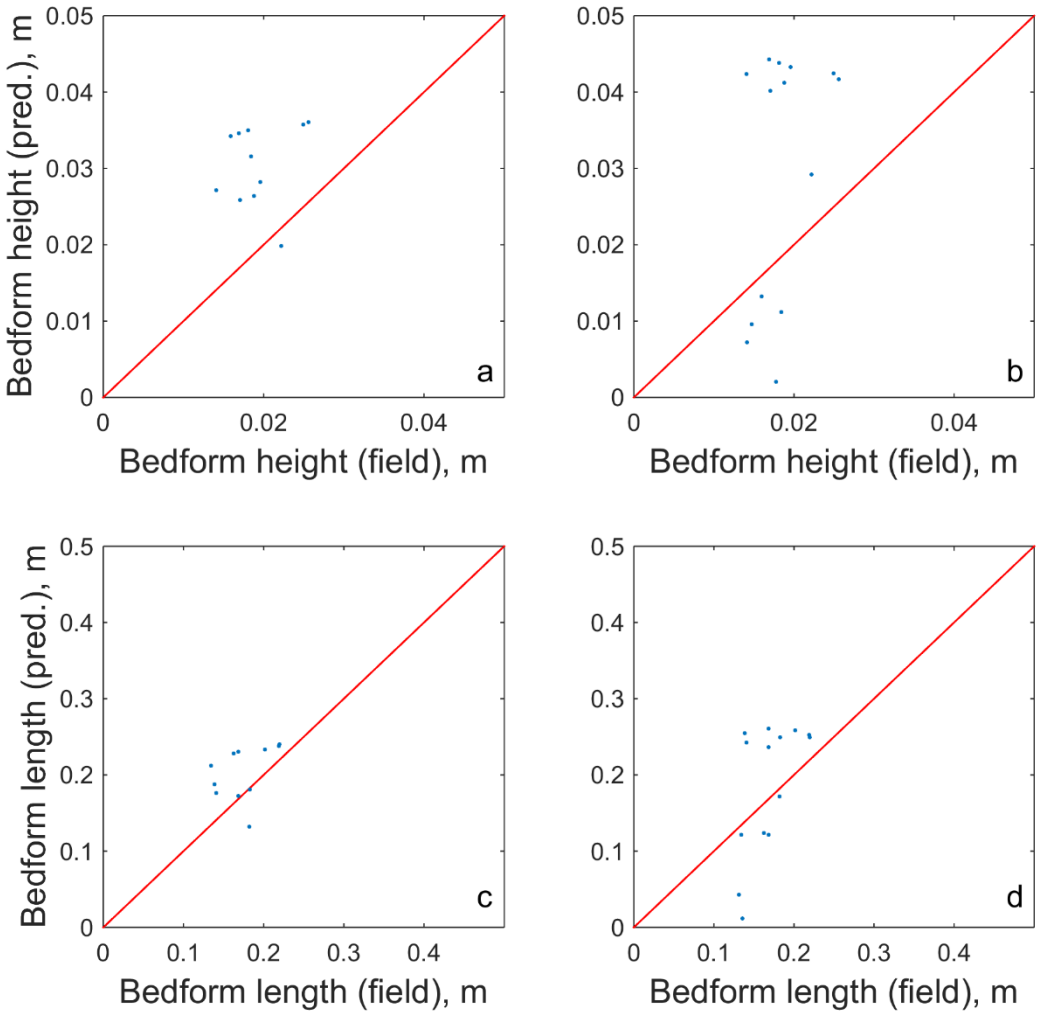

Figure 4-34: Comparison of bedform dimensions between field data and predictors for wave ripples. Red line – 1:1 relationship. In order to show wave-dominated bedforms only, the data from tidal periods 2 to 4 and above the critical threshold of motion are shown only (Figure 4-10b). (a, c) Soulsby *et al.*'s (2012) predicted height and length, (b, d) Wiberg & Harris' (1994; modified by Malarkey and Davies, 2003) predicted height and length.

4.6.5 Logistic regression of the planform dimensionality classification

The parameters used in the logistic regression were current skin-friction Shields parameter, θ'_c, wave skin-friction Shields parameter, θ'_w, water depth, h, wave-current angle, φ, and bed cohesive clay content, c. The data points were tested for statistical leverage. Removing 3 outliers with a leverage greater than 0.11 (2 times the number of coefficients divided by the number of observations), out of 114 data points, improved the p-values of the overall model and the individual parameters. The effect of the cohesive clay and depth parameters on dimensionality were found to be not significant at the p = 0.05 or 95% confidence level, and were removed. Overall, the model is significant to p = 0.05 or 95% confidence level (Table 4-4).

The logistic regression model gives a probability that a set of hydrodynamic conditions result in bedforms that are fully 3D or 2D. The coefficients in equation 4-6 show that θ'_c and φ increase the probability of bedforms being 3D and that θ'_w reduces this probability (Table 4-4):

$$P_{3D} = 18.84\theta'_c - 33.90\theta'_w + 0.07\varphi + 0.24$$

$$P_{2D} = 1 - P_{3D}$$

4-6

where P_{3D} is the probability of 3D bedforms, in the range 0 to 1, and P_{2D} is the probability of 2D bedforms. The predictions of dimensionality in equation 4-6 agree with a large body of previous work, in that wave-generated ripples are typically two-dimensional, equilibrium current bedforms are three-dimensional, and a high wave-current angle promotes three-dimensionality of combined-flow bedforms (Allen, 1982; Lee Young and Sleath, 1990; Baas *et al*., 1993; Baas, 1999; Andersen and Faraci, 2003; Dumas *et al*., 2005; Venditti *et al*., 2005; Perillo *et al*., 2014). This model is only valid for conditions where the bed shear stress is sufficient to move sediment and therefore change the bed morphology.

Bed cohesive clay content has been found to affect the transition of bedforms from 2D to 3D (Baas *et al*., 2013; Schindler *et al*., 2015; Parsons *et al*., 2016), therefore the lack of significance of the cohesive clay term in the logistic regression is unexpected. However, the range of cohesive clay contents in non-relict bedforms may have been too small to show this relationship as significant in the field dataset. This is probably due to the exclusion of the 2.5D bedforms from the analysis, as at Site 3 they are mainly present during the period when the bed cohesive clay content is higher and increasing.

Taking this into consideration the results of the logistic regression agree with existing work on the transition of bedforms from 2D to 3D.

Table 4-4: Logistic regression model of the probability of conditions producing 3D bedforms (field data and 238 µm data of Baas *et al*. (2000)). Parameters included in the model where: current skin-friction Shields parameter, θ'_c, wave skin-friction Shields parameter, θ'_w, and wave-current angle, φ (0-90°).

Parameter	Coefficient	Units	Standard error	t-statistic	p-value	% influence
Intercept	0.243	-	0.708	0.343	0.731	4.0
ϑ'_c	18.844	-	7.820	2.410	0.016	28.3
ϑ'_w	-33.899	-	11.844	-2.862	0.004	33.6
ϕ	0.073	-	0.025	2.895	0.004	34.0
111 observations, 107 error degrees of freedom, Dispersion: 1, Chi^2-statistic vs. constant model: 20.4, p-value = 0.000141						

Although the logistic regression model describes the probability that bedforms fall into either one of two classes, *i.e.* 3D or 2D, these classes can be seen as part of a continuum between fully 3D and fully 2D, as shown in Figure 4-35. This figure shows that most bedforms in the time-series are predicted to be strongly 3D by equation 4-6 agree well with the visual classification of these bedforms. Even though 2.5 dimensionality was not included in the statistical model, the largely relict current ripples at Site 3, which showed some evidence for 2.5-dimensionality in the form of short sinuous crestlines, are correctly predicted to have weaker three-dimensionality than the generally strongly 3D linguoid/lunate bedforms at Site 2. However, the 2D bedforms at Site 1 have lower 2D probability than expected from their straight/sinuous crestlines, possibly because the field data, and therefore the model input, was skewed towards 3D bedforms. The agreement between visual classification and model is poor only during tidal periods 6 and 7, which may be caused by the dominance of washed-out bedforms, which are difficult to classify in terms of dimensionality.

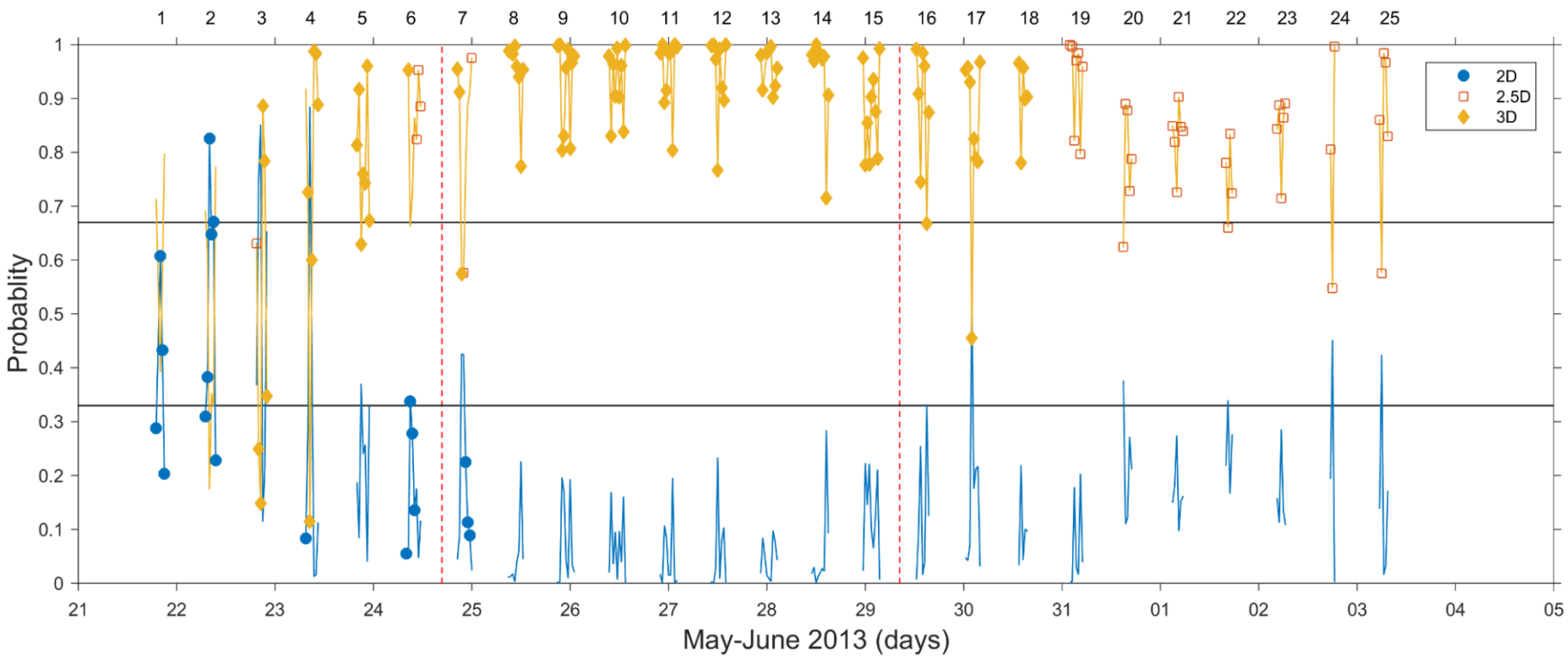

Figure 4-35: Bedform 3D and 2D planform probability from the logistic regression model. Blue line – 2D, yellow line – 3D (from equation 4-6). Markers indicate the visual classification, the 2.5D points were not used in the logistic regression. The vertical red dashed lines mark the times when the instruments were moved between sites. The numbers in denote the tidal periods for reference.

4.6.6 Stepwise regression of the bedform dimensions

The key physical factors of the modelled processes must be kept in mind when applying the stepwise regression model. Initially, the stepwise regression was run for 10 primary parameters, including cohesive clay content, forming a set of 66 parameters, which resulted in a regression model that contained no current or wave parameters. This model was considered to be physically unrealistic for the bedforms in this field study (Figure 4-10d,e and Section 0), which can be expected to vary in size with current forcing, wave forcing and water depth (*e.g.* van Rijn, 1984c; Wiberg & Harris 1994; Baas and De Koning, 1995; Soulsby, 1997; Soulsby *et al*. 2012). Therefore, the cohesive clay content parameter was removed from the data set before re-running the stepwise regression, for a set of 55 primary and derived parameters, which created a more realistic model of the current and wave forcing, with the parameters automatically selected by the stepwise process based on the variance in the data. The cohesive clay content parameter was added to this model manually, resulting in an overall significant model of the current forcing, wave forcing and bed cohesion.

4.6.6.1 Multiple linear regression analysis of bedform height

The above two-step procedure in multiple linear regression analysis was applied to bedform height first. The model for the first step in the analysis, without cohesive clay content, is shown in Table 4-5, and the model after adding the percentage cohesive clay, in the second step of the analysis, is shown in Table 4-6.

Table 4-5: Multiple linear regression model of bedform height, excluding the cohesive clay parameter (field data and 238 µm data of Baas *et al*. (2000)). Parameters included in the model where: current skin-friction Shields parameter, θ'_c, wave skin-friction Shields parameter, θ'_w, water depth, *h*, and wave-current angle, φ (0-90°). The units of the coefficients are shown.

Parameter	Coefficient	Units	Standard error	t-statistic	p-value	% influence
Intercept	0.006	m	0.002	3.063	0.003	10.0
ϑ'_c	0.051	m	0.011	4.560	1.242×10^{-5}	14.9
ϑ'_w	0.031	m	0.053	0.578	0.564	1.9
h	0.007	-	0.001	8.831	1.027×10^{-14}	28.8
φ	-4.35×10^{-5}	m	0.000	-2.623	0.010	8.6
$\vartheta'_c \times \vartheta'_w$	-1.202	m	0.269	-4.466	1.812×10^{-5}	14.6
$\vartheta'_w \times h$	-0.062	-	0.023	-2.740	0.007	8.9
ϑ'^2_w	0.764	m	0.201	3.806	2.236×10^{-4}	12.4
Number of observations: 128, Error degrees of freedom: 120 Root Mean Squared Error: 0.0041 R-squared: 0.51, F-statistic vs. constant model: 18.1, p-value = 2.99×10^{-16}						

As part of the second step, parameters with p-values above the 0.05 limit were removed. Overall, the multiple linear regression model with cohesive clay is significant to the p = 0.05 limit ($p = 1.69\times10^{-24} < 0.05$). From the model coefficients listed in Table 4-6, the following predictive equation can be formulated for bedform height, η:

$$\eta = 0.019 + 0.004h - 0.521\theta'_c\theta'_w$$
$$-0.065\theta'_w h + 0.88\theta'^2_w - 0.005c$$

4-7

As the data used to create the model is for stress above the critical threshold for sediment motion, based on a median grain size of 227 µm, the intercept of the model represents the theoretical minimum bedform height expected for clay-free sediment of this grain size (Table 4-6). Because of the rarity of purely wave-dominated conditions in the data set, this intercept value is expected to be mainly influenced by current forcing, and it should therefore represent the height of current ripples in clay-free, 227 µm sand. The intercept value of 0.019 m (19 mm) is indeed within the range 17-19 mm predicted for the height of equilibrium ripples in this type of fine-grained sand (Baas, 1999; Soulsby *et al*., 2012).

Table 4-6: Multiple linear regression model of bedform height, including the cohesive clay parameter (field data and 238 μm data of Baas *et al*. (2000)). Parameters included in the model where: current skin-friction Shields parameter, θ'_c, wave skin-friction Shields parameter, θ'_w, water depth, *h*, and % cohesive clay content. The units of the coefficients are shown.

Parameter	Coefficient	Units	Standard error	t-statistic	p-value	% influence
Intercept	0.019	m	0.001	14.961	2.22×10^{-29}	33.9
h	0.004	-	0.001	6.779	4.58×10^{-10}	15.4
$\vartheta'_c \times \vartheta'_w$	-0.521	m	0.199	-2.614	0.01	5.9
$\vartheta'_w \times h$	-0.065	-	0.012	-5.418	3.08×10^{-07}	12.3
ϑ'^2_w	0.880	m	0.151	5.809	5.11×10^{-08}	13.2
c	-0.005	m	0.001	-8.541	4.44×10^{-14}	19.4
Number of observations: 128, Error degrees of freedom: 122 Root Mean Squared Error: 0.00357 R-squared: 0.63, F-statistic vs. constant model: 40.8, p-value = 1.69×10^{-24}						

According to equation 4-7, the height of the bedforms at the study sites increased as *h* increases. This may be a reflection of the spring tide at Site 2, during which the maximum water depth and the bedform height were larger than at Sites 1 and 3, where hydrodynamic conditions were closer to neap tide. In addition, when waves were present, they produced smaller bedforms than at Site 2. Given that equilibrium current ripples do not scale with water depth (Baas, 1999; Soulsby *et al*., 2012), this regression model provides further evidence that most bedforms at Site 2 can be classified as large ripples (Bennett and Best, 1996; Baas, 1999), transitional to dunes, which are different from standard current ripples in that they do scale with *h*.

The wave skin-friction Shields stress parameter in the model, θ'^2_w, is positively correlated with the bedform height. This relationship is non-linear, but the quadratic relationship is probably an oversimplification associated with the limited range of pure wave conditions during data acquisition, as wave ripple height predictors normally use a function with a different power (*e.g.*, Nielsen, 2009).

Some of the multiple regression parameters might be expected to have a strong linear relationship with each other or co-vary, known as multicollinearity (Chatterjee and Hadi, 2015). Wind stress causes waves to develop, and the water depth modulates the wave growth. Therefore, the water depth does

not fully co-vary with wave stress, as the wind forcing is the cause of the wave stress. This results in separate parameters for wave stress and water depth being included in the model created by the stepwise regression. If multicollinearity did have a negative effect on these parameters, the associated coefficients would not be significant and be excluded from the model by the stepwise process (Chatterjee and Hadi, 2015). In addition, the coefficients would exhibit large changes in value with the addition or removal of parameters, or the removal of data points, and these effects were not seen in the final regression model (Table 4-6. Chatterjee and Hadi, 2015). The current stress and wave angle parameters in the height regression both had p-values above the limit of significance. Current stress and bedform height showed a significant relationship in Figure 4-32. However, the current stress was not significant at the p = 0.05 limit in the multiple linear regression analysis (Table 4-6), possibly due to the close relationship between water depth and current stress in tidal currents.

The wave and current stress interaction parameter, $\theta'_c \times \theta'_w$ (Table 4-6), is predicted to reduce the bedform height, suggesting that wave-current stress enhancement promoted the development of smaller bedforms, possibly of the washed-out variety. The presence of the $\theta'_w \times h$ parameter in equation 4-7 implies that the effect of water depth on the wave parameters is non-linear, and that $\theta'_w \times h$ corrects for this non-linearity (Wolf, 1997; Gordon and Lohrmann, 2001).

Increasing the bed cohesive clay content is predicted to reduce the bedform height (Table 4-6). This agrees with laboratory results that show a similar reduction in bedform height with bed cohesive content (Baas *et al*., 2013; Malarkey *et al*., 2015; Schindler *et al*., 2015). The bed cohesive clay content is expected to decrease by winnowing of clay and EPS from the bed under waves and currents that are strong enough to move the sediment, and increase during deposition of fines at bed shear stresses below the threshold of sediment movement. Baas *et al*. (2013) and Malarkey *et al*. (2015) found that the bed shear stress modulates the rate of winnowing, and therefore the amount of cohesive material in the bed. However, the effect of bed cohesive clay content co-varying with bed shear stress was not predicted by the model, possibly because the bed cohesive clay values were modelled from the bed samples collected in between tidal periods rather than sampled during acquisition of the wave and current data. Calculating equation 4-7 for zero bedform height (with, θ'_w equal to zero and h = 0.1 m, a non-zero value of water depth close to zero) predicts that for cohesive clay values of about 4 vol% and above, bedforms would not be expected to form or change. The value for the critical cohesive clay content increases with increasing water depth ($c_{crit} = 0.92h + 4.08$, based on the unrounded regression coefficients). This balance between the water depth and critical cohesive clay content may be due to the relationship between water depth and current shear stress in tidal currents. High stress at spring tide is required to cause sediment motion in beds with high cohesive clay content.

4.6.6.2 Multiple linear regression analysis of bedform length

Stepwise multiple linear regression analysis was also applied to bedform length. The regression model predictions without cohesive clay content are shown in Table 4-7. Overall, this model was significant to the p = 0.05 confidence limit. Table 4-8 shows the regression model after adding the percentage cohesive clay parameter, in the second step of the analysis.

Table 4-7: Multiple linear regression model of bedform length, excluding the cohesive clay parameter (field data and 238 µm data of Baas *et al*. (2000)). Parameters included in the model were wave skin-friction Shields parameter, θ'_w and water depth, *h*. The units of the coefficients are shown.

Parameter	Coefficient	Units	Standard error	t-statistic	p-value	% influence
Intercept	0.135	m	0.006	24.042	1.63×10^{-48}	50.6
h	0.031	-	0.003	9.195	1.11×10^{-15}	19.3
$\vartheta'_w \times h$	-0.469	-	0.060	-7.810	2.07×10^{-12}	16.4
ϑ'^2_w	5.465	m	0.842	6.491	1.85×10^{-09}	13.7
Number of observations: 128, Error degrees of freedom: 124 Root Mean Squared Error: 0.02 R-squared: 0.43, F-statistic vs. constant model: 31.6, p-value = 3.04×10^{-15}						

The wave skin-friction Shields parameter, θ'_w, stood out as having a high p-value and low percentage influence on the model (p = 0.92, influence = 0.21%), and was therefore removed from the model. However, the influence of the wave forcing is still present in the form of θ'^2_w. Overall the model is significant to the p = 0.05 limit ($p = 2.13\times10^{-15} < 0.05$). From the model coefficients listed in Table 4-8, the following predictive equation can be formulated for bedform length, λ:

$$\lambda = 0.143 + 0.029h - 0.444\theta'_w h + 5.341\theta'^2_w - 0.006c \quad \text{4-8}$$

Table 4-8: Multiple linear regression model of bedform length, including the cohesive clay parameter (field data and 238 µm data of Baas *et al*. (2000)). Parameters included in the model were wave skin-friction Shields parameter, θ'_w, water depth, *h*, and % cohesive clay content. The units of the coefficients are shown.

Parameter	Coefficient	Units	Standard error	t-statistic	p-value	% influence
Intercept	0.143	m	0.007	20.859	3.27×10^{-42}	46.0
h	0.029	-	0.003	8.563	3.75×10^{-14}	18.9
$\vartheta'_w \times h$	-0.444	-	0.060	-7.354	2.36×10^{-11}	16.2
ϑ'^2_w	5.341	m	0.832	6.417	2.72×10^{-09}	14.2
c	-0.006	m	0.003	-2.127	0.035	4.7
Number of observations: 128, Error degrees of freedom: 123 Root Mean Squared Error: 0.0197 R-squared: 0.453, F-statistic vs. constant model: 25.5, p-value = 2.13×10^{-15}						

As for the bedform height model, the intercept of the bedform length model in equation 4-8: (a) represents the theoretical minimum length expected for clay-free, 227 µm, sand; and (b) is expected to be mainly influenced by current forcing, and it should therefore represent the equilibrium length of current ripples in clay-free, 227 µm sand. The intercept value of 0.143 m is indeed within the range of 0.141-0.153 m predicted for the length of such ripples (Baas, 1999; Soulsby *et al*., 2012).

Equation 4-8 predicts that bedform length increases with increasing water depth. As for bedform height, this is interpreted to represent the relatively large bedform lengths during spring tide as opposed to neap tide. Therefore, wave ripples, dominant at Site 1 and formed mainly under oscillatory flow, and 'classic' current ripples, dominant at Site 3 and formed by relatively weak currents, have smaller lengths than the ripple-dune transitional bedforms, which were dominant at Site 2 and formed by relatively strong currents. The squared wave skin-friction Shields stress parameter, θ'^2_w, signifies a non-linear relationship with the bedform length. As for the bedform height (Section 4.6.6.1), this trend agrees with available bedform predictors, but the quadratic relationship might be an oversimplification associated with the limited range of pure wave conditions during data acquisition on the tidal flats.

As for the analysis of the bedform height, the $\theta'_w \times h$ parameter in equation 4-8 suggests that the effect of non-linearity on the wave parameters was not accounted for in the determination of wave skin-friction Shields stress. The low R-squared value of the regression (Table 4-8) is probably due to

the difficulty in determining the bedform orientation of 3D bedforms and resulting in noise in the bedform length values.

Finally, increasing the bed cohesive clay content is predicted to reduce the bedform length (Table 4-8), which agrees with available laboratory data (Baas *et al*., 2013; Schindler *et al*., 2015).

The length of current ripples, washed-out ripples, and dunes does not scale with θ'_c (Yalin, 1977; van Rijn, 1984c; Baas, 1994, 1999; Oost and Baas, 1994; Baas and De Koning, 1995). It is therefore likely that the lengths of bedforms transitional between ripples and dunes at Site 2 also do not scale with the current stress. This is supported by the multiple regression model, since θ'_c does not appear in equation 4-8. The model also predicts that, in contrast to the model for bedform height, non-linear interaction between waves and currents, in the form of $\theta'_c \times \theta'_w$, does not significantly change bedform length within the field dataset, despite the large non-linear effect of wave stress on bedform length.

4.6.6.3 Comparison of the regression model to the field data and bedform predictors

By comparing the multiple linear regression models to the field data used to create them (Figure 4-36), the quality of the models can be assessed. Overall, there is a good match between the field data and the regression model, as would be expected, especially where long-term changes in bedform height and length are concerned. However, there are examples of larger discrepancies between the predictions and data, in the order of a few millimetres, especially for bedform lengths at Site 2. Yet, the variation with water depth over a tide, *e.g.* in tidal periods 3, 8 and 13, is predicted reasonably well. Although the model correctly predicts a lower height and length for the washed-out bedforms in tidal periods 5 and 6, it predicts larger bedforms than those in the 3D-ARP scans (Figure 4-36a). The modelled bedform lengths in tidal periods 1 and 2 are too high (Figure 4-36b); this may be caused by the effect of hysteresis, as the bedforms in tidal period 1 were relict (see section 4.6.2.2).

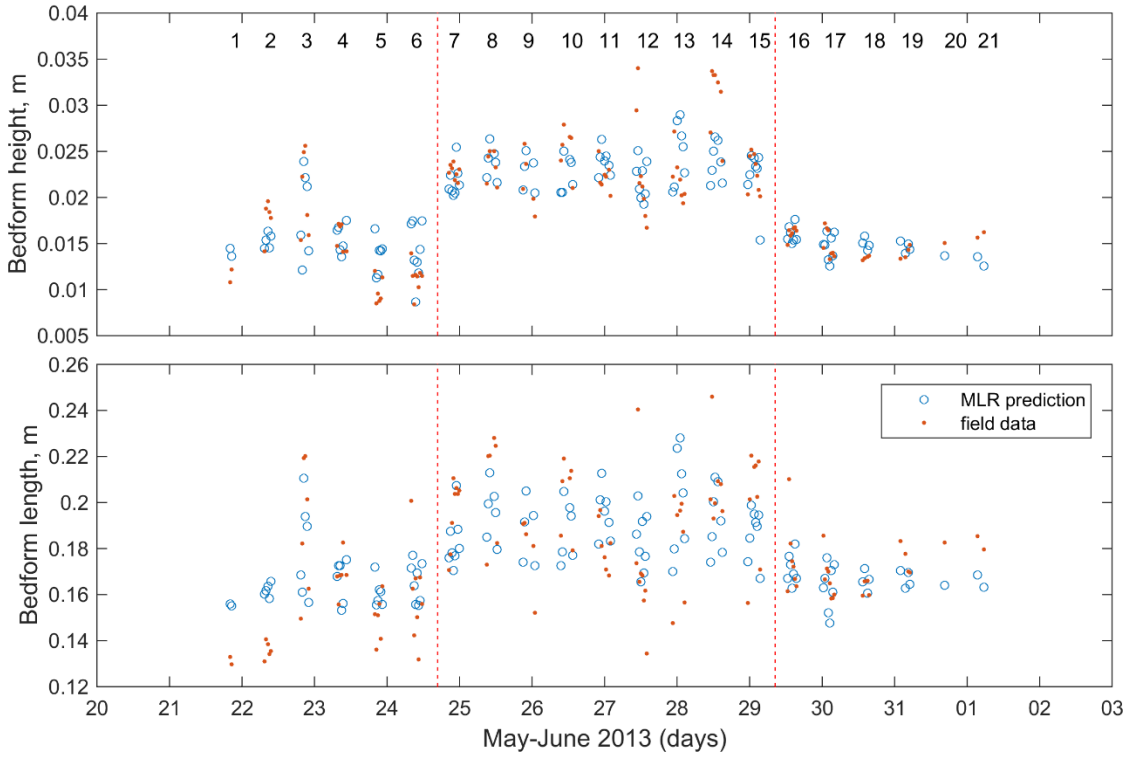

Figure 4-36: Comparison of MLR-modelled bedform heights and lengths with 3D-ARP derived bedform heights and lengths. Field data were extracted for combined Shields stress above the threshold of motion, from Soulsby and Whitehouse's equation (Soulsby, 1997), for D_{50} = 227 µm (n = 121). (a) Bedform height. (b) Bedform length.

The multiple linear regression models for bedform height and length (Equations 4-7 and 4-8), can be used as bedform predictors for the hydrodynamic (wave and current) and cohesive clay content forcing on tidal flats in the Dee estuary within the limits of the data set. A comparison of these models to existing bedform predictors is made below.

A comparison of the model intercepts to the equilibrium current ripple predictors of Baas (1999) and Soulsby *et al.* (2012) was made in Section 4.6.6.1. Table 4-9 provides a similar comparison based on the threshold Shields parameter for the movement of 227 µm sand, which is 0.051 (Soulsby, 1997). The heights and lengths of the current ripples predicted in this study to form just above this threshold compare remarkably well with those predicted by the existing predictors.

Table 4-9: Bedform height predictions for current ripples compared to the multiple linear regression model (MLR), for a water depth = 0.4 m, similar to the flume depth of the data of Baas (1999) and Soulsby *et al.* (2012), and no current or wave stress or cohesive clay.

Predictor	Height, η (m)	Length, λ (m)
Baas (1999), D_{50} = 238 μm	0.017	0.141
Soulsby *et al*. (2012), D_{50} = 227 μm	0.019	0.153
MLR, D_{50} = 227 μm	0.020	0.155

Figure 4-37 compares the measured wave ripple heights and lengths, and the regression models for 0% and 1.6 % cohesive clay, to the predicted heights and lengths of Wiberg & Harris (1994) and Soulsby *et al.* (2012) for tidal periods 2 to 4, when current forcing was insignificant or very small. Above the threshold velocity for sediment movement of 227 μm sand of 0.15 m s^{-1}, the predicted height and lengths for c = 0% agree well with the state-of-the-art Soulsby *et al.* (2012) predictor, but the wave-generated bedforms in the field area had lower predicted heights and lengths than in the older Wiberg & Harris (1994) predictor. In addition, the regression model predicts a small, but steady, increase in bedform height and length with increasing u_w, which agrees with the Soulsby *et al.* (2012) predictions, but not with the Wiberg & Harris (1994) predictions, which suggest a maximum in height and length at $0.25 < u_w < 0.3$ instead.

Figure 4-37 also shows the effect in cohesive clay in reducing the wave ripple height and length, based on the average cohesive clay content of 1.6% at tidal period 2 to 4. This reduction is largest for wave ripple height, and leads to the important observation that 1.6% cohesive clay in the bed noticeably offsets the regression model from the predicted bedform height values of Soulsby *et al*. (2012). The principal conclusion is that accounting for the effect of cohesive clay on bedform dimensions will improve the results of wave ripple predictors for mixed cohesive sediment.

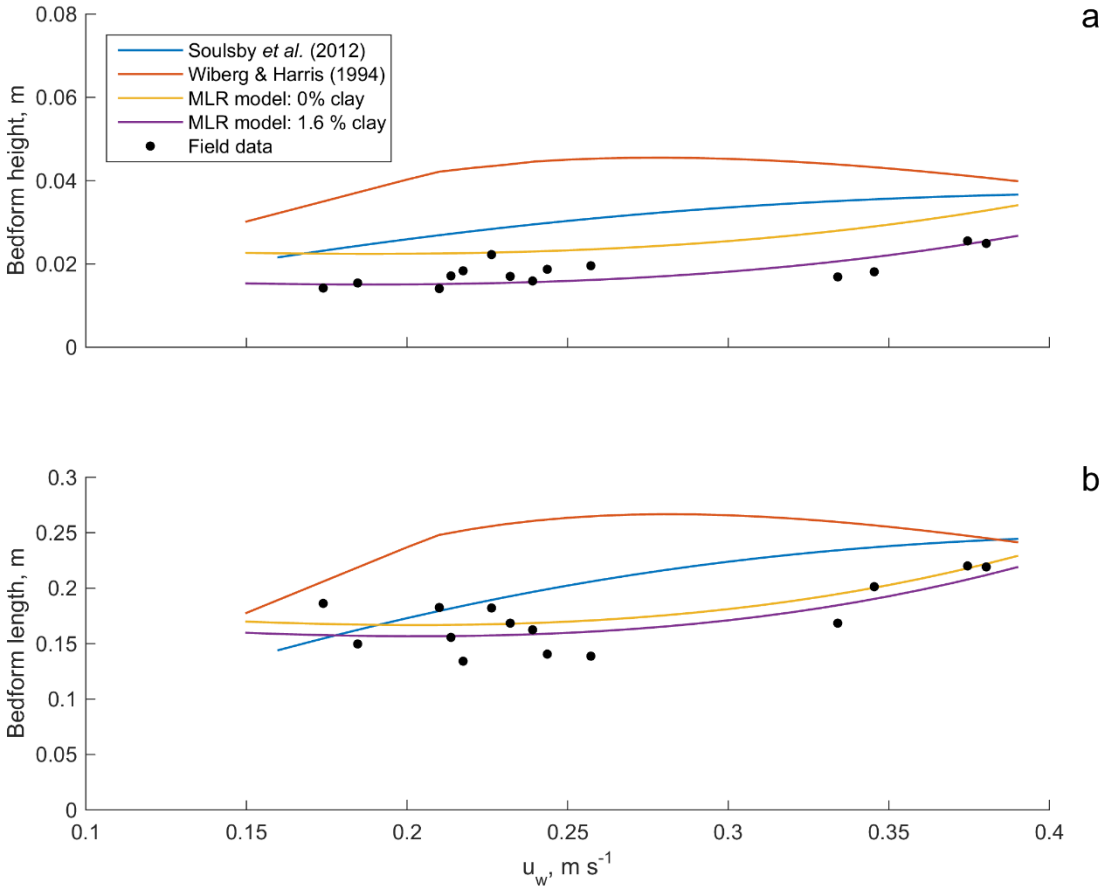

Figure 4-37: Comparison of the wave ripple predictors of Soulsby *et al*. (2012) and Wiberg and Harris (1994; Malarkey and Davies, 2003), multiple linear regression models (MLR) and the field data for bottom orbital amplitude velocity, u_w. (a) Bedform height and (b) bedform length. In order to compare wave-dominated conditions, the field values were selected for data from tidal periods 2 to 4 only (Figure 4-10b). The values shown are for above the critical threshold of sediment motion from Soulsby and Whitehouse's equation (Soulsby, 1997), for D_{50} = 227 µm. The wave ripple predictors are computed for wave period, T, = 6 s (an average value from the field data plotted) and grain diameter, D_{50}, = 227 µm. The MLR models are computed for current skin-friction Shields parameter, θ'_c, = 0 and water depth, h, = 1.6 m, and for cohesive clay, c, values 0% and 1.6%.

4.7 Discussion

4.7.1 Bedform classification, phase diagrams and size predictions

Even though the classification is based on well-cited previous work (Allen, 1968, 1982; Reineck & Singh, 1980; Amos *et al*. 1988b), there may be some subjectivity in the visual classification of the plan

morphologies of the bedforms from the 3D-ARP scans. Despite this reservation, several interesting relationships were observed in the data:

- Wave ripples and combined flow bedforms were dominant at Site 1. These were relict and 2D classic symmetrical wave ripples early on, and active and 3D asymmetrical combined flow ripples later in the record. The planforms of the 3D combined-flow bedforms included linguoid, lunate, and segmented. These bedform types have similarities with bedforms described in the literature for similar hydrodynamic forcings.
- Some bedforms formed in high-energy flows at Site 1 were washed-out ripples and flat beds with sand ribbons. In particular, the small-scale sand ribbons have not been reported in the field before.
- Site 2 had mainly 3D current-generated bedforms that were larger than equilibrium current ripples; some had a linguoid planform, others were more irregular (segmented), possibly linked to tidal rotation. These large current ripples, which scale with the water depth and are known from laboratory experiments, have not been reported from tidal flats before.
- The large current ripples at Site 2 were higher and longer than the 'classic' current ripples at Site 3. These large ripples, although varying with the water depth as expected for dunes, were closer to ripples in height and length. Further work is needed to verify if these bedforms were non-equilibrium dunes, or a newly discovered equilibrium phase between current ripples and dunes.
- Site 3 was dominated by 2.5D and 3D current ripples. These were mainly relict bedforms after about tidal period 19. Tidal periods 16 and 17 showed evidence of 3D combined-flow bedforms generated at high current-wave angles.
- The wave ripples at Site 1 were generally relatively small, and their size was predicted well by the Soulsby *et al.* (2012) predictor, especially when accounting for the effect of clay in the bed.
- The size of the current ripples at Site 3 was also predicted well by the Soulsby *et al.* (2012) current ripple size predictor.
- Water depth had no obvious effect on bedform dimensionality. In contrast, current and wave skin-friction Shields parameter and wave-current angle did have a significant effect, revealing logistic regression as a valuable tool for quantifying bedform dimensionality and distinguishing between wave and current forcing.
- The phase diagram for combined-flow bedforms and the classification scheme for bedform dimensionality of Perillo *et al.*'s (2014) did not agree well with the field dataset from the Dee estuary. The phase diagram of combined-flow bedform of Kleinhans (2005) showed a better match between predicted and observed bedform types.

- A new bedform phase diagram based on cohesive clay content and combined-flow Shields stress was proposed, which showed a transition from washed-out bedforms via wave ripples to current ripples, as θ'_{max} decreased and cohesive clay content increased above 1%. Below a clay content of 1%, this relationship broke down, suggesting that such mixed sand-clay bed behaved as if they were free of clay.

4.7.2 Limitations of matching the hydrodynamics to the bedform dimensions

The importance of the lag or hysteresis between bedform development and changes in flow forcing is evident from the presence of relict bedforms in the field dataset. However, it has not been possible to assess bedform hysteresis in more detail in the field dataset, because of the low temporal resolution of 3D-ARP data acquisition. Accurately matching the current and wave forcing to the bedform dynamics is also severely hampered by the unknown lag time between forcing and response, driven by the complex hydrodynamic conditions on the tidal flats. For example, large bedforms take longer to react to changing conditions than small bedforms; this time lag depends on the rate of sediment transport, which in turn is controlled by the shear stress acting upon the bed (Kleinhans, 2005; Traykovski, 2007). Despite the 3D-ARP being state-of-the-art, a relatively long time is needed to collect each scan. Therefore, this method is not suited to resolve the development of small-scale bedform within the short tidal inundation periods. Part of this problem could be resolved by reducing the time between 3D-ARP scans. Using a 2D-ARP would provide a much higher temporal resolution, but would not allow the planform morphology of the bedforms to be imaged. Controlled laboratory flume experiments for combined waves and currents in varying water depth would be a suitable method for simulating bedform hysteresis on tidal flats.

4.7.3 Logistic regression of the dimensionality

The predictions of logistic regression model of bimodal dimensionality (Figure 4-35) agree well with the visual observation that wave ripples and current ripples had predominantly 2D and 3D planforms, respectively, and the model even correctly predicts that the current ripples at Site 3 were not fully 3D. In general, however, 2.5D bedforms were predicted to be rare in the field dataset. Using binomial logistic regression for bedform dimensionality may be an oversimplification, applied here for convenience, and future work should use multinomial logistic regression on the three classes: 2D, 2.5D, and 3D. This would allow the inclusion of the 2.5D data that contained the high cohesive clay values at Site 3, and the cohesive clay term should then be found to be significant in the analysis.

4.7.4 Stepwise multiple linear regression analysis of bedform height and length

Stepwise multiple linear regression is a useful method for analysis complex systems with many influencing factors, but its imperfections should not be ignored. The inclusion or exclusion of controlling parameters is dependent on the range and quality of the input data, and it is not possible to test every combination of parameters. In addition, the user has to assess whether the model predictions make sense from the point of view of existing knowledge of basic controlling processes. For example, median grain size was not found to be significant by the stepwise multiple linear regression process, because of the narrow range of grain sizes in the data set. However, median grain size is represented in the intercepts and the threshold stress predictions of the models for bedform height and length, resulting in values close to the expected equilibrium dimensions for ripples in clay-free, 227 μm sand. In cases with a wider range of bed sediment size, median grain size is expected to be selected as significant control on bedform dimensions by the stepwise regression process, because it is well known from existing bedform predictors that grain size is an important parameter (*e.g.*, van Rijn, 1984c; Soulsby, 1997).

It was assumed in the regression analysis that the bedforms respond instantaneously to changes in the flow forcing. By using the rate of change of parameters, *e.g.* $\mathrm{d}\theta'_c/\mathrm{d}t$, the effect of time-varying current, waves and water depth could be incorporated into the regression model. This would help to account for hysteresis effects.

In general, the multiple linear regression models compare well to the predictors for current-generated and wave-generated bedforms. Current ripple dimensions are represented particularly well (Table 4-9), whereas the predicted wave ripple dimensions are close to the dimensions forecast by the latest wave ripple predictor (Soulsby *et al.*, 2012) (Figure 4-37). It comes as no surprise that the dune predictors tested in this chapter do not compare well with the dimensions of the studied bedforms in the Dee estuary, because their size is much closer to the typical size of current ripples. The current-dominated bedforms at Site 2, which varied in height with varying water depth, show evidence of being large ripples growing towards dune dimensions (*cf.* Bennett and Best, 1996; Baas, 1999). The regression model predicts the size of these bedforms reasonably well, and provides evidence that their size depends on the water depth, which differentiates them from 'classic' current ripples.

Despite the fact that cohesive clay content was added only as a linear parameter, without incorporating any potential interaction with the hydrodynamics, a higher cohesive clay content generally resulted in smaller bedforms. Following equation 4-7, bedform development would not

expected for a critical cohesive clay content of 4 vol% and above, and a flat bed or relict bedforms should be seen in such conditions. This critical cohesive clay limit increases with increasing water depth ($c_{crit} = 0.92h + 4.08$) and this is probably due to the relationship between water depth and current stress in tidal currents. As bed cohesive clay content was modelled from the bed samples collected when the tidal flats were exposed, between periods of tidal inundation, the behaviour of the clay and EPS in the system (*e.g.* by winnowing, deposition, filter feeding and bed re-working) cannot be resolved within tidal periods. This limits the analysis of the effect of cohesive forces in the bed to the spring-neap cycle. Yet, this study is valuable in that it has shown that cohesion is important on this time scale.

The stepwise regression has produced a model that predicts the size of wave-generated, current-generated, and combined-flow bedforms in varying flows, varying water depth, and varying bed clay-EPS content on the West Kirby tidal flats. For the bedform predictor to be more widely applicable, more field and laboratory flume data for a wider range of controlling factors should be acquired to further develop and independently test the model as a predictor for bedform dimensions.

4.7.5 The transition from ripples to dunes

The data in Figure 4-27 show that the large bedforms at Site 2 are current-generated bedforms transitional between ripples and dunes. The remaining bedforms in Figure 4-27 were predominantly relict, 'common', 3D current ripples found at Site 3. The height and length of the large ripples at Site 2 scale with the water depth. This sets these bedforms apart from 'common' current ripples that scale only with sediment size, but compares well with the scaling relationships for dunes. The transition between ripples and dunes is assumed to be abrupt in bedform phase diagrams (*e.g.* Southard and Boguchwal, 1990; van den Berg & van Gelder, 1993). However, as the change in size cannot be instantaneous, it is hypothesised that the large ripples at Site 2 were in an unstable state. In other words, ripples and dunes could been seen as stable equilibrium states for different hydrodynamic regimes (Bennet and Best, 1996), whereas the transition between these states is unstable, and not represented in bedform phase diagrams and bedform predictors. This would explain the lack of height and length data for bedforms in between ripples and dunes (Flemming, 1988; Ashley, 1990), as these bedforms would be transient, and relatively rare, under most flow conditions in rivers and estuaries. On the intertidal flats in the Dee estuary, where the flows and water depth changed continuously, these unstable transitional bedforms were present, because these bedforms were prevented from reaching equilibrium dune dimensions within a tidal period. Testing this hypothesis requires further work. However, Baas (1999) found, in laboratory flume experiments of fixed depth, that the

equilibrium size of current ripples increases with increasing current forcing at high current velocities in 238 μm sand, as would be expected for dunes. This suggests that there may be a stability field in between that of current ripples and dunes, in which bedforms have height and lengths intermediate between ripples and dunes, and these height and lengths scale with current forcing. The fact that these bedforms are relatively rare might indicate that the stability field of this transient bedform type covers a narrow range of bed shear stresses.

4.7.6 The effect of bed cohesion on bedform morphology and size

The new phase diagram for cohesive clay and combined bed shear stress shows a transition from washed-out bedforms to 3D current ripples, as the bed cohesive clay content increases and the bed shear stress decreases, but only when the bed cohesive clay content is greater than 1% (Figure 4-31). This was suggested above to denote a decreasing rate in clay winnowing with reducing bed shear stress.

The multiple linear regression models show that the cohesive clay content has a significant effect on bedform dimensions. Increasing the cohesive clay content reduces the bedform height and length. This is agrees with the laboratory results of Baas *et al*. (2013), Schindler *et al*. (2015) and Parsons *et al*. (2016). Baas *et al*. (2013) found that cohesive clay had a greater effect on bedform height than bedform length. The multiple linear regression model data has shown a similar result, with cohesive clay having a 19% relative influence on bedform height and a 5% influence on bedform length (Table 4-6 and Table 4-8).

4.7.7 Implications of reduced bedform dimensions due to cohesion

This field study confirms previous laboratory studies (Baas *et al*., 2013; Schindler *et al*. 2015; Parsons *et al*. 2016) that showed that small amounts of cohesive material can significantly reduce the dimensions of sandy bedforms. The presence of clay and EPS therefore affects the roughness of the seabed, which in turn lead to a reduction in the friction experienced by the currents and waves, turbulence generation, energy dissipation above the bed and physical disturbance of the bed (Aldridge *et al*., 2015; Parsons *et al*., 2016). On a regional scale, this is likely to have a significant effect on the transport of sediment, pollutants, and nutrients, on biochemical processes at the seabed-water interface, and on larger-scale morphological change (Precht and Huettel, 2003; Aldridge *et al*., 2015; Parsons *et al*., 2016). At present, numerical models for sediment transport seldom incorporate mixed sand-mud-EPS. This study suggests that this should be an essential next step in improving such models,

and, in addition, help optimise the design of coastal structures and management interventions (Aldridge *et al*., 2015; Parsons *et al*., 2016).

4.8 Conclusions

The effect bed cohesive clay reducing bedform dimensions and affecting the development of bedform plan morphology to 3D forms has been demonstrated in field conditions, with a greater effect on bedform height reduction than bedform length. These results confirm the laboratory flume results of Baas *et al*. (2013), Schindler *et al*. (2015) and Parsons *et al*. (2016).

Many of the current dominated bedforms present on the tidal flats did not conform well to ideal types, when compared to bedform phase diagrams and equilibrium bedform predictors. It is concluded that as these current bedforms scaled with water depth and were larger than the expected equilibrium dimensions for current ripples, they represent transitional bedforms developing towards dunes (*e.g.* Bennet and Best, 1996) and may show evidence of an intermediate type of bedform, 'large current ripple', seen in the laboratory (Baas, 1999).

From the multiple linear regressions, empirical relationships were determined for bedform height and length, for wave and current forcing in varying water depth and for mixed cohesive sediment. In addition, the critical cohesive clay limit for bedform development was found to increase with increasing water depth and this may be due to the relationship of tidal height with current stress. Although limited by the local cohesive properties on the tidal flats studied, these relationships may be applicable to similar intertidal areas, of sandy cohesive sediment and tidal range of a few metres, though consideration must be made to the specific sediment grain size and bed cohesion. More data covering varying sediment grain sizes and bed cohesive compositions, in different environments and laboratory conditions, would make the relationships more widely applicable, though the effect of hydrodynamics, waves and water depth will be universal.

By improving the parameterisation of bedforms formed of mixed cohesive sediment in shallow tidally varying flows, better characterisation of bed roughness effects can be applied to work on tidal and wave energy dissipation, sediment transport, flooding and processes occurring across the seabed-water interface. These results can also help in the interpretation of bedforms in the sedimentary record, leading to improved interpretation of the hydrodynamic and wave processes acting when the beds were deposited.

5 Bedform migration and bed material transport in a mixed sand-mud intertidal environment

5.1 Summary

The migration rate of bedforms, such as ripples and dunes, in coastal and estuarine environments is important in determining bed material transport rates to inform and validate numerical models of sediment transport and geomorphology. However, these models tend to ignore parameters describing the physical and biological cohesion in natural mixed sediment (resulting from cohesive clay and extracellular polymeric substances, EPS, in the mud), largely because of a scarcity of relevant field data. To address this gap in knowledge, data were collected on intertidal flats over a spring-neap cycle to determine the bed material transport rates of bedforms in biologically active mixed sand-mud.

When the effect of waves had been accounted for, the bedform migration rate for mixed cohesive sediments in the field was significantly different from that of sand-only bedforms. Using multiple linear regression, the bed material transport rate was found to depend on the Shields stress parameter and vol% bed cohesive clay. Transport rates decreased with increasing cohesive clay and EPS, when the bed cohesive clay and EPS contents were below 2.8 vol% and 0.05 wt%, respectively. These limits correspond approximately to the points where cohesive clay and EPS began to significantly affect the migration rate and bedform dimensions in the mixed clay-sand laboratory experiments of Baas *et al*. (2013) and the mixed sand-EPS laboratory experiments of Malarkey *et al*. (2015). This work has important implications for the circumstances under which existing sand-only bedform migration transport formulae may be applied in a mixed sand-clay environment, as even small amounts of cohesive material can have an effect on what appears to be clean sand.

5.2 Introduction

Knowing the rate of migration of sedimentary bedforms, such as ripples and dunes, in coastal and estuarine environments is important in determining the bed material transport rate in sediment transport models (*e.g.*, Hubbell, 1964; Simons, 1965; van Rijn, 1984c, 2006; van den Berg, 1987; Hoekstra *et al*., 2004). Even though many of these environments are dominated by mixed cohesive sediment, models still tend to ignore that mixed sand-mud and non-cohesive, mud-free sand, behave differently (Amoudry *et al*., 2009; Amoudry and Souza, 2011). Improvements in model predictions, or at least better insights into the range of conditions to which these models are relevant, should be

possible by investigating the relationship between hydrodynamic forcing and bedform migration rate for mixed cohesive sediment.

Mixtures of cohesive mud and sand have an increased critical shear stress for erosion compared to pure sand or mud (Mitchener and Torfs, 1996; Panagiotopoulos *et al*., 1997; Jacobs *et al*., 2011). The transition from erosion dominated by non-cohesive sand to cohesive clay has been found to occur at 3-5 wt% (5-8 vol%) clay (van Ledden *et al*., 2004). Laboratory experiments and field measurements have demonstrated that bedforms can be inhibited from forming (Hagadorn and McDowell, 2012) and stabilized once formed (Grant *et al*., 1986), due to biogenic cohesion from Extracellular Polymeric Substances (EPS) produced benthic organisms. More recent laboratory experiments using mixed cohesive and non-cohesive sediment, have shown that the development rate of the bedforms is reduced by both physical and biological cohesion (Baas *et al*., 2013; Malarkey *et al*., 2015; Schindler *et al*., 2015; Parsons *et al*., 2016). These authors also showed that the clay and EPS were selectively entrained into suspension while the ripples and dunes formed and migrated on the bed. This entrainment process of clay and EPS has been referred to as winnowing (*e.g.*, Lisle and Hilton, 1992; Harris *et al*., 1993). Winnowing in the experiments of Baas *et al*. (2013), Malarkey *et al*. (2015), Schindler *et al*. (2015) and Parsons *et al*. (2016) caused the bedforms to migrate as if they were composed of clean sand, due to the reduction in bed clay and EPS content, despite their reduced development rate.

Bed mud content and biological production of EPS can be affected by the magnitude of the bed shear stress. Low stress promotes biological production and mud deposition, whereas high stress winnows cohesive material and provides poor conditions for microbial growth (van de Koppel *et al*., 2001), and has been proposed as an explanation for the occurrence of ripple stabilization in the field (Friend *et al*., 2008). Friend *et al*. (2008) found that a microalgal bloom coinciding with neap tides was sufficient to stabilize ripples on tidal flats for a period of four weeks. The influence of bed shear stress may lead to switching between alternate stable seabed states of cohesive erosion-resistant beds with well-developed biofilms and non-cohesive mobile beds, in environments with varying bed shear stress (van de Koppel *et al*., 2001).

Sediment transport, by the movement of current-generated bedforms on beds comprising biologically active mixtures of sand and mud, is assumed to be controlled by the migration rate and the height of the bedforms, similar to bed material transport in pure sand (Hubbell, 1964; van den Berg, 1987). However, the cohesive forces within the bed might affect the bed material transport rate, as a few percent of clay and less than 0.1 wt% of EPS can be sufficient to significantly slow bedform growth (Baas *et al*., 2013; Malarkey *et al*., 2015). The migration rate of current ripples in clean sand and silt

for unidirectional currents has been studied in laboratory flumes (van den Berg and van Gelder, 1993b; Baas *et al*., 2000). Here, these experimental data are compared with the migration rate of similar bedforms in mixed sand-mud on natural intertidal flats in the Dee Estuary, near West Kirby, north-west England.

5.3 Aims

- To extend the widely used relationship between bedform migration rate and bed material transport rate (Hubbell, 1964; van den Berg, 1987) from laboratory to field conditions
- To determine the effect of cohesion by clay and EPS on bed material transport rate.

To start, a description of a method for relating the field-based hydrodynamic data to bedform migration rate and bed material transport rate is outlined. Subsequently, the calculated bedform migration rates for the mixed sand-mud in the field are compared to laboratory flume data for pure sand with a similar grain size. Thereafter, a multiple linear regression analysis is applied to quantify the effect of bed cohesion on the bed material transport rate in relation to bed shear stress. Finally, recommendations are made for sediment transport modelling in mixed cohesive sediment.

5.4 Relating current bedform migration rate to bed material transport rate

Current-generated bedforms migrate in the direction of the hydrodynamic forcing by erosion of sediment from the low-angle slope of the upstream face and deposition by avalanching on the steep downstream face of these bedforms (Deacon, 1894; Sternberg, 1967; Allen, 1968; Smyth and Li, 2005). The rate of migration of these bedforms depends on the sediment characteristics, chiefly its grain size, the size of the bedforms, and the hydrodynamic forcing (*e.g.*, van den Berg, 1987). Successive bed profile measurements with a known time interval can be used to calculate the migration rate of bedforms (Sternberg, 1967; van den Berg, 1987; Bell and Thorne, 1997a; Hoekstra *et al*., 2004; Masselink *et al*., 2007). The bed material transport rate can then be calculated from this migration rate, if the size, geometry, and porosity of the bedforms are known (Hubbell, 1964; Simons, 1965; van den Berg, 1987; Hoekstra *et al*., 2004). This procedure is described below. The hydrodynamic forcing that drives bedform migration has been detailed in section 3.8.1.2.

5.4.1 Migration rate of current-generated bedforms

Sediment transport is commonly parameterized in terms of dimensionless quantities (Yalin, 1977), for example the Shields parameter. The skin friction component of the shear stress determines the movement of sediment particles on the bed, and is therefore important for the migration of bedforms and the bed material transport rate. Plotting the bedform migration rate against skin friction mobility parameter allows a comparison to be made between these parameters for different sediment sizes (Baas *et al*., 2000). Baas *et al*. (2000) proposed a simple power law relationship between experimental data on the bedform migration rate, u_b, for current ripples and the skin-friction related Shields parameter, θ' (Figure 5-1):

$$u_b = \alpha\theta'^{\beta} \qquad \textbf{5-1}$$

where α and β are coefficients that vary with the size of the sediment on the bed (Baas *et al*., 2000). Baas *et al*. (2000) showed that α and β increase with increasing median grain diameter. Hence, bedforms composed of coarser grains migrate faster than bedforms composed of finer grains at the same Shields parameter (Figure 5-1).

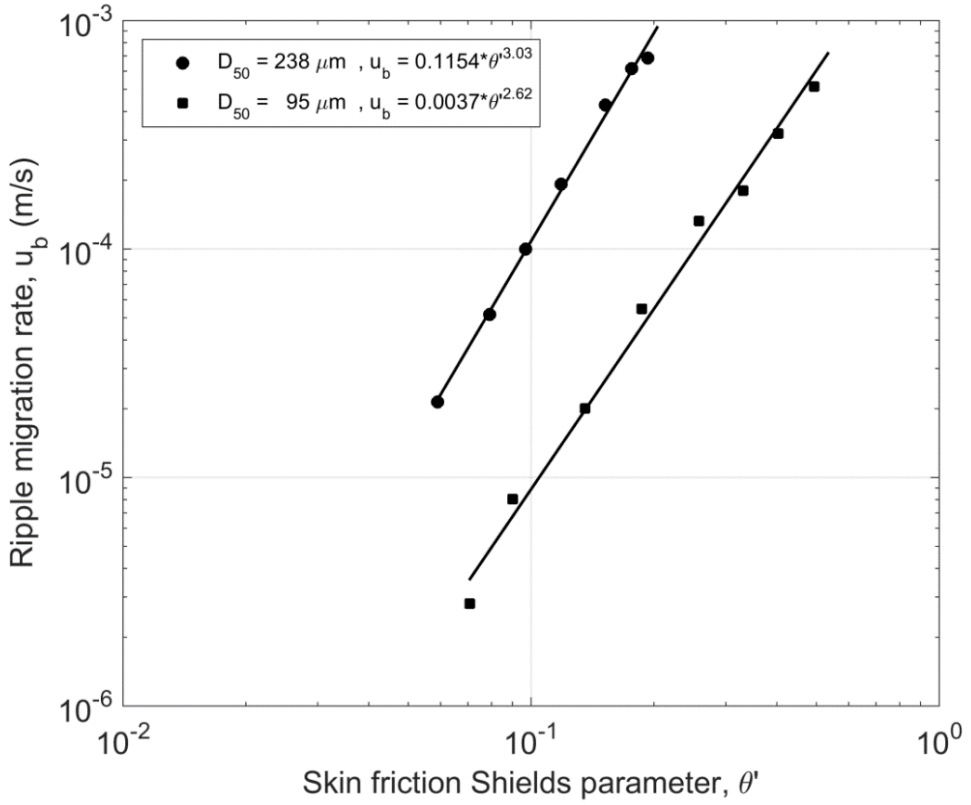

Figure 5-1: Empirical relationships between the migration rate of equilibrium current ripples and the skin-friction Shields mobility parameter for two median grain sizes: 238 µm and 95 µm (modified after Baas *et al*. (2000)). The raw data have been re-processed using the same roughness-length specification of skin friction as for the field data ($z_0 = D_{50}/12$).

5.4.2 Bed material transport rate

Richardson *et al*. (1961) assumed a triangular bedform shape in vertical cross-sections parallel to the flow direction to propose the basic equation for the transport rate of bed material through bedform migration:

$$q_b = 0.5\,(1 - P)\,u_b\,\eta \qquad \textbf{5-2}$$

where q_b is the volume transport rate per unit width, η is the bedform height and P is the porosity of the bed. However, most ripples and dunes do not have a perfectly triangular shape in cross-section. Therefore, van Rijn (2006) replaced the factor 0.5 in equation 5-2 with a bedform shape factor, f, which has been shown to be approximately 0.6 for current ripples and dunes (van den Berg, 1987; Hoekstra *et al*., 2004; Baas *et al*., 2011). Equation 5-2 also assumes that mean bedform height does not change during bedform migration (i.e., the bedforms are in perfect equilibrium with the flow conditions), and

losses or gains of sediment from the sampling area by resuspension or deposition are absent (van den Berg, 1987). Hubbell (1964) proposed a factor, K, to account for sediment loss by resuspension and sediment gain by deposition. In order to calculate the mass transport rate, Q_b, the volume transport rate, q_b, needs to be multiplied by the sediment density (van Rijn, 1984c, 2006; van den Berg, 1987):

$$Q_b = K\rho_s(1-P)fu_b\eta \qquad \textbf{5-3}$$

Equation 5-3 thus accounts for variations in bedform shape through *f*, and for net resuspension and net deposition through *K*.

5.5 Methods

The background to the field site, details of the instrumentation deployed and sampling carried out were described in Chapter 3. The migration rates and bed material transport rates of small-scale bedforms in biologically active, mixed sand-mud, were determined and compared with data from laboratory bedforms in pure sand (Baas *et al*., 2000), mixed sand-clay (Baas *et al*., 2013) and mixed sand-EPS (Malarkey *et al*., 2015). The bed cohesive clay content were in the range of 0.6 to 5.4 vol% and due to the relationship between EPS and cohesive clay, shown in section 3.9.4,the cohesive clay content refers to both physical and biological cohesion.

5.5.1 Bedform migration data

While 1D cross-correlation techniques have been used previously to determine bedform migration (Smyth and Li, 2005; Masselink *et al.*, 2007), here these are generalized by using 2D techniques (Giachetti, 2000; Sutton *et al.*, 2009). 1D methods only resolve the bedform migration in a single axis, and assume that waves and currents are in the same direction, by using 2D cross-correlation tidal rotation and wave forcing at different angles can be accounted for. The bedform migration rate was calculated from the spatial difference between successive half-hourly 3D-ARP bed scans, determined by 2D cross-correlation (Figure 5-2a, b), the distance migrated between two scans divided by the 30-minute interval. Prior to the 2D cross-correlation, large-scale bed topography was removed from each scan using orthogonal least squares regression (Borradaile, 2003), also known as major axis regression. This method assumes that all the variables have errors, in contrast to standard linear regression, which assumes that only the dependent variable has errors (Borradaile, 2003). The 3D-ARP scans used for the 2D cross-correlation were sub-sampled over areas of 0.5×0.5 m to remove the potential influence

of the instrument frame on bedform dynamics. The 2D cross-correlation of the half-hourly scan pairs yielded 143 bedform migration rates. The 3D-ARP data were processed to a spatial resolution of 0.005 m. For the half-hourly sampling interval, the minimum ripple migration rate detectable was 2.8×10^{-6} m s^{-1}. All migration rates at and below this limit were excluded from the regression model.

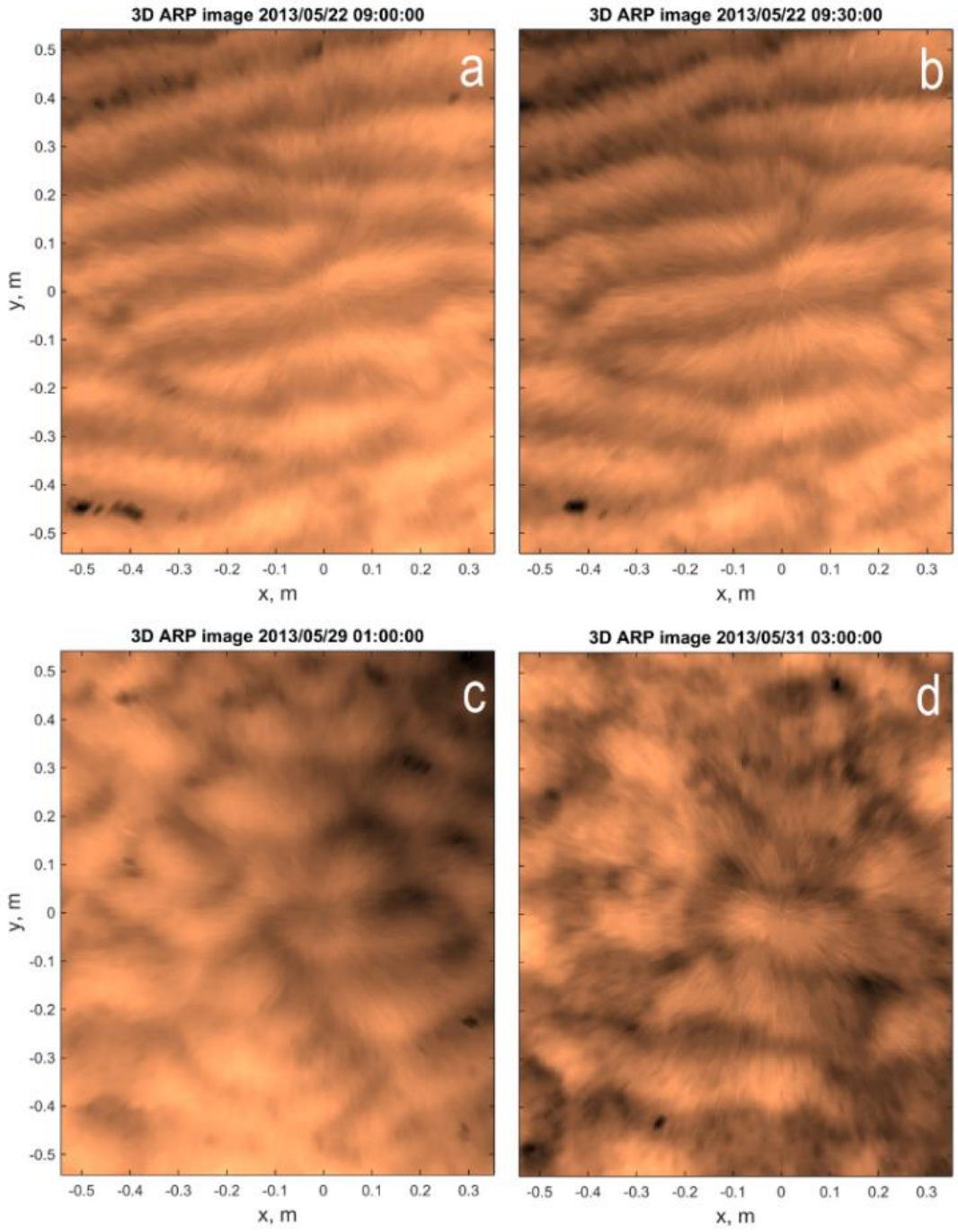

Figure 5-2: (a, b) A pair of 3D Acoustic Ripple Profiler (3D-ARP) scans from Site 1. The migration distance and migration rate were 0.015 m and 8.33×10^{-6} m s^{-1}, respectively. (c) A 3D-ARP scan from Site 2 showing short-crested, three-dimensional bedforms. (d) A 3D-ARP scan from Site 3 showing two-dimensional sinuous bedforms.

The error of the cross-correlation of bedform migration distance was estimated from the peak normalized cross-correlation value, $\rho_{12}(\tau^*)$, the bandwidth of the data, B, and the record length, T_{rl}, in the vector direction of the 2D lag (to reduce the problem from two dimensional to one dimensional). The estimate of the normalized RMS error, E_{nrms}, for the peak correlation lag, τ^*, is (Bendat and Piersol, 1986):

$$E_{nrms} = \frac{1}{\sqrt{2BT_{rl}}}\left[1 + \frac{1}{\rho_{12}^2(\tau^*)}\right]^{0.5}$$

5-4

where the normalized cross-correlation function, $\rho_{12}(\tau^*)$, is:

$$\rho_{12}(\tau^*) = \frac{R_{12}(\tau^*)}{\sqrt{R_{11}(0)R_{22}(0)}}$$

5-5

and $R_{12}(\tau^*)$ is the cross-correlation function, $R_{11}(0)$ is the autocorrelation function for scan 1 at zero lag, and $R_{22}(0)$ is the autocorrelation function for scan 2 at zero lag. The normalized root-mean square (RMS) error was used to estimate the standard deviation, $\sigma(\tau^*)$, and the 95% confidence interval, C, (Bendat and Piersol, 1986):

$$\sigma(\tau^*) = \frac{0.93}{\pi B}\sqrt{E_{nrms}}$$

5-6

$$C = 1.96\sigma(\tau^*)$$

5-7

where the bandwidth, B, is the wave number of the lag interval, which in the present study is the inverse of the horizontal resolution of 0.005 m. The standard deviation and confidence interval values were divided by the time interval to determine the error for the migration rate.

5.5.2 Hydrodynamic data analysis

The ADV time series was processed in 30-minute windows, to match the interval used to collect the bedform migration rate data, to extract current, wave and bed shear stress values, using the procedure described in section 3.8.1. The skin friction Shields parameter, θ'_{max}, was calculated for τ'_{max}, and θ'_{max} was then used to compare to the bedform migration rates and bed material transport

rates. In the absence of waves, $\theta'_{max} = \theta'$. The original velocity data of Baas *et al.* (2000) were re-processed using the same roughness length specification of skin friction as for the field data ($z_0 = D_{50}/12$), so that all bed shear stress calculations in the present study were based on the same procedure.

5.5.3 Bed material transport rate

Equation 5-3 was used to calculate bed material transport rate. The bedform migration rates were derived from the 3D-ARP data via 2D cross-correlation, as described in section 5.5.1, and the bedform dimensions were computed using the zero-crossing method described in section 3.8.2.3. For the purpose of verifying if the bedforms had reached equilibrium dimensions, the measured bedform dimensions were compared with the equilibrium ripple dimensions for D_{50} = 238 µm, measured by Baas (1999) (height η_{eq} = 0.017 m; length, λ_{eq} = 0.141 m), and predicted by the empirical relationships of Soulsby *et al.* (2012) (height, η_{eq}, = 0.019 m and length, λ_{eq}, = 0.153 m, for D_{50} = 227 µm) as detailed in section 4.4.4.1.

The shape factor, f, the sediment loss-gain factor, K, and the sediment density, ρ_s, in equation 5-3 were kept constant at 0.6, 1, and 2650 kg m^{-3}, respectively (van den Berg, 1987; van Rijn, 2006). The shape factor of 0.6 assumes that all the bedforms have a cross-section similar to common ripples and dunes, and the sediment loss-gain factor of 1 assumes no significant loss or gain of bed sediment. A porosity of 0.4 was used for both the laboratory and field sand, which is a compromise between loosely packed and tightly packed natural sand (*e.g.*, Allen 1984). It has been assumed that the change in porosity because of the presence of mud (< 15%) was small.

5.6 Results

5.6.1 Flow forcing

During the study period in 2013, the tide advanced from neap to spring and back to neap (Figure 5-3a, b). The measurements at Site 1 were conducted during the transition from neap to spring tide, spring tide prevailed at Site 2, and Site 3 was sampled during the transition from spring to neap tide. North-westerly winds dominated when Site 1 was sampled, with wind conditions from moderate breezes up to gale force (Beaufort scale 4-8; 5.8 - 17.6 m s^{-1}). These high winds caused wave height to increase (Figure 5-3c), albeit modulated by the depth of the tidal flows (Brown, 2010; Friedrichs, 2011). The wave periods ranged from 2 to 10 seconds (Figure 5-3d). The strong winds at Site 1 generated wind-

driven flow that increased the velocity magnitude of the flood tide, compared to the fair-weather conditions present Site 3, and prevented a clear slack water from occurring at high tide (Figure 5-3a, b). The bed shear stress data reveal similar patterns (Figure 5-4a,b,c). The wind-driven flow caused an increase in the current-only bed shear stress on 22-25 May (Figure 5-4a), when the wave bottom orbital velocities were highest (Figure 5-3e). Despite experiencing spring tide, the peak current-only bed shear stress for Site 2 was similar to that at Site 1 (Figure 5-4a). Relatively weak currents dominated the neap tide for Site 3, resulting in low bed shear stresses (Figure 5-4a). Wave-only bed shear stresses were significant during the strong north-westerly wind conditions at Site 1 (Figure 5-4b).

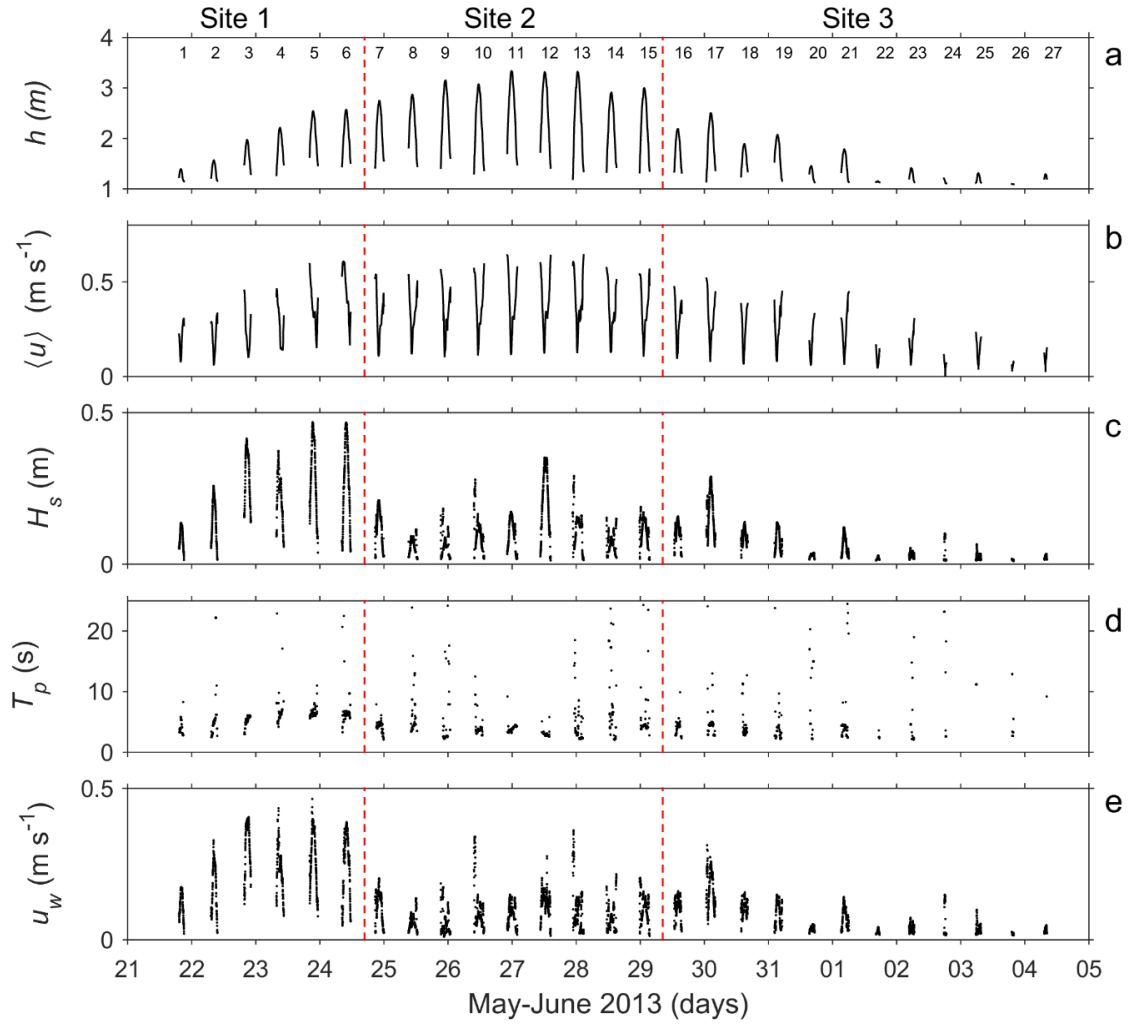

Figure 5-3: Times series of (a) water depth, h; (b) depth-averaged flow velocity (30 minute running mean), $\langle u \rangle$; (c) significant wave height, H_s; (d) peak wave period, T_p; and (e) wave bottom orbital amplitude velocity, u_w. The vertical red dashed lines mark the times when the instruments were moved between sites. The data shown are for when the tidal flats were inundated with water above the height of the sensors, processed for a 30-minute window. The wave period data have been filtered to show only the wind-generated waves of periods less than 25 seconds (USACE, 2002a). The numbers in (a) denote the tidal periods for reference.

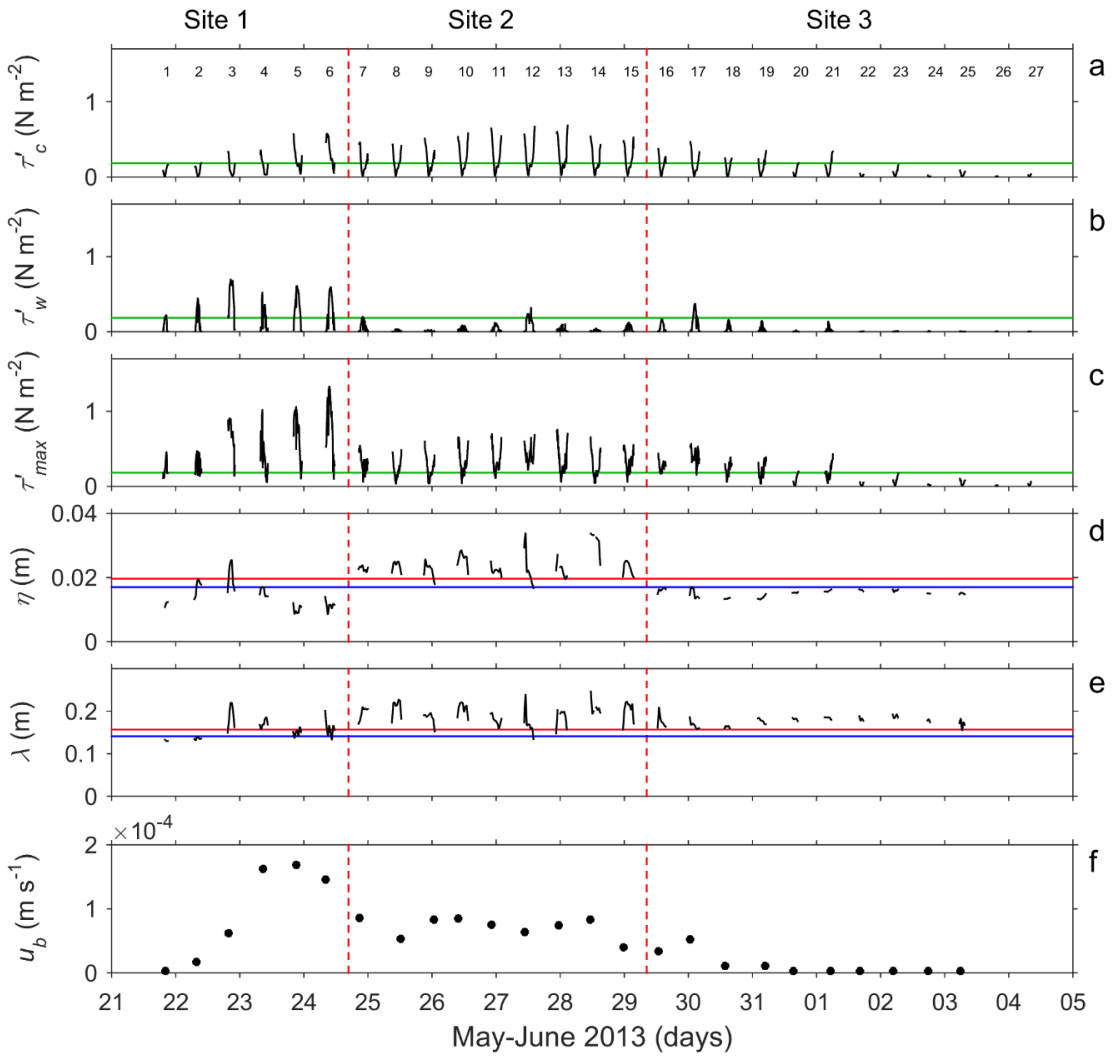

Figure 5-4: Times series of (a) current-only bed shear stress, τ'_c; (b) wave-only bed shear stress, τ'_w; (c) combined maximum bed shear stress, τ'_{max} and linear maximum bed shear stress, τ'_{maxl} (magenta dashed line); (d) bedform height, η; (e) bedform length, λ; and (f) maximum bedform migration rate, u_b, for each tidal cycle derived from the 3D-ARP scans. The vertical red dashed lines mark the times when the instruments were moved between sites. The horizontal green lines denote the critical stress limit of sediment motion from Soulsby and Whitehouse's equation (Soulsby, 1997), for D_{50} = 227 µm, 0.18 N m^{-2}. In d and e, the blue and red lines are the equilibrium ripple dimensions of Baas (1999) and Soulsby *et al.* (2012), respectively. The data shown are for when the tidal flats were inundated with water above the height of the sensors, processed for a 30-minute window. The numbers in (a) denote the tidal periods for reference.

5.6.2 Bedform types and migration

The seabed was covered by two-dimensional and three-dimensional bedforms. Two-dimensional bedforms evolved into three-dimensional bedforms on the evening of 22 May at Site 1 and persisted over Site 2 (Figure 5-2c). The three-dimensional bedforms were replaced by two-dimensional bedforms on 30 May at Site 3 (Figure 5-2d). Two characteristic 3D-ARP scans, 30 minutes apart from Site 1, shown in Figure 5-2a and b, exhibit two-dimensional bedforms with distinct bifurcations, thus suggesting a significant wave influence (Allen, 1968). Examples of the three-dimensional bedforms from Site 2 and the two-dimensional bedforms with sinuous crest lines from Site 3 are shown in Figures 6c and 6d, respectively. The time-series of mean bedform height and length for each 3D-ARP scan are plotted in Figure 5-4d and e. The predicted equilibrium heights and lengths for current ripples of 0.017 m and 0.141 m (Baas, 1999) and of 0.020 m and 0.157 m (Soulsby *et al.*, 2012) are shown for comparison. The bedforms that developed at Site 1 were wave-influenced current ripples, Site 2 was dominated by transitional bedforms between ripples and dunes, while current ripples close to equilibrium dimensions prevailed at Site 3 (Figure 5-4d, e).

A time-series of maximum bedform migration rate for each tidal cycle was derived from the 3D-ARP scans (Figure 5-4f). The migration rates at Site 1 appear to have been enhanced by wind-driven flow and waves. The bedforms at Site 2, which was sampled during a period of relatively fast-flowing tidal currents, had higher migration rates than the bedforms at Site 3, where bed shear stresses were only able to move the bedforms during the last two days in May. It appears that the bedforms stopped migrating on 31 May at Site 3.

5.6.3 Comparing flow forcing and ripple migration

The relationship between bedform migration rate, u_b, and skin friction Shields parameter, θ'_{max}, is shown in Figure 5-5. The bedform migration rate was assumed to have the same direction as the maximum shear stress, without any lag in the response to changes in θ'_{max}. An orthogonal least squares regression model was used to fit the bedform migration rate to the Shields parameter. The regression fit line for the laboratory-derived data of Baas *et al*. (2000) is shown for comparison (black line in Figure 5-5). The field data reveal a strong positive correlation between u_b and θ'_{max}. This relationship can be described by a power function (Equation 5-1), as in Baas *et al*. (2000), with R^2 = 0.89 based on an orthogonal least squares regression with α = 0.2267 m s^{-1} and β = 4.28 (solid grey line in Figure 5-5). The data along the line of 'no migration' (dashed horizontal grey line in Figure 5-5) were excluded from the regression analysis, as these data are at or below the resolution limit of the 3D-ARP. It is unclear whether these bedforms moved very slowly or were stationary. Based on Soulsby

and Whitehouse's formula for the critical Shield parameter of motion (Soulsby, 1997), migration in 227 µm sand is expected for θ' > 0.051. 'No migration' points in the field data for stresses higher than this threshold correspond to high wave stress combined with very low current stress or high bed cohesive clay and EPS content (Figure 5-5). These high cohesive clay fractions were present at Site 3, where the bed shear stresses were small compared to the other two sites (Figure 5-4c). The mobile bedforms with low cohesive clay and EPS content, which dominated during the sampling of Sites 1 and 2, scatter round the regression fit line of θ'_{max} and u_b (Figure 5-5). The migration rates of the mixed-sediment bedforms in the field were lower than the migration rates of the pure-sand bedforms in the laboratory (Figure 5-5, *cf*. filled circles with black line).

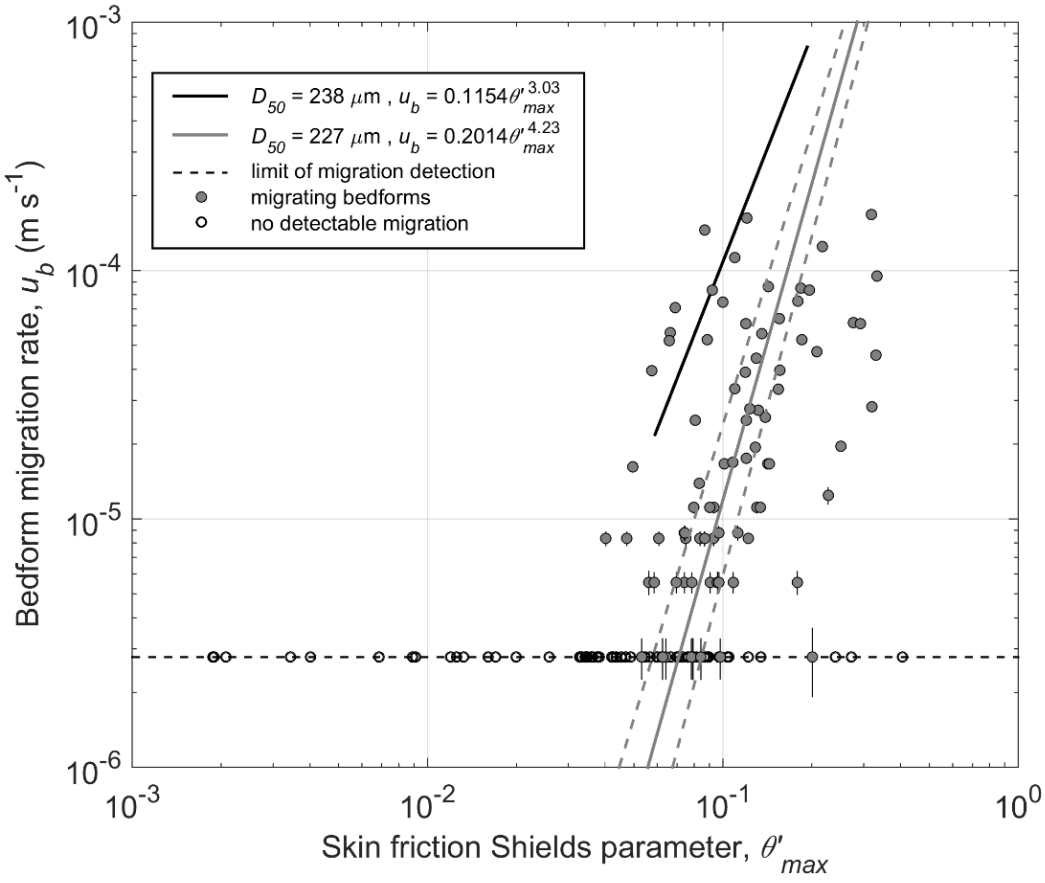

Figure 5-5: Bedform migration rate against skin friction Shields parameter for combined currents and waves. The black line denotes the 238 µm regression fit for the clean sand laboratory data of Baas *et al*. (2000), as in Figure 5-1. The dashed black horizontal line and the superimposed open circles denote the lowest measurable migration rates by the 3D-ARP. These data were excluded from the regression analysis. Extreme values greater than 2.58 standard deviations (outside 99% of the data) were also excluded from the regression analysis (n = 81 values in the regression fit). The regression fit equation for the field data is represented by the solid dark grey line, and the dashed dark grey lines denote the 95% confidence limits of the regression fit line. The error bars for u_b represent the 95% confidence limits of the migration points.

5.6.4 Bed material transport rate

The scatter in the migration rates for the field data (Figure 5-5), and the fact that these rates are lower than the pure-sand migration rates, suggests that in addition to the maximum skin friction bed shear stress, the varying bed cohesive clay content also has an effect on migration rates. As the Equation 5-3, for the bed material transport rate, Q_b, depends on the bedform migration rate, u_b, it will also depend on both the bed shear stress and be affected by the bed cohesive clay content. Hence, α and β in equation 5-1, and in its equivalent for Q_b, should depend on the cohesive clay present in the bed. In order to investigate this dependence, bedform migration rates were extracted for the peak θ'_{max} during the flood and ebb of each tidal inundation period, as these values occur at the beginning and end of the inundation (Figure 5-4c), and are therefore temporally closest to the cohesive clay contents from the bed samples collected between inundations.

Added to the extracted subset of the field data are the clean sand data (D_{50} = 238 µm) from the laboratory-based migration data of Baas *et al*. (2000) to provide values for sediment without cohesive clay (Figure 5-1), since all the field sediment samples contained some cohesive clay. There was a significant inverse linear relationship between bed material transport rate and bed cohesive clay content for this composite dataset (R^2 = 0.44, $p < 0.05$ and RMS error = 0.46, for n = 41; Figure 5-6). Baas *et al*. (2013) found a similar inverse relationship between bed material transport rate and kaolin clay content in laboratory experiments. However, there is far greater scatter in the present case because of the additional dependence on shear stress and the data are from natural sites with other influencing factors.

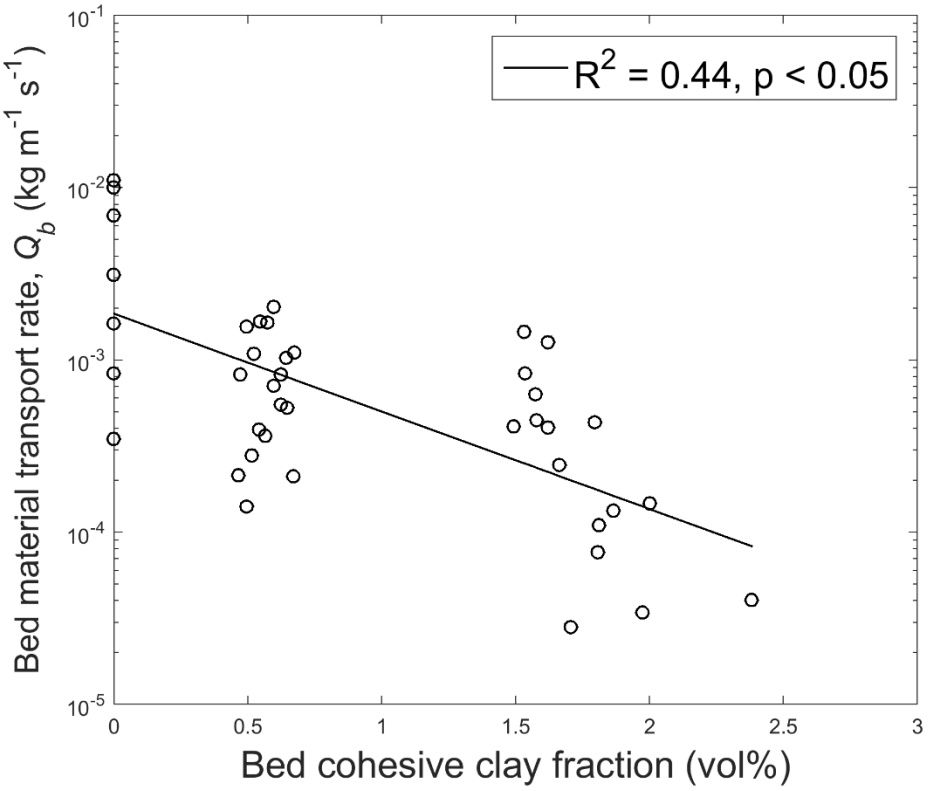

Figure 5-6: Relationship between bed material transport rate and bed cohesive clay fraction (maximum flood and ebb values for each tidal inundation period, n = 41). The data for clay-free sand (D_{50} = 238 µm) from Baas et al. (2000) are also included for zero cohesive clay values.

In equation 5-1, the nature of the dependence of α and β on the bed cohesive clay content can be explored by using a multiple linear regression, for which the laboratory data provides values for zero cohesive clay (Kennedy and Neville, 1976; Chatterjee and Hadi, 2015). After performing ordinary least squares multiple linear regression, a two-sample F-test demonstrated that the laboratory data of Baas *et al.* (2000) have a significantly lower error variance than the field data, probably because these data were collected under controlled laboratory conditions. A robust multiple linear regression method, in the form of an iteratively re-weighted least squares method, was used to control for the differences in variance of the combined data set (Wilcox, 2012; Chatterjee and Hadi, 2015). The initial weights for this regression method were estimated from the inverse of the variance of the errors of the field and laboratory data, determined by ordinary least squares regression (Wilcox, 2012; Chatterjee and Hadi, 2015). This robust regression also reduces the effect of extreme outliers as part of the iterative re-weighting process. The inclusion of the laboratory data forced the fit to zero cohesive clay values. A limit of 0.05 significance was chosen for the multiple linear regression model. Overall, the model was

significant, with an R^2 = 0.993, p < 0.05 and RMS error = 0.33, for n = 41 (Table 5-1; Kennedy and Neville (1976)), and yielded the following equation:

$$Q_b = 10^{0.13-1.70c} \times (\theta'_{\max})^{2.98-1.06c} \qquad \text{for } 0 \leq c < 2.8 \text{ vol\%}$$

5-8

where Q_b is the mass transport rate (kg m^{-1} s^{-1}), $\theta'_{\max}$ is the skin-friction related Shields parameter, and c is the bed cohesive clay content (vol%). The power coefficient of $\theta'_{\max}$ in equation 5-8 at 0 vol% cohesive clay, 2.98, is close to 3.03, the power coefficient for 238 µm sand, showing that equation 5-8 reduces close to the slope of the equation of Baas *et al*. (2000; Figure 5-1) for zero bed cohesive clay content. Equation 5-8 predicts a very small, constant bed material transport rate for a bed cohesive clay content equal to 2.8 vol%. c = 2.8 vol% corresponds to a bed EPS content of 0.05 wt% (equation 3-5), which is close to the 0.063 wt% limit for bedform development of Malarkey *et al.* (2015). The relative importance of the parameters in equation 5-8 can be determined by dividing the coefficients by their standard errors (t statistic in Table 5-1) and comparing the magnitude of the values (Borradaile, 2003). The maximum skin-friction related Shields parameter has the highest value, 55.7, and greatest relative influence on the bed transport (52%), followed by the cohesive clay content, 31.67 (28%), and then the interaction between Shields stress and cohesive clay, 17.7 (17%) (Table 5-1).

Table 5-1: Multiple linear regression statistics for bed material transport analysis

$\log_{10}(Q_b) = a_1 + a_2 \times c + a_3 \times \log_{10}(\theta'_{max}) + a_4 \times c \times \log_{10}(\theta'_{max})$

	Coefficient	Standard Error	*t* Statistic	*p-value*	*% influence*
a_1 (intercept)	0.13	0.050	2.654	1.165×10^{-2}	2.5
a_2 (c)	-1.70	0.056	-30.160	1.190×10^{-27}	28.4
a_3 (θ'_{max})	2.98	0.054	55.658	2.812×10^{-37}	52.4
a_4 (c×θ'_{max})	-1.06	0.060	-17.683	1.235×10^{-19}	16.7

Number of observations: 41, Error degrees of freedom: 37

RMS Error: 0.327, R^2: 0.993

F-statistic vs. constant model: 1.83×10^3, *p* for model overall = 2.86×10^{-40}

Equation 5-8 is plotted for set values of bed cohesive clay content (0 to 2.5 %) in Figure 5-7. The line of no motion corresponds to 2.8 %, which is the effective limit of detection of bed material transport, with an equivalent bedform height of 0.008 m associated with the minimum migration rate. It can be seen in Figure 5-7 that as bed cohesive clay content increases, a higher bed shear stress is required to produce a given bed material transport rate. The critical Shields parameter for sediment motion (the crossover of all lines with the 'no-motion' line), 0.025, is independent of cohesive clay content, and this is a consequence of the absence of a critical Shields parameter in equation 5-8. The critical Shields parameter of 0.025 is lower than the 0.051 predicted by Soulsby (1997) for D_{50} = 227 μm. This difference may be caused by flow enhancement at the bedform crest, resulting in very slow bedform migration below the shear stress threshold for a flat bed (Best, 2005).

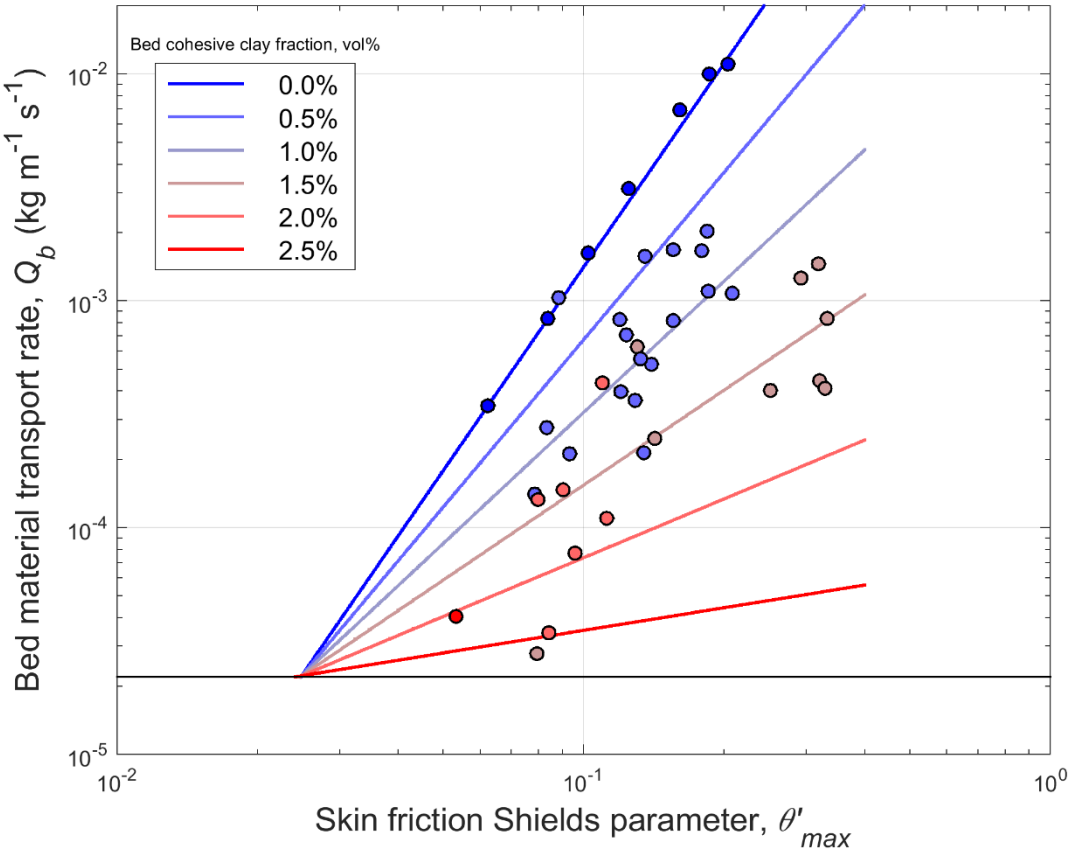

Figure 5-7: Maximum bed material transport rate, for flood and ebb, against skin friction Shields parameter for combined currents and waves. The colour-filled circles denote the measured data, where the colours represent the bed cohesive clay fraction binned in 0.5 vol% intervals. The black horizontal line represents the minimum bed material transport rate, based on the lowest measurable migration rate by the 3D-ARP and a 0.008 m high bedform (or c = 2.8 vol% in equation 5-8) and can be treated as the line of no motion. The coloured lines denote the multiple linear regression fit (equation 5-8) calculated for set bed cohesive clay content values. The data for clay-free sand (D_{50} = 238 µm) from Baas *et al*. (2000) were included in regression analysis, forcing the fit to these zero cohesive clay fractions. Bedform migration rates that were too low to be determined with sufficient confidence from the 3D-ARP data (Figure 5-5) were excluded from the regression analysis.

5.7 Discussion

5.7.1 Comparing the laboratory and field data

Bedform migration rates in the field were lower than in the experiments of Baas *et al.* (2000) (Figure 5-5) at times when the bed cohesive clay content in the field was below about 2.5 vol%. At higher cohesive clay contents, which coincided with high EPS contents and were most common for Site 3, bedform migration was not detectable and bed material transport appeared to stop (Figure 5-5). The lack of mobility of the sediment from 31 May onward at Site 3 cannot be explained solely by the relatively weak neap tides (Figure 5-4c, f), because there were instances when the bedforms did not migrate even though the bed shear stress was above the expected threshold of sediment movement, *i.e.*, $\tau'_{max} > 0.18$ N m^{-2} for D_{50} = 227 µm (Soulsby, 1997).

The multiple regression analysis reveals that the bed cohesive clay and EPS content, in conjunction with bed shear stress, had a large influence on the bed material transport rate. The clay minerals and the EPS matrix are inferred to have formed cohesive bonds between the sand particles, which: (1) increased the bed shear stress required for bed material transport; (2) progressively reduced the bed material transport rate between bed cohesive clay contents of 0 vol% and 2.8 vol%; and (3) halted detectable bedform migration and bed material transport at the field sites at bed cohesive clay contents above about 2.8 vol% and bed EPS contents above about 0.05 wt%. This value of 2.8 vol% cohesive clay is remarkably low, and well within the 'clean sand' category of Shepard (1954) and the 'mature sand' (arenite) category of Dott (1964). Although a direct comparison with the mixed mud-sand experiments of Baas *et al.* (2013) is not possible, because the sand size, clay type, and flow conditions differed from those at the field sites, it is notable that the bed material transport rates in these experiments were reduced by low bed clay fractions of < 5% (Baas *et al.*, 2013).

The positive correlation between bed cohesive clay and EPS fractions (Figure 3-20) may explain the large difference between sediment mobility at Sites 1 and 2 compared to Site 3. The beds sampled towards the end of data collection at Site 3 were sufficiently cohesive (biologically and physically) to reduce the migration of bedforms below the limit of detection, whereas bedform development and migration occurred throughout data collection at Sites 1 and 2, because biological and physical cohesion were weak enough to allow sediment movement. Malarkey *et al.* (2015) found that the rate of bedform development was substantially reduced on a flat sand bed that contained more than 0.063 wt% EPS. Using the laboratory experiments of Malarkey *et al.* (2015) as a guide, the EPS fractions of 0.02-0.04 wt% for Sites 1 and 2 may therefore have been too low to significantly hinder bed sediment movement and bedform development, whereas the EPS fractions of 0.08-0.21 wt% for Site 3 may have been too high for bedform development.

5.7.2 Limitations

The scatter in the field data was greater than for the laboratory results (Figure 5-5), despite the strong correlation between ripple migration rate and skin friction Shields parameter for the field data and the similar behaviour between the field and laboratory data for cohesive clay and EPS fractions below 2.8 vol% and 0.05 wt%, respectively. This probably reflects the fact that field conditions are inherently more complex, and therefore more variable than laboratory conditions. The main sources of this data scatter are outlined below.

The dynamics of the bedforms in the Dee Estuary depended on the combined action of waves and tides, whereas the bedforms in the laboratory formed in steady, uniform flow. Waves enhance sediment transport when they coincide with currents (Grant and Madsen, 1979; Pattiaratchi and Collins, 1984). This promoted bedform migration at the wind-forced Site 1 (Figure 5-4f) in comparison to the other sites and the laboratory experiments of Baas *et al*. (2000), where the waves were much smaller and absent, respectively. This wave enhancement would also explain the small amounts of mud at Site 1 compared to Site 3, due to the greater effect of winnowing of fine sediment and EPS by waves at Site 1 (Baas *et al*., 2014).

The combined maximum bed shear stress was used to account for the effect of wave enhancement of current bed shear stress on bedform migration and material transport, for the few tidal periods when wave forcing was significant, in order to compare the field data with the current only data from the laboratory. As waves were only significant for five of the twenty-five tidal periods (Figure 5-4b), the effects of wave asymmetry and skewness on bedform migration has not been looked at.

The laboratory ripples of Baas *et al.* (2000) were given enough time to attain equilibrium size in steady, uniform flows, before migration rates were measured. In contrast, the bedforms in the Dee Estuary were probably not in equilibrium with the constantly changing tidal flows, wave forcing, water levels, and sediment cohesive properties. It is more likely that most bedforms were continually adapting to changes in the hydrodynamic forcing. Non-equilibrium current ripples have been shown to migrate faster than equilibrium ripples (Baas, 1999). Non-equilibrium dunes, on the other hand can move faster or slower than equilibrium dunes, depending on whether the non-equilibrium dunes evolve to a smaller or larger equilibrium size (Allen, 1984). This so-called bedform hysteresis may have introduced scatter in the relationship between the instantaneous flow forcing and bedform migration rate (Figure 5-5) and therefore bed material transport rate (Figure 5-7).

It was assumed that the shape factor, *f*, and the sediment loss-gain factor, *K*, in equation 5-3 were constant at 0.6 and 1, respectively. These assumptions were made as the data of Baas *et al.* (2000) lacked the measurements for the calculation of the bedform shape, or the sediment loss or gain from and to the bed. As the Baas *et al.* (2000) data were from a unidirectional current in a flume, the assumption of $f = 0.6$ for current ripples and dunes should be fair. However, from the 3D-ARP data it was possible to roughly determine the shape factor the field bedforms and this resulted in a mean value from the whole data set of $f = 0.52$, with a standard deviation of 0.09. The low average *f* may be due to the reversing tidal current and wave action preventing the bedforms from reaching the ideal shape in the field. The peaked form of wave ripples could have caused *f* values lower than an ideal triangle (0.5). This lower mean value of $f = 0.52$ results in a reduction of bed material transported by about 10% compared to the value of 0.6. Using the 3D-ARP data, the mean level of the bed and therefore the change in bed level from erosion or deposition could be calculated. This allowed an estimate for *K* of 0.991, with a standard deviation of 0.015, to be determined from the data used in the multiple linear regression. This represents an error of a few percent in the transport values.

Uncertainties in the value of bed porosity used in equation 5-3 would also affect the bed material transport rate. The value for natural sand of 0.4 was used. Silt has a porosity of 0.35, as the particles have a plate-like form that can pack more easily. and dominated sediment in this study, with a small of percentage of fine material, would be expected to have a porosity of less than 0.4 but not as low as 0.35. This decrease in porosity would increase the amount of sediment transported in the order of a few percent.

Other possible sources of the data scatter include: (1) uncertainties in calculating the non-linear effect of wave forcing on bed shear stress (Malarkey and Davies, 2012); (2) the effects of non-translational changes in plan morphology of the rippled beds, caused by, for example, bedform hysteresis and flow rotation, on the 2D cross-correlation procedure used to calculate bedform migration rate from the 3D-ARP scans; (3) spatial and temporal variations in the clay-mud ratio used to convert bed mud fractions into cohesive clay fractions; and (4) variation in biogenic effects such as biostablisation and bioturbation (Black *et al*, 2002).

5.7.3 Implications for sediment transport modelling, geomorphology and coastal engineering

Given the above limitations, it has been shown that the bed material transport rates for the biologically active mixed sand-mud under field conditions in the Dee Estuary were significantly reduced for bed cohesive clay fractions below 2.8 vol% and for EPS fractions below 0.05 wt%, due to physical and biological cohesion. This is below the 5-8 vol% clay content found for the transition to a cohesive dominated eroding bed (van Ledden *et al.,* 2004), but above the EPS fraction (0.026%) found to stabilize wave ripples by Friend *et al.* (2008). These results have important implications for sediment transport modelling. Since the bed material transport rate depends on the strength of biological and physical cohesion, clean sand formulae should only be used if bed cohesive clay and EPS contents are close to zero. In addition, bed material transport reduced below the limit of detection for bed cohesive clay content above about 2.8 vol%, in the present study. Equation 5-8 can be used to estimate bed material transport rates for different bed cohesive clay contents below 2.8 vol%. The implications of this work for sediment transport modelling also extend to larger-scale geomorphology and coastal engineering. For example, slowing down bedform migration at the unexpectedly low bed mud contents found in this study may add to the stability of nearshore environments and therefore influence shoreline change, longshore sediment transport, intertidal channel switching, and other nearshore processes.

5.8 Conclusions

A comparative analysis of bedform migration and sediment transport in a biologically active mixed sand-mud environment in the Dee Estuary, north-west UK, under the influence of currents and waves, and sand-only steady-current laboratory experiments was conducted. Even when cohesive clay and EPS fractions in the bed were below 2.8 vol% and 0.05 wt%, respectively (Figure 5-5) the results demonstrate that, once the effect of waves had been accounted for, the bedform migration rate of mixed sediments in the field was significantly different from that of sand-only bedforms. Below these limits the bed material transport rate reduced as the bed cohesive clay and EPS content increased (Figure 5-7). Above these limits, which correspond approximately to the points where cohesive clay and EPS began to significantly affect the migration rate and bedform dimensions in the mixed clay-sand laboratory experiments of Baas *et al*. (2013) and the mixed sand-EPS laboratory experiments of Malarkey *et al*. (2015), bedform migration and bed material transport were below measureable limits in the study area. Presumably, the cohesive bonding of sand particles by clay and EPS was sufficiently

strong to resist the boundary shear stress from currents and waves above 2.8 vol% cohesive clay and 0.05 wt% EPS.

These results have important practical implications for the wider prediction of sediment transport in models, since existing formulae for the transport rate associated with bedform migration should only be applied when cohesive clay and EPS content is close to zero. On a broader scale, the management of coastal morphological change, the assessment of the environmental impact of dredging operations in estuaries, and the understanding of the effects of climate-induced habitat change in shallow-marine environments are expected to benefit from the present study, by means of improved predictions of bed material transport.

6 Discussion

6.1 Introduction

In this chapter, the bedform dimensional and migration data of chapters 4 and 5 are compared, the limitations of the fieldwork and data analysis are examined, and recommendations for future research are made. One of the key questions of this thesis was how the cohesive content of the bed interacts with hydrodynamic forcing over the spring-neap cycle. In order to extend this interaction to other physical and biological processes, a conceptual model of cohesive mud transfer between bed and water column is proposed.

6.2 Summary of the main results

The SEDbed suite of instruments was deployed on the Hilbre tidal flats in the Dee Estuary to collect data on the effect of physical and biological cohesion on the dynamics of small-scale bedforms. The near-bed hydrodynamics and changing bed morphology were measured over a spring-neap cycle. In addition, bed sediment samples were collected for particle size analysis and biological analysis, to measure the amounts of cohesive material within the sediments. The cohesive clay content of the bed was found to vary with the hydrodynamic forcing, within the spring-neap cycle, and the amount of biological cohesive material (Extracellular Polymeric Substances, EPS) in the bed sediment was found to correlate linearly with the cohesive clay content.

The field data showed the effect of bed cohesive clay in reducing bedform dimensions and on the development of bedform plan morphology. The reduction of bedform migration and bed material transport rate due to bed cohesive clay was also demonstrated. These results confirm findings from the flume experiments of Baas *et al*. (2013), Schindler *et al*. (2015) and Parsons *et al*. (2016) on the effect of clay and EPS on current ripple and dune dynamics. Standard bedform predictors applied to sediments with only a few percent of cohesive clay were found to overestimate bedform dimensions and bed material transport rate. This implies that bed roughness values used in models for calculating hydrodynamics and sediment transport need to be re-assessed even for near-to clean sand. Without this re-assessment, local errors are introduced to these calculations, which may multiply to larger errors in regional models.

The combined wave and current flow produced segmented bedforms in the 3D-ARP scans, possibly linked to tidal rotation. Using logistic regression to relate the planform dimensionality classifications to hydrodynamics, the current and wave bed shear stress and wave-current angle were shown to

effect planform dimensionality, distinguishing between wave and current forcing. A new bedform phase diagram based on cohesive clay content and combined-flow bed shear stress was proposed, which showed a transition of planform type as the bed shear stress decreased and cohesive clay content increased. This relationship broke down below a cohesive clay content of 1%, suggesting that the mixed sand-clay bed behaved as a cohesionless bed. In addition, small-scale sand ribbons were observed, bedforms usually associated with sand and gravel beds, and have not been described in muddy-sand sediment before.

Many of the current-dominated bedforms present on the tidal flats did not compare well to standard bedform predictors for current ripples and dunes. As these current bedforms scaled with water depth, and were larger than the expected equilibrium dimensions for current ripples, they are best described as transitional or intermediate bedforms between current ripples and dunes (e.g. Bennet and Best, 1996; Baas, 1999).

6.3 Comparison of bedform dimensions, bedform migration and changing bed cohesive content

In this section, the results of the previous chapters are revisited and elaborated on. The cohesive clay limits of the bedform development and material transport regressions are compared, and the bed cohesive clay content is looked at in comparison to the processes over an ideal tidal cycle and to the alternate stable states model.

6.3.1 Bedforms in transition from ripples to dunes

The transition of bedforms from current ripples to dunes can be seen to be analogous to the transition of wave ripples from anorbital ripples to orbital ripples. Both current ripples and anorbital wave ripples scale with the sediment grain size. Dunes and orbital wave ripples scale with hydrodynamic parameters, water depth or wave orbital amplitude. For wave ripples, there is a transitional state between anorbital and orbital ripples, suborbital ripples, when the bedforms scale with both grain size and wave properties. The field data show a similar transition between current ripples and dunes, as the bedforms change in size from approximating to equilibrium current ripples, expected for the sediment grain size present, to scaling with water depth, in the bedform size range of the field data.

6.3.2 The critical limits of bedform development and material transport

Low values of bed cohesive clay content did not appear to affect the threshold of sediment motion, based on the convergence of the multiple linear regression of bed material transport (section 5.6.4). In addition, the regression equation predicted no detectable motion at a cohesive clay content of about 3 vol% and above. From the relationship between cohesive clay and EPS (Equation 3-5), this cohesive clay content corresponded to an EPS fraction of 0.05 wt%.

The prediction of the bedform height multiple linear regression indicated it would not be expected for bedforms to develop above 4 vol% cohesive clay, with this critical cohesive clay limit increasing with increasing water depth (probably due to the tidal co-variance of water depth and current shear stress; section 4.6.6.1), corresponding to an EPS fraction of 0.07 wt%. The predicted cohesive clay values from the bed material transport and bedform height regressions agree well. As bedform migration has to be detectable by the 3D-ARP, for the bed material transport to be determined, some discrepancy between the predictions of the two regressions may be expected.

6.3.3 Duration of tidal inundation and bed cohesive clay content

The duration of tidal inundation encompasses many of the processes involved in the addition and removal of cohesive clay into and from the bed, over a spring-neap cycle on tidal flats (section 3.9.5). For example: bed shear stress and duration of applied stress, and therefore the bedform migration rate; EPS production; filtering, excretion and bed re-working by benthic organisms; and bed strengthening during tidal flat exposure (Winterwerp and van Kesteren, 2004). Long periods of inundation on tidal flats (*i.e.* at spring tide) may carry greater amounts of sediment and allow more time for settling to occur than short periods (*i.e.* at neap tide), leading to increased deposition of sediment (Friedrichs, 2011; Kirwan and Guntenspergen, 2012). However, this increased deposition relies on an asymmetry in the tide and low wave forcing, or the reduction in stress by salt marsh plants, to promote deposition and prevent the erosion of newly deposited sediment (Friedrichs, 2011; Fagherazzi, 2012). The opposite trend is apparent in the bed cohesive clay content data presented here (Figure 3-22), with reducing duration of tidal inundation towards neap tide at Site 3 leading to increasing bed cohesive clay content.

The duration of bed exposure, between tidal inundation periods, and the magnitude and duration of the tidal current stress depend on the tidal range, with respect to the bed elevation, and these will affect the change in bed cohesive clay content. From spring to neap tide, the tidal range decreases relative to the bed level and the inundation period decreases, when deposition is expected. However,

as the tidal inundation period decreases the period of bed strengthening due to exposure increases, making the bed more resistant to erosion (Amos *et al*., 1988a; Whitehouse *et al*., 2000). At spring tide, the bed has less time to consolidate, so the deposited material is more easily removed with next flood tide. At neap tide, the bed strengthening time is longer and deposited material is more resistant to erosion on the flood.

High bed shear stress during spring tide can prevent the permanent deposition of clay, increases winnowing and breaks up flocs. Water pressure gradients due to wave action and from currents across bedforms cause flow through the bed, processes respectively known as hydraulic pumping and topographic advection, that can filter fine particles from the water (Huettel *et al*., 1996; Precht and Huettel, 2003). The reduced peak flow velocity and stress at neap tide will allow greater flocculation and the deposition of clay, with the addition of bed filtering of fine sediment due to pressure gradient effects and cohesion, will reduce re-suspension and winnowing on the ebb. In addition to these physical processes, the effects of biological EPS production, filtering and excretion will also promote the transfer sediment from suspension to the bed and bed strengthening (Huettel *et al*., 1996; van de Koppel *et al*., 2001; Precht and Huettel, 2003; Friend *et al*., 2008). Although increasing flow velocity increases the particle encounter rate for filter feeders, it can also reduce filtering efficiency, resulting in less sediment being removed from suspension to the bed (Shimeta and Jumars, 1991). This means in high bed shear stress the transfer rate of fine sediment into the bed may be reduced, with a greater effect at spring tide than neap tide. In addition to these processes, biological mixing will work the clay into the bed (Passarelli *et al*, 2014). These physical and biological processes are proposed as an explanation for the inverse relationship between duration of tidal inundation and bed cohesive clay content (Figure 3-22), though not directly shown by the results, this will be discussed further as part of the conceptual model (section 6.3.3).

Although the net removal or addition of cohesive clay to the bed over a spring-neap cycle can be seen in the data from the bed samples (Figure 3-21 and Figure 3-22), how the bed composition varies during tidal inundation, a semi-diurnal period, cannot be resolved by the intertidal bed samples. From the physical and biological processes, it can be hypothesised that the bed will go through periods of cohesive clay addition and removal during a single tidal inundation period (Figure 6-1). At the start of an inundation period, water will flood across the tidal flat and bed shear stress will increase. If the stress produced by the flow is greater than the threshold of bed erosion, sediment will be entrained into the water column instead of being removed from suspension by pressure gradient filtering and filter feeding. The water velocity and bed shear stress will quickly peak, with a period of bed erosion and resuspension, and then start to decline towards high water. Around high water, the bed shear

stress will be at a minimum, if there are no additional effects due to wind driven flow, tidal rotation or local morphology that would prevent slack water at high tide, and the processes of deposition and filter feeding dominate the transfer of fine particles to the bed. From high water, the water velocity will increase to a peak and then decrease as the water drains from the flats. This will result in another period of erosion and suspension, followed by physical filtering through the bed, filter feeding and deposition. Whether this sequence of results in net transfer of cohesive clay into or from the bed depends on the balance of processes, which will depend on the state of tide (spring to neap), type of sediment (size grain size of the sand and cohesiveness of the fine sediment), biological production (species composition of the ecosystem) and wind strength. At Site 2, during spring tide, the bed cohesive clay content was low as the processes removing fine sediment dominated (Figure 3-21 and Figure 3-22). At Site 3 the maximum bed shear stress during tidal inundation periods reduced towards neap tide, as the exposure period between tides increased, resulting in the addition of fine material into the bed and increasing bed cohesive clay content.

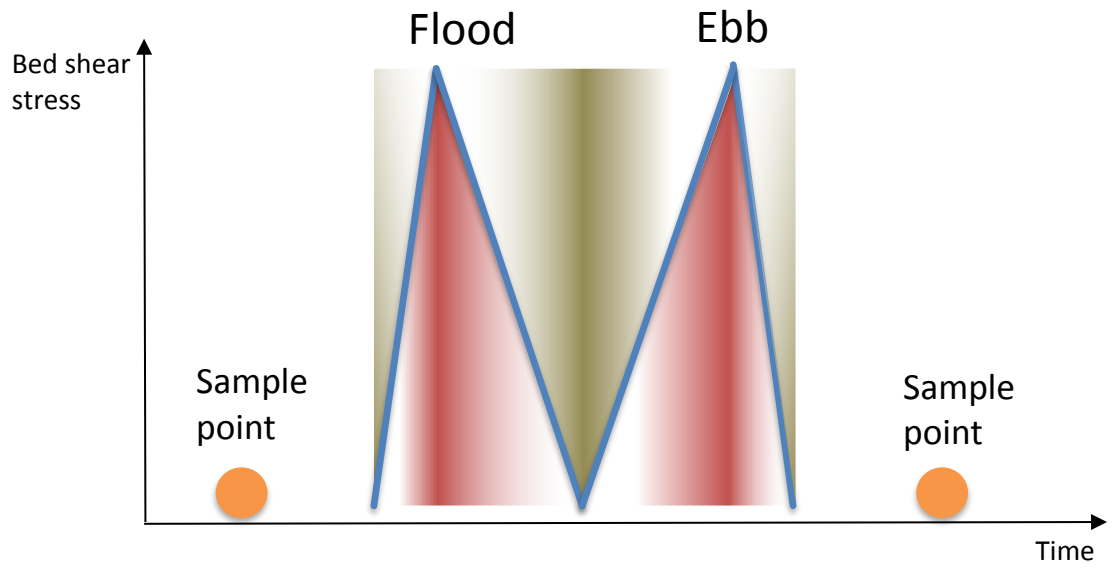

Figure 6-1: A conceptual model of the processes during a single tidal cycle or inundation period. Blue – bed shear stress profile, Red – winnowing and entrainment, Brown – deposition and bed filtering, Orange circle – intertidal manual bed sample point.

6.3.4 Alternate stable states

The clustering of bed cohesive clay content and bed EPS content data (Figure 3-20), and the relationship between tidal forcing and bed cohesive clay content (Figure 3-22), may support the alternate states model of van de Koppel *et al*. (2001, see also Friend *et al.*, 2008). The alternate states model advocates that a sediment bed tends to switch between two stable states: low concentrations of diatoms (main EPS producers) and high bed shear stress (*i.e.* during spring tide and strong wind events as for Sites 1 and 2), versus high concentrations of diatoms and low bed shear stress (*i.e.* during neap tide as for Site 3). The bed would have been in an unstable state between these limits, if the model of van de Koppel *et al.* (2001) applies to the studied sites in the Dee estuary. Specifically, the bed cohesive clay content increased as the hydrodynamic forcing decreased at Site 3 and the bedform dimensions and migration reduced due to the increased bed cohesive clay content. This implies that the behaviour of the bed changed from being dominated by non-cohesive processes to being dominated by cohesive processes over the spring-neap cycle. This transition between states should be enhanced by the production of EPS, and the production of EPS is increased by the increasing bed clay content (van de Koppel *et al*., 2001). For the energetic conditions at Sites 1 and 2, caused by strong wave action and high maximum current velocities during spring tides, non-cohesive sediments prevail, allowing bedforms to form and migrate much more easily than for the calmer conditions of Site 3.

6.4 A conceptual model of bed cohesive mud processes on tidal flats

The effect of cohesive material on sediment dynamics over a spring-neap cycle has been the theme of this thesis. As the bed sediment samples were collected during the exposure of the tidal flats, the semi-diurnal processes of the cohesive sediment during tidal inundation could not be resolved. In the introduction chapter, a simple conceptual model was shown. This will now be elaborated on as a framework to explore qualitatively the processes that affect the cohesive content of the bed, which could not be fully resolved by the instrument measurements and bed sampling, and how they relate to each other. In section 6.3.3, the sequence of winnowing and deposition events over a single tidal inundation cycle were described and in this section the processes involved will be considered in greater detail.

Many different processes contribute to the transfer of cohesive mud between the bed and water column (Whitehouse *et al*., 2000; van Ledden, 2002; Winterwerp and van Kesteren, 2004; Sanford, 2008; van Kessel *et al*. 2012). By developing a conceptual model, the relationship between these processes can be explored and gaps in knowledge highlighted (van Ledden, 2002). Sand-mud sediment processes for erosion and deposition, including the effects of biology on deposition, bed stabilisation

and bed destabilisation, are now included in regional models (van Ledden, 2002; Paarlberg *et al*., 2005; Sanford, 2008; van Kessel *et al*. 2012). The conceptual model presented here will be a simple box model bringing together the processes involved in the exchange of cohesive mud between the bed and water column, over a spring-neap cycle, to hypothesise how the effect of cohesive sediment on bedform size and migration fits into this system.

For this model, cohesive mud is considered to be composed of clay, silt and biological cohesive material (EPS). Only the processes that effect the transfer of the cohesive mud between the bed and water column are included in the model. As discussed in Section 0, the bed would be expected to switch between alternate stable states, of cohesionless and cohesive, as the dominance of hydrodynamic stress and bed cohesion changes (van de Koppel *et al.*, 2001; Friend *et al.*, 2008; Passarelli *et al*., 2014). The bed can be seen as a system balancing between factors increasing bed cohesion and stability, in opposition to those that decrease bed strength, promoting bed erosion and sediment transport.

6.4.1 Processes affecting the bed cohesive mud content

In this section, the processes of the sediment system included in the conceptual model are described (listed in Table 6-1). Water pressure gradients due to wave action and from currents across bedforms cause flow through the bed, processes respectively known as hydraulic pumping and topographic advection, that can trap fine particles (Huettel *et al*., 1996; Precht and Huettel, 2003). The filtering of fine particles by topographic advection of water through the bedforms will depend on the dimensions of the bedforms, the bed shear stress and the porosity of the sediment, and as the pores of the sediment are filled up the filtering efficiency will decrease. In the present model, the pressure gradient filtering effect only adds cohesive mud to the bed, filtering fine sediment from the water column, with the removal of cohesive mud form the bed by pressure gradients considered part of the winnowing process. When bedforms migrate, fine material deposited in the bedform troughs can be buried (Sato *et al*., 2011). However, the turn over of sediment in the active layer by bedform migration can also release fine material, which is also included in the winnowing term. The net effect of bedform migration on the reworking of cohesive mud into the bed, or aiding winnowing from the bed, will be determined by the magnitude of bed shear stress and the size of the bedforms. As has been shown in the previous chapters the cohesive properties of the bed will reduce the bedform dimensions and bedform migration rate, and therefore effect the efficiency of winnowing and pressure gradient filtering. As the cohesive mud content increases, the bed will change from being dominated by sand to being dominated by mud, increasing the resistance to erosion (Mitchener and Torfs, 1996;

Panagiotopoulos *et al.,* 1997). Winnowing, due to the action of currents and waves, selectively removes fine material from bed sediment into the water column until an armouring layer of sand is left (Komar and Li, 1986; Lisle and Hilton, 1992; Harris *et al*., 1993; Baas *et al*., 2013, 2014). For high bed shear stress, the sediment will erode and suspend, exposing the sub-surface sediment layers.

Biological action is known to effectively filter suspended material from the water column and mix it into the bed (Jørgensen *et al*., 1984; Shimeta and Jumars, 1991; Passarelli *et al*., 2014). In producing EPS, microflora stabilise the bed and improve their habitat (van de Koppel *et al*., 2001; Passarelli *et al*., 2014). Bioturbation and grazing by benthic fauna can destabilise the bed, in opposition to the stabilising effect of microflora, mixing the bed sediment and redistributing nutrients making them available for consumption by other organisms (Grant and Daborn, 1994; van de Koppel *et al*., 2001; Passarelli *et al*., 2014). Bio-resuspension occurs as filter feeders eject waste in to the water column, to avoid re-ingesting waste material, and as surface feeders graze the sediment (Graf and Rosenberg, 1997; Andersen and Pejrup, 2011). Bioconstruction stabilises the sediment as fauna create and maintain burrows to live in, and in this process fine martial can be transferred to the surface (Reise, 2002).

Suspended cohesive sediments will flocculate, aiding the deposition of sediment during periods of low bed shear stress. Flocs form when turbulence brings cohesive sediment grains together and the shear velocity is not too strong to break the flocs apart (Whitehouse *et al*., 2000; Winterwerp and van Kesteren, 2004). Therefore, the flocculation process is a balance of sediment concentration, turbulent shear stress, seawater salinity and cohesive properties of the sediment in suspension.

Table 6-1: Processes affecting the cohesive mud content of the bed.

Addition		Removal		Strengthening		Weakening
Pressure gradient filtering		Winnowing and erosion		Evaporation		Bioturbation
Filter feeding		Bio-resuspension		EPS production		Grazing
Flocculation and settling				Clay and silt content		
Burial by bedform migration				Bioconstruction		

Many of the addition and removal processes are dependent on the strength of the hydrodynamic forcing. For weak forcing, pressure gradient filtering and burial by bedform migration will add cohesive mud to the sediment. As the bed shear stress increases, the bedforms will start to migrate and overturn the sediment and winnowing starts to have an effect. For higher bed shear stress, the bed will erode down to deeper layers with any stored cohesive mud becoming part of the active layer.

Filter feeding can also be restricted by strong currents (Shimeta and Jumars, 1991) and flocs broken up into primary particles, which reduces the rate of settling and deposition to the bed (Winterwerp and van Kesteren, 2004). Bed strengthening depends on the length of exposure and daylight. Evaporation, promoted by daylight, during exposure of the tidal flats leads to increased bed strengthening, in addition to the weight of sediment expelling water (Amos *et al*., 1988a; Whitehouse *et al*., 2000). Diatoms produce EPS and store energy during daylight, but increase EPS production when the tidal flats are inundated by water and in darkness, using up the stored energy, and this production may be aided high nutrient concentrations available in mud (Smith and Underwood, 1998; van de Koppel *et al*., 2001).

Brought together these processes form a complex system in which cohesive mud is transferred into and out of the bed, modulated by biological action, the bed strengthening effect of exposure at low tide and the sediment cohesion. Measuring and quantifying many of these processes in field conditions presents a major challenge and some will be site specific for the mineralogy of the sediment and ecosystem. These processes will be brought together in the next section as part of the conceptual model and in the following section the gaps in the knowledge will be discussed.

6.4.2 Outlining the conceptual model

The sources of cohesive mud are suspended sediment advected into the system, available for deposition, and a store of cohesive mud in the bed, available for transfer to the water column (Figure 1-1).

Over a tidal inundation cycle, there is a balance between pressure gradient filtering and filter feeding removing suspended material from the water column to the bed and winnowing removing the fine material from the bed into the water column. The bed strengthens when it is exposed at low tide. These processes form a balance, resulting in the variation of the bed mud content with tidal cycles and wind events. If the effects of bioturbation and bedform migration can be considered constant during inundation, this balance of processes can be simplified to:

- Fast flow: strong winnowing and filter feeding is reduced
- Short bed exposure period: bed material has little time to strengthen and is easily eroded
- Slow flow: pressure gradient filtering and filter feeding rate is high
- Long bed exposure period: bed material has a longer time to strengthen and resists erosion

So the rate of mud transfer into the bed may be related as:

$$\boldsymbol{rate\ of\ mud\ transfer\ to\ the\ bed} = (\boldsymbol{deposition} \times \boldsymbol{mixing}) - \frac{\boldsymbol{winnowing}}{\boldsymbol{bed\ strength}}$$

6-1

The rate of winnowing may be taken as a function of current and wave bed shear stress and water content as determined by the previous exposure period, with a lower stress limit when winnowing stops. Filter feeding and pressure gradient filtering may be taken as a function of current and wave bed shear stress, and bedform size, with a stress range for when the filtering is optimum. As these processes are determined by bed shear stress, the amount of mud removed from or entrained to the water column is a function of the magnitude of bed shear stress relative to these limits, varying with tidal cycles and wind forcing. Mixing efficiency of bed sediment is function of the bioturbation. Bed strength is a function of water content due to duration of aerial exposure and cohesive mud content. To refine the model, these additional processes can be introduced as separate terms, with respect to time, to result in a predictive model of bed cohesive mud content (

Figure 6-2):

$$\text{Rate of mud transfer into bed} = (filtering + floc\ deposition) \times mixing\ efficiency - \frac{Winnowing}{bed\ strength}$$

6-2

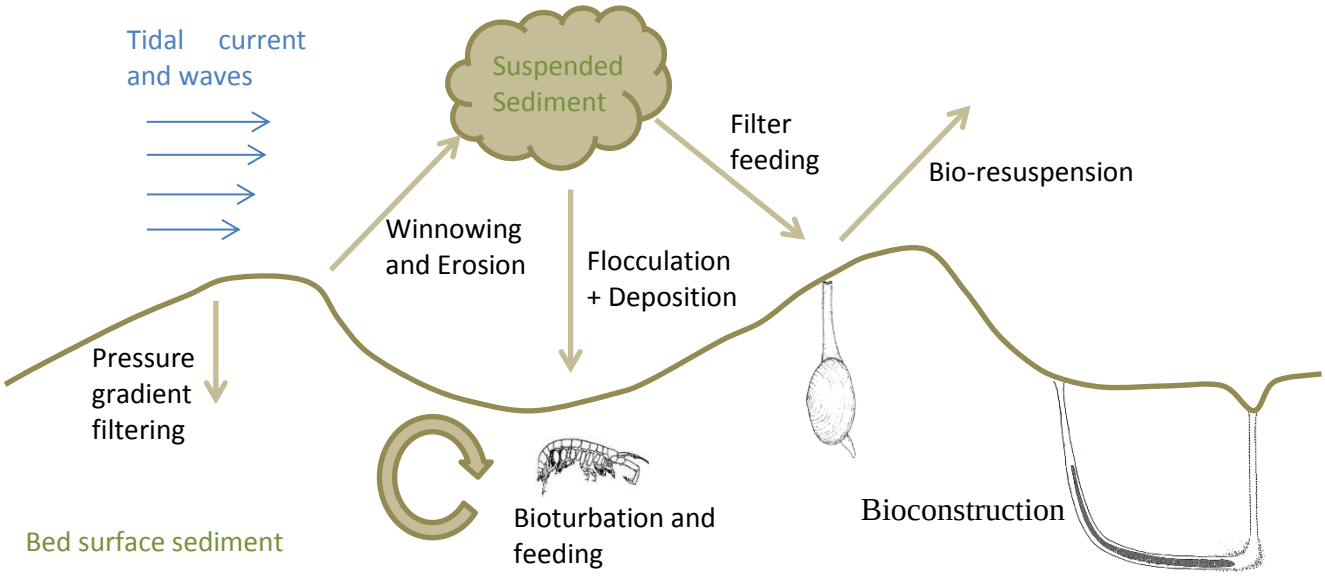

Figure 6-2: The bed mud content model considering the balance between the winnowing caused by bed shear stress, biological action and flocculation deposition. The sediment populations are shown in green, the forcing hydrodynamics are shown in blue and the processes in black.

6.4.3 A Qualitative look at the suspended sediment data

Looking at data from the Acoustic Backscatter System (ABS) and Laser *In Situ* Scattering and Transmissometry instrument (LISST), a qualitative view of some of the processes in the conceptual model affecting the transfer of fine sediment between the bed and the water column can be gained. The ABS was mounted about 0.5 m above the bed and the LISST about 0.08 m below the ABS. The ABS gives a profile of the backscatter intensity due to the suspended sediment in the water column and the LISST measures the concentration and particle size distribution at a single point.

When the tide dominates the sediment dynamical processes, it would be expected that the suspended sediment concentration (SSC) would vary with current velocity as bed sediment is suspended. The trend of SSC increasing with the flood tide, decreasing at slack water and then increasing again with the ebb can be seen in Figure 6-3 a and b. Around slack water, an increase in the D_{50} and standard deviation of the particle size suggests that flocculation may be occurring, as the range of particle sizes has increased when re-suspension would not be expected, Figure 6-3 b and c. Flocculation would suggest the presence of cohesive material to bind particles. The increase in SSC on the ebb suggests that fine sediment is being advected away from the area, Figure 6-3b.

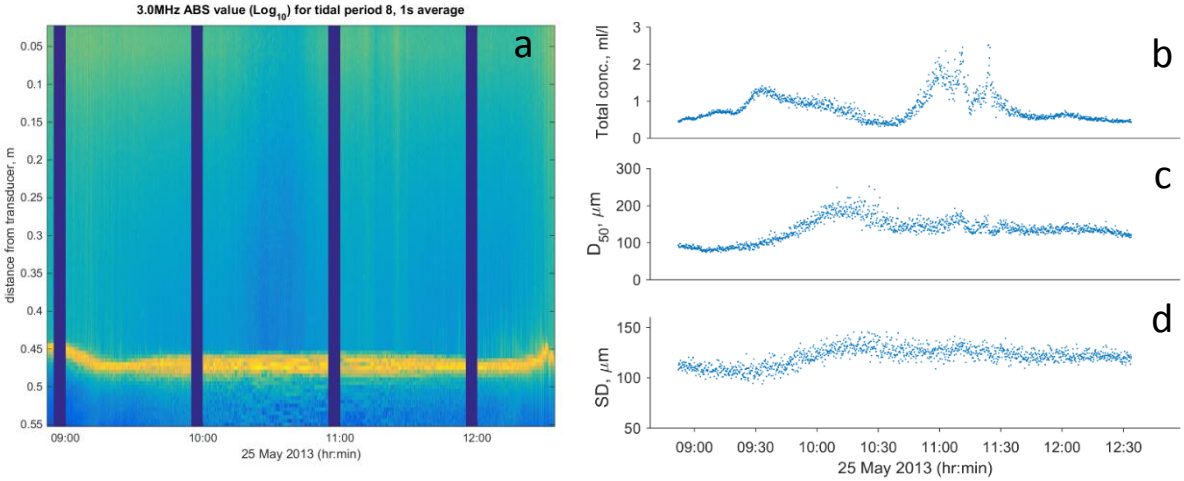

Figure 6-3: Suspended sediment times series for tidal period 8, current dominated. a) ABS time section of backscatter response (with a 5-minute gap each hour due to the instrument settings). LISST times series of suspended sediment properties: b) volume concentration, c) median particle diameter, D_{50}, d) standard deviation of particle diameter.

For strong wave conditions, near bed suspension of sediment and winnowing would be expected in short peaks, Figure 6-4a. However, this material may not reach further up into the water column and may settle quickly to the bed. The LISST shows a uniformly low SSC with little change in the trend of particle size or distribution due to current or waves, Figure 6-4 b to d, therefore at this height from the bed, the sediment has probably been advected into the area.

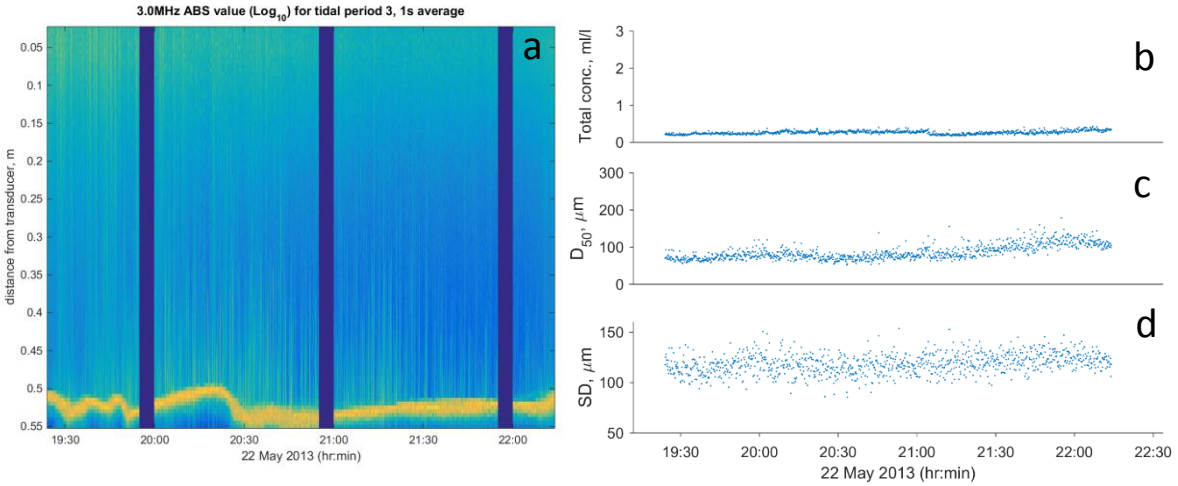

Figure 6-4: Suspended sediment times series for tidal period 3, wave dominated. a) ABS time section of backscatter response (with a 5-minute gap each hour due to the instrument settings). LISST times series of suspended sediment properties: b) volume concentration, c) median particle diameter, D_{50}, d) standard deviation of particle diameter.

Without significant forcing from the current or waves to erode or winnow the bed, advection of suspended sediment is the dominating factor. Compared to the wave dominated case, Figure 6-4, Figure 6-5 b-d shows a higher SSC with a larger particle size and standard deviation. Given the weak tidal current and lack of waves, this suspended sediment is probably composed of fine primary particles and flocs advected into the area. In such a low energy environment, deposition would be expected.

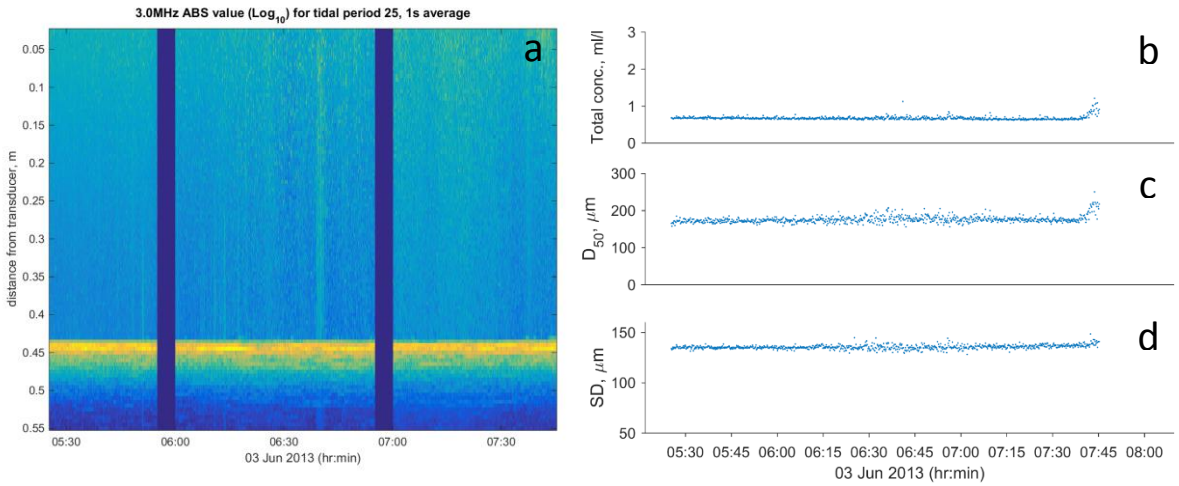

Figure 6-5: Suspended sediment times series for tidal period 25, advection dominated. a) ABS time section of backscatter response. LISST times series of suspended sediment properties: b) volume concentration, c) median particle diameter, D_{50}, d) standard deviation of particle diameter.

8.4.4 Questions arising from the conceptual model

By setting out the processes affecting cohesive mud transfer between the bed and water column, and relating them in a conceptual model, knowledge gaps can be assessed. Due to the limitations of the field measurements and sampling, the intra-tidal effects have only been speculated on here, in a qualitative manner. In comparison to the field data, at Sites 1 and 2 high stress due to waves, wind driven flow and spring tide resulted in the dominance of winnowing and low bed cohesive content. Site 3 experienced low stress and the filtering and deposition processes dominated resulting in high bed cohesive content, as fine sediment advected into the area was worked into the bed.

Both filter feeding and pressure gradient filtering are limited by the flow forcing. The filter feeding will depend on the fauna present, population density and feeding behaviour. The pressure gradient filtering will depend on the properties of the bed sediment and cohesive mud in suspension. Quantifying the change between filtering, adding cohesive mud to the bed, and winnowing, removing cohesive mud from the bed, with varying flow forcing requires further investigation.

In a similar manner, the process of cohesive mud burial by bedform migration may occur only under certain low stress flow conditions. However, in the field the features resulting from this process are likely to be destroyed by bioturbation and bed re-working, and therefore it will be difficult to measure the contribution of this process. Determining if this process is important on tidal flats and quantifying its effect would require a combination of laboratory flume and fieldwork.

Describing the effects of biological action, filter feeding and bioturbation, presents a major challenge in quantifying physical processes of cohesive mud in the changing environmental conditions experienced on tidal flats. Investigating the sediment system as a whole would require close collaboration between physical and biological scientists in future studies. By describing the bed cohesive mud system as a conceptual model, and identifying processes that need quantification, future investigations can be effectively targeted to fill these gaps in the knowledge of the system.

6.5 Limitations

In this section, the limitations of the data collection, processing and analysis are discussed, and recommendations are made for the improvements to the methods. The effect of lag between forcing and response of the bed sediment system is also looked into.

6.5.1 How realistic were the assumptions made for the field study and data processing?

In chapter 3 (section 3.4.1), the assumptions made during the fieldwork planning and data processing were listed (repeated here in Table 6-2). During the data analysis, it became apparent that some of these assumptions were oversimplified, though in spite of this useful results have been obtained from this novel data set. Each of these assumptions will be examined below in turn.

Table 6-2: Assumptions made during the fieldwork planning and data processing.

1) The bed sediment composition at the three deployment sites are contrasting, composed of clean sand, weakly cohesive sand and strongly cohesive sand.
2) Tidal current direction is mainly linear, back and forth with the flood and ebb through the SEDbed frame, rather than rotational.
3) There is no spatial variation in hydrodynamic and wave forcing between the three sites.
4) There is no spatial variation in the effect of biological cohesion between the sites.
5) The sampling area of the bed and volume under frame have uniform flow conditions, so that all measurements can be considered co-located.
6) The frame does not move or settle during the deployments.

1) The initial plan was to select three contrasting sites of clean sand, weakly cohesive sand and strongly cohesive sand. However, the cohesive clay content varied with the spring-neap cycle and wave conditions over the deployment period. In addition, EPS was present at all the sites, varying with the mud content of the bed (Section 3.9.4). Due to the time of year, a high level of biological growth was

expected in the estuary. The variation of bed cohesive clay has been shown in this thesis to modulate the sediment dynamical processes of bedform development and migration, despite the fact that the processes affecting the cohesive content of the bed were not directly observed. Due to the variation of bed cohesive content with hydrodynamics, which varied with wind and tidal forcing, the overall data set was treated as a single time series and not three separate sites.

2) The SEDbed frame was designed to work best in linear flow, through the main section underneath the instruments where there is the least interference from the frame components. In rotating flow, the vertical sections of the frame can interfere with the flow and generate turbulence, which may result in bed scour that would affect the derived bedform dimensions and migration rates (Bolaños *et al*., 2011). From the 3D-ARP images and visual inspection, the only evidence of scour was due to the lead weights at the corners of the frame and below the multi-tier sediment trap and these areas were excluded from the analysis of bedform dimensions and migration.

The effect of tidal rotation is reduced in the bedform migration analysis by using 2D cross-correlation to measure distance migrated in the direction of migration and matching it to the combined bed shear stress. The 3D-ARP scans were rotated to the orientation of the bedforms, before determining values for the bedform height and length, also to account for the effect of tidal rotation. Although the tidal current rotated for part of the study period, the effects of tidal rotation were reduced by the way the data were processed and analysed.

3) Although the SEDbed frame was moved between sites, the trends in the hydrodynamics were continuous over the spring-neap cycle. Wave forcing was strongest at Site 1 and then died off. The processing of the hydrodynamic data accounted for the wave-current enhancement of bed shear stress, which mainly effected Site 1. The tidal cycle progressed from neap to spring to neap across the three sites. The bedforms started as relics with neap tide at the being of the study at Site 1, became mobile and later changed to a relict state at Site 3 when the tide progressed to neaps and the bed cohesive content increased. The three sites were within 140 m of each other and Site 2, in the creek feature, differed in bed elevation by only 0.2 m from Site 1, the highest deployment location. For all the sites, the bed was submerged in about 0.5 m of water before the instruments were covered and started measurement. In addition, the data were corrected for the angle of the SEDbed frame to north. Therefore, moving sites should of had little effect on the data analysis and the hydrodynamic data can be considered as a continuous time series for the purpose of the data analysis.

4) Only EPS data were available for this thesis, for biological cohesion, as measurements of the sediment carbohydrate content. It is assumed that the ecosystem was uniform over the area of the

three sites and that biological cohesion was only due to the EPS, so that there is a direct relationship between bed cohesive clay and EPS content. While the ecosystem may have been uniform over the area, biological populations are patchy in nature. This can be seen the scatter of the EPS-clay plot (section 3.9.4). For future work, collecting more bed sediment samples for EPS and particle analysis, and carrying out a more in depth data analysis, would give greater confidence in the relationship between EPS and bed clay content, and confirm if the relationship is linear or depends on additional factors.

5) The SEDbed frame was designed to allow free flow in the instrument sampling volume, with the minimum of obstructions, accepting the limitations discussed in point 3 above. The instruments are closely spaced and all measure within this sample volume. Flow acceleration due to the frame was considered to be uniform under the instruments and not cause differences in the water velocity between the ADV measurement volume and above the bed scanned by the 3D-ARP.Therefore, it is reasonable to assume that the instrument measurements are co-located for the purpose of the data analysis.

6) The SEDbed frame was well bedded into the subsurface sediment. Measurements from the tilt sensor in the ADV show that the frame had a variation in tilt of about one degree over the deployment record, with an accuracy of ±1°. From the 3D-ARP data, bed level measurements increased and decreased over the deployment without an increasing trend that would be expected if the frame were settling.

6.5.2 Reaction time, lag, equilibrium and hysteresis

The reaction time is the lag between a change in forcing and the response of the system (Allen, 1974). The relaxation time is the time required to reach an equilibrium state, after the system has started to respond to a change in forcing (Allen, 1974). Together, these effects create a lag in time between a change in forcing and reaching the new equilibrium state that will vary with the rate of change of forcing. This dependence on the history of forcing is known as hysteresis. The reaction and relaxation time of sediment properties and morphology in response to the unsteady bed shear stress is a source of uncertainty in the data set used in this thesis.

The complexity of natural sediment systems may result in the lag time being the sum of several factors, such as bed strength, cohesion and bedform dimensions (Allen, 1974). The problem with the response of bedform morphology and bed sediment composition is that they are two linked systems. As bed shear stress increases past the threshold of motion, bedforms start to migrate and change in

morphology, affected by the bed cohesive content. At the same time, with the same increase in bed shear stress, for high stress the cohesive content of the bed sediment will change due to winnowing and the bed reworking processes affected by the bedform migration and bed morphology. For low stress, filtering and deposition will add cohesive material to the bed, processes also dependent on the bed morphology and migration. The result is a feedback loop between the bed morphology and bed composition driven by the hydrodynamic stress and modulated by the sediment cohesion and grain size. With high stress and low bed cohesive content this will be a positive feedback resulting in a clean sand bed and increasing the rate bedform change and migration, and reducing the lag between hydrodynamic change and bedform response. For low stress, the feedback will be negative reducing the rate bedform change and migration with increasing bed cohesive content, and increasing the lag time. To resolve the effect of hysteresis on this system would require increasing the rate of sampling of both the bedform morphology and bed composition. This could be done in the controlled conditions of a laboratory flume, to get around the current limitations in field sampling methodology.

6.6 Recommendations for improvements and future work

From the fieldwork, data processing and data analysis, improvements could be seen for similar work in the future and other avenues of investigation for the data set as it is, were time available. This section outlines some recommendations for future work for the instrument setup and sampling, wave-current hydrodynamics, and the effects of biology.

6.6.1 Improvements to the instrument set up and bed sampling

Although there are many small improvements that could be made for future deployments, a few improvements are outlined here, related to the 3D-ARP, the measurement of water depth and the bed sampling. When choosing the instruments settings, a balance has to be made between high-resolution sampling, memory space and battery capacity for the deployment period. In a new area, without prior measurements, instrument settings are best kept conservative to cover a wide range of possible conditions. However, if a similar deployment were to be made in the same area, the instrument settings should adjusted to gain better resolution of the expected dynamical processes.

The time taken by the 3D-ARP to collect a scan is fixed by the time taken for the instrument to move the transducer head. However, reducing the interval between scans from 30 minutes to 15 or 20 minutes would lead to improvements in the resolution of the changes in the bedform morphology and

dimensions during periods of strong flow and for short inundation periods, although this would require more frequent instrument servicing.

A bed-mounted pressure sensor could provide a near-complete water depth time series. These data could be used to determine if the start of the flood and end of the ebb deviated from the expected tidal curve. This would provide a more complete picture of the hydrodynamics and be used to infer the processes occurring when the acoustic transducers were not submerged.

The frame, and mounted instruments, channel the horizontal flow and affect the vertical flow (Bolaños *et al*., 2011). The current velocity represented the flow conditions at the bed, as it was measured in the channelled flow beneath the instruments. The wave parameters were determined from the water elevation, above the frame, and the resulting values for wave bottom orbital amplitude velocity could be overestimated due to the dampening effects of the frame, as this could reduce the effect of the waves on the sediment. An additional upward pointing ADV could resolve this effect and determine if the additional non-linear term seen the bedform dimensions multiple linear regression was the result of this dampening effect.

For future deployments, selecting a single site for the entire study period, over at least a month long spring-neap cycle, would produce better results. This would reduce uncertainties in the spatial variation sediment composition and due to high wind events producing, waves and wind driven flow on top of the tide, by providing a longer time series for analysis.

6.6.2 Wave-current hydrodynamics

The effects of wave skewness and asymmetry have not been looked at in this thesis, as waves dominated for only a small part of the record. The residual flow, due to wave skewness and streaming effects, was included in the current velocity when the data were averaged. However, the data set presented here does include periods of waves and wind driven flow, with and against the tide. This could potentially be used to explore the relationship of wave skewness and asymmetry with the suspended sediment results from the Acoustic Backscatter System, which samples at a much higher rate than the 3D-ARP and would resolve processes on the time scale of waves.

The combined wave-current bed shear stress parameter included the effect of wave-current stress enhancement on the bedform migration. When the current stress drops below the limit of motion, wave-current stress enhancement keeps the total stress above the limit of motion. When the wave and current stresses were separated, for multiple linear regression analysis of bedform height, the

wave-current stress interaction parameter was found to be significant in reducing the height. This shows that the wave-current stress enhancement has an important effect on sediment dynamics.

6.6.3 The effects of biology on bed morphology

Worm mounds and feeding pits can disturb the flow, causing scour, creating stationary bedforms or aiding the formation of migrating ripples (Fries *et al*., 1999; Passarelli *et al*., 2014). The 3D-ARP scans during tidal inundation and photos of the bed at exposure suggest that these features were present during tidal inundation (section 4.6.2.6). The supposed feeding pit in Figure 4-13 was only seen in the 3D-ARP scans for tidal period 1, when the measured bed shear stress due to tide and waves was the low and only above the limit for motion due to wave-current enhancement. This implies that these biogenic features were eroded away by high bed shear stress and overwritten by bedform migration seen throughout most of the record. However, the 3D-ARP resolution was such that individual biogenic features would have to be a few centimetres in size to be clearly distinguished.

The migration rate values were based on the cross-correlation of 3D-ARP scans as whole images and this would effectively average out the effect of individual bedforms kept stationary by biological action, adding error to the result. Detecting these stationary features on a moving bed could be done using more complex image analysis, by a moving window cross-correlation on the scale of individual features (Giachetti, 2000; Sutton *et al*., 2009). Correcting for stationary features, due to the presence of the frame as well as biogenic features, would reduce the error in calculating the average migration rates of bedforms. In addition, by determining the migration rate for windows within the 3D-ARP scans the variation in migration rate over the scans and therefore for different types of bedforms within the scan could be determined, as well as the effect of biogenic features.

6.6.4 Intra-tidal processes of cohesive sediment

As discussed in sections 6.3.3 and 6.4.1, the processes of cohesive sediment within a tidal period have not been well described in this thesis, due to the limitations of the measurements and sampling. Investigating the physical processes of winnowing, pressure gradient filtering and burial by bedform migration in relation to mixed cohesive sediment should initially be done in controlled laboratory flume studies. This would allow the methods and instrumentation to be developed to describe these small-scale processes, before moving to the more complex conditions in the field to confirm the results. Many laboratory experiments have been carried out on mixed sand-mud flocs (Manning *et al*., 2011) and field instruments to measure flocculation and settling are available (*e.g.* cameras and

holographic particle imagers). Measuring suspended sediment concentration and particle size distribution at high temporal resolution are routine in the field, using laser scattering and acoustic backscatter instruments. By improving methods of near-bed measurement and data analysis for mixed sand-mud sediment, using these instruments, future work on mixed cohesive sediments and hydrodynamics on tidal flats could resolve these small-scale processes within a tidal cycle.

The bed sediment samples collected when the tidal flats were exposed were not able to resolve changes in bed composition during tidal inundation. To relate instrument measurements to *in situ* sediment properties during inundation, a specialised sampler that could take timed sediment samples of the bed at set locations could be built, for example an automatic push corer using hydraulic pistons based on designs used by ROVs. A simpler alternative would be to sample from a small moored boat using a sediment grab or corer to take regular samples over the inundation period. However, this would be less precise, as the boat would move with the tide, and be more labour intensive. Bed strength is also currently measured by manual methods (*e.g.* shear vane, sediment penetrometer or cohesive strength meter) and it may be possible to automate these measurements to obtain a time series of bed strength during aerial exposure and tidal inundation.

The EPS content of the bed is currently measured from sediment samples, with the limitations of obtaining bed samples, though as the production of EPS by diatoms is light dependent (Lundkvist *et al.,* 2007) it may be possible to estimate the biological cohesion from instrument measurements of chlorophyll (photosynthetic pigment) fluorescence and light levels (Anderson and Pejrup, 2011). However, the relationships between these measurements and the EPS content would have to be determined in laboratory conditions and calibrated with samples, though the result would be a continuous time series of EPS estimates during inundation. The effect of bioturbation would also require prior knowledge of animal behaviour and mixing rates, with data collect in the field to obtain population numbers, in order to quantify the effect.

By improving the temporal resolution of measurements and bed sampling, the intra-tidal processes could be quantified more accurately. This could lead to better estimates of cohesive sediment transfer to and from the bed, and improved predictions of the fate of cohesive sediment in the coastal system.

6.6.5 Change of season and climate

To describe the balance between physical and biological processes over seasonal cycles would require fieldwork to be carried out at different times of the year, to capture the variation in biological activity and the effect of strong wind events. Due to the instrument maintenance and sampling requirements

of the data collection, this would be best done in a series of month long field studies over a year at a single set location in order to resolve the tidal dynamics and any meteorological events. In winter, it would be expected that physical processes dominate and that the effect of biological processes is reduced, due to light availability and the effect of low temperature (Anderson and Pejrup, 2011). However, high stress events may erode the down to the sub-surface sediment layers and release nutrients into the system for consumption. As light levels increase in spring, biological production will increase until the available nutrients are used up. Cyclical events of bloom and die off may occur until the light levels and temperature decrease again in the following winter.

Different locations will have different sediment types and properties. Biological processes and interactions that affect sediment transport are found worldwide, with ecosystems composed of different species, and changes in habitat and climate effect the deposition of cohesive sediment (Anderson and Pejrup, 2011). Global climate change in weather patterns and sea level would be expected to affect these processes in coastal areas (Jones *et al*., 2013; Passarelli *et al*., 2014). To assess the effect of different climates, for comparison with the temperate site of the COHBED project, sites should be selected that are similar in sediment type and ecosystem function. This could be done by selecting suitable sites in tropical, sub-tropical, sub-polar regions. Monitoring these sites at intervals over many years would be required to observe the effects of climate change. Therefore, numerical models could be used, with validation from fieldwork, to study these long-term effects.

6.7 Implications for sediment transport modelling, geomorphology and coastal engineering

On a regional scale, cohesive sediment dynamics could have a significant effect on the bed roughness, transport of sediment and the pollutants adhered to them, biochemical processes occurring across the seabed-water interface and regional morphological change (Precht and Huettel, 2003; Aldridge *et al*., 2015; Parsons *et al*., 2016). Although many of the processes involving cohesive sediment are parameterised in some regional models, the effect of cohesive sediment on bedform dimensions and material transport is not currently not included (Paarlberg *et al*., 2005; Sanford, 2008; van Kessel *et al*. 2012). Therefore, the effect of cohesive sediment would be a source of error in numerical models that treat sediment as only cohesionless. This will affect the design of coastal structures and management interventions for maintenance of navigation channels and habitat conservation.

In reducing bedform dimensions and bed material transport, cohesive clay will have an effect on predictions of bed roughness and bed material transport in numerical models. However, as

distribution of cohesive sediment is patchy scaling these results up to regional models may be difficult. Defining the processes affecting cohesive sediment, using laboratory and field data, relative to parameters that can be easily measured, modelled or be tuned within a model, such as water level, daylight exposure, wind, wave height, bed shear stress and bed clay content, would lead to improvements to the characterisation of cohesive sediments in regional models. Although the relationships developed in this thesis are site specific for bed cohesive content, they are a step towards providing better parameterisation of cohesive sediment processes in numerical models.

7 Conclusions

The aim of this thesis was to determine the effect of physically and biologically cohesive bed material on bedform dimensions, planform and migration, in a field environment. The SEDbed suite of instruments was deployed on the Hilbre tidal flats in the Dee Estuary to collect data on the effect of physical and biological cohesion on the dynamics of small-scale bedforms. The near-bed hydrodynamics and changing bed morphology were measured over a spring-neap cycle. In addition, bed sediment samples were collected for particle size and biological analysis, to measure the amounts of cohesive material within the sediments. These field measurements were compared to existing laboratory flume data, planform types and standard predictors for bedform dimensions.

From the results of the fieldwork undertaken on tidal flats in the Dee estuary, it has been shown that:

- The cohesive clay content of the bed varies with hydrodynamic forcing on the Hilbre tidal flats, within the spring-neap cycle.
- The amount of biological cohesive material (Extracellular Polymeric Substances, EPS) in the bed sediment correlates linearly with the cohesive clay content, with EPS = 0.013 × cohesive clay + 0.015.
- Increasing bed cohesive clay content reduced bedform dimensions and it would not be expected for bedforms to develop above 4 vol% cohesive clay, with a corresponding EPS fraction of 0.07 wt%, in these field conditions.
- Bed material transport rate is reduced by increasing bed cohesive clay content, below about 3 vol% cohesive clay with a corresponding EPS fraction of 0.05 wt%, and above this limit the bedforms appeared to stop migrating.
- Bed cohesive clay content did not appear to affect the threshold of sediment motion below about 3 vol% cohesive clay.
- Standard bedform predictors applied to sediments with only a few percent of cohesive clay overestimate bedform dimensions and bed material transport rate.
- A new bedform phase diagram based on cohesive clay content and combined-flow bed shear stress was proposed, which showed a transition of planform type as the bed shear stress decreased and cohesive clay content increased, above about 1 vol%.
- This relationship for cohesive clay content, combined-flow bed shear stress and planform type broke down below a cohesive clay content of about 1 vol%, suggesting that the mixed sand-clay bed behaved as a cohesionless bed.
- Combined wave and current flow produced segmented bedforms in the 3D-ARP scans, possibly linked to tidal rotation.

- Using logistic regression to relate the planform dimensionality classifications to hydrodynamics, the current and wave bed shear stress and wave-current angle were shown to effect planform dimensionality, distinguishing between wave and current forcing.
- Small-scale sand ribbons were observed, bedforms that are usually associated with sand and gravel beds, and have not been described in muddy-sand sediment before.
- Some current bedforms were seen to scale with water depth, and were larger than the expected equilibrium dimensions for current ripples, these are best described as transitional or intermediate bedforms between current ripples and dunes.
- A conceptual model has been developed that qualitatively explains the change in cohesive clay seen in the field data.

Brought together, these results have shown the effect of physically and biologically cohesive material on bedform dynamics in mixed mud-sand sediment for a field environment. Sediment cohesion has the effect of making bedforms lower in height and shorter in length, and slows the bedform migration and material transport. Otherwise, the bedforms seen in the field study conformed to predicted types for current and wave ripples, with the exception of transitional bedforms seen to have dimensions between current ripples and dunes and scale with the water depth. A conceptual model was used to explore the processes that could result in the transfer of cohesive mud into and from the bed, to put the field results into context. This improvement in the understanding of cohesive sediment processes dynamics has the potential to affect the modelling of coastal morphology and dynamics, transport of sediment and the pollutants adhered to them, the design of coastal structures and management interventions for maintenance of navigation channels and habitat conservation.

8 Appendices

8.1 List of abbreviations and acronyms

ABS	Acoustic Backscatter System (instrument)
ADV	Acoustic Doppler Velocimeter (instrument)
ADVP	Acoustic Doppler Velocity Profiler (instrument)
ARP or 3D-ARP	Three-dimensional Acoustic Ripple Profiler (instrument)
BASSI	Bedform And Suspended Sediment Imager (instrument)
COHBED	'Realistic Sedimentary Bedform Prediction: Incorporating Physical and Biological Cohesion (COHBED)' project
CTD	Conductivity, Temperature and Depth (instrument)
EPS	Extracellular Polymeric Substances (biogenic cohesive material)
LISST	Laser *In Situ* Scattering and Transmissometry (instrument)
NOCL	National Oceanography Centre, Liverpool
OBS	Optical Backscatter Sensor (instrument)
PSD	Particle size distribution

8.2 List of symbols

c	Bed cohesive clay content (vol%)
e	Bed Extracellular Polymeric Substances or total carbohydrate fraction (wt%)
h	Depth of water (m)
H	Wave height (m)
f	Bedform shape factor (-)
K	Coefficient of erosion/deposition
n	Number of measurements or values (-)
p	Probability extreme value occurrence (-)
q_b	Volume bed material transport rate ($m^3\ m^{-1}\ s^{-1}$)
Q_b	Mass bed material transport rate ($kg\ m^{-1}\ s^{-1}$)
s	Relative density of sediment to water (-)
$\langle u \rangle$	Depth mean current velocity ($m\ s^{-1}$)

u_b	Bedform migration rate (m s^{-1})
u_w	Bottom wave orbital amplitude velocity (m s^{-1})
z_0	Bed roughness length (m)
B	Bandwidth of migration rate (m^{-1})
C	95% correlation confidence interval (m)
D_{50}	Median grain diameter (m)
D_*	Dimensionless grain diameter
E_{nrms}	Normalized RMS correlation error (-)
H_s	Significant wave height (m)
K	Hubbell's loss-gain factor (-)
P	Bed porosity (-)
Q_b	Mass bed material transport rate (kg m^{-1} s^{-1})
R^2	Correlation coefficient (-)
T_p	Peak wave period (s)
T_{rl}	Record length of cross-correlation (m)
α	Coefficient in equation 5-1
β	Coefficient in equation 5-1
η, η_{eq}	Bedform height, ripple equilibrium height (m)
θ, θ'_{max}	Total Shields parameter, combined maximum skin friction Shields parameter
λ, λ_{eq}	Bedform length, ripple equilibrium length (m)
ν	Kinematic viscosity of water (m^2 s^{-1})
ρ, ρ_s	Water density, sediment density (kg m^{-3})
$\rho_{12}(\tau^*)$	Peak normalized cross-correlation (-)
$\sigma(\tau^*)$	Standard deviation of the peak cross-correlation (m)

τ'_c, τ'_w, τ'_{max}, $\tau'_{max/}$	Current-only bed shear stress, wave-only bed shear stress, combined maximum bed shear stress, linear maximum bed shear stress (skin friction only) (N m^{-2})
τ^*	Peak correlation lag (m)
φ	Angle between wave and current direction (degrees)

8.3 Fieldwork log

8.3.1 20 May 2013, Site selection

8.3.1.1 Low water 13:05

Site 1

Suitable sites for the sampling and instrument deployments were identified. In particular, areas of clean sand, mixed sand & mud, and sediment with biological influence (worm burrows and biofilms). Handheld GPS positions were recorded for the sand and mixed sites (Table 8-1).

Table 8-1: Handheld GPS (Garmin) positions (accuracy 4-5m)

	Waypoint	Latitude Degrees	Latitude Minutes		Longitude Degrees	Longitude Minutes		Notes
Sand site	1	53	22.504	N	3	12.708	W	
Sand site	2	53	22.505	N	3	12.708	W	
Muddy site	3	53	22.484	N	3	12.648	W	JB's WP26
Sand site	4	53	22.504	N	3	12.705	W	JB's WP27, sample

8.3.2 21 May 2013, first SEDbed deployment, Site 1

8.3.2.1 Low water 14:09

Site 1

SEDbed was set up on a sandy area (site 1). The area around the frame was trampled flat during this process. The sediment was sand in the top few centimetres with consolidated mud beneath this.

The height from the top of the BASSI to half way up a ripple on the bed below was measured as 66 cm. The SEDbed frame is aligned to the NW (310°). Sediment sample 1 was taken from the seaward (Northerly) side of the frame (only a small sample maybe only good for laser diffraction).

8.3.3 22 May 2013

8.3.3.1 Low water 15:04

Site 1

Conditions at the site were very windy. The area under the frame has well defined ripples, possibly because it wasn't trampled during the frame construction with the existing ripples accentuated with new ripples taking time to form. Photos of the ripples were taken with the tape measure as reference. The ripples were measured with an approximate three wavelength measurement of 53 cm and height of 4 to 5 cm, from a rough average of 3 measurements. The BASSI height was measured as 65 cm. Sediment sample 2 was collected (about 1 kg in two sample bags).

The instrument locations on the frame were measured from the landward-right hand corner looking seaward. Photos were taken. Sediment sample 2 was taken from the area just landward of the frame. High accuracy DGPS positions were recorded of the frame corners.

The top cup of the multi-tier sediment trap was empty possibly as the tide did not reach this high or possibly the wind blew and evaporated it away or the bolts were loose and the water drained away but as there was not much sediment nothing was left. The cups below had more water with the bottom cup completely full.

8.3.4 23 May 2013

8.3.4.1 Low water 15:54

Site 1

The conditions on site were very windy. The frame was checked and photos taken. The top cup of the multi-tier sampler was empty.

Ripple measurements were taken for three wavelengths, 46, 52 and 38 cm, the mean height was 1 - 2 cm. The sand ripples were irregular and it was difficult to get good measurements; the crests had been flattened. Photos of the ripples were taken with the tape measure extended to 1 m. The top of the BASSI was measured as 66 cm.

The poles of the frame that had been sunk into the sediment showed scour, measurements were taken to estimate the changes in scouring over the deployment. The scour hole depths were measured to the bottom of the frame: NE corner 9.25 cm, SE corner 11 cm, NW corner 14.5 cm, SW corner 13 cm, middle N 17 cm and middle S 13 cm.

Sediment sample 3 was collected from the landward side of the frame (same as for sample 2) and waypoint 6 was recorded on the Garmin GPS.

Two filter mesh sizes were tested, 5 µm and 10 µm, as well as funnel coffee filters. Strong winds made the filtering difficult. The square filter fabrics were especially awkward as they had to be held in place at all four corners, the coffee filter was easier as it fitted in the funnel and could be held at a single point because of its rigidity. 2-3 scoops of liquid sand and a few more scoops of water were used in each case. The 5 µm filter was the slowest, the 10 µm and coffee filter were about the same.

The mud layer beneath the sand was exposed in the troughs of the ripples. Also in the troughs were nodules of mud that had been formed. The mud layer could be seen in the scour holes.

At first arrival on site there was a pool of water below the frame, which later drained away, and the area under the frame was more eroded than the surrounding area.

8.3.5 24 May 2013, move from site 1 to site 2

8.3.5.1 Low water 16:43

Site 1

An attempt was made to filter the multi-tier sediment trap samples, which was quite difficult due to the wind. The filter fabric squares were difficult to handle in conjunction with the funnel. The grey lid above the cup and turbulence baffle was removed. The sediment trap cup had to be handled carefully by first loosening the bolts, which went right through the side of the cup, to allow the cup to be raised. Then the top bolts were removed to drain some of the water and allow the cup to be tilted independently of the frame. The sample could then be poured into the filter.

The fine material meant that the filtering took a long time. There was no sample in the top cup, number 1, as its bottom was not attached properly and it leaked. The second cup was filtered using a 5 µm filter and this took a long time and some material was lost. The other samples were filtered using 10 µm filter fabric and this also seemed quite slow in the weather conditions.

It was thought to be better put the samples in air tight containers (Tupperware) and do the filtering back at the laboratory. Sewing up the filter fabric into cones to fit the funnel would also make the filtering easier. This may not be required as the samples would be allowed to settle, most of the seawater siphoned off and then diluted with distilled water for laser diffraction analysis.

The depth of scour was measured to the bottom of the cross pieces of the frame, which were level with the bed at the start of the deployment: NE corner 19.5 cm, SE corner 15 cm, NW corner 17.5 cm and SW corner 16 cm.

Site 2

The second site is in a channel with the bed always under water. The sediment is mixed sand and mud with lugworm casts, and other biology, over the measurement area. The sediment samples collected at this site had to be drained of water, after being allowed to settle, so some of the fines may have been lost.

8.3.6 25 May 2013

8.3.6.1 Low water 17:31

Site 2

Ripple measurements were taken from seawards of the frame. The sediment was fine and suspended when disturbed making it difficult to measure the ripple height.

The instrument heights were recorded and the positions of the cups on the multi-tier sediment trap. Measurements of the worm cast spacing were taken approximately from centre to centre: 16, 19, 9, 5, 19 and 8 cm. The bed under the frame was uneven.

Richard fixed a trapped cable and LED fault in the ADVP and re-started it with a different memory card (the same card used for the first deployment. It was set to start sampling at 16:30 GMT.

8.3.7 26 May 2013

8.3.7.1 Low water 18:19

Site 2

The weather was sunny and calm. A compass reading of the frame (296°), ripple dimensions, instrument heights, scour depths and sediment sample 4 were collected. Photos of the frame, with the tape measure next to the instrument positions, were taken. One of the lids on the multi-tier sediment trap was adjusted to make them all about the same height from the cups.

The bed beneath the frame undulates and there are scour channels that suggest that the water flow has not always been perpendicular to the frame. Seaward of the frame the ripples were fairly regular, under the frame irregular and lumpy, and landward of the frame the ripples were closer spaced and irregular. The ripples were difficult to measure as the fine sediment suspended when disturbed.

The high water springs draining into the main channel caused runnels to form through the bed ripples and suggest that there was significant flow lateral to the main channel. This increased flow due to the high tide and the position of the frame in the channel probably resulted in the scour and uneven bed around the frame.

8.3.8 27 May 2013

8.3.8.1 Low water 06:44

Site 2

The weather was windy, blowing from the southerly direction, with clouds and sunny spells. Ripple dimensions, instrument heights and scour depths were recorded and sediment sample 5 collected. The scour seaward of the frame was more pronounced than the previous day. The ripples seaward of the frame were more regular. The ripples landward of the frame were also more regular and extended under the frame, running south to north, changing to become rounder with smoother crests. There are also more worm casts beneath the frame than the surrounding area.

When the frame is uncovered at low tide the ripples will be wind dominated. If the sediment dries out then Aeolian transport will occur.

The top cup of the multi-tier trap has lots of sediment compared to the previous site, more than cups two and three.

Later in the day the sun faded and the sky became more overcast and the wind increase. This made taking photos of the ripples underwater difficult.

At about 10:15 the tide had started to flood the site area (seen from car park).

8.3.8.2 Low water 19:07

Site 2

The wind had further increased since the morning. There was increased scour seaward of the frame. Ripple lengths were taken but not heights, due to cold fingers, instrument heights measured and sediment sample 7 collected.

8.3.9 29 May 2013, move from site 2 to site 3

8.3.9.1 Low water 08:25

Site 2

Ripple dimensions were recorded and sediment sample 7 collected. The multi-tier sediment trap was measured to get the spacing of the cups, lids and base (Table 8-2). The samples were decanted into pots after draining some of the water, being careful not to disturb the sediment, and rinsed to collect as much sediment as possible.

The top cup was empty and on closer inspection it was found that the bottom wasn't glued on properly. Cup 2 had also partially drained. After inspecting the other cups the leaking cups were set aside. The sediment trap was re-built to the dimensions noted down, with cups that were thought to be watertight taken from both frames. The bottom cups, 3-5, were known to be watertight from the previous deployment.

Table 8-2: Multi-tier sediment trap lid and cup (to mouth of cup) positions from the base.

	Cup height, cm	Lid height, cm
5	5.5	21.0
4	26.5	40.0
3	44.0	57.5
2	59.5	73.0
1	86.0	Fixed in place

Site 3

While the multi-tier samples were being taken the SEDbed frame was moved to the next site. Site 3 was muddier and dried out at low tide; Site 2 had become sandier. A compass reading of the frame (274°), ripple dimensions, instrument heights and sediment sample 8 were collected. Photos of the ripples were taken.

8.3.10 30 May 2013

8.3.10.1 Low water 09:17

Site 3

There was a northerly wind and the sky was overcast with intermittent rain, the weather improved during the day. The site had been reworked and the area was covered by 3D ripples, with flattened crests, textured by rainfall. Worm casts were seen over the area. The top two cups of the multi-tier sediment trap had drained of water, but the bottom three were all full. Ripple dimensions, instrument heights and scour depths were recorded and sediment sample 9 collected.

8.3.11 31 May 2013

8.3.11.1 Low water 10:13

Site 3

It was a clear sunny day with a brisk northerly wind. Ripple dimensions, instrument heights and scour depths were recorded and sediment sample 12 collected. Ripple photos were taken with the tape measure extended to 1 m and the steel ruler (scale 0-30.5 cm) in shot. The BASSI was showing a green light, meaning that it was in sleep mode. The multi-tier sediment trap cups were measured from the bed (5 - 20.5 cm, 4 - 42.0 cm, 3 - 60.0 cm, 2 - 75.0 cm and 1 - 100.0 cm). Photos were taken of the ripples starting as usual from the seaward side of the frame. The sun was from the south east.

To compare NOCL sampling with the sampling methods of Bangor University a set of co-located samples were collected from the surface, approximately 0.5 cm deep, and no deeper than the ripple trough. Samples were collected seaward of the frame and under the frame (10 & 11). A gouge in the sediment under the ripple scanner was left where the sediment sample was taken under the frame, towards the landward side.

8.3.12 1 June 2013

8.3.12.1 Low water 11:14

Site 3

Ripple dimensions, instrument heights and scour depths were recorded and sediment sample 13 collected. Baby mussels were growing in some of the stored sediment samples

8.3.13 2 June 2013

8.3.13.1 Low water 12:20

Site 3

It was a clear sunny day and there was a northerly wind blowing. There was a lot of interest in the frame; the area around it had been well trampled. Ripple dimensions, instrument heights and scour depths were recorded and sediment sample 14 collected. The SEDbed frame tube diameter was measured as 4.75 cm. The conductivity cell on the ripple scanner was at 54.5 cm above the frame (61.5 cm above the rim of the scanner dome). The CTD conductivity cell is 6.5 cm above the pressure sensor and 3 cm above the frame. The vertical offset between the two conductivity cells is 51.5 cm.

8.3.14 3 June 2013

8.3.14.1 Low water 13:27

Wide area survey for particle size distribution of surface sediments

To put the COHBED intertidal survey into context a wider survey of the surface sediments was carried out. From the car park at West Kirby out to the water edge at about low tide, a zigzagging line was walked to cover a strip about 100 m wide around the channel. About every 200-250 m sediment samples were collected. This was not initially planned as part of the fieldwork and may be worked up as part of an MSc project.

The sediment sample numbering matched the waypoint numbers on JB's GPS. There is no sediment sample 65 due to an accidental waypoint mark.

Site 3

It was a clear sunny day with light winds. The frame was covered in fine sediment sprayed onto the frame and dried out or from the receding tide (a sample was taken of this sediment by JB). There was lots of seaweed and dry grass as well. The top two cups of the multi-tier sediment trap were half full

of water for the first time at this site (previously they had drained completely). The ripples under the frame were well developed, while the ripples seaward and landward of the frame were shallower and flatter. Sediment sample 15 was collected.

8.3.15 4 June 2013, SEDbed recovery

8.3.15.1 Low water 14:28

Site 3

Ripple dimensions and BASSI height were recorded and sediment sample 16 collected. The sediment trap samples were collected. The top cup of the multi-tier trap was half full of water and the second cup about ¾ full of water. Sediment must be blocking the leaks. SEDbed was dismantled and the site cleared.

8.4 Full classification of bedforms in the 3D-ARP scans

Time	Site	Period	Type	Dimensionality	State of tide	current stress, N m^{-1}	wave stress, N m^{-1}	wave-current angle, degrees	Figure
21/05/2013 19:00	1	1	sinuous/straight	2D	flood	0.09	0.02	0	Figure 4-13
21/05/2013 20:00	1	1	sinuous/straight	2D	ebb	0.01	0.19	0	
21/05/2013 20:30	1	1	sinuous/straight	2D	ebb	0.12	0.12	0	
21/05/2013 21:00	1	1	sinuous/straight	2D	ebb	0.18	0	0	
22/05/2013 07:00	1	2	sinuous/straight	2D	flood	0.13	0	0	Figure 4-14
22/05/2013 07:30	1	2	sinuous/straight	2D	flood	0.13	0.2	0	
22/05/2013 08:00	1	2	sinuous/straight	2D	flood	0.02	0.48	0	
22/05/2013 08:30	1	2	sinuous/straight	2D	ebb	0.02	0.32	0	
22/05/2013 09:00	1	2	sinuous/straight	2D	ebb	0.09	0.03	0	

Time	Site	Period	Type	Dimensionality	State of tide	current stress, N m^{-1}	wave stress, N m^{-1}	wave-current angle, degrees	Figure
22/05/2013 09:30	1	2	sinuous/straight	2D	ebb	0.13	0	0	
22/05/2013 19:30	1	3	sinuous/straight/lunate	2D/3D	flood	0.34	0.08	0	
22/05/2013 20:00	1	3	lunate	3D	flood	0.16	0.78	0	Figure 4-15
22/05/2013 20:30	1	3	lunate	3D	turning	0.07	0.8	45	
22/05/2013 21:00	1	3	segmented	3D	turning	0.01	0.63	90	Figure 4-16
22/05/2013 21:30	1	3	sinuous/segmented	3D	turning	0.03	0.39	90	
22/05/2013 22:00	1	3	segmented	3D	ebb	0.18	0.02	0	
23/05/2013 07:30	1	4	sinuous	2D	flood	0.25	0	0	
23/05/2013 08:00	1	4	lunate	3D	flood	0.3	0.06	0	

Time	Site	Period	Type	Dimensionality	State of tide	current stress, N m^{-1}	wave stress, N m^{-1}	wave-current angle, degrees	Figure
23/05/2013 08:30	1	4	lunate	3D	flood	0.2	0.05	0	
23/05/2013 09:00	1	4	lunate	3D	turning	0.08	0.34	45	
23/05/2013 09:30	1	4	sinuous	3D	turning	0.04	0.19	45	
23/05/2013 10:00	1	4	segmented/sinuous	3D	turning	0.03	0.03	90	
23/05/2013 10:30	1	4	segmented	3D	ebb	0.27	0.01	0	
23/05/2013 20:00	1	5	lunate/washed out	3D	flood	0.63	0.04	0	
23/05/2013 20:30	1	5	washed-out/sand ribbons	3D	flood	0.36	0.47	0	
23/05/2013 21:00	1	5	washed-out	3D	flood	0.2	0.65	45	
23/05/2013 21:30	1	5	washed-out/sinuous	3D	turning	0.14	0.67	45	

Time	Site	Period	Type	Dimensionality	State of tide	current stress, N m^{-1}	wave stress, N m^{-1}	wave-current angle, degrees	Figure
23/05/2013 22:00	1	5	washed-out/sinuous	3D	turning	0.17	0.54	90	Figure 4-17
23/05/2013 22:30	1	5	segmented/sinuous	3D	turning	0.05	0.25	90	
23/05/2013 23:00	1	5	segmented/sinuous	3D	ebb	0.16	0.01	0	
24/05/2013 08:00	1	6	sinuous	2D	flood	0.39	0.01	0	
24/05/2013 08:30	1	6	washed-out/sinuous/segmented	3D	flood	0.59	0.16	0	
24/05/2013 09:00	1	6	washed-out/sand ribbons	2D	flood	0.55	0.16	0	
24/05/2013 09:30	1	6	washed-out/sand ribbons	2D	flood	0.37	0.84	45	Figure 4-18
24/05/2013 10:00	1	6	washed-out/sand ribbons	2D	flood	0.25	0.73	90	
24/05/2013 10:30	1	6	lunate/sand ribbons	2D/3D	turning	0.26	0.51	45	

Time	Site	Period	Type	Dimensionality	State of tide	current stress, N m^{-1}	wave stress, N m^{-1}	wave-current angle, degrees	Figure
24/05/2013 11:00	1	6	sinuous/sand ribbons	2D/3D	turning	0.05	0.14	90	
24/05/2013 11:30	1	6	sinuous/sand ribbons	2D/3D	ebb	0.23	0.01	0	
24/05/2013 20:30	2	7	sinuous	3D	flood	0.42	0.01	45	
24/05/2013 21:00	2	7	lunate	3D	flood	0.48	0.02	0	
24/05/2013 21:30	2	7	lunate	3D	flood	0.09	0.2	45	
24/05/2013 22:00	2	7	sinuous/lunate	2D/3D	turning	0	0.2	0	
24/05/2013 22:30	2	7	sinuous	2D	ebb	0.1	0.11	0	Figure 4-19
24/05/2013 23:00	2	7	sinuous	2D	ebb	0.12	0.01	0	
24/05/2013 23:30	2	7	sinuous	2D	ebb	0.23	0.01	0	

Time	Site	Period	Type	Dimensionality	State of tide	current stress, N m^{-1}	wave stress, N m^{-1}	wave-current angle, degrees	Figure
25/05/2013 00:00	2	7	sinuous/lunate	2D/3D	ebb	0.25	0	0	
25/05/2013 09:00	2	8	sinuous/linguoid	3D	flood	0.5	0.02	45	
25/05/2013 09:30	2	8	sinuous/segmented	3D	flood	0.18	0.02	45	
25/05/2013 10:00	2	8	sinuous/segmented	3D	flood	0.09	0.01	90	
25/05/2013 10:30	2	8	sinuous/segmented	3D	turning	0.03	0.03	90	
25/05/2013 11:00	2	8	sinuous/segmented	3D	ebb	0.1	0.03	90	
25/05/2013 11:30	2	8	sinuous/segmented	3D	ebb	0.17	0.02	45	
25/05/2013 12:00	2	8	sinuous/segmented	3D	ebb	0.22	0.01	0	
25/05/2013 12:30	2	8	sinuous/segmented	3D	ebb	0.48	0.01	90	

Time	Site	Period	Type	Dimensionality	State of tide	current stress, N m^{-1}	wave stress, N m^{-1}	wave-current angle, degrees	Figure
25/05/2013 21:00	2	9	washed-out/sinuous/segmented	3D	flood	0.53	0	0	
25/05/2013 21:30	2	9	sinuous/segmented	3D	flood	0.43	0.01	45	
25/05/2013 22:00	2	9	sinuous/segmented	3D	flood	0.28	0.02	0	Figure 4-20
25/05/2013 22:30	2	9	sinuous/segmented	3D	flood	0.04	0.01	0	
25/05/2013 23:00	2	9	sinuous/segmented	3D	ebb	0.04	0.01	90	
25/05/2013 23:30	2	9	sinuous/segmented	3D	ebb	0.09	0.01	0	
26/05/2013 00:00	2	9	sinuous/segmented	3D	ebb	0.15	0.01	0	
26/05/2013 00:30	2	9	sinuous/segmented	3D	ebb	0.19	0	0	
26/05/2013 01:00	2	9	washed-out/sinuous/segmented	3D	ebb	0.39	0.01	0	

Time	Site	Period	Type	Dimensionality	State of tide	current stress, N m^{-1}	wave stress, N m^{-1}	wave-current angle, degrees	Figure
26/05/2013 09:30	2	10	sinuous/segmented	3D	flood	0.54	0.01	90	
26/05/2013 10:00	2	10	sinuous/segmented	3D	flood	0.46	0.04	90	
26/05/2013 10:30	2	10	sinuous/segmented	3D	flood	0.25	0.06	45	
26/05/2013 11:00	2	10	sinuous/segmented	3D	flood	0.05	0.01	45	
26/05/2013 11:30	2	10	sinuous/segmented	3D	ebb	0.1	0.05	45	
26/05/2013 12:00	2	10	sinuous/segmented	3D	ebb	0.12	0.08	45	
26/05/2013 12:30	2	10	sinuous/segmented	3D	ebb	0.19	0.03	0	
26/05/2013 13:00	2	10	sinuous/segmented	3D	ebb	0.29	0.01	0	
26/05/2013 13:30	2	10	segmented/washed-out/sand ribbons	3D	ebb	0.7	0	0	

Time	Site	Period	Type	Dimensionality	State of tide	current stress, N m^{-1}	wave stress, N m^{-1}	wave-current angle, degrees	Figure
26/05/2013 22:00	2	11	linguoid/lunate	3D	flood	0.62	0	0	
26/05/2013 22:30	2	11	linguoid/lunate	3D	flood	0.47	0.04	90	
26/05/2013 23:00	2	11	linguoid/lunate/segmented	3D	flood	0.22	0.02	90	
26/05/2013 23:30	2	11	linguoid/lunate/segmented	3D	turning	0.01	0.09	0	
27/05/2013 00:00	2	11	linguoid/lunate/segmented/sinuous	3D	ebb	0.11	0.08	90	
27/05/2013 00:30	2	11	linguoid/lunate/segmented/sinuous	3D	ebb	0.13	0.05	45	
27/05/2013 01:00	2	11	linguoid/lunate/segmented/sinuous	3D	ebb	0.22	0.01	45	
27/05/2013 01:30	2	11	sinuous/segmented	3D	ebb	0.35	0	45	
27/05/2013 02:00	2	11	washed-out	3D	ebb	0.62	0	0	

Time	Site	Period	Type	Dimensionality	State of tide	current stress, N m^{-1}	wave stress, N m^{-1}	wave-current angle, degrees	Figure
27/05/2013 10:30	2	12	sinuous/linguoid/lunate	3D	flood	0.41	0.02	45	
27/05/2013 11:00	2	12	linguoid/lunate/segmented	3D	flood	0.31	0.02	90	
27/05/2013 11:30	2	12	linguoid/lunate/segmented	3D	flood	0.12	0.19	90	
27/05/2013 12:00	2	12	linguoid/lunate/segmented/sinuous	3D	turning	0	0.23	0	
27/05/2013 12:30	2	12	linguoid/lunate/segmented/sinuous	3D	ebb	0.17	0.23	90	
27/05/2013 13:00	2	12	sinuous/segmented	3D	ebb	0.16	0.18	90	
27/05/2013 13:30	2	12	segmented	3D	ebb	0.22	0.08	45	
27/05/2013 14:00	2	12	sinuous/segmented	3D	ebb	0.41	0	90	
27/05/2013 22:30	2	13	sinuous/linguiod/lunate	3D	flood	0.58	0	0	

Time	Site	Period	Type	Dimensionality	State of tide	current stress, N m^{-1}	wave stress, N m^{-1}	wave-current angle, degrees	Figure
27/05/2013 23:00	2	13	sinuous/linguiod/lunate	3D	flood	0.58	0.03	45	
28/05/2013 00:00	2	13	sinuous/linguiod/lunate	3D	flood	0.11	0.01	45	
28/05/2013 00:30	2	13	sinuous/linguiod/lunate	3D	ebb	0.06	0.08	90	
28/05/2013 01:00	2	13	sinuous/linguiod/lunate	3D	ebb	0.2	0.09	90	
28/05/2013 01:30	2	13	sinuous/linguiod/lunate	3D	ebb	0.2	0.03	45	Figure 4-21
28/05/2013 02:00	2	13	sinuous/segmented	3D	ebb	0.23	0.01	90	
28/05/2013 02:30	2	13		3D	ebb	0.61	0	0	
28/05/2013 11:00	2	14		3D	flood	0.58	0	0	
28/05/2013 11:30	2	14	liguiod/sinuous	3D	flood	0.47	0.01	0	

Time	Site	Period	Type	Dimensionality	State of tide	current stress, N m^{-1}	wave stress, N m^{-1}	wave-current angle, degrees	Figure
28/05/2013 12:00	2	14		3D	flood	0.3	0.01	90	
28/05/2013 12:30	2	14		3D	flood	0.1	0.03	90	
28/05/2013 13:30	2	14		3D	ebb	0.11	0.03	45	
28/05/2013 14:00	2	14		3D	ebb	0.16	0.01	90	
28/05/2013 14:30	2	14		3D	ebb	0.17	0.01	0	
28/05/2013 15:00	2	14		3D	ebb	0.52	0.04	45	
28/05/2013 23:30	2	15	sinuous/segmented	3D	flood	0.47	0	0	
29/05/2013 00:00	2	15	sinuous/segmented	3D	flood	0.44	0.03	0	
29/05/2013 00:30	2	15	segmented/linguoid/lunate	3D	flood	0.2	0.09	0	

Time	Site	Period	Type	Dimensionality	State of tide	current stress, N m^{-1}	wave stress, N m^{-1}	wave-current angle, degrees	Figure
29/05/2013 01:00	2	15	segmented/linguoid/lunate	3D	turning	0.04	0.04	0	
29/05/2013 01:30	2	15	segmented/linguoid/lunate	3D	ebb	0.08	0.09	90	
29/05/2013 02:00	2	15	sinuous/segmented/linguoid/lunate	3D	ebb	0.13	0.07	90	
29/05/2013 02:30	2	15	sinuous/segmented/linguoid/lunate	3D	ebb	0.19	0.05	0	
29/05/2013 03:00	2	15	sinuous/segmented	3D	ebb	0.29	0.01	0	
29/05/2013 03:30	2	15	sinuous/segmented	3D	ebb	0.45	0.01	45	
29/05/2013 12:30	3	16	linguoid/lunate/segmented	3D	flood	0.38	0.01	0	Figure 4-22
29/05/2013 13:00	3	16	linguoid/lunate/segmented	3D	flood	0.23	0.02	0	
29/05/2013 13:30	3	16	linguoid/lunate/segmented	3D	flood	0.03	0.13	0	

Time	Site	Period	Type	Dimensionality	State of tide	current stress, N m^{-1}	wave stress, N m^{-1}	wave-current angle, degrees	Figure
29/05/2013 14:00	3	16	linguoid/lunate/segmented	3D	ebb	0.06	0.16	90	
29/05/2013 14:30	3	16	linguoid/lunate/segmented	3D	ebb	0.12	0.08	45	
29/05/2013 15:00	3	16	linguoid/lunate/segmented/sinuous	3D	ebb	0.23	0.01	0	
29/05/2013 15:30	3	16	linguoid/lunate/segmented/sinuous	3D	ebb	0.2	0.01	0	
30/05/2013 00:30	3	17	linguoid/lunate/segmented/sinuous	3D	flood	0.48	0.01	0	
30/05/2013 01:00	3	17	linguoid/lunate/segmented	3D	flood	0.41	0.03	90	
30/05/2013 01:30	3	17	linguoid/lunate/segmented	3D	flood	0.13	0.21	45	
30/05/2013 02:00	3	17	linguoid/lunate/segmented	3D	flood	0.01	0.37	0	
30/05/2013 02:30	3	17	segmented	3D	ebb	0.08	0.28	45	

Time	Site	Period	Type	Dimensionality	State of tide	current stress, N m^{-1}	wave stress, N m^{-1}	wave-current angle, degrees	Figure
30/05/2013 03:00	3	17	segmented	3D	ebb	0.09	0.19	45	Figure 4-23
30/05/2013 03:30	3	17	segmented	3D	ebb	0.18	0.08	45	
30/05/2013 04:00	3	17	segmented	3D	ebb	0.35	0.01	45	
30/05/2013 13:30	3	18	sinuous/linguoid/lunate/segmented	3D	flood	0.27	0	0	
30/05/2013 14:00	3	18	sinuous/linguoid/lunate/segmented	3D	flood	0.17	0.01	45	
30/05/2013 14:30	3	18	sinuous/linguoid/lunate/segmented	3D	turning	0	0.08	0	
30/05/2013 15:00	3	18	sinuous/linguoid/lunate/segmented	3D	ebb	0.06	0.13	0	
30/05/2013 15:30	3	18	sinuous/linguoid/lunate/segmented	3D	ebb	0.15	0.07	0	
31/05/2013 02:00	3	19	sinuous/segmented	2D/3D	flood	0.3	0.01	0	

Time	Site	Period	Type	Dimensionality	State of tide	current stress, N m^{-1}	wave stress, N m^{-1}	wave-current angle, degrees	Figure
31/05/2013 02:30	3	19	sinuous/segmented	2D/3D	flood	0.08	0.04	90	
31/05/2013 03:00	3	19	sinuous/segmented	2D/3D	turning	0	0.02	0	
31/05/2013 03:30	3	19	sinuous/segmented	2D/3D	ebb	0.07	0.12	45	
31/05/2013 04:00	3	19	sinuous/segmented	2D/3D	ebb	0.12	0.01	90	
31/05/2013 04:30	3	19	sinuous/segmented	2D/3D	ebb	0.16	0.01	0	
31/05/2013 05:00	3	19	sinuous/segmented	2D/3D	ebb	0.37	0	0	
31/05/2013 15:00	3	20	sinuous/segmented	2D/3D	flood	0.06	0	0	
31/05/2013 15:30	3	20	sinuous/segmented	2D/3D	flood	0.02	0.02	0	
31/05/2013 16:00	3	20	sinuous/segmented	2D/3D	turning	0.02	0	0	

Time	Site	Period	Type	Dimensionality	State of tide	current stress, N m^{-1}	wave stress, N m^{-1}	wave-current angle, degrees	Figure
31/05/2013 16:30	3	20	sinuous/segmented	2D/3D	ebb	0.12	0.01	0	
31/05/2013 17:00	3	20	sinuous/segmented	2D/3D	ebb	0.2	0	0	
01/06/2013 03:00	3	21	sinuous/segmented	2D/3D	flood	0.17	0	0	
01/06/2013 03:30	3	21	sinuous/segmented	2D/3D	flood	0.13	0.04	0	
01/06/2013 04:00	3	21	sinuous/segmented	2D/3D	flood	0.04	0.02	0	
01/06/2013 04:30	3	21	sinuous/segmented	2D/3D	ebb	0.02	0.1	45	
01/06/2013 05:00	3	21	sinuous/segmented	2D/3D	ebb	0.11	0.01	45	
01/06/2013 05:30	3	21	sinuous/segmented	2D/3D	ebb	0.18	0.01	0	
01/06/2013 16:00	3	22	sinuous/segmented	2D/3D	flood	0.07	0	0	

Time	Site	Period	Type	Dimensionality	State of tide	current stress, N m^{-1}	wave stress, N m^{-1}	wave-current angle, degrees	Figure
01/06/2013 16:30	3	22	sinuous/segmented	2D/3D	flood	0.01	0	0	
01/06/2013 17:00	3	22	sinuous/segmented	2D/3D	ebb	0.01	0	0	
01/06/2013 17:30	3	22	sinuous/segmented	2D/3D	ebb	0.04	0	0	Figure 4-24
02/06/2013 04:30	3	23	sinuous/segmented	2D/3D	flood	0.08	0	0	
02/06/2013 05:00	3	23	sinuous/segmented	2D/3D	flood	0.02	0	0	
02/06/2013 05:30	3	23	sinuous/segmented	2D/3D	ebb	0.02	0.01	0	
02/06/2013 06:00	3	23	sinuous/segmented	2D/3D	ebb	0.08	0.01	0	
02/06/2013 06:30	3	23	sinuous/segmented	2D/3D	ebb	0.12	0.01	45	
02/06/2013 17:30	3	24	sinuous/segmented	2D/3D	flood	0.03	0.01	45	

Time	Site	Period	Type	Dimensionality	State of tide	current stress, N m^{-1}	wave stress, N m^{-1}	wave-current angle, degrees	Figure
02/06/2013 18:00	3	24	sinuous/segmented	2D/3D	flood	0	0.01	0	
02/06/2013 18:30	3	24	sinuous/segmented	2D/3D	ebb	0	0.01	0	
03/06/2013 05:30	3	25	sinuous/segmented	2D/3D	flood	0.1	0.01	0	
03/06/2013 06:00	3	25	sinuous/segmented	2D/3D	flood	0.04	0	0	
03/06/2013 06:30	3	25	sinuous/segmented	2D/3D	turning	0	0	0	
03/06/2013 07:00	3	25	sinuous/segmented	2D/3D	ebb	0.04	0	0	
03/06/2013 07:30	3	25	sinuous/segmented	2D/3D	ebb	0.05	0.01	0	

8.5 Instrument specifications and settings

Table 8-3 shows the settings of all the instruments deployed as part of the COHBED fieldwork on the West Kirby tidal flats, in the Dee estuary.

Table 8-3: Settings for instruments deployed on SEDbed

Number	Instrument	Notes
1	Marine Electronics 3D Sand Ripple Profiling Logging Sonar (s/n: 161), with 0-150 dbar pressure sensor and conductivity cell (3D-ARP or Ripple scanner)	Sample interval: 30 minutes Swath angle : 150° to vertical, 0.9° resolution Blanking distance : 0.4 m Range : 2.5 m Transmit pulse : 10 µs.
2	Marine Electronics Suspended Sediment Imaging Sonar (s/n: 1, 2, 3 & 4), with 0-20 dbar pressure sensor (SSIS, ASSI, BASSI)	4 sonar modules Profile rate : 500 Hz 8 averages to give 12.5 Hz recording rate 5 mm bins 1 m range Start range : 100 mm Burst Length : 10 minutes Sample interval: 30 minutes
3	NOCL ADVP	Recording rate : 8 Hz Dual PRF : 450 Hz/375 Hz 10 mm bins 0.6 m range
4	Aquatec Aquascat 1000 ABS (s/n:512-025)	4 transmit frequencies, 1 MHz, 1.5 MHz, 2.5 MHz, 3.0 MHz Pulse rate : 64 Hz Averaged Profile recording rate : 4 Hz 5 mm bins 1 m range Burst Length : 55 minutes Sample interval: 60 minutes

Number	Instrument	Notes
5	SonTek Hydra-ADV (s/n: G412 & B331), compass, pressure and temperature sensors, down looking orientation	Recording rate : 8Hz Burst Length : 55 minutes Sample interval: 60 minutes
7 & 6	SeaBird SBE16+ CTD v. 1.8c (s/n: 5310) with a 0-500 FTU Seapoint turbidity (OBS) sensor 0-5 v analogue output	Sample interval: 1 minute
8	Multi-tiered Sediment Trap.	Traps at five heights
9	Sequoia Scientific LISST 100X (s/n: 1291) Optical particle size distribution, optical transmission, volume concentration, volume scattering function, pressure and temperature.	Sample interval: 10 seconds Continuous recording Optical sensing area turned into the tidal flow. 50% Path Reduction Module (PRM) installed

8.5.1 3D Acoustic Ripple Profiler (3D-ARP)

Marine Electronics 3D Sand Ripple Profiling Logging Sonar, s/n: 161

Mechanical	
Length	318 mm
Diameter	89 mm
Max. Operating depth	1000 m
Operating temperature	0 to 40 °C
Weight in air	2.9 kg
Weight in water	0.9 kg
Acoustic	
Transducer diameter	40 mm
Acoustic frequency	1.1 MHz
Beamwidth	1° (-3 dB full angle)
Swath width	150° (depressed -15° from horizontal)
Transmit pulse	10 µseconds to 1millisecond (programmable)

Sample interval	1 to 4 µseconds (programmable)
Auxiliary sensors	
Tilt sensor range	±10°
Tilt resolution	0.01°
Tilt accuracy	0.02°
Pressure range	0 to 150 dbar
Additional sensors	Temperature, conductivity

Settings for COHBED deployment	
Sample interval	30 minutes
Time to collect a scan	≈12 minutes
Height above bed	≈0.6 m
Swath range	150° centred to vertical
Angular resolution	0.9°
Blanking distance	0.4 m
Range	2.5 m
Transmit pulse	10 µs
Sample interval	4 µs
No. of samples per ping	800

8.6 Bed sediment sample record

Sediment samples were collected from the area of the frame to characterise the particle size distribution as it varied over the study period and for later use in laboratory validation of the Acoustic Backscatter instrument (Table 8-4). Extra samples were taken on 31/05/2013 to check the assumption of homogenous sediment distribution over the deployment area.

Table 8-4: List of bed sediment sample details

Date	Time (GMT)	Site	Sample number	Latitude, Decimal °	Longitude, Decimal °	GPS accuracy, m	Location
21/05/2013	15:21	1	1	53.375067	-3.211683	5	north/seaward edge of frame
22/05/2013	17:00	1	2				landward of frame-general area
23/05/2013	16:20	1	3				landward of frame-general area
26/05/2013	18:41	2	4	53.374500	-3.210233	4	landward of frame-general area
27/05/2013	08:25	2	5	53.374517	-3.210233	4	landward of frame-general area
27/05/2013	18:44	2	6	53.374500	-3.210217		landward of frame-general area
29/05/2013	07:43	2	7	53.374517	-3.210233	4	landward of frame-general area
29/05/2013	10:28	3	8	53.374217	-3.210067	4	landward of frame-general area
30/05/2013	10:54	3	9	53.374250	-3.210067	3	landward of frame-general area
31/05/2013	11:25	3	10	53.374250	-3.210067	4	seaward of frame[1]
31/05/2013	11:52	3	11	53.374233	-3.210050	3	under frame[1]
31/05/2013	12:07	3	12	53.374250	-3.210033	4	landward of frame-general area
01/06/2013	11:56	3	13	53.374250	-3.210033	3	landward of frame-general area
02/06/2013	13:20	3	14	53.374250	-3.210000	4	landward of frame-general area
03/06/2013	12:13	3	15	53.374250	-3.210017	3	landward of frame-general area
04/06/2013	13:30	3	16				landward of frame-general area

[1] repeat samples take for comparison with Bangor University samples.

8.7 Bedform measurement record

Measurements of ripple wavelength and height range in centimetres (Table 8-5). The ripple wavelengths and height ranges are approximate measurements or averages of multiple readings to give an indication of the ripple morphology over an area.

Table 8-5: Measurements of ripple wavelength and height range in centimetres

		Seaward of frame			under frame			Landward of frame		
Time of LW (GMT)	Site	wavelength	height range		wavelength	height range		wavelength	height range	
22/05/2013 15:04	1				17.7	4.0	5.0			
23/05/2013 15:54	1				15.1	1.0	2.0			
25/05/2013 17:31	2	17.3	1.0	4.0						
26/05/2013 18:19	2	10.7	1.0	2.0	10.3	2.0	3.0	8.2	1.0	2.0
27/05/2013 06:44	2	14.7	2.0	3.0	12.7	1.0	3.0	15.9	1.0	3.0
27/05/2013 19:07	2	8.7			12.0			15.1		
29/05/2013 08:25	2				11.0	1.0	2.0	8.5	1.0	3.0
29/05/2013 08:25	3	15.0	2.0	5.0	17.5	3.0	5.0	20.0	3.0	5.0
30/05/2013 09:17	3	12.8	1.0	3.0	14.9	2.0	3.0	14.1	1.0	3.0
31/05/2013 10:13	3	15.6	2.0	3.0	16.8	2.0	3.0	16.0	2.0	4.0
01/06/2013 11:14	3	15.8	1.0	2.0	21.3	2.0	3.0	14.0	1.0	2.0
02/06/2013 12:20	3	16.7	1.0	2.0	17.3	1.5	2.5	14.7	1.0	2.0
04/06/2013 14:28	3	17.3	1.5	2.0	20.3	2.0	4.0	20.8	1.5	3.0

8.8 Instrument height record

The instrument heights measured from the bed (half way up the ripple height) in centimetres, Table 8-6.

Table 8-6: Instrument heights measured from the bed in centimetres for the SEDbed deployment sites

Time of LW (GMT)	Site	Ripple scanner	BASSI	ADVP	ABS	ADV	OBS	CTD	LISST	sediment trap base
21/05/2013 14:09	1		66							
22/05/2013 15:04	1	61	65	58	51	53	64	67	43	10
23/05/2013 15:54	1		66							
24/05/2013 16:43	2	57.5	54	50	47	49		63	39	7
25/05/2013 17:31	2	51	52.5	50.5	47	48		59	38	8
26/05/2013 18:19	2	50	52.5	47	40	42	51.5	57	33	2
27/05/2013 06:44	2	49	52	45.5	39	40		54	33	3
27/05/2013 19:07	2	46.5	49	44	36	38	48	52	30	7
29/05/2013 08:25	3	57	50	51.5	45	47.5	59	60	37	4
30/05/2013 09:17	3	54	58	50.5	44	46.5	58	61	38	4.5
31/05/2013 10:13	3	54	55	50	44	45	59	60	37.5	5.5
01/06/2013 11:14	3	53.5	57.5	50	43.5	46	57	61	37	4

Time of LW (GMT)	Site	Ripple scanner	BASSI	ADVP	ABS	ADV	OBS	CTD	LISST	sediment trap base
02/06/2013 12:20	3	53.5	57	50	43.5	45.5	57	60.5	36.5	4
04/06/2013 14:28	3	57								

8.9 SEDbed frame scour

The depths of the scour holes around the bottom of the sedbed frame were measured to get an idea of the how the frame and water flow interacted and affected the bed sediment. The measurements were rough, to the nearest 0.5 cm.

Time of LW (GMT)	Site	NE	SE	NW	SW	mid-N	mid-S	Mean
23/05/2013 15:54	1	9.0	11.0	14.5	13.0	17.0	13.0	13.0
24/05/2013 16:43	2	19.5	15.0	17.5	16.0			17.0
26/05/2013 18:19	2	4.0	6.0	8.0	11.0	10.0	6.0	7.5
27/05/2013 06:44	2	11.0	13.0	12.0	11.0	12.0	3.0	10.3
30/05/2013 09:17	3	9.5	7.0	10.0	7.5		6.0	8.0
31/05/2013 10:13	3	7.0	7.5	9.0	9.0	8.0	6.5	7.8
01/06/2013 11:14	3	6.0	6.5	8.0	8.0	7.5	6.0	7.0
02/06/2013 12:20	3	5.0	4.5	8.0	7.5	6.0	6.0	6.2

8.10 A note on Malarkey and Davies's (2012) bed shear stress model

(written by J. Malarkey to address reviewer comments on a paper based on the bedform migration chapter)

The Malarkey and Davies (2012) model, which is a modification of the Soulsby and Clarke (2005) model, requires the following input quantities:

$$h, \quad z_0, \quad u_w, \quad T_p, \quad \langle u \rangle, \quad \varphi. \tag{B1}$$

depth, bed roughness length, wave bottom orbital amplitude velocity, peak wave period, depth mean velocity and wave-current angle.

These inputs allow the calculation of the equivalent current-alone and wave-alone stresses, τ_c and τ_w, respectively. Here, $\tau_c = \rho C_D \langle u \rangle^2$ and $\tau_w = \frac{1}{2}\rho f_w u_w^2$, where $C_D = \kappa^2/\log^2(h/z_0 e)$ is the drag coefficient, κ = 0.4 is the von Kármán constant, $f_w = 1.39(a_w/z_0)^{-0.52}$ is the friction factor, $a_w = u_w/\omega$ is the wave orbital amplitude and $\omega = 2\pi/T_p$. If the process is completely linear, the maximum stress, $\tau_{max,l}$, is given by:

$$\tau_{\max l} = \sqrt{\tau_c^2 + \tau_w^2 + 2\tau_c \tau_w |\cos\varphi|}. \tag{B2}$$

However, in the case of Malarkey and Davies' (2012) stronger non-linear option, the combined maximum stress in the wave cycle, τ_{max}, is given by:

$$\tau_{\max} = \sqrt{\tau_m^2(1+\varepsilon_1+\varepsilon_2) + \tau_p^2 + 2\tau_m \tau_p \sqrt{1+\varepsilon_1+\varepsilon_2}\,|\cos\varphi|}, \tag{B3}$$

where τ_m is the combined-mean stress, τ_p is the combined-wave stress and ε_1 and ε_2 are additional scaling terms that were introduced to make the maximum stress more consistent with numerical model results. Since τ_m, τ_p, ε_1 and ε_2 are all determined in terms of the input conditions (see Malarkey and Davies, 2012), τ_{max} can also be determined in terms of the input conditions.

8.11 E-mail correspondence

8.11.1 Correspondence relating to the 3D-ARP problems

From: Bell, Paul S.
Sent: 05 September 2013 19:39
To: Lichtman, Ian D. <doulich@noc.ac.uk>
Subject: Re: ripple profiler problem

The speed of sound turned out not to be the issue and can be returned to your estimate. The swath azimuth needed a slight tweak to make it match up on each side of the scan circle - I'm not sure why but might be as simple as a small amount of play in the gearbox. The correction adds a small but progressively increasing azimuth offset to each successive sweep, and that seems to have sorted it.

Cheers

Paul

Sent from my iPhone

----- Original Message -----
From: Lichtman, Dougal
To: gordon@marine-electronics.co.uk
Sent: Thursday, February 06, 2014 5:23 PM
Subject: 3D Sand Ripple Profiler

Hello Gordon

I'm PhD student working with Pete Thorne and Richard Cooke at NOCL. I had a couple of questions about the 3D Sand Ripple Profiler and Pete suggested sending you an e-mail.

Is there a formula to calculate the scan rate of the 3D SRP? Richard has been timing it with a stopwatch, before deployment, to check the interval between scans is ok. A formula to estimate the scan rate would make planning easier.

Also the scans we got back from our deployment in the Dee last spring had an odd feature. The images were split into two hemispheres. Paul Bell adjusted his processing program and made the following comment:

'The swath azimuth needed a slight tweak to make it match up on each side of the scan circle - I'm not sure why but might be as simple as a small amount of play in the gearbox. The correction adds a small but progressively increasing azimuth offset to each successive sweep, and that seems to have sorted it.'

Here is an example scan, the first two images uncorrected and a corrected image:

Have you seen this effect before?

Regards,

Dougal Lichtman

From: Gordon Collier [mailto:gordon@marine-electronics.co.uk]
Sent: 07 February 2014 09:13
To: Lichtman, Dougal
Subject: Re: 3D Sand Ripple Profiler

Dear Dougal,

The feature you are seeing is caused by the fact that the sonar only rotates 180 degrees for a full 360 degree scan, hence has to be calibrated to adjust for any offsets in the drive mechanism so that the plot is in alignment when the 180 rotation is complete. There is a parameter called "Head Offset" in the software which needs to be set correctly so that when the unit is mounted vertically above a flat surface the two halves of the plot line up. The tilt sensors should also be reading zero for X and Y at this point. It is feasible that if the software has been installed on a different computer to that previously used the head offset figure may not have been correct when the unit was programmed. As Paul explained, a small incremental offset applied to the data in post processing would correct this, I would recommend looking at the difference between the first and last sweep and apply 1/200th of this per swath.

Best regards

Gordon Collier

Marine Electronics

From: Lichtman, Dougal
To: Gordon Collier
Sent: Monday, March 03, 2014 10:40 AM
Subject: RE: 3D Sand Ripple Profiler

Hello Gordon

The correction worked, thanks. But we are still none the wiser to why the problem happened, as the “Head Offset” value was the same as the previous deployment, 340. The only difference was the laptop used.

I'm working on the resolution and accuracy now. Could you tell me the transducer diameter? And the resolution and accuracy of the pitch and roll sensor?

Regards,

Dougal

From: Gordon Collier [mailto:gordon@marine-electronics.co.uk]
Sent: 07 March 2014 10:03
To: Lichtman, Dougal
Subject: Re: 3D Sand Ripple Profiler

Hi Dougal,

If the head offset value is correct and there is still a significant shear in the data then it is possible that there may have either been a fault with the optical sensor that is used to reference the transducer tilt position, or the battery voltage was low hence reducing the torque to the stepper motor. The system has just been upgraded and showed no problems of this sort whilst testing using the programmer box with the mains charger plugged in.

The transducer diameter is 40mm.

The tilt sensors used are the 20º span version of the model 900 from Applied GeoMechanics who have now been bought out by Jewell Instruments, attached is the datasheet. The sensors are digitised using a 12 bit convertor with a +/-2.5V full scale range, and the 5th order correction polynomial is applied to improve their linearity by 10x.

Best regards

Gordon Collier

Marine Electronics

----- Original Message -----
From: "Cooke, Richard D." <rdco@noc.ac.uk>
To: "Gordon Collier" <gordon@marine-electronics.co.uk>
Sent: Tuesday, February 03, 2015 5:21 PM
Subject: 3D Ripple Profiler sn:161 query

Hi Gordon,

We managed to deploy our 3D Sand Ripple Profiling instrument sn: 161 successfully post-piston repairs, for 6 weeks off the Dutch coast back in September/October last year.

I'm getting the instrument ready for a new deployment in the Celtic Sea starting in March and have a few questions regarding the instrument I hope you might be able to help out with.

First set of questions relate to the stainless steel USB memory stick cover. Whilst preparing the instrument for its next deployment, I've noticed the USB memory stick cover exterior is becoming pitted with corrosion and there is crevice corrosion on both surfaces where the bottom edge of the cover touches the bulkhead connector; I've attached some photos to show you what I mean. This corrosion is developing faster that I would have expected so I was wondering what your thoughts are on this? Also, at some point the USB memory key bulkhead connector and cover I can imagine are going to need replacement due to the corrosion. What would be the costs and timescales involved and would it be possible to carry out the repairs ourselves?

I'm also seeking some technical information regarding instrument's "head-offset" setting in the MS Windows registry; what exactly does this registry key setting do and how does the instrument software use it? The question came up again after looking at datasets from the deployment back in Sept/Oct last year. The registry key is present for the "Program3DProfiler" software and is set to a value of 340 using the updated instrument software received back in July 2012. The copy of the "LoggingProfiler3D" instrument software I have (used to record bed-scans direct to a PC) doesn't have this head-offset registry key. If the Program3DProfiler software is used to program the instrument for autonomous recording, then there is a consistent and notable step formed between the bed echoes from the right and left hemispheres of a bed-scan. Yet no such step occurs for bed-scans recorded directly to PC with the LoggingProfiler3D software. I'm aware my colleagues were in contact with you last year regarding this topic so they could post-process data from a deployment in 2013; they arrived at a head-offset correction of 3.36deg, to be implemented during post-processing of data. I've received no instruction to make any changes to software nor registry settings, yet can't help but think this value of 340 in the registry is incorrect. If so what should I increase or decrease it to, to remove the need for the post-processing correction? It would be nice if possible to put this issue to bed to save on the head scratching it is causing.

Cheers,

Richard.

_____

From: Gordon Collier [gordon@marine-electronics.co.uk]
Sent: 04 February 2015 16:41
To: Cooke, Richard D.
Subject: Re: 3D Ripple Profiler sn:161 query

Hi Richard,
Although the corrosion of the stainless is unusual, it has been observed before, particularly in warm climates though, where we had the stainless steel bands around a 3013 transponder boot corrode badly. As far as we know the machine shop fabricated these parts from the same stock 316 so without having the parts tested we can't comment if the corrosion has been advanced due to dissimilar metals or not. I wonder if the nearby conductivity probe could have had any influence? I'll get you a price and delivery for replacements as they are parts that you could easily fit yourself.

As regards the offset setting, the value represents the count in 0.3° increments necessary to drive the transducer head from its reference position to be exactly horizontal (if the body of the unit is vertical). This adjustment is necessary to compensate for the variation in reference detection position. If the figure is not correct then as you observed there is a shear in the data around the 0°-180° axis. Because the rotational
scanning covers 180° rather than the full 360° there can be a height differential between the first and last scan either side of the 0-180 axis as the swath scanning direction of the transducer is now reversed.

An anomaly exists in the naming convention for this offset variable in the registry settings. For the "live" PC software "LoggingProfiler3D" the variable is called "Head Offset", whereas for the "programmer" software used prior to setting the unit recording autonomously "Prog3DProfiler" the variable is called "Slot Offset". The values for both of these parameters in the registry were calibrated at 340 when the unit was re-tested here after upgrading.

To re-calibrate if the value of 340 is causing a sheared data set I suggest setting the unit up vertically in a tank and running the LoggingProfiler3D software whilst trying scans with different settings (you can change the head offset on the "Advanced" page of the control panel then do another sweep until happy that the parameter produces a flat data set). Then set the new offset number in the registry for the Prog3DProfiler before programming the unit for autonomous recording. Capture a few sweeps autonomously and verify that the data is again flat.
One problem may arise if the registry settings are different on your lab computer and the field laptop? When installing the software on a blank machine it should set the registry default back to 340, however, a re-install on a machine should not affect the registry settings.

Hope this helps clarify the offset

Best regards
Gordon Collier
Marine Electronics

----- Original Message -----
From: "Cooke, Richard D." <rdco@noc.ac.uk>
To: "Gordon Collier" <gordon@marine-electronics.co.uk>
Sent: Thursday, February 05, 2015 2:35 PM
Subject: RE: 3D Ripple Profiler sn:161 query

Hi Gordon,

Thanks for the reply. It's good to know that we could easily fit the replacement stainless steel parts ourselves; there are so many deployments for the instrument this year I doubt we'll have opportunity to return the instrument to Marine Electronics.

Digging around in the Windows Registry for all the machines I've used to operate the 3D-ARP, confirms they all have the same registry key settings. So the problem doesn't appear to be machine related. Curious though, the instrument software versions I'm using have the "slot offset" registry key listed under "Logger3D" which is set to a value of 335. The "head offset" registry key is listed under "Profiler3D" and is set to 340. My understanding was the Profiler3D registry key belongs to the "Program3DProfiler" software with "Logger3D" belonging to the "LoggingProfiler3D" software judging from the way the registry keys appear as each software is installed. Is this correct as from your email it looks like this should be the other way around and Profiler3D registry key belongs to the LoggingProfiler3D software? I've attached two text files containing the parameter registry sub-keys for both Profiler3D and Logger3; can you compare these against your records just to make sure I'm working with the correct settings?

Cheers,

Richard.

Dr Richard Cooke
OTEG
National Oceanography Centre
(formerly Proudman Oceanographic Laboratory)
Joseph Proudman building
6 Brownlow Street
Liverpool
L3 5DA
UK

Tel: +44 (0) 151 795 4800 (switchboard)
Fax: +44 (0) 151 795 4801

-----Original Message-----
From: Gordon Collier [mailto:gordon@marine-electronics.co.uk]
Sent: 05 February 2015 16:18
To: Cooke, Richard D.
Subject: Re: 3D Ripple Profiler sn:161 query

Hi Richard,

The "Logger3D" registry key belongs to the "Prog3DProfiler" programmer software and uses the "SlotOffset" parameter in the registry

The "Profiler3D" registry key belongs to the "LoggingProfiler3D" live software and uses the "HeadOffset" parameter in the registry

For a given system the SlotOffset and the HeadOffset should be set to the same value.

The LoggingProfiler3D software can write the HeadOffset parameter back to the registry after adjusting it in the Advanced Settings of the Control Panel. The Prog3DProfiler software cannot modify the registry parameter but will write a default setting if the registry key is deleted manually.

The last image I saved when the unit came back to have the oil leak sorted was taken in our small test tank with a 341 offset

Best regards
Gordon Collier
Marine Electronics

-----Original Message-----
From: Cooke, Richard D.
Sent: 06 February 2015 11:13
To: Souza, Alejandro J.; Lichtman, Dougal
Cc: Thorne, Peter D.; Bell, Paul S.
Subject: FW: 3D Ripple Profiler sn:161 query

Hi guys,

When I carried out a quick post-process of the MegaPEX 2014 3D Ripple Profiler dataset to check for quality, I noted signs of the same head-offset problem as was discovered during with the COHBED 2013 fieldwork dataset. I've been back in contact with Gordon Collier to try and get to the bottom this so we don't have to compensate during post-processing in future; a copy of the email exchanges is below and it looks like we may have found the cause.

It looks like the instrument software has been storing the head offset setting for autonomous operation mode, in a different Microsoft Windows Registry key to the one previously understood and the install software has been putting the wrong setting there. I'll be manually updating the Windows Registry on all the PC's used to drive the 3D-ARP to reflect the correct setting. I've also asked Gordon if they can supply this and other calibration information as a report in future whenever the instrument is returned for servicing.

Just so you know, the head offset setting is according to Gordon, the number of steps in 0.3deg increments to bring the transducer head from its reference position to the horizontal position. Previously the instrument software was using a count of 335 for autonomous deployments and 340 for LiveView lab-mode; it should be 341 as of the last time the instrument was with them to repair the oil leak problem.

Cheers,

Richard.

Dr Richard Cooke
Ocean Technology and Engineering Group
National Oceanography Centre - Liverpool Joseph Proudman building
6 Brownlow Street
Liverpool
L3 5DA
UK

Tel: +44 (0) 151 795 4800 (switchboard)
Fax: +44 (0) 151 795 4801

8.11.2 Other correspondence

From: Baas, Jaco
Sent: Fri, Jun 14, 2013 10:00 am
Subject: COHBED Dee work, first results from Bangor

Hi All,

Just to convey my enthusiasm to you...

Megan Baker has processed the first batch of granulometric data (from rig site 3), and there appears to be a good correlation between ripple length and mud content. Ripple length decreases with increasing mud content, and no ripples form above c. 13% mud. This agrees remarkably well with our

experimental data. Fully developed 3D ripples contain about 5% mud. She is now looking into the data in more detail.

Regards,

Jaco

****
Dr JACO H. BAAS
Senior Lecturer in Fine Particle Dynamics

Bangor University
School of Ocean Sciences
Centre for Catchment and Coastal Research
Menai Bridge
Anglesey, LL59 5AB
United Kingdom

From: Jaco Baas [mailto:j.baas@bangor.ac.uk]

Sent: 28 July 2014 11:55

To: Lichtman, Dougal; Amoudry, Laurent O.; Thorne, Peter D.

Subject: RE: Meeting minutes 24 July

Thanks Dougal,

We have 8 cores in total from around site 2 and 6 cores from around site 3. Three cores taken on May 26th seem most relevant, because these were collected along a line perpendicular to the channel on the bank where the sand flux is thought to originate from. The other cores are more scattered. but worth a check as well. I do not have my field notes at hand, but can check when I am back in office, if you like.

The graph below shows granulometric data plus text from Megan Baker's field report. These are data from May 26th, the location is up the bank furthest away from the channel, corresponding to one of the three cores mentioned above. The vertical scale of the graph is in cm. I think the mud content in the upper 3 cm (except for the surficial sample) corresponds to that found below the rig. Is this right? Please note that these data were sampled in the field by hand from a trench. We also have an untouched core at the same location.

Should I be even more excited now?

Regards,

Jaco

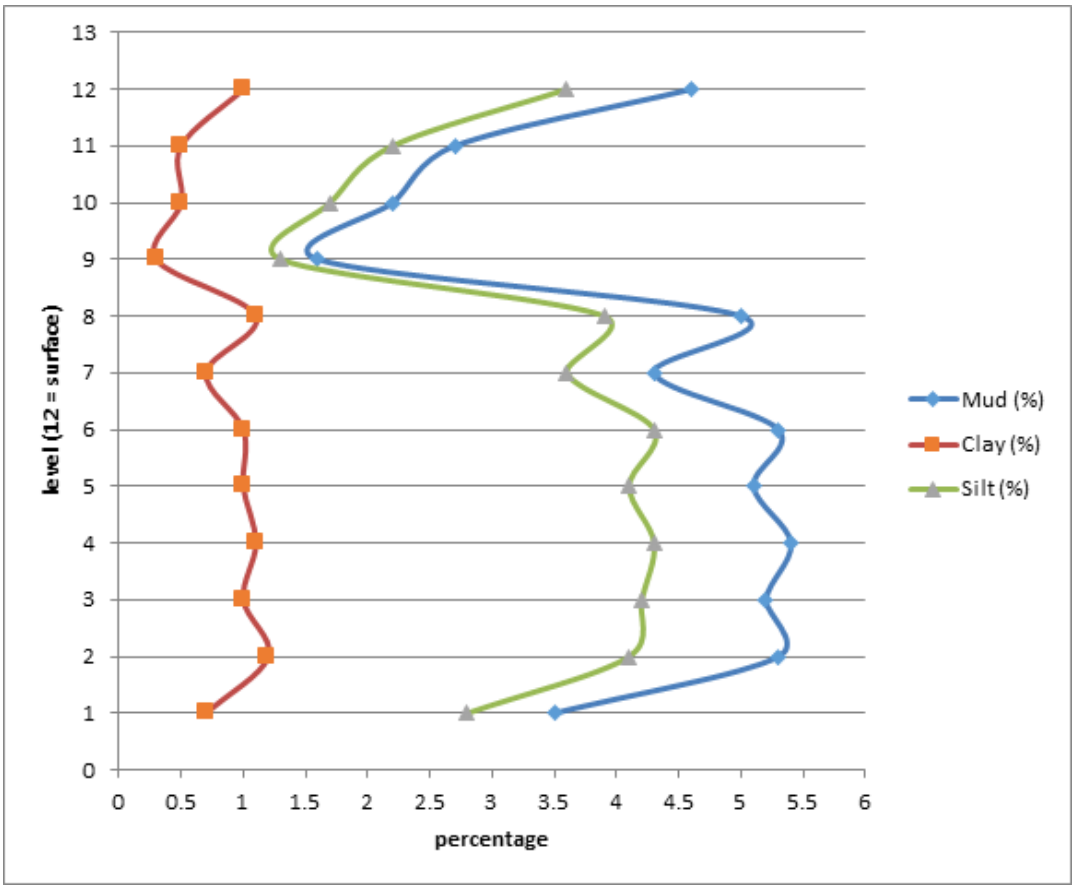

The value from the top of the bed has a very high mud content, compared to the 2nd sample which was just 1cm lower. This high % is probably due to sediment settling out of suspension at the very end of the tide. The samples at 11, 10 and 9 are all very low, this could be due to winnowing taking the fines out of the sediment. However it could also be from sediment with a low mud content being advected to the sample area. Between 9 and 8 there is a large change in mud content, this is not supported by the change in colour of the sediment in the trench. The colour change to a darker black sediment with sand filled burrows occurs between 7 and 6 where there is a slight increase in mud, silt and clay content. But there is no real correlation between the change in mud content and the change in colour. Below level 6 there is little change in the percentages of the sediments, apart from the value at 1 where the values are anomalously low. (Megan Baker)

From: Jaco Baas [mailto:j.baas@bangor.ac.uk]

Sent: 13 July 2017 10:40

To: Lichtman, Dougal <doulich@noc.ac.uk>

Subject: RE: COHBED push core data for thesis corrections

Hi Dougal,

We still have the cores, but none of these have been analysed for gsize. However, the trench samples in the graph below should be useful. My interpretation is that they show winnowing the upper 3 cm, corresponding to the ripple height, and no winnowing below. The higher mud content near the bed surface may be caused by suspension settling of flocs during the last phase of the ebb tide.

Regards,

Jaco

8.12 Malvern Mastersizer 2000 laser diffraction analyser procedure

8.12.1 Summary

The Malvern Mastersizer 2000 is used to determine the particle size distribution of a suspension. The results are reported as percentage volume concentrations in 100 size classes from 0.2 to 2000 µm. As the measurement depends on the number of particles in suspension, samples that contain a lot of fine material can be used in smaller quantities than coarser samples.

The equipment required is listed, safety risks assessed and pre-processing of samples described, as well as the analysis procedure.

Document created: 22/08/2013 D.L., 1.0

Updated: 09/03/2015 D.L., 1.1, corrections to the analysis section

: 27/04/2015 D.L., 1.2, size classes list added to appendices

8.12.2 Introduction

The Malvern Mastersizer 2000 is used to determine the particle size distribution of a suspension (Malvern Instruments Ltd, 2013a). To resolve a wide size range two lasers are used, red and blue, and the particle sizes are determined using Mie scattering and Fraunhofer diffraction theories (Malvern Instruments Ltd, 2013a). The system at the school of ocean sciences, Bangor University, has a Hydro 2000mu wet dispersion unit that keeps the sample in suspension during analysis and the data is logged to a computer running the Malvern Mastersizer software. The wet dispersion unit uses ultra sound to break up aggregations of particles. The results are reported as percentage volume concentrations in 100 size classes from 0.2 to 2000 µm. A full description of the Mastersizer 2000 instrument and software can be found in the user manual (Malvern Instruments Ltd, 2007a).

Before the samples were analysed they were dried and sieved with a 2 mm sieve to remove any large particles that would block the Mastersizer. This is not required for samples that are mainly fine material. As the measurement depends on the number of particles in suspension, samples that contain a lot of fine material can be used in smaller quantities than coarser samples. The sample needs to have an obscuration in the range 10-20% for the analyser to get a good reading, shown as a green area by the software.

8.12.3 Equipment

Malvern Mastersizer 2000 optical bench unit

Hydro 2000mu wet dispersion unit

Mastersizer 2000 software (v 3.01 for Windows 98 is used, the current version is 5.60 (Malvern Instruments Ltd, 2013b))

Windows 98 PC with two serial ports or one serial port and one parallel port with converter

A laboratory with sink

Distilled water

1 x 1 l beaker

3 x 500 ml beaker

Spatula

Paper towel

Brush

2 mm separating sieve

Collecting pan

Evaporating dishes (one for each sample)

Drying oven set to 75 °C

Wash bottle

8.12.4 Health and safety

The risk assessment for the Mastersizer and drying oven is in appendix 8.12.13; other risk assessments should be consulted for manual handling and general laboratory work. Further details of the risks involved in using the Mastersizer 2000 can be found in the Mastersizer 2000 Essentials User Manual (Malvern, 2007b).

The main risks involved are getting water on electronic equipment, either the computer used to log the data or the Mastersizer itself. Liquids should be kept away from the back of the instruments and completely away from the computer. The lasers are contained within the instrument and are not accessible to the user. Putting your fingers in the beaker with the pump-stirrer unit could cause sonication of the blood or damage from the stirrer.

When removing samples from the oven suitable heat resistant gloves should be used to avoid burns.

8.12.5 Pre-processing of samples

Wet samples that require sieving need to dried in an oven at 60-80 °C. The can then be sieved with reduced loss of fine material. Fine samples can be treated the same, drying completely, or the amount of water reduced before analysis.

The evaporating dishes were brushed out to check that they were clean before use. For the fine samples, some of which were small, the pots were rinsed with distilled water to get all the material out. The samples were then dried overnight. Samples that contained a lot of water were allowed to settle and the excess removed using an empty wash bottle (some fine material may have been removed). The dried samples were broken up with a brush until they ran smoothly.

Han Winterwerp recommends sieving into coarse and fine fractions before laser scattering analysis as larger particles block the smaller ones (fines underrepresented. INTERCOH 2015).

8.12.6 Mastersizer setup

If the previous user has switched everything off, switch on the Mastersizer, dispersion unit and computer. The dispersion unit should be set up using the details in Table 8-7. Press the top on button (in between the arrows) to switch the stirrer-pump to automatic, a red light show illuminate on. The stirrer-pump on the dispersion unit will now switch off and on automatically as it is raised and lower (the motion is damped so you may need to hold onto the rest of the unit to prevent it moving).

Table 8-7: Hydro 2000mu wet dispersion unit settings

Pump speed	2000 rpm
Ultrasonic displacement	20.00 µm
Ultrasonic timer	01:00 minutes

A standard operating procedure (SOP) file should have been set up for the analysis (see appendix 8.12.12 for settings used for COHBED sample analysis), if not read the manual and use the setup wizard.

8.12.7 Analysis of samples (Software v 3.01)

- Before analysis the Mastersizer should be washed through using tap water. Three beakers of water are used consecutively each for 1 minute. The holes in the stirrer-pump head should be under water.

- Place a 1 l beaker in under the dispersion unit filled with about 750 ml of distilled water and lower the stirrer-pump. (or a 500 ml beaker with 450 ml of water)

- On the Mastersizer software click **Measure** on the menu bar then select **Start SOP** (or click the icon that looks like sheet of paper with lines on it next to a downward pointing arrow).

- Select the required SOP from the file list.

- Let the bubbles in the beaker settle and click the **start** icon to measure the distilled water blank. The background levels are measured and then it asks you to enter the sample name.

- When prompted add some of the sediment sample to the beaker, to start with try half a spatula (use less if the sample is has a lot of fines), until the blue bar on the screen goes up about half way in the red area.

- Press the ultrasound timer start button on the dispersion unit (bottom button in between the arrows). The bar should now go into the green area, if it is still in the red add more of the sample and use the ultrasound again (if it goes over the green into the red you may need to start again).

- Click the **start** icon to begin the measurement cycle, three measurements are taken.

- Click the **Cancel** button when asked to repeat the SOP.

- Check the D_{50} values in the record list, there should be the three measurements and then the average, if they are greater than 5% different repeat the measurement cycle an additional time.

- Repeat this procedure twice for each sample with additional cycles if the D_{50} values are not good.

8.12.8 Exporting the data

To export the data highlight all the records and click **File** on the menu bar then select **Export data**. Select the required options and enter a filename.

To export the class sizes select **Edit** on the menu bar then **User sizes**. Click the **Save sizes** button and enter a file name.

8.12.9 Troubleshooting

The blue bar has gone over the green area into the red

If it is only a little way over add more distilled water to the beaker to dilute the sample, otherwise you will have to start again.

I need to start again but I've run out of sample

If you have time decant the sample into evaporating dish, allow to settle, remove the excess water and dry in the oven. If not start with a new beaker of distilled water but just enough to cover the pump holes then add your wet sample (being sure to swill the sample to keep it suspended). If the blue bar is just outside the green area try measuring anyway as the results might be good.

I'm getting error messages

The system can be a bit temperamental. Restart the software if there are problems. If they continue switch off the whole system and then back on. The existing data will not be lost but you will have to repeat the sample if it crashed half way through.

8.12.10 Conclusions

Switch everything off at the end of the day. Data should be checked for quality before disposing of analysed samples.

8.12.11 References

Malvern Instruments Ltd, 2007a. Mastersizer 2000 User Manual (MANO384, issue 1.0) [online] http://www.malvern.com/malvern/kbase.nsf/search?readform [Accessed: 21/08/2013].

Malvern Instruments Ltd, 2007b. Mastersizer 2000 Essentials User Manual (MANO393, issue 1.0) [online] http://www.malvern.com/malvern/kbase.nsf/search?readform [Accessed: 21/08/2013].

Malvern Instruments Ltd, 2013a. Malvern Mastersizer web page [online] http://www.malvern.com/labeng/products/mastersizer/MS2000/mastersizer2000.htm [Accessed: 20/08/2013].

Malvern Instruments Ltd, 2013b. Malvern Mastersizer software download [online] http://www.malvern.com/common/software/ms2000/ms2000_software.htm [Accessed: 20/08/2013].

8.12.12 COHBED standard operating procedure (SOP) settings

SOP name	Dee_muds
Particle name	Silica 0.1
Particle refractive index	1.544
Particle absorption index	0.1
Dispersant name	Water
Dispersant refractive index	1.33
Accessory name (dispersal unit)	Hydro 2000MU (A)
Analysis model	General purpose
Range, µm	0.2-2000
Result emulation	Off
Result transform type	Volume

8.12.13 Bangor Univeristy and NERC risk assessment forms for Mastersizer and drying oven use

PRIFYSGOL BANGOR UNIVERSITY **(College / School / Department):** School of Ocean Sciences

NERC Risk Assessment: Working with Malvern Mastersizer 2000 particle size analyser

Location / Building / Area:	Menai Bridge/Craig Mair Building/Sediment lab	**Activity (Summary):**	The Malvern Mastersizer 2000 is used to determine the particle size distribution of a particle suspension in water. Lasers are used to take the measurement and a pump-stirrer unit, with an ultrasonic system to prevent the particles from flocculating, keeps the particles suspended. Only trained users will be allowed to operate the Mastersizer.
Date of Assessment:	22/08/2013	**Name of Assessor:**	D. Lichtman

What are the dangers/hazards?	Who might be harmed?	What are you already doing to prevent harm?	What further action is necessary?	Action by whom	Action by when	Done (Date)
Working with Malvern Mastersizer 2000 (electronic instrumentation in conjunction with water): electric shock	User	Care should be taken to avoid spills onto the instrument or computer. The laboratory is arranged to reduce the likelihood of this occurring.	None			
Working with Malvern Mastersizer 2000: lasers	User	User has no access to lasers in instrument.	None			
Working with Malvern Mastersizer 2000: ultrasonic pump-stirrer unit	User	Don't put fingers in the beaker with the pump pump-stirrer unit.	None			
Working with drying oven: burns, scalding	User	Heat resistant gloves should be used and care taken when handling vessels with hot contents	None			

Name of Assessor: D. Lichtman **Date of Assessment:** 22/08/2013

Assess the Level of Risk				**Control Measures and Re-Assessment**			
Description of Activity and Associated Hazards	Hazard Consequence (a)	Likelihood: (b)	Risk Rating: = (a) x (b)	**Controls in place or to be Implemented**	Hazard Consequence (a)	Revised likelihood (b)	Revised = (a) x (b)
	3 – Major, 2 – Serious, 1 – Slight		High (6 to 9), Med (3 to 4), Low (1 to 2)		3 – Major, 2 – Serious, 1 – Slight		High (6 to 9), Med (3 to 4), Low (1 to 2)
Working with Malvern Mastersizer 2000 (electronic instrumentation in conjunction with water): electric shock	2	2	4	Care should be taken to avoid spills onto the instrument or computer. The laboratory should be arranged to reduce the likelihood of this occurring.	2	1	2
Working with Malvern Mastersizer 2000: lasers	2	1	2	User has no access to lasers in instrument			
Working with Malvern Mastersizer 2000: ultrasonic pump-stirrer unit	2	1	2	Don't put your fingers in the beaker with the pump pump-stirrer unit			
Working with drying oven: burns, scalding	1	2	2	Heat resistant gloves should be used and care taken when handling vessels with hot contents	1	1	1

8.12.14 Master size standard size classes (logarithmic spacing)

0.20	3.17	50.24	796.21
0.22	3.48	55.08	873.03
0.24	3.81	60.40	957.26
0.26	4.18	66.23	1049.61
0.29	4.58	72.62	1150.88
0.32	5.02	79.62	1261.91
0.35	5.51	87.30	1383.66
0.38	6.04	95.73	1517.16
0.42	6.62	104.96	1663.53
0.46	7.26	115.09	1824.02
0.50	7.96	126.19	2000.00
0.55	8.73	138.37	
0.60	9.57	151.72	
0.66	10.50	166.35	
0.73	11.51	182.40	
0.80	12.62	200.00	
0.87	13.84	219.30	
0.96	15.17	240.45	
1.05	16.64	263.65	
1.15	18.24	289.09	
1.26	20.00	316.98	
1.38	21.93	347.56	
1.52	24.05	381.09	
1.66	26.37	417.86	
1.82	28.91	458.17	
2.00	31.70	502.38	
2.19	34.76	550.85	
2.40	38.11	603.99	
2.64	41.79	662.26	
2.89	45.82	726.16	

8.13 An example of the multiple linear regression method

The migration data from Baas *et al* (2000) were used to demonstrate the multiple regression method on a set of data with known results (Figure 8-1, top). Baas *et al* (2000) found three separate relationships for migration rate from three different grain size classes (33, 95 & 238 µm), in the form:

$$u_r = a\theta'^b \qquad \textbf{8-1}$$

Here the data are used to recreate the fits based on three separate regressions with a single multiple linear regression. Terms for $log_{10}(theta)$, D_{50} and $log_{10}(theta) \times D_{50}$ were used initially with the expectation of removing the $log_{10}(theta)$ and D_{50} as unnecessary or causing collinearity problems, but the best model used all the terms (comfortably significant by all tests; Table 8-8). After checking the slopes of the regression fits of Baas *et al.* (2000) it was found that $log_{10}(D_{50})$ gave a better fit than D_{50}. This resulted in relationship:

$$u_r = 10^{a+d\times\log_{10}(D_{50})}\theta'^{b+c\times\log_{10}(D_{50})}$$

$$u_r = 10^{10.4+3.2\times\log_{10}(D_{50})}\theta'^{6.2+0.9\times\log_{10}(D_{50})} \qquad \textbf{8-2}$$

This relationship can be used to predict the bedform migration rate for any grain size in the region 33-238 µm. Applying the grain size classes (33, 95 & 238 µm) to equation 8-2 regression lines can be plotted and the relationship visually assessed (Figure 8-1, bottom). The regression fit is significant ($p = 1.39\times10^{-16} < 0.05$, $F = 222 > 3.05$; Table 8-8; Kennedy & Neville, 1976), most of the variance is explained ($R^2 = 0.97$) and visually it looks good. Table 8-9 shows the multiple linear regression equation (8-2) calculated for the grain size classes 33, 95 & 238 µm and the equations of Baas *et al* (2000), so that a direct comparison can be made.

Although this is just an exercise to demonstrate how multiple linear regression works, the equation produced can be used to predict the bedform migration rate for any grain size in the region 33-238 µm with reasonable confidence. Other data to check the fit would give more confidence in the relationship.

Table 8-8: Regression model output from Baas *et al.* (2000) data.

Linear regression model: Migration Rate ~ 1 + $\log_{10}$(theta) + $\log_{10}$(D50) + $\log_{10}$(theta)* $\log_{10}$(D50) int

Estimated Coefficients:	Estimate	SE	t Stat	p Value
(Intercept)	10.401	0.9984	10.417	5.7089×10^{-10}
$\log_{10}$(theta)	6.2206	1.1561	5.3805	2.1074×10^{-5}
$\log_{10}$(D50)	3.2182	0.22694	14.181	1.5125×10^{-12}
$\log_{10}$(theta) ×$\log_{10}$(D50)	0.93983	0.26795	3.5075	0.001988

Number of observations: 26, Error degrees of freedom: 22
Root Mean Squared Error: 0.144
R-squared: 0.968
F-statistic vs. constant model: 222, p-value = 1.39×10^{-16}

Table 8-9: Regression fit coefficients for Baas *et al.* (2000) and the multiple linear regression for the same D_{50} values.

D_{50}, µm	Baas *et al.* (2000)	Multiple linear regression
33	$u_r = 0.0001\theta'^{1.8808}$	$u_r = 0.0001\theta'^{2.0088}$
95	$u_r = 0.0030\theta'^{2.6041}$	$u_r = 0.0029\theta'^{2.4404}$
238	$u_r = 0.0965\theta'^{3.0199}$	$u_r = 0.0549\theta'^{2.8152}$

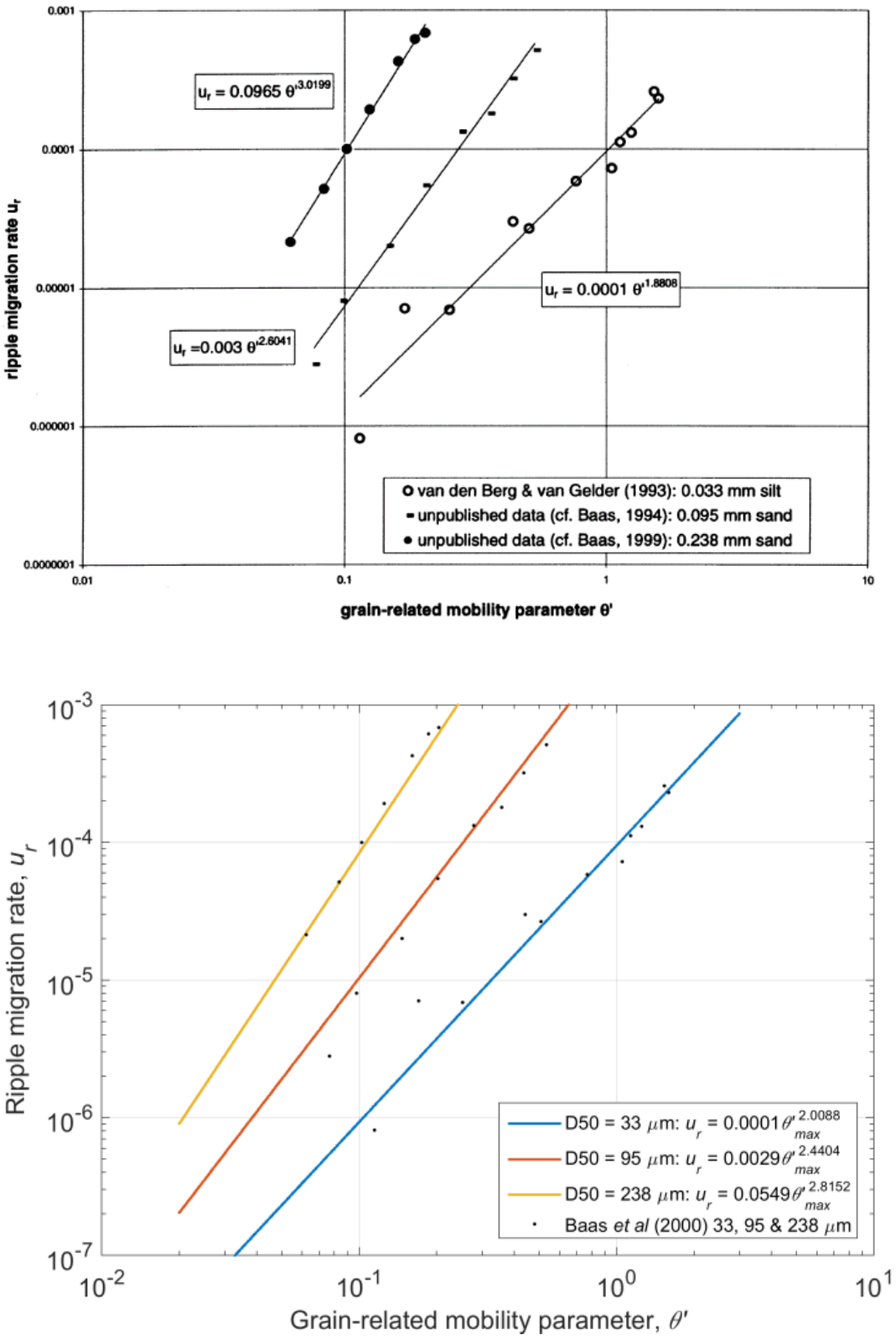

Figure 8-1: Top – the migration rate data and individual relationships of Baas *et al.* (2000). Bottom – the data of Baas *et al.* (2000) reanalysed using multiple linear regression plotted for the D_{50} values of 33, 95 and 238 µm.

10 References

(e-mail correspondence is reproduced in the appendices)

Agrawal, Y. C. and Pottsmith, H. C., 2000. Instruments for particle size and settling velocity observations in sediment transport. *Marine Geology*, 168, pp. 89-114.

Aldridge, J. N., Parker, E. R., Bricheno, L. M., Green, S. L., and van der Molen, J., 2015. Assessment of the physical disturbance of the northern European Continental shelf seabed by waves and currents, *Continental Shelf Research*, 108, pp. 121-140. doi: 10.1016/j.csr.2015.03.004.

Allen, J. R. L., 1968. *Current Ripples: Their relation to patterns of water and sediment motion*. Amsterdam: North-Holland Publishing Company. p. 433.

Allen, J. R. L., 1974. Reaction, Relaxation and Lag in Natural Sedimentary Systems: General Principles, Examples and Lessons. *Earth-Science Reviews*, 10, pp. 263-342.

Allen, J. R. L., 1982. *Sedimentary Structures: Their character and physical basis, volume 1*. Amsterdam: Elsevier, p. 593.

Allen, J. R. L. and Leeder, M. R., 1980. Criteria for the instability of upper-stage plane beds. *Sedimentology*, 27, pp. 209-217.

Amos, C.L., 1995. Siliclastic tidal flats In: G.M.E. Perillo, Ed. 1995. *Geomorphology and Sedimentology of Estuaries*, Amsterdam: Elsevier, pp. 273–306.

Amos, C.L., Van Wagoner, N. A. and Daborn, G. R., 1988a. The influence of subaerial exposure on the bulk properties of fine-grained intertidal sediment from Minas Basin, Bay of Fundy. *Estuarine, Coastal and Shelf Science*, 27, pp. 1-13.

Amos, C.L., Bowen, A. J., Huntley, D. A. and Lewis, C. F. M., 1988b. Ripple generation under the combined influences of waves and currents on the Canadian continental shelf. *Continental Shelf Research*, 8 (10), pp. 1129-1153.

Amos, C.L., Daborn, G. R., Christian, H. A., Atkinson, A. and Robertson, A., 1992. In situ erosion measurements on fine-grained sediments from the Bay of Fundy. *Marine Geology*, 108, pp. 175-196.

Amoudry, L. O., 2008. *A review on coastal sediment transport modelling*. [pdf] Liverpool: Proudman Oceanographic Laboratory. Available at: http://nora.nerc.ac.uk/8360/1/POL_ID_189.pdf [Accessed 30 October 2013], p. 21

Amoudry, L. O., Bell, P. S., Black, K. S., Gatliff, R. W., Helsby, R., Souza, A. J., Thorne, P. D., Wolf, J., 2009. A Scoping Study on: Research into Changes in Sediment Dynamics Linked to Marine Renewable Energy Installations. [pdf] Available at: https://tethys.pnnl.gov/sites/default/files/publications/Amoudry_2009.pdf [Accessed 23 July 2014], p. 120.

Amoudry, L. O. and Souza, A. J., 2011. Deterministic coastal morphological and sediment transport modelling: a review and discussion. *Reviews of Geophysics*, 49, pp. 1-21.

Amoudry, L. O., Ramirez-Mendoza, R., Souza, A. J. and Brown, J., 2014. Modelling-based assessment of suspended sediment dynamics in a hypertidal estuarine channel. *Ocean Dynamics*, 64, pp. 707-722.

Andersen, K. H. and Faraci, C., 2003. The wave plus current flow over vortex ripples at an arbitrary angle. *Coastal Engineering*, 47, pp. 431-441.

Anderson, T. J., Jensen, K. T., Lund-Hansen, L., Mouritsen, K. N. and Pejrup, M., 2002. Enhanced erodibility of fine-grained marine sediments by *Hydrobia ulvae*. *Journal of Sea Research*, 48, pp. 51-58.

Anderson, T. J., Fredsøe, J. and Pejrup, M., 2007. In situ estimation of erosion and deposition thresholds by Acoustic Doppler Velocimeter (ADV). *Estuarine, Coastal and Shelf Science*, 75, pp. 327-336.

Anderson, T. J. and Pejrup, M., 2011. Biological influences on sediment behaviour and transport. In: R. J. Uncles and S. G. Monismith, Eds. *Treatise on Estuarine and Coastal Science Volume 2: Water and Fine Sediment Circulation*. Waltham: Academic Press. Ch. 2.14.

Arnott, R.W. and Southard, J.B., 1990. Exploratory flow-duct experiments on combined-flow bed configurations, and some implications for interpreting storm event stratification, *Journal of Sedimentary Petrology*, 60, pp. 211–219.

Ashley, 1990. Classification of large-scale subaqueous bedforms: a new look at an old problem. *Journal of Sedimentary Petrology*, 60(1), pp. 160-172.

Aquatec, 2013. AQUAscat 1000 suspended sediment profiler specification sheet, DS010 Rev. 1.0 [pdf] Available at: http://www.aquatecgroup.com/images/datasheets/aquatec%20group%20-%20aquascat%201000.pdf [Accessed: 24/06/2013].

Austin, M. J., Masselink, G., O'Hare, T. J., and Russell, P. E., 2007. Relaxation time effects of wave ripples on tidal beaches. Geophysical Research Letters, 34 (16), L16606, doi:10.1029/ 2007GL030696, pp. 1-5.

Baas, J. H., Oost, A. P., Sztano, O. K., de Boer, P. L. and Postma, G., 1993. Time as an independent variable for current ripples developing towards linguoid equilibrium morphology. *Terra Nova*, 5, pp. 29-35.

Baas, J. H., 1994. A flume study on the development and equilibrium morphology of current ripples in very fine sand. *Sedimentology*, 41, pp. 185-209.

Baas, J. H., 1999. An empirical model for the development and equilibrium morphology of current ripples in fine sand. *Sedimentology*, 46, pp. 123-138.

Baas, J. H., van Dam, R. L. and Storms, J. E. A., 2000. Duration of deposition from decelerating high-density turbidity currents. *Sedimentary Geology*, 136, pp. 71-88.

Baas, J.H., 2003. Ripple, Ripple Mark, Ripple Structure. In: G.V. Middleton, ed. 2003. *Encyclopedia of Sediments and Sedimentary Rocks*. Dordrecht, Netherlands: Kluwer Academic Publishers, pp. 565-568.

Baas, J. H., Best, J. L. and Peakall, J. , 2011. Depositional processes, bedform development and hybrid bed formation in rapidly decelerated cohesive (mud-sand) sediment flows. *Sedimentology*, 58, pp. 1953-1987, doi: 10.1111/j.1365-3091.2011.01247.x.

Baas, J. H., 2013a. Realistic sedimentary bedform prediction: Incorporating physical and biological cohesion (COHBED). *Research councils UK, Gateway to research* [online] Available at: http://gtr.rcuk.ac.uk/project/7A336E6E-BD29-44C0-ABAA-EF8F90C5778D [Accessed 30 September 2013].

Baas, J. H. 2017. Push core sample data from the COHBED Dee fieldwork. [e-mail] Message from Baas, J. H., sent 13 July 2017, 10:40.

Baas, J. H. and Baker, M., 2013. COHBED Dee work, first results from Bangor. [e-mail] Message to COHBED project team from Baas, J. H., sent Friday 14 June 2013, 10:00.

Baas, J. H. and Baker, M., 2014. Push core samples from the COHBED Dee fieldwork. [e-mail] Message from Baas, J. H., sent 28 July 2014, 11:55.

Baas, J. H., Davies, A. G. and Malarkey, J., 2013. Bedform development in mixed sand-mud: The contrasting role of cohesive forces in flow and bed. *Geomorphology*, 182, pp. 19-39.

Baas, J. H. and De Koning, H., 1995. Washed-out ripples: their equilibrium dimensions, migration rate, and relation to suspended-sediment concentration in very fine sand. *Journal of Sedimentary Research*, A65 (2), pp. 431-435.

Baas, J. H., Westlake, A., Eggenhuisen, J., Amoudry, L., Cartigny, M., Coultish, N., McLelland, S., Mouazé, D., Murphy, B., Parsons, D., Rosewell, K., Ruessink, G., Schrijvershof, R., Wu, X., and Ye, L., 2014. Wave ripples in mixtures of cohesive clay and cohesionless sand: Preliminary results, in *Proceedings of the HYDRALAB IV Joint User Meeting, Lisbon, July 2014,* pp. 1-9.

Baldock, T. E., Tomkins, M. R., Nielsen, P. and Hughes, M. G., 2004. Settling velocity of sediments at high concentrations. *Coastal Engineering*, 51, pp. 91-100.

Bartholdy, J., Ernstsen, V. B., Flemming, B. W., Winter, C., Bartholomä, A. & Kroon, A., 2015. On the formation of current ripples. Scientific Reports, 5, 11390, doi:10.1038/srep11390, pp. 1-8.

Bell, P. S. and Thorne, P. D., 1997a. Application of a high resolution acoustic scanning system for imaging sea bed mircotopography. *7th International Conference on Electronic Engineering in Oceanography – Technology transfer from research to industry, IEEE conference Publication no.* 439, pp. 128-133.

Bell, P. S. and Thorne, P. D., 1997b. Measurements of sea bed ripple evolution in an estuarine environment using a high-resolution acoustic sand ripple profiling system. In: *Oceans '97*, vol. 1, MTS/IEEE conference proceedings, Washington D. C.: IEEE, pp. 339–343.

Bell, P. S., 2013. *Re: ripple profiler problem*. [e-mail] (Personal communication, 5 September 2013).

Bell, P. S., 2016. An outline of a bedform rotation correction method based on a radon transform. [Conversation] (Personal communication, 9 February 2016).

Bendat, J. S. and Piersol, A. G., 1986. *Random Data: Analysis and Measurement Procedures*. 2nd edition. New York: John Wiley & Sons. p. 566.

Bennett, S. and J. Best, 1996. Mean flow and turbulence structure over fixed ripples and the ripple-dune transition. In: P. J. Ashworth, S. J. Bennett, J. L. Best, and S. J. McLelland eds. 1996. *Coherent Flow Structures in Open Channels*. Hoboken, N. J.: John Wiley. pp. 67– 125.

Best, J., 2005. The fluid dynamics of river dunes: A review and some future research directions. Journal of Geophysical Research, 110, F04S02, doi:10.1029/2004JF000218, pp. 1-21.

Betteridge, K. F. E., Thorne, P. D. and Cooke, R. D., 2008. Calibrating multi-frequency acoustic backscatter systems for studying near-bed suspended sediment transport processes. *Continental Shelf Research*, 28, pp. 227-235.

Black, K. S., Tolhurst, T. J., Paterson, D. M. and Hagerthey, S. E., 2002. Working with natural cohesive sediments, *Journal of Hydraulic Engineering*, 128 (1), pp. 1-7.

Blondeaux, P., 2012. Sediment mixtures, coastal bedforms and grain sorting phenomena: An overview of the theoretical analyses. *Advances in Water Resources*, 48, pp. 113-124.

Blott, S. J. and Pye, K., 2001. Gradistat: A grain size distribution and statistics package for the analysis of unconsolidated sediments. *Earth Surface Processes and Landforms*, 26, pp. 1237-1248.

Bolaños, R. and Souza, A., 2010. Measuring hydrodynamics and sediment transport processes in the Dee Estuary. *Earth System Science Data*, 2, pp. 157-165.

Bolaños, R., Amoudry, L. O. and Doyle, K., 2011. Effects of Instrumented Bottom Tripods on Process Measurements. *Journal of Atmospheric and Oceanic Technology*, 28, pp. 827–837.

Bolaños, R., Thorne, P. D. and Wolf, J., 2012. Comparison of measurements and models of bed stress, bedforms and suspended sediments under combined waves. *Coastal Engineering*, 62, pp.19-30.

Bolaños, R., Brown, J. M. and Souza, A., 2014. Wave-current interactions in a tide dominated estuary. *Continental Shelf Research*, 87, pp. 109-123.

Borradaile, G. J., 2003. *Statistics of Earth Science Data: Their Distribution in Time, Space and Orientation*, Berlin: Springer-Verlag. p. 351.

Bradshaw, P., 1971. *An introduction to turbulence and its measurement*. Oxford: Pergamon Press Ltd. p. 218.

British Geological Survey, 2013. World Magnetic Model 2010 calculator [Online calculator] Available at: http://www.geomag.bgs.ac.uk/data_service/models_compass/wmm_calc.html [Accessed: 14/06/2013].

Brockhus, J. W. Q., 2011. *Bedform appearance and dimension in the nearshore under mixed wave and current conditions*. MSc. Utrecht University. Available at <http://dspace.library.uu.nl/bitstream/handle/1874/249173/MScThesisJWQBrockhus3057542.pdf> [Accessed 17/02/2016]

Brown, J. M., and Wolf, J., 2009. Coupled wave and surge modelling for the eastern Irish Sea and implications for model wind-stress. *Continental Shelf Research*, 29, pp. 1329-1342.

Brown, J. M. 2010. A case study of combined wave and water levels under storm conditions using WAM and SWAN in a shallow water application. *Ocean Modelling*, 35 (3), pp. 215-229, doi: 10.1016/j.ocemod.2010.07.009.

Brown, J. M., Phelps, J. J. C., Barkwith, A., Martin D. Hurst, M. D., Ellis, M. A., Plater, A. J., 2016. The effectiveness of beach mega-nourishment, assessed over three management epochs. *Journal of Environmental Management*, 184(2), pp. 400–408.

Brueckner, S., 2007. *Crossing: Detect zero (or any other) level crossing of signals*. [online] Available at: <http://uk.mathworks.com/matlabcentral/fileexchange/2432-crossing> [Accessed 7 August 2012].

Buffington, J. M., 1999. The Legend of A. F. Shields. *Journal of Hydraulic Engineering*, 125 (4), pp. 376-387.

Bunt, J. A. C., Larcombe, P. and Jago, C. F., 1999. Quantifying the response of optical backscatter devices and transmissometers to variations in suspended particulate matter. *Continental Shelf Research*, 19, pp. 1199-1220.

Camenen, B., 2009. Estimation of the wave-related ripple characteristics and induced bed shear stress. *Estuarine, Coastal and Shelf Science*, 84, pp. 553–564.

Cameron, W. M. and D.W. Pritchard, 1963. Estuaries. In: M. N. Hill, ed. *The Sea*, Vol. 2. New York: John Wiley & Sons. Ch. 15.

Castro-Orgaz, O., Giráldez, J. V., Mateos, L. , and Dey, S., 2012. Is the von Kármán constant affected by sediment suspension? *Journal of Geophysical Research*, 117, F04002, pp. 1-16, doi:10.1029/2011JF002211.

Cataño-lopera, Y. A., Abad, J. D. and Garcia, M. H., 2009. Characterization of bedform morphology generated under combined flows and currents using wavelet analysis. *Ocean Engineering*, 36, pp.617-632.

Cazenave, P. W., Dix, J. K., Lambkin, D. O. and McNeill, L. C., 2013. A method for semi-automated objective quantification of linear bedforms from multi-scale digital elevation models. *Earth Surface Processes and Landforms*, 38, pp. 221-236.

Chatterjee,S and Hadi, A. S., 2015. *Regression analysis by example*, 5th Ed. Hoboken, New Jersey: Wiley & sons. p. 424.

Clifton, H. E. and Dingler, J. R., 1984. Wave-formed structures and paleoenvironmental reconstruction. *Marine Geology*, 60, pp. 165-198.

Collier, G., 2014. *Head offset correction for the 3D sand ripple profiler (Marine Electronics Ltd.)*. [e-mail] Message to D. Lichtman (doulich@noc.ac.uk) Sent 7 February 2014.

Collins, M. B., Ke, X. and Gao, S., 1998. Tidally-induced flow structure over intertidal flats. *Estuarine, Coastal and Shelf Science*, 46, pp. 233-250.

Cooke, R. D., 2015. *3D Ripple Profiler sn:161 query* (head offset problem). [e-mail] (Personal communication, 6 February 2015).

Cowell, P. J., Roy, P. S. and Jones, S. A., 1995. Simulation of large-scale coastal change using a morphological behaviour model. *Marine Geology*, 126, pp. 45-61.

Davies, A. G. and Villaret, C., 1999. Eulerian drift induced by progressive waves above rippled and very rough beds. *Journal of Geophysical Research: Oceans*, 104 (C1), pp. 1465–1488.

Davies, A. G., and Thorne, P. D., 2008. Advances in the Study of Moving Sediments and Evolving Seabeds. *Surveys in Geophysics*, 29 (1), pp. 1-36.

Davis, J. P., Walker, D. J., Townsend, M., and Young, I. R., 2004. Wave-formed sediment ripples: Transient analysis of ripple spectral development, Journal of Geophysical Research: Oceans, 109(C7), pp. 1-15.

Deacon G. F., 1894. In: Discussion on the training of rivers, *Minutes of the Proceedings of the Institute of Civil Engineers*, 118, pp. 93-96. Available: http://www.jiscjournalarchives.ac.uk/openurl.html?ref=ice/pdf/imotp/1894/118/1894/imotp_1894.19891/imotp_1894_19891.pdf [Accessed 5 August 2014].

Debnath, K. and Chaudhuri, S., 2010. Bridge pier scour in clay-sand mixed sediments at near-threshold velocity for sand. *Journal of Hydraulic Engineering*, 136(9), pp. 597-609.

Decho, A. W., 2000. Microbial biofilms in intertidal systems: an overview. *Continental Shelf Research*, 20, pp. 1257-1273.

Dietrich, W. E., 1982. Settling velocity of natural particles. *Water Resources Research*, 18(6), pp. 1615-1626.

Dott Jr., R. L., 1964. Wacke, greywacke and matrix – What approach to immature sandstone classification? *Journal of Sedimentary Petrology*, 34, pp. 625-632.

Downing, A., Thorne, P. D. and Vincent, C. E., 1995. Backscattering from a suspension in the near field of a piston transducer. *J. Acoust. Soc. Am.*, 97 (3), pp. 1614-1620.

Downing, J, 2006. Twenty-five years with OBS sensors: The good, the bad and the ugly. *Continental Shelf Research*, 26, pp. 2299-2318.

Dubois, M., Gilles, K. A., Hamilton, J. K., Rebers, P. A., and Smith, F., 1956. Colorimetric method for determination of sugars and related substances. *Analytical Chemistry*, 28, pp. 350–356.

Dumas, S., Arnott, R., and Southard, J.B., 2005, Experiments on oscillatory-flow and combined-flow bedforms: implications for interpreting parts of the shallow-marine sedimentary record. *Journal of Sedimentary Research*, 75, pp. 501–513.

Dronkers, J., 2005. *Dynamics of Coastal Systems*. Singapore: World Scientific Publishing, p.519.

Dyer, K. D., 1995. Sediment transport processes in estuaries. In: G. M. E. Perillo ed. 1995. *Developments in Sedimentology 53: Geomorphology and Sedimentology of Estuaries*. Amsterdam: Elsevier. Ch. 14.

Dyer, K. D., 1997. *Estuaries: A physical introduction*. 2nd edition. Chichester: John Wiley & Sons Ltd.

Eisma, D., Bernard, P., Cadée, G. C., Ittekkot, V., Kalf, J., Laane, R., Martin, J. M., Mook, W. G., Van Put, A. and Schuhmacher, T., 1991. Suspended-matter particle size in some West-European estuaries; Part 1: Particle-size distribution. *Netherlands Journal of Sea Research*, 28(3), pp. 193-214.

Eisma, D. and Kalf, J., 1987. Distribution, organic content and particle size of suspended matter in the North Sea. *Netherlands Journal of Sea Research*, 21(4), pp. 265-285.

Emery, W. J. and Thomson, R. E., 2001. *Data analysis methods in physical oceanography*. 2nd Edition. Amsterdam: Elsevier Science., p. 638.

Englert, C. M., 2010. *Development of a spectral 2-D Fast Fourier Transform analysis for sand ripple morphology* interpretation. B. Sc. Colby College, Maine.

Epperl, J., 2012. Answer to: How to eliminate the lines that joins the discontinued points in a data? MATLAB Central: Answers [online forum] Available at: https://www.mathworks.co.uk/matlabcentral/answers/52673#answer_64230 [accessed 25 November 2014].

Fagherazzi, S., Kirwan, M. L., Mudd, S. M., Guntenspergen, G. R., Temmerman, S., D'Alpaos, A., van de Koppel, J., Rybczyk, J. M., Reyes, E., Craft, C., and Clough, J., 2012. Numerical models of salt marsh evolution: Ecological, geomorphic, and climatic factors, *Reviews of Geophysics*, 50, RG1002, doi:10.1029/2011RG000359.

Faraci, C. and Foti, E., 2002. Geometry, migration and evolution of small-scale bedforms generated by regular and irregular waves. *Coastal Engineering*, 47, pp.35-52.

Fenton, J.D. and McKee, W.D., 1990. On calculating the lengths of water waves. *Coastal Engineering,* 14, pp. 499-513.

Fernandez, R., Best, J. and López, F., 2006. Mean flow, turbulence structure, and bed form superimposition across the ripple-dune transition. *Water Resources Research*, 42, W05406, pp. 1-17, doi:10.1029/2005WR004330.

Flemming, B. W. (2002), *Geographic distribution of muddy coasts, in Muddy Coasts of the World: Processes, Deposits and Function*. Proceedings in Marine Science 4, 99–201, The Netherlands: Elsevier Science, p. 556.

Folk, R. L. and Ward, W. C., 1957. Brazos Bar: A study in the significance of grain size parameters. Journal of Sedimentary Petrology, Vol. 27, No. 1, pp. 3-26.

Friedman, G. M., 1961. Distinction between dune, beach and river sands from their textural characteristics. *Journal of Sediment Petrology*, Vol. 31, No. 4, pp. 514-529.

Friedrichs, C.T., 2011. Tidal Flat Morphodynamics: A Synthesis, In: Eric Wolanski and Donald McLusky, Ed. 2011. *Treatise on Estuarine and Coastal Science*, Waltham: Academic Press, pp. 137-170.

Friend, P. L., Lucas, C. H., Holligan, P. M., and Collins, M. B., 2008. Microalgal mediation of ripple mobility. *Geobiology*, 6, pp. 70–82.

Fries, J. S., Butman, C. A. and Wheatcroft, R. A., 1999. Ripple formation induced by biogenic mounds. *Marine Geology*, 159, pp. 287-302.

Fugate, D. C. and Friedrichs, C. T., 2002. Determining concentration and fall velocity of estuarine particle populations using ADV, OBS and LISST. *Continental Shelf Research*, 22, pp. 1867-1886.

Gallagher, E. L., Elgar, S. and Thornton, E. B., 1998. Megaripple migration in a natural surf zone. *Nature*, 394, pp. 165-168.

García, M. H., Laursen, E. M., Michel, C. and Buffington, J. M., 2000. Discussions and closure of 'The Legend of A. F. Shields'. *Journal of Hydraulic Engineering*, 126 (9), pp. 718-723.

Giachetti, A., 2000. Matching techniques to compute image motion. *Image and Vision Computing*, 18, pp. 247–260.

Gordon, L. and Lohrmann, A., 2001. Near-shore Doppler current meter wave spectra. in *Ocean Wave Measurement and Analysis: Proceedings of ASCE Waves 2001 conference*, ASCE, Reston, VA. Available at: http://www.nortek-as.com/lib/bibliography/near-shore-doppler-curent-meter-wave-spectra [Accessed 30 September 2014]. pp. 1-12.

Goring, D. G. And Nikora, V. I., 2002. Despiking Acoustic Doppler Velocimeter Data. *Journal of Hydraulic Engineering*, 128, pp. 117-126.

Grabowski, R. C., Droppo, I. G. and Wharton, G., 2010. Estimation of critical shear stress from cohesive strength meter derived erosion thresholds. *Limnology and Oceanography: Methods*, 8, pp. 678-685.

Grabowski, R. C., Droppo, I. G. and Wharton, G., 2011. Erodibility of cohesive sediment: The importance of sediment properties. *Earth-Science Reviews*, 105, pp. 101-120.

Graf, G. and Rosenberg, R., 1997. Bioresuspension and biodeposition: a review. *Journal of Marine Systems*, 11, pp. 269-278.

Grant, J., Bathmann, U. V. and Mills, E. L., 1986. The interaction between benthic diatom films and sediment transport, *Estuarine, Coastal and Shelf Science*, 23, pp. 225-238.

Grant, W. D. and Madsen, O. S., 1979. Combined wave and current interaction with a rough bottom. *Journal of Geophysical Research*, 84 (C4), pp. 1797-1808.

Grant, W. D. and Madsen, O. S., 1982. Movable bed roughness in unsteady oscillatory flow. *Journal of Geophysical Research*, 87 (C1), pp. 469-481.

Grant, W. D. and Madsen, O.S., 1986. The continental bottom boundary layer. *Annual Review of Fluid Mechanics*, 18, pp. 265-305.

Grant, J. and Daborn, G., 1994. The effects of bioturbation on sediment transport on an intertidal mudflat. *Netherlands Journal of Sea Research*, 32(1), pp. 63-72.

Green, M. O., 1992. Spectral estimates of bed shear stress at subcritical Reynolds numbers in a tidal boundary layer. *Journal of Physical Oceanography*, 22, pp. 903-917.

Günter, A., 1971. *Die kritische mittlere Sohlenschubspannung bei Geschiebe-mischungen unter Berücksichtigung der Deckschichtbildung und der turbulenzbedingten Sohlenschubspannungsschwankungen*. PhD. ETH Zurich. Available at: < http://e-collection.library.ethz.ch/eserv/eth:32583/eth-32583-02.pdf > [Accessed 15 February 2017].

Hagadorn, J. W. and McDowell, C., 2012. Microbial influence on erosion, grain transport and bedform genesis in sandy substrates under unidirectional flow, *Sedimentology*, 59, 795-808.

Halcrow, 2010a. *North West England and North Wales Shoreline Management Plan SMP2 (Main SMP2 Document)*. [pdf] North West & North Wales Coastal Group Available at: <http://www.allerdale.gov.uk/downloads/nw_shoreline_management_plan_2.pdf> [Accessed 18 February 2014], p.57.

Halcrow, 2010b. *Cell Eleven Tidal and Sediment Transport Study (CETaSS) Phase 2 (ii): Main Report – Summary of findings*. [pdf] North West & North Wales Coastal Group Available at: <https://web.archive.org/web/20130509181845/http://www.mycoastline.org/documents/CETaSS/CETaSS2ii.pdf> [Accessed 20 January 2017], p.159.

Halcrow, 2013. *North West Estuaries Processes Reports: Dee Estuary*. [pdf] Sefton Council, Available at: <https://www.liverpool.ac.uk/~cmi/dee/Dee_rep2013.pdf> [Accessed 23 June 2015], p.63.

Hallermeier, R. J., 1981. Terminal settling velocity of commonly occurring sand grains. *Sedimentology*, 28, pp. 859-865.

Hansen, D.V. and Rattray, Jr., M., 1966. New dimensions in estuary classification. *Limnology and Oceanography*, 11, pp. 319–326.

Harris, P. T., Baker, E. K., Cole, A. R. and Short, S. A., 1993. A preliminary study of sedimentation in the tidally dominated Fly River delta, Gulf of Papua. *Continental Shelf Research*, 13(4), pp. 441-472.

Hoekstra, P., Bell, P., van Santen, P., Roode, N., Levoy, F., and Whitehouse, R., 2004. Bedform migration and bedload transport on an intertidal shoal. *Continental Shelf Research*, 24, pp. 1249-1269.

Hubbell, D. W., 1964. *Apparatus and techniques for measuring bedload*, U.S. Geol. Survey Water-Supply Paper 1748, Washington: United States Government Printing Office. p.74.

Huettel M., Ziebis, W., and Forster, S., 1996. Flow-induced uptake of particulate matter in permeable sediments. Limnology and Oceanography, 41(2), pp. 309-322.

Huntley, D. A., 1988. A modified method for estimating seabed stresses at low Reynolds numbers, with application to wave/current boundary layer measurements. *Journal of Physical Oceanography*, 18, pp. 339-346.

Jacobs, W., Le Hir, P., Van Kesteren, W. and Cann, P.,2011. Erosion threshold of sand–mud mixtures. *Continental Shelf Research*, 31(10), p.14–25.

Jafari-Khouzani, K and H. Soltanian-Zadeh, 2005. Radon transform orientation estimation for rotation invariant texture analysis, IEEE Transactions on Pattern Analysis and Machine Intelligence, 27 (6), 1004-1008.

Jiménez, J. A. and Madsen, O. S., 2003. A simple formula to estimate settling velocity of natural sediments. Journal of Waterway, Port, Coastal and Ocean Engineering. 129(2), pp. 70-78.

Jones, L., Garbutt, A., Hansom, J. and Angus, S., 2013. Impacts of climate change on coastal habitats. *MCCIP Science Review 2013*, pp. 167-179. doi:10.14465/2013.arc18.167-179. Available at: http://www.mccip.org.uk/media/22503/2013arc_sciencereview_18_chab_final.pdf [Accessed 13 April 2015].

Jørgensen, C. B., Kiørboe, Møhlenberg, F. and Riisgård, H. U., 1984. Ciliary and mucus-net filter feeding, with special reference to fluid mechanical characteristics. Marine Ecology Progress Series 15, pp. 283–292.

Kennedy, J. B. & Neville, A. M., 1976. *Basic Statistical Methods for Engineers and Scientists*, 2nd Ed., New York: Harper and Row. p.490.

Kenyon, N.H., 1970. Sand ribbons of European Tidal Sea. *Marine Geology*, 9, pp. 25-39.

Kim, S.-C., Friedrichs, C. T., Maa, J. P.-Y. and Wright, L. D., 2000. Estimating bottom stresses in tidal boundary layer from acoustic Doppler velocimeter data, *Journal of Hydraulic Engineering*, *126*, pp. 399-406.

Kirwan, M. L. and Guntenspergen G. R., 2012. Feedbacks between inundation, root production, and shoot growth in a rapidly submerging brackish marsh, Journal of Ecology, 100, 764-770. doi:10.1111/j.1365-2745.2012.01957.

Kleinhans, M. G., 2005. Phase diagrams of bed states in steady, unsteady and, oscillatory and mixed flows. In: L. C. van Rijn, R. L. Soulsby, P. Hoekstra & A. G. Davies, ed. 2005. *SANDPIT, Sand transport and morphology of offshore sand mining pits*. The Netherlands: Aqua Publications. Ch. Q.

Krumbein, W. C., 1936. Application of logarithmic moments to size frequency distributions of sediments. *Journal of Sedimentary Petrology*, 6(1), pp. 35-47.

Komar, P. D. and Li, Z., 1986. Pivoting analyses of the selective entrainment of sediments by shape and size with application to gravel threshold. *Sedimentology*, 33, pp. 425-436.

Lanuru, M., Riethmüller, R., van Bernem, C. and Heymann, K., 2007. The effect of bedforms (crest and trough systems) on sediment erodibility on a back-barrier tidal flat of the East Frisian Wadden Sea, Germany. Estuarine, Coastal and Shelf Science, 72, pp. 603-614.

Larson, F., Lubarsky, H., Gerbersdorf, S. U. and Paterson, D. M., 2009. *Limnology and Oceanography: Methods*, 7, pp. 490-497.

Le Hir, P., Monbet, Y. and Orvain, F., 2007. Sediment erodibility in sediment transport modelling: can we account for biota effects? *Continental Shelf Research*, 27, pp. 1116-1142.

Le Hir, P., Cayocca, F. and Waeles, B., 2011. Dynamics of sand and mud mixtures: A multiprocess-based modelling strategy. *Continental Shelf Research*, 31, pp. 135-149.

Lee Young, J. S. and Sleath, J. F. A., 1990. Ripple formation in combined transdirectional steady and oscillatory flow. *Sedimentology*, 37, pp. 509-516.

Lefebvre, A., Ernstsen, V. B. and Winter, C., 2011. Bedform characterization through 2D spectral analysis. *Journal of Coastal Research*, SI 64, pp. 781-785.

Li, M. Z. and Amos, C. L., 1998. Predicting ripple geometry and bed roughness under combined waves and currents in a continental shelf environment. *Continental Shelf Research*, 18, pp. 941-970.

Li, M. Z. and Amos, C. L., 1999. Field observations of bedforms and sediment transport thresholds of fine sand under combined waves and currents. *Marine Geology*, 158, pp. 147-160.

Libes, S. M., 1992. An Introduction to Marine Biogeochemistry. John Wiley & Sons, p.734.

Lichtman, I. D., 2012. *A comparison of methods for turbulence investigations of bed shear stress*. MSc. University of Southampton. p.161.

Lindenbergh, R., van Dijk, T., and Egberts, P., 2006. Separating bedforms of different scales in echo sounding data. *Coastal Dynamics 2005*, pp. 1-14.

Lisle, T. E., Hilton, S., 1992. The volume of fine sediment in pools: an index of sediment supply in gravel-bed streams. *Water Resources Bulletin*, 28, pp. 371-383.

Liu, Z., 2001. *Sediment Transport*. [e-book/pdf] Aalborg: Laboratoriet for Hydraulik og Havnebygning Instituttet for Vand, Jord og Miljøteknik Aalborg Universitet. Available at: http://lvov.weizmann.ac.il/lvov/Literature-Online/Literature/Books/2001_Sediment_Transport.pdf [accessed 16 September 2013], p. 71.

Lundkvist, M., Gangelhof, U., Lunding, J. and Flindt, M. R., 2007. Production and fate of extracellular polymeric substances produced by benthic diatoms and bacteria: A laboratory study. Estuarine, Coastal and Shelf Science, 75, pp. 337-346.

Maa, J. P. –Y. And Kwon, J. –I., 2007. Using ADV for cohesive sediment settling velocity measurements. *Coastal, Esturine and Shelf Science*, 73, pp. 351-354.

Madsen, O. S., 1994. Spectral wave-current bottom boundary layer flows. In: Proceedings of the 24th International Conference on Coastal Engineering, Kobe, Japan, 1994, ICCE. [pdf] https://journals.tdl.org/icce/index.php/icce/article/view/4970/4650 [Accessed: 11 May 2015]. p. 384–398.

Malarkey, J. and Davies, A.G., 2012. A simple procedure for calculating the mean and maximum bed stress under wave and current conditions for rough turbulent flow based on Soulsby and Clarke's (2005) method. Computers & Geosciences, 43, pp. 101-107.

Malarkey, J., Baas, J.H., Hope, J.A., Aspden, R.J., Parsons, D.R., Peakall, J., Paterson, D.M., Schindler, R.J., Ye, L., Lichtman, I.D., Bass, S.J., Davies, A.G., Manning, A.J. and Thorne, P.D., 2015. The pervasive role of biological cohesion in bedform development. *Nature Communications*, 6:6257, doi: 10.1038/ncomms7257.

Malvern Instruments Ltd, 2007. Mastersizer 2000 User Manual (MANO384, issue 1.0) [online] http://www.malvern.com/malvern/kbase.nsf/search?readform [Accessed: 21/08/2013].

Malvern Instruments Ltd, 2013. Malvern Mastersizer web page [online] http://www.malvern.com/labeng/products/mastersizer/MS2000/mastersizer2000.htm [Accessed: 20/08/2013].

Manning, A. J., Baugh, J. V., Spearman, J. R., Pidduck, E. L., and Whitehouse, R. J. S., 2011. The settling dynamics of flocculating mud-sand mixtures: Part 1 – Empirical algorithm development. *Ocean Dynamics*, 61(2), pp. 311-350, doi: 10.1007/s10236-011-0394-7.

Manning, A. J., Spearman, J. R., Whitehouse, R. J.S., Pidduck, E. L., Baugh, J. V. and Spencer, K. L., 2013. Flocculation dynamics of mud-sand mixed suspensions. In: A. J. Manning, ed. 2013. *Sediment Transport Processes and Their Modelling Applications*, Ch. 6.

Marine Electronics, 2009. User Manual for the 3D Sand Ripple Profiling Logging Sonar, issue 1.1. [Instrument manual] Marine Electronics Ltd., Unit 10, Barras Lane Industrial Estate, Vale, Guernsey, Channel Islands, GY6 8EQ., p. 25.

Marine Electronics, 2010. User Manual for the Suspended Sediment Imaging Sonar, issue 1.0. [Instrument manual] Marine Electronics Ltd., Unit 10, Barras Lane Industrial Estate, Vale, Guernsey, Channel Islands, GY6 8EQ.

Masselink, G. and Short. A. D., 1993. The effect of tide range on beach morphodynamics and morphology: A conceptual beach model. *Journal of Coastal Research*, 9(3), pp785-800.

Masselink, G. and Hughes, M. G., 2003. *Introduction to Coastal Processes and Geomorphology*. London: Hodder Arnold, p. 354.

Masselink, G., Austin, M. J., O'Hare, T. J. and Russell, P. E., 2007. Geometry and dynamics of wave ripples in the nearshore zone of a coarse sandy beach. *Journal of Geophysical Research*, 112, C10022, pp. 1-19.

McDougall, T. J. and Barker, P. M. 2011. *Getting started with TEOS-10 and the Gibbs Seawater (GSW) Oceanographic Toolbox*, SCOR/IAPSO WG127, [pdf] Available at: http://www.teos-10.org/pubs/Getting_Started.pdf. p. 32. [Accessed 2 June 2015].

McLean, S.R., 1981. The role of non-uniform roughness in the formation of sand ribbons. *Marine Geology*, 42, pp. 49-74.

Mehta, A. J., 1989. On estuarine cohesive sediment suspension behaviour. *Journal of Geophysical Research*, 94, No. C10, pp. 14,303-14,314.

Mehta, A. J., 2014. *An Introduction to Hydraulics of Fine Sediment Transport*. Advanced Series on Ocean Engineering, 38, Singapore: World Scientific Publishing Company, p. 1039.

Mikkelson, O. A. and Pejrup, M., 2001. The use of a LISST-100 laser particle sizer for *in-situ* estimates of floc size, density and settling velocity. *Geo-Marine Letters*, 20, pp. 187-195.

Mitchener, H. and Torfs, H., 1996. Erosion of mud/sand mixtures. *Coastal Engineering*, 29, pp. 1-25.

Moate, B. D., Thorne, P. D. and Cooke, R. D., 2011. Acoustic backscatter measurements in two dimensions: The Acoustic Suspended Sediment Imager. In: Papadakis, J.S. & Bjorno, L., eds. *Proceedings of the 4th International Conference on Underwater Acoustic Measurements: Technologies and Results, Kos, Greece, 20-24 June 2011,* pp. 1579-1584.

Moate, B. D., Thorne, P. D. and Cooke, R. D., 2016. Field deployment and evaluation of a prototype autonomous two dimensional acoustic backscatter instrument: The Bedform And Suspended Sediment Imager (BASSI). *Continental Shelf Research*, 112, pp. 78-91.

Moore, D. M., and Reynolds Jr., R. C., 1997. *X-Ray Diffraction and the Identification and Analysis of Clay Minerals*. 2nd Edition, Oxford University Press, New York, p. 332.

Moore, R. D., Wolf, J., Souza, A. J. and Flint, S. S., 2009. Morphological evolution of the Dee Estuary, Eastern Irish Sea, UK: A tidal asymmetry approach. *Geomorphology*, 103, pp. 588-596.

Morang, A. and Parson, L. E., 2002. Coastal Morphodynamics. In: *Coastal Engineering Manual: Part 4 Coastal geology*, *Engineer Manual 1110-2-1100*, [pdf] U.S. Army Corps of Engineers, Washington, D.C. Available at: http://140.194.76.129/publications/eng-manuals/EM_1110-2-1100_vol/PartIV/PartIV.htm [Accessed 19 July 2013]. Ch 3.

Mori, N., Suzuki, T. And Kakuno, S., 2007. Noise of Acoustic Doppler Velocimeter Data in Bubbly Flows. *Journal of Engineering Mechanics*, 133, pp. 122-125.

Natural England, 1998. *SSSI citation: Dee Estuary* [pdf] Available at: http://www.sssi.naturalengland.org.uk/citation/citation_photo/1000595.pdf [Accessed 30 April 2013].

Natural England and the Countryside Commission for Wales, 2010. *The Dee Estuary European Marine Site, comprising: Dee estuary/Aber Dyfrdwy Special Area of Conservation, The Dee Estuary Special Protection Area and the Dee Estuary Ramsar Site*, [pdf] Available at: http://www.naturalengland.org.uk/Images/DeeEstuary-Reg33-Vol1_tcm6-16646.pdf, [Accessed 15 April 2017], p. 259.

Nelson, T. R., Voulgaris, G. and Traykovski, P., 2013. Predicting wave-induced ripple equilibrium geometry. *Journal of Geophysical Research: Oceans*, 118, pp. 3202–3220, doi:10.1002/jgrc.20241.

Nikuradse, J., 1933. *Strömungsgesetze in rauhen Rohren*. VDI-Forschungsheft 361. Beilage zu Forschung auf dem Gebiete des Ingenieurwesens Ausgabe B Band 4. Translated by A. A. Brielmaier, 1950 as Laws of flow in rough pipes, Technical Memorandum 1292, National Advisory Committee for Aeronautics). Available at: http://ntrs.nasa.gov/archive/nasa/casi.ntrs.nasa.gov/19930093938.pdf [Accessed 29 July 2014].

Nielsen, P., 1984. Sediment concentrations under waves, *Coastal Engineering*, 8, pp. 51-72.

Nielsen, P., 2009. *Coastal and Estuarine Processes*. Singapore: World Scientific Publishing, p. 343.

O' Hara Murray, R. B., Thorne, P. D. and Hodgson, D. M., 2011. Intrawave observations of sediment entrainment processes above sand ripples under irregular waves. *Journal of Geophysical Research: Oceans*, 116(C1), pp. 1-25.

O' Hara Murray, R. B., Hodgson, D. M. and Thorne, P. D., 2012. Wave groups and sediment resuspension processes over evolving sandy bedforms. *Continental Shelf Research*, 46, pp. 16-30.

Oost, A. P and Baas, J. H., 1994. The development of small scale bedforms in tidal environments: an empirical model for unsteady flow. *Sedimentology*, 41, pp. 883-903.

Paarlberg, A.J., Knaapen, M.A.F., de Vries, M.B., Hulscher, S.J.M.H. and Wang, Z.B., 2005. Biological influences on morphology and bed composition of an intertidal flat. *Estuarine, Coastal and Shelf Science*, 64, pp. 577-590.

Panagiotopoulos, I., Voulgaris, G. and Collins, M. B., 1997. The influence of clay on the threshold of movement of fine sandy beds. *Coastal Engineering*, 32, pp. 19-43.

Paphitis, D., 2001. Sediment movement under unidirectional flows: an assessment of empirical threshold curves. *Coastal Engineering*, 43, pp. 227-245.

Parsons, A. J., Cooper, J. and Wainwright, J., 2015. What is suspended sediment? *Earth Surface Processes and Landforms*, 40, pp. 1417-1420.

Parsons, D. R., Schindler, R. J., Hope, J. A., Malarkey, J., Baas, J. H., Peakall, J., Manning, A. J., Ye, L., Simmons S., Paterson, D. M., Aspden, R. J., Bass, S. J., Davies, A. G., Lichtman, I. D., and Thorne, P. D., 2016. The role of biophysical cohesion on subaqueous bed form size. *Geophysical Research Letters*, 43, pp. 1-8, doi:10.1002/2016GL067667.

Passarelli, C., Olivier, F., Paterson, D. M., Meziane, T. and Hubas, C, 2014. Organisms as cooperative ecosystem engineers in intertidal flats. *Journal of Sea Research*, 92, pp. 92-101.

Parchure, T. M. and Mehta, A. J., 1985. Erosion of soft cohesive sediment deposits. Journal of Hydraulic Engineering, 111, pp. 1308-1326.

Paterson, D. M. and Black, K. S., 1999. Water Flow, Sediment Dynamics and Benthic Biology, in *Advances in Ecological Research 29*, D.B. Nedwell and D.G. Raffaelli, (Eds.), London: Academic Press, pp. 155-193.

Pattiaratchi, C. B. and Collins, M. B., 1984. Sediment transport under waves and tidal currents: A case study from the northern Bristol Channel, U.K., *Marine Geology*, 56, pp. 27-40.

Pedocchi, F. and García, M. H., 2009a. Ripple morphology under oscillatory flow: 1. Prediction, *Journal of Geophysical Research*, 114, C12014, doi:10.1029/2009JC005354, pp. 1-16.

Pedocchi, F. and García, M. H., 2009b. Ripple morphology under oscillatory flow: 2. Experiments, *Journal of Geophysical Research*, 114, C12015, doi:10.1029/2009JC005356, pp. 1-17.

Perillo, M.M., 2013. *Flow, Sediment Transport and Bedforms under Combined-Flows*. Ph.D., University of Illinois at Urbana–Champaign, Available at: <https://www.ideals.illinois.edu/handle/2142/44484> [Accessed 30/09/2016], p. 327.

Perillo, M.M., Best, J. L. and García, M. H., 2014. A new phase diagram for combined-flow bedforms. *Journal of Sedimentary Research*, 84, pp. 301–313.

Pentney, R. M. and Dickson, M. E., 2012. Digital grain size analysis of a mixed sand and gravel beach. *Journal of Coastal Research*, 28(1), pp. 196-201.

Precht, E. and Huettel, M., 2003. Advective pore-water exchange driven by surface gravity waves and its ecological implications. *Limnology and Oceanography*, 48(4), pp. 1674–1684.

Rahman, R. and Plater, A. J., 2014. Particle-size evidence of estuary evolution: A rapid and diagnostic tool for determining the nature of recent saltmarsh accretion. Geomorphology, 213, pp. 139-152.

Ramsay, P. J., Cooper, J. A. G., Wright, C. I. and Mason, T. R., 1989. The occurrence and formation of ladderback ripples in subtidal, shallow-marine sands, Zululand, South Africa. *Marine Geology*, 86, pp. 229-235.

Raudkivi, 1997. Ripples on stream bed. *Journal of Hydraulic Engineering*, 123(1), pp. 58-64.

Reddering, J. S. V, 1987. Subtidal occurrences of ladder-back ripples: their significance in palaeo-environmental reconstruction. *Sedimentology*, 34, pp. 253-257.

Reineck, H. E. and Singh, I. B., 1980. *Depositional sedimentary environments*. 2nd Ed. Berlin: Springer-Verlag. p. 549.

Reise, K., 2002. Sediment mediated species interactions in coastal waters. *Journal of Sea Research*, 48, pp. 127-141.

Richardson, E. V., Simons, D. B. and Posakony, G. J., 1961. Sonic depth sounder for laboratory and field use. *U.S. Geol. Survey Circular*, 450, pp. 1-7.

Rouse, H., Posey, C. J., Yasines, S. F., Miller, B., Powell, R. W., Johnson, J. W., Wilson, W. E. and von Kármán, T., 1937. Modern conceptions of the mechanics of fluid turbulence, with discussion. *Transactions of the American Society of Civil Engineers*, 102 (1), pp. 463-543.

Rusello, P. J., Lohrmann, A., Siegel, E. and Maddux, T., 2006. Improvements in Acoustic Doppler Velocimetery. *Proceedings of the7th International conference on Hydroscience and Engineering September 10-13, 2006*, pp. 1-16.

Sanford, L. P. and Maa, J. P.-Y., 2001. A unified erosion formulation for fine sediments. *Marine Geology*, 179, pp. 9-23.

Sanford, L. P., 2008. Modeling a dynamically varying mixed sediment bed with erosion, deposition, bioturbation, consolidation, and armouring. *Computers & Geosciences*, 34, pp. 1263-1283.

Sato, T., Taniguchi, K., Takagawa, T. and Masuda, F., 2011. Generation of tidal bedding in a circular flume experiment: formation process and preservation potential of mud drapes. Geo-Marine Letters, 31, pp. 101-108.

Schindler, R. J. and Robert, A., 2005. Flow and turbulence structure across the ripple-dune transition: An experiment under mobile bed conditions. *Sedimentology*, 52, pp. 627–649, doi:10.1111/j.1365-3091.2005.00706x.

Schindler, R. J., Parsons D. R., Ye, L., Hope, J. A., Baas, J. H., Peakall, J., Manning, A. J., Aspden, R. J., Malarkey, J., Simmons, S., Paterson, D. M., Lichtman, I. D., Davies, A. G., Thorne, P. D., and Bass, S. J., 2015. Sticky stuff: Redefining bedform prediction in modern and ancient environments, *Geology*, 43 (5), pp. 399-402.

Sea-Bird Electronics, 2007. SBE 16*plus* SEACAT manual, #018 [pdf] Available at: http://www.seabird.com/pdf_documents/manuals/16plus_rs232_018.pdf [Accessed 26 June 2013].

Seapoint, 2000. Seapoint turbidity meter user manual, 6/00 [pdf] Available at: http://www.seapoint.com/pdf/stm_um.pdf [Accessed 26 June 2013].

Sekiguchi, T. and Yokokawa, M., 2008. Effect of wave period on combined-flow bedforms: a flume experiment. In: Parsons, D., Garlan, T., and Best, J., eds., *Marine and River Dune Dynamics III*. Leeds: U.K., pp. 281–284.

Sequoia Scientific Inc., 2009. LISST-100X particle size analyzer user manual, v 4.65. [pdf] Available at: http://www.sequoiasci.com/library/software_updates.aspx?Product=LISST-100&id=1 [Accessed 26 June 2013].

Sequoia, 2012. LISST-100X particle size analyzer user manual, v 5.0. [pdf] Available at: http://www.sequoiasci.com/library/software_updates.aspx?Product=LISST-100&id=1 [Accessed 10 July 2013].

Shepard, F. P., 1954. Nomenclature based on sand-silt-clay ratios. *Journal of Sedimentary Petrology*, 24, pp. 151-158.

Shields, A., 1936. Anwendung der Ähnlichkeitsmechanik und der Turbulenzforschung auf die Geschiebebewegung. *Mitteilungen der Preussischen Versuchsanstalt für Wasserbau und Schiffbau*, 26, pp. 1-26. Translated to English by W. P. Ott and J. C. van Uchelen, CalTech, Pasadena, CA. Available at: http://authors.library.caltech.edu/25992/1/Sheilds.pdf [Accessed 26 March 2015].

Shimeta, J and Jumars, P. A. , 1991. Physical mechanisms and rates of particle capture by suspension feeders, *Oceanog. Mar. Biol. Ann. Rev.*, 29, 191–257.

Sheng, J. and Hay, A. E., 1988. An examination of the spherical scatter approximation in aqueous suspensions of sand. *Journal of the Acoustic Society of America*, 83(2), pp. 598-610.

Short. A. D., 1991. Macro-mesal tidal beach morphodynamics – an overview. *Journal of Coastal Research*, 7(2), pp. 417-436.

Simons, D. B., Richardson, E. V. and Nordin, C. F., 1965. *Bedload equation for ripples and dunes*, Professional paper 462-H, USGS, Washington: United States Government Printing Office. p. 9.

Smith, D. J. and Underwood, G. J. C., 1998. Exopolymer production by intertidal epipelic diatoms. *Limnology and Oceanography*, 43(7), pp. 1578-1591.

Smyth, C. E. & Li, M. Z., 2005. Wave-current bedform scales, orientation and migration on Sable Island Bank. *Journal of Geophysical Research*, 110, C02023, pp. 1-12.

Sontek, 2001. [pdf] SonTek/YSI ADV Field/Hydra Acoustic Doppler Velocimeter (Field) technical documentation. Available at: http://cleveland2.ce.ttu.edu/software/instruments/SonTek/ADV_Instruments/ADVManual.pdf [Accessed 26 June 2013].

Soulsby, R. L., 1980. Selecting record length and digitization rate for near-bed turbulence. *Journal of Physical Oceanography*, 10, pp. 208-219.

Soulsby, R. L., Hamm, L., Klopman, G., Myrhaug, D., Simons, R. R., and Thomas, G. P., 1993. Wave-current interaction within and outside the bottom boundary layer. *Coastal Engineering*, 21, pp. 41-69.

Soulsby, R., 1997. *Dynamics of marine sands: A manual for practical applications*. London: Thomas Telford.

Soulsby, R., 2006. Simplified calculation of wave orbital velocities. HR Wallingford Report TR 155 Available at: http://eprints.hrwallingford.co.uk/692/1/TR155.pdf [Accessed 19 September 2014].

Soulsby, R.L., and Clarke, S., 2005. Bed Shear-Stresses Under Combined Waves and Currents on Smooth and Rough Beds. Report TR 137. HR Wallingford, Wallingford, UK. Available at: http://books.hrwallingford.co.uk/acatalog/free_downloads/TR137.pdf [Accessed 29 October 2014].

Soulsby, R. L. and Whitehouse, R. J. S., 2005a. *Prediction of ripple properties in shelf seas-Mark 1 Predictor*. [pdf] Technical Report TR 150, R1.1. Wallingford: HR Wallingford. Available at: http://eprints.hrwallingford.co.uk/280/1/TR150.pdf [Accessed 25 April 2014].

Soulsby, R. L. and Whitehouse, R. J. S., 2005b. *Prediction of ripple properties in shelf seas-Mark 2 Predictor for time evolution*. [pdf] Technical Report TR 154, R2.0. Wallingford: HR Wallingford. Available at: http://eprints.hrwallingford.co.uk/281/1/TR154_-_REPRO_-_Shelf_seas_Mark_2_predictor-_rel2_0.pdf [Accessed 25 April 2014].

Soulsby, R. L., Whitehouse, R. J. S. and Marten, K. V., 2012. Prediction of time-evolving sand ripples in shelf seas. *Continental Shelf Research*, 38, pp. 47-62.

Southard, J. B. and Boguchwal, L. A., 1990. Bed configurations in steady unidirectional water flows part 2: Synthesis of flume data. *Journal of Sedimentary Petrology*, 60(5), pp. 658-679.

Southard, J. B., 1991. Experimental determination of bed-form stability. Annual Review of Earth and Planetary Sciences, 19, pp. 423-455.

Souza, A. J., Bell, P. S., Amoudry, L., 2010. Working toward a common strategy for U.K. sediment transport research. *EOS, Transactions American Geophysical Union*, 91 (5), pp. 45-46.

Souza, A.J. and Lane, A., 2013. Effects of freshwater inflow on sediment transport. *Journal of Operational Oceanography*, 6 (1), pp. 27-31.

Spearman, J. R., Manning, A. J. and Whitehouse, R. J. S., 2011. The settling dynamics of flocculating mud and sand mixtures: part 2-numerical modelling. *Ocean Dynamics*, 61, pp. 351-370.

Stapleton K.R. & Huntley D.A., 1995. Seabed stress determinations using the inertial dissipation method and the turbulent kinetic energy method. *Earth Surface Processes and Landforms*, 20, pp. 807-815.

Stanton, T. K., Chu, D. and Wiebe, P. H., 1996. Acoustic scattering characteristics of several zooplankton. ICES Journal of Marine Science, 53, pp. 289-295.

Sternberg, R. W., 1967. Measurements of sediment movement and ripple migration in a shallow marine environment, *Marine Geology*, 5, pp. 195-205.

Stokes, G. G., 1851. On the effect of the internal friction of fluids on the motion of pendulums. Transactions of the Cambridge Philosophical Society, Vol. IX, Part II, pp. 8-106.

Sutherland, T. F., Amos, C. L. and Grant, J., 1998. The effect of buoyant biofilms on the erodibility of sublittoral sediments of a temperate microtidal estuary. *Limnology and Oceanography*, 43(2), pp. 225-235.

Sutton, M. A., Orteu, J.-J. and Schreier, H., 2009. *Image Correlation for Shape, Motion and Deformation Measurements: Basic Concepts, Theory and Applications*. New York, Springer Science, p. 322.

Tennekes, H. and Lumley, J. L., 1972. A first course in turbulence. Cambridge: The MIT Press. p. 300.

Thompson, C. E. L and Amos, C. L., 2004. Effect of sand movement on a cohesive substrate. *Journal of Hydraulic Engineering*, 130(11), pp. 1123-1125.

Thompson, C.E.L., Kassem, H. and Williams, J., 2013. Nearshore sediment resuspension and bed morphology (BARDEX II). *In:* Conley, D.C., Masselink, G., Russell, P.E. and O'Hare, T.J. (eds.), *Proceedings 12th International Coastal Symposium* (Plymouth, England), *Journal of Coastal Research*, Special Issue No. 65, pp. 1593-1598.

Thompson, C. E. L., Williams, J. J., Metje, N. , Coates, L. E. and Pacheco, A., 2012. Turbulence based measurements of wave friction factors under irregular waves on a gravel bed, *Coastal Engineering*, 63, pp. 39-47.

Thorne, P. D., Vincent, C. E., Hardcastle, P. J., Rehman, S. and Pearson, N, 1991. Measuring suspended sediment concentrations using acoustic backscatter devices. *Marine Geology*, 98, pp. 7-16.

Thorne, P. D., Hardcastle, P. J. and Soulsby, R. L., 1993. Analysis of acoustic measurements of suspended sediments. *Journal of Geophysical Research*, 98, C1, pp. 899-910.

Thorne, P. D. and Hanes, D. M., 2002. A review of acoustic measurement of small-scale sediment processes. *Continental Shelf Research*, 22, pp. 603-632.

Thorne, P. D., Davies, A. G. and Williams, J. J., 2003. Measurements of near-bed intra-wave sediment entrainment above vortex ripples. Geophysical Research Letters, 30, 2028, doi: 10.1029/2003GL018427, pp. 1-4.

Tolhurst, T. J., Jesus, B., Brotas, V. and Paterson, D. M., 2003. Diatom migration and sediment armouring – an example from the Tagus Estuary, Portugal. *Hydrobiologia*, 503, pp. 183-193.

Tolhurst, T. J., Friend, P.L., Watts, C., Wakefield, R., Black, K. S. and Paterson, D. M., 2006. The effects of rain on the erosion threshold of intertidal cohesive sediments. *Aquatic Ecology*, 40, pp. 533-541.

Tolhurst, T. J., Black, K. S., and Paterson, D. M., 2009. Muddy Sediment Erosion: Insights From Field Studies. *Journal of Hydraulic Engineering*, 135 (2), pp. 73-87.

Torfs, H., Mitchener, H., Huysentruyt, H. and Toorman, E., 1996. Settling and consolidation of mud/sand mixtures. *Coastal Engineering*, 29, pp. 27-45.

Tucker, M. E., 1991. *Sedimentary Petrology: an introduction to the origin of sedimentary rocks*. 2nd edition, Blackwell Science, p. 260.

Traykovski, P., Hay, A. E., Irish, J. D. and Lynch, J. F., 1999. Geometry, migration, and evolution of wave orbital ripples at LEO-15. *Journal of Geophysical Research*, 104 (C1), pp. 1505-1524.

Traykovski, P., 2007. Observations of wave orbital scale ripples and a non-equilibrium time-dependent model, *Journal of Geophysical Research: Oceans*, 112, C06026, doi:10.1029/2006JC003811, pp. 1-19.

Underwood, G. J. C ., Paterson, D. M. and Parkes, R. J., 1995. The measurement of microbial carbohydrate exopolymers from intertidal sediments. *Limnology and Oceanography*, 40(7), pp. 1243-1253.

U.S. Army Corps of Engineers, 2002a. *Coastal Engineering Manual: Part 2 Coastal Hydrodynamics*, *Engineer Manual 1110-2-1100*. [e-book] Washington, D.C.: U.S. Army Corps of Engineers. Available at: http://140.194.76.129/publications/eng-manuals/EM_1110-2-1100_vol/PartII/PartII.htm [Accessed 19 July 2013].

U.S. Army Corps of Engineers, 2002b. *Coastal Engineering Manual: Part 3 Coastal sediment processes*, *Engineer Manual 1110-2-1100*. [e-book] Washington, D.C.: U.S. Army Corps of Engineers. Available at: http://140.194.76.129/publications/eng-manuals/EM_1110-2-1100_vol/PartIII/PartIII.htm [Accessed 19 July 2013].

U.S. Army Corps of Engineers, 2002c. *Coastal Engineering Manual: Part 4 Coastal geology*, *Engineer Manual 1110-2-1100*. [e-book] Washington, D.C.: U.S. Army Corps of Engineers. Available at: http://140.194.76.129/publications/eng-manuals/EM_1110-2-1100_vol/PartIV/PartIV.htm [Accessed 19 July 2013].

Valle-Levinson, A., 2010. Definition and classification of estuaries. In: Valle-Levinson, A. (Ed.), *Contemporary Issues in Estuarine Physics*. Cambridge: Cambridge University Press, pp. 27–61.

van de Koppel, J., Herman, P. M. J., Thoolen, P., and Heip, C. H. R. , 2001. Do alternate stable states occur in natural ecosystems? *Ecology*, 82 (12), 3449-3461.

van den Berg, J. H., 1987. Bedform migration and bed-load transport in some rivers and tidal environments. *Sedimentology*, 34, pp. 681-698.

van den Berg, J. H. and van Gelder, A., 1993a. Prediction of suspended bed material transport in flows over silt and very fine sand. *Water Resources Research*, 29(5), pp. 1393-1404.

van den Berg, J. H. and van Gelder, A., 1993b. A new bedform stability diagram, with emphasis on the transition of ripples to plane bed in flows over fine sand and silt. In: *Alluvial Sedimentation* (ed. by M. Marzo & C. Puigdefabregas), International Association of Sedimentologists Special Publication 17. Oxford: Blackwell Publishing Ltd., pp. 11–21.

van der Mark, C. F., Blom, A. and Hulscher, S. J. M. H., 2008. Quantification of variability in bedform geometry. *Journal of Geophysical Research*, 113, pp. 1-11.

van Kessel, T., Spruyt-de Boer, A., van der Werf, J., Sittoni, L., van Prooijen, B. and Winterwerp, H., 2012. *Bed module for sand-mud mixtures: in framework of BwN project NTW 1.3 mud dynamics*. Delft: Deltares. Available at: <https://publicwiki.deltares.nl/display/BWN1/Morphological+predictor+for+mixed+beds?preview=%2F114197213%2F115048893%2FNTW13_endreport_merged.pdf> [accessed 5 April 2017], p. 129.

van Ledden, M., 2002. A process-based sand-mud model. In: J.C. Winterwerp and C. Kranenburg, Eds. 2002. *Proceedings in Marine Science volume 5: Fine Sediment Dynamics in the Marine Environment*. Elsevier. pp. 577-594.

van Ledden, M., van Kesteren, W. G. M and Winterwerp, J. C., 2004. A conceptual framework for the erosion behaviour of sand-mud mixtures. Continental Shelf Research, 24, pp. 1-11.

van Rijn, L. C., 1984a. Sediment transport, part I: Bed load transport. *Journal of Hydraulic Engineering*, 110(10), pp.1431-1456.

Van Rijn, L. C., 1984b. Sediment transport, part II: suspended load transport. *Journal of Hydraulic Engineering*, 110(11), pp. 1613-1641.

van Rijn, L.C., 1984c. Sediment transport, Part III: Bed forms and alluvial roughness. *Journal of Hydraulic Engineering*, 110, pp. 1733–1754.

van Rijn, L. C., 1993. *Principles of sediment transport in rivers, estuaries and coastal seas*. Amsterdam: Aqua Publications, p. 500.

van Rijn, L. C., 2006. *Manual Sediment Transport Measurements in Rivers, Estuaries and Coastal Seas*. Amsterdam: Aqua Publications, p. 356.

van Rijn, L. C., 2007. Unified view of sediment transport by currents and waves III: graded beds. *Journal of Hydraulic Engineering*, 133(7), pp. 761-775.

Vanoni, V. and Brooks, N. H., 1957. *Laboratory studies of the roughness and suspended load of alluvial streams*. Sedimentation Laboratory Report E-86. Pasadena, California: California Institute of Technology, p. 130.

Venditti, J. G., Church, M. and Bennett, S. J., 2005. On the transition between 2D and 3D dunes. *Sedimentology*, 52, pp. 1343-1359.

Villaret, C., Huybrechts, N., Davies, A. G., and Way, O., 2011. Effect of bed roughness prediction on morphodynamic modelling: application to the Dee estuary (UK) and to the Gironde estuary (France). In *Proceedings of 34th IAHR World Congress*, pp. 1149–1156.

Vincent, C. E., Marsh, S. W., and Webb, M.P., 1999. Spatial and temporal structures of suspension and transport over megaripples on the shore face. *Journal of Geophysical Research: Oceans*, 104 (C5), pp. 11215-11224.

von Kármán, T., 1930. Mechanische Ähnlichkeit und Turbulenz. Nachrichten von der Gesellschaft der Wissenschaften zu Göttingen, Fachgruppe 1 (Mathematik), 5, pp. 58–76. Translated by J. Vanier, 1931, as Mechanical Similitude and Turbulence, Technical Memorandums, National Advisory Committee for Aeronautics, no. 611. Available at: http://ntrs.nasa.gov/archive/nasa/casi.ntrs.nasa.gov/19930094805.pdf [Accessed 29 July 2014].

Voulgaris, G. and Trowbridge, J. H., 1998. Evaluation of the acoustic Doppler velocimeter (ADV) for turbulence measurements. *Journal of atmospheric and oceanic technology*. 15, pp. 272-289.

Waeles, B., Le Hir, P. and Lesueur. P., 2008. A 3D morphodynamic process-based modelling of a mixed sand/mud coastal environment: the Seine estuary, France. In: T. Kusuda, H. Yamanishi, J. Spearman and J. Z. Gailani, eds. *Proceedings in marine science Volume 9, Sediment and Ecohydraulics: INTERCOH 2005*, pp. 477-498.

Wentworth, C. K., 1922. A Scale of Grade and Class Terms for Clastic Sediments, The Journal of Geology, Vol. 30, No. 5, pp. 377-392.

Wahl, T. L., 2003. Discussion of “Despiking Acoustic Doppler Velocimeter Data” by Derek G. Goring and Vladimir I. Nikora (2002), Journal of Hydraulic Engineering, 129, pp. 484-487.

Wiberg, P. L., and Sherwood, C. R., 2008. Calculating wave-generated bottom orbital velocities from surface-wave parameters. *Computers & Geosciences*, 34, pp. 1243-1262.

Widdows, J. and Brindsley, M., 2002. Impact of biotic and abiotic processes on sediment dynamics and the consequences to the structure and functioning of the intertidal zone. Journal of Sea Research, 48, pp. 143-156.

Wilcox, R. R., 2012. *Introduction to Robust Estimation and Hypothesis Testing*. 3rd Ed., Waltham, MA: Elsevier. p. 700.

Wilkinson, R. H., 1986. Variation of roughness length of a mobile sand bed in a tidal flow. *Geo-Marine Letters*, 5, pp. 231-239.

Williams, J. J., Bell, P. S. and Thorne, P. D., 2005. Unifying large and small wave-generated ripples. *J. Geophys. Res.,* 110, pp. 1-18. doi:10.1029/2004JC002513.

Williams, J. J., 2012. Recent advances in instrumentation used to study sediment transport, In: eds by M. Z. Li, C. R. Sherwood, P. R. Hill 2012. *Sediments, morphology, and sedimentary processes on*

continental shelves: advances in technologies, research and applications. Hoboken, USA: Wiley-Blackwell. pp. 173-196.

Whitehouse, R., Soulsby, R., Roberts, W. And Mitchener, H., 2000. *Dynamics of estuarine muds: A manual for practical applications*. London: Thomas Telford, p. 210.

Winterwerp, J. C. and van Kesteren, W. G. M., 2004. *Introduction to the physics of cohesive sediment in the marine environment*. *Developments in sedimentology 56*. Amsterdam: Elsevier B. V., p. 466.

Winterwerp, J. C., Manning, A. J., Martens, C., de Mulder, T. and Vanlede, J., 2006. A heuristic formula for turbulence-induced flocculation of cohesive sediment. *Estuarine, Coastal and Shelf Science*, 68, pp. 195-207.

Wolf, J., 1997. The analysis of bottom pressure and current data for waves. In: *Proceedings of the 7th International Conference on Electronic Engineering in Oceanography*. Southampton, June 1997, Conference Publication 439, London: Institution of Electrical Engineers, pp. 165-169.

Wotton, R. S., 2004. The essential role of exopolymers (EPS) in aquatic systems. In *Oceanography and Marine Biology: An Annual Review*, 42, CRC, pp. 57-64.

Yalin, M. S., 1977. *Mechanics of Sediment Transport*, 2nd ed., Pergamon Press, Oxford. p. 298.

Yam, K., Burns, A. D., Ingham, D. B. and McCaffrey, W. D., 2013. The influence of the lift force on the settling velocities of rotating particles in two-dimensional shear flow. Journal of Hydraulic Engineering, preview manuscript [online] http://ascelibrary.org/doi/abs/10.1061/%28ASCE%29HY.1943-7900.0000792 [Accessed 20 September 2013]

Yokokawa, M., 1995. Combined-flow ripples: genetic experiments and applications for geologic records. *Earth and Planetary Sciences, Memoirs of the Faculty of Science*, *Kyushu University*, Series D, 29, pp. 1–38.

Zanke, U.C.E. 2003. On the influence of turbulence on the initiation of sediment motion, *International Journal of Sediment Research*, 18(1), pp. 17-31.

11 Index